Virtual sensors for active noise control

Jacqueline M. Munn

Department of Mechanical Engineering

The University of Adelaide

South Australia 5005

Australia

Printed 13th of May 2004. Submitted for the degree of Ph.D in Mechanical Engineering on the

17th of July 2003; awarded 27th of October 2003

Abstract

The need to attenuate noise transmitted into enclosed spaces such as aircraft cabins, automobiles and mining cabins has provided the impetus for many active noise control studies. Studies into active interior noise control began with a pressure squared cost function utilising multiple error sensors and control sources in an attempt to produce global control of the interior sound field. This work found problems with observability of the primary disturbances and a large number of error sensors and control sources were required to produce global control. Since this early work in the 1980's, many new acoustic based cost functions have been developed to improve on the performance of the pressure squared cost function.

This thesis will focus on one novel acoustic cost function, virtual error sensing. Virtual error sensing is a relatively new technique which produces localised zones of attenuation at a location remote to the physical sensors. The practical advantage of this method is the people within these enclosed spaces are able to observe a reduction in sound pressure level without their movement being restricted by error sensors located close to their ears.

The aim of this thesis is to further investigate the performance of forward-difference virtual error sensors in order to understand the factors that affect the accuracy of the pressure prediction at the virtual location and use this information to develop more accurate and efficient forward-difference virtual sensors.

These virtual sensors use linear arrays of microphones containing two or more microphone elements and a linear or quadratic approximation is used to predict the sound at the virtual location. The prediction method determines the weights applied to each microphone signal to predict the sound pressure level at the virtual location. This study investigates susceptibility of the sensors to corruption as a result of phase and sensitivity mismatch between the microphones, as well as in the location of the elements in the error sensing array. A thorough error analysis of the forward-difference virtual microphones was performed in a one-dimensional sound field and in a plane wave sound field. The accuracy of the quadratic virtual microphone was found to be strongly affected by the presence of short wavelength extraneous noise.

From this study, two novel virtual error sensing techniques were developed, namely; higher-order virtual sensors and adaptive virtual sensors. The higher-order virtual error sensors still employ the linear and quadratic prediction method but extra microphone elements are added to the array. The aim of these higher-order virtual microphones is to produce a more accurate prediction of the pressure at the virtual location by spatially filtering out any short wavelength extraneous noise that may corrupt the prediction. These virtual sensors were tested in a real-time control scenario in both a one-dimensional reactive sound field and in a free field. This work found that the higher-order virtual microphones can improve the prediction accuracy of the original virtual sensors but are still prone to problems of phase, sensitivity and position errors.

Finally, the adaptive LMS virtual sensors were investigated in a SIMULINK simulation and tested experimentally using real-time control in a one-dimensional sound field. It was hoped that an adaptive LMS algorithm could overcome previous difficulties arising from inherent and transducer errors by adapting the weights of the signals from the sensing elements which form the array. The algorithm adapts the sensing microphone signals to produce the same signal as the microphone at the virtual location. Once this has been achieved, the sensing microphone weights are fixed and the microphone at the virtual location is removed, thus creating a virtual microphone. The SIMULINK simulation allowed the performance of the fixed weight and

virtual microphones to be investigated in the presence of only phase errors, sensitivity errors and position errors and in the presence of all three combined. This work showed that the adaptive virtual sensors had the ability to compensate for the errors. The number of modes used in the simulations was varied to observe the performance of all virtual sensors in the presence of higher-order modes. The prediction accuracy of the fixed weight virtual sensors was found to be greatly affected by the presence of higher-order modes.

The use of the adaptive virtual microphones to produce localised zones of quiet was examined experimentally using real-time control. The study found the real-time control performance is superior to that of the fixed weight higher-order virtual microphones and the original forward-difference virtual microphones.

Statement of originality

To the best of my knowledge, except where otherwise referenced and cited, everything that is presented in this thesis is my own original work and has not been presented previously for the award of any other degree or diploma in any University. If accepted for the award of the degree of Ph.D. in Mechanical Engineering, I consent that this thesis be made available for loan and photocopying.

Jacqueline M. Munn

Acknowledgments

Most of all I would like to thank my three supervisors, Professor Colin Hansen, Dr. Ben Cazzolato and Dr. Colin Kestell. Thanks to Colin Hansen for his experience, time and furious red pen. Thanks to Colin Kestell for convincing me not to quit. Big thanks to Ben Cazz for all his time, endless support, great ideas and for putting up with me saying “I’m over it” too many times. Without Ben this thesis would never have been completed.

Thanks to George Osbourne, Silvo De Ieso and Derek Franklin for assisting me with my experiments. Extra appreciation is extended to George for building me the most exquisite experimental equipment.

I would like to acknowledge the friendship and support of Richard Craig, Daniel Handley, Tonia Camporeale, Xiaojun Qiu, Xun Li and Nick Burgan. To Ricky Rick Morgans, with whom I shared an office, thank you for the many laughs, in depth political, ethical and scientific discussions and keeping me level headed during the most stressful times.

Deep gratitude is expressed to my parents, Roselie Copley and John Munn, for the sacrifices you both made to provide me with a good education.

I would like to thank Benjamin Soulé de Bas for his understanding, support and for the life we share.

Contents

List of Figures

Chapter 1

Introduction

Active noise control has the potential to be an effective solution to noise problems which commonly exist in space restricted enclosures such as aircraft, automobiles and mining vehicle cabins. These environments are not amenable to practical passive noise control because they are characterised by low frequency disturbances, and the consequent space and mass requirements for passive noise control are unacceptable. Active noise control has been found to be effective at providing low frequency control without requiring significant space or significant additional mass.

The first attempts to control enclosed sound fields using active noise control systems used a pressure squared cost function, with the aim of achieving global control. There were observability problems with the sensing system and in order to achieve control a number of requirements concerning the location of the control and sensing elements have to be met. Results were especially poor in modally dense acoustic environments where active control resulted in small zones, a fraction of a wavelength in size of localised attenuation centred around the error sensors.

An important factor is the amount of occupant-observed reduction within the enclosure, not the level of attenuation achieved at the error sensors or throughout the enclosure. Therefore,

attempting global control may be unnecessary and local control could be sufficient to achieve the required attenuation for the observer. Local control is designed to produce localised zones of control generally centralised around the error sensors. The spatial extent of these localised zones have been quantified by a number of researchers. For a 10 dB reduction in the primary sound field, the localised zone of attenuation around a pressure error sensor is a sphere of diameter one tenth of a wavelength (Joseph et al., 1994). This is quite small and therefore, for the observer to detect any reduction in the sound pressure level, the error sensor needs to be located effectively at the observer's ear. This is clearly not practical, as this would restrict the free movement of the observer's head. One possible solution is to move the error sensor away from the observer's ear and project the zone of quiet away from the error sensors toward the observer's ear. This is known as virtual error sensing.

Cazzolato (1999) suggested a one-dimensional virtual microphone using a forward-difference prediction array of two or three microphones to predict the sound pressure level at a remote location. Kestell (2000) quantified the performance of these forward-difference virtual microphones using simulated control in analytical models and post-processed experimental data. This work found that the performance of the virtual sensors was compromised by experimental errors and the presence of short wavelength extraneous noise. The purpose of the work presented in this thesis is to investigate and solve the problems observed by Kestell (2000) with the aim of developing a robust virtual sensing system. In this thesis two novel virtual sensing systems are presented; higher-order forward-difference virtual microphones, and adaptive LMS virtual microphones. In addition, it is important to understand the effects of experimental errors on the prediction accuracy of the virtual microphone. An attempt has been made to quantify such errors.

1.1 Aims

The aims of this research are to

⋆ investigate the performance of forward-difference virtual microphones in a real-time control scenario in a one-dimensional reactive sound field;

⋆ perform an error analysis of forward-difference virtual microphones to determine the effect of phase and sensitivity mismatch in a one-dimensional reactive sound field and in a plane wave sound field; and

⋆ develop and assess the performance of alternative virtual error sensing techniques that will improve the accuracy of the pressure and particle velocity prediction at the virtual location.

1.2 Overview of the Thesis

This thesis begins with a literature review in Chapter 2. Chapter 3 presents real-time control results using the forward-difference virtual microphones in a one-dimensional waveguide. Four acoustic conditions are investigated: an acoustic resonance and anti-resonance in both a lightly and a heavily damped one-dimensional waveguide. The real-time results were compared against simulated and post-processed control results. These results highlighted the susceptibility of the virtual microphones to corruption from short wavelength extraneous noise, due to the presence of higher-order modes, as well as calibration errors. A thorough theoretical error analysis is presented in Chapter 4. Here equations are derived quantifying the effect that errors such as phase, sensitivity, position and inherent errors due the finite separation of the microphones have on the prediction accuracy of the virtual microphone formulations.

Because the forward-difference virtual microphones were affected by short wavelength extraneous noise, a new type of forward-difference virtual microphone was developed in an attempt

to spatially filter out this noise. These virtual microphones, called higher-order virtual microphones, used novel over-constrained forward-difference prediction algorithms which are derived in Chapter 5. Also in this chapter, the results of real-time control experiments in a one-dimensional waveguide are presented. Chapter 5 also presents the real-time control results achieved in a free-field using all the different types of forward-difference virtual microphones. These experiments were conducted in the anechoic chamber located at The University of Adelaide.

Chapter 6 introduces the adaptive virtual microphone which uses the gradient descent algorithm to determine the optimal microphone weights. The performance of the adaptive virtual microphone was first tested in a MATLAB SIMULINK simulation. This allowed errors such as phase, sensitivity and position to be included in the model individually and combined to observe the effect that the errors have on the performance of the virtual microphones. In particular, the ability of the adaptive virtual microphone to compensate for these experimental errors was tested. In addition, the effect that the higher-order modes have on the prediction accuracy of the virtual microphone formulations was investigated in the SIMULINK model. Finally, real-time control experiments were conducted in a one-dimensional waveguide and the results compared with other real-time control experiments.

The first virtual microphone technique was suggested by Elliott and David (1992) and investigated by Garcia-Bonito and Elliott (1995b,a) and Garcia-Bonito et al. (1996). This method involves the modification of transfer functions to predict the pressure at the virtual location. In Chapter 7 the performance of the transfer function virtual microphone technique is compared against that of the forward-difference virtual microphone and the adaptive virtual microphone in both a one-dimensional waveguide and a free field.

Chapter 8 summarises the major findings from this thesis from which conclusions are drawn and recommendations for future work are presented.

Chapter 2

Literature Review

The published literature on active noise control is vast. Thus this review will concentrate on work involving the active control of noise in an enclosed space. The topics covered in the literature review relate to the methods investigated by other researchers to achieve noise control within enclosures, including different cost functions as well as acoustic and structural sensing and control methods. The following topics on active control of enclosed sound fields will be discussed:

Global control Global control attempts to achieve sound attenuation throughout an enclosure. This has been attempted using a number of different cost functions including squared pressure and energy density. A review of methods used to achieve global control is presented.

Active Structural Acoustic Control (ASAC) Active structural acoustic control attempts to control the interior sound field by controlling the vibrations of the surrounding structure. Researchers found that minimising structural vibration levels does not necessarily guarantee a reduction in the interior sound field.

Radiation Modes This is a method of ASAC in which the structural vibrations are decomposed into orthogonal modes which are combinations of the structural modes. Radiation modes are orthogonal in terms of radiated sound power so a reduction in the amplitude of a radiation mode guarantees a reduction in radiated sound power. On the other hand, vibration modes are orthogonal in terms of structural vibration, not radiated power, so a reduction in the amplitude of a vibration mode does not guarantee a reduction in radiated sound power.

Local control Local control is the term used when a localised zone of noise control is achieved at a few desired locations at the expense of increased noise levels at other locations. Realising that global control is difficult, a number of researchers began to investigate production of localised zones of control at desired locations.

Energy Density Energy density is a cost function sometimes used in active noise control. Energy density is the sum of the acoustic kinetic and potential energy densities, and is given by:

$$ED = \frac{p^2}{2\rho c^2} + \frac{\rho v^2}{2} \tag{2.1}$$

where p is the pressure amplitude at some location, ρ is the density of the fluid, c is the speed of sound and v is the particle velocity at same location. This cost function offers a number of advantages over the traditional squared pressure cost function. Energy density control does not have the observability problems that pressure control does and control also results in broader zones of attenuation than is achievable using the pressure squared cost function. Observability (thus controllability) problems occur with pressure control when the error microphone is located at the node of a mode. Since there are fewer nodal surfaces in an energy density field than a pressure field and therefore the likelihood of observability problems occurring with energy density sensing are less than with pressure sensing. For a more detailed discussion of the observability problems associated with pressure control see Section 2.1.1.

Sound Intensity Sound intensity is the product of sound pressure and particle velocity, given by:

$$I(r,t) = p(r,t)v(r,t) \tag{2.2}$$

where $p(r,t)$ is the instantaneous sound pressure and $v(r,t)$ is the instantaneous acoustic particle velocity. Sound intensity is a vector quantity. There are two forms of sound intensity; namely, active and reactive sound intensity. Active sound intensity has a time averaged non-zero value which indicates a local net transport of energy. Reactive intensity has a time-averaged value of zero which indicates local oscillatory transport of energy. The use of sound intensity as a cost function for active noise control has been mainly restricted to the control of free field sound radiation.

Active Headsets

Active headsets employ active control technology to improve the low frequency sound attenuation, a well known deficiency of passive personal hearing protection. Many researchers have looked at feedforward active headsets, feedback headsets and hybrid controller headsets.

Virtual error sensing

Virtual error sensing projects a zone of attenuation away from error sensors to produce a localised zone of attenuation at a desired location such as at an observer's ear. Two types of virtual sensors currently exist: transfer function based virtual microphones and forward-difference virtual microphones.

2.1 Global Control

2.1.1 Squared pressure cost function

The need to provide a safe acoustic environment for people within light aircraft, heavy mining vehicles and even automobiles has provided the impetus for much of this study. Active noise control within enclosed spaces began with using a pressure squared cost function with a number of error microphones and secondary sources to achieve global control. In a series of papers, several authors, Nelson et al. (1987b), Bullmore et al. (1987) and Elliott et al. (1987) have studied the active minimisation of harmonic enclosed sound fields. This work involved using quadratic optimisation theory to control the sound field generated by a single primary point source using either the sum of the squared pressures at a number of points (in an attempt to achieve global control) or the global acoustic potential energy with a number of secondary point sources throughout the lightly damped rigid enclosure. Most of this work looked at enclosures with low modal densities where fewer error sensors are required for control.

The effect of the location of the error microphones and secondary sources in an enclosure was investigated by Bullmore et al. (1987). Standing waves exist at the resonance frequencies of the enclosure which means there are locations of maximum and minimum acoustic pressure which do not change with time. Therefore it is important to know the location of primary field nodes and anti-nodes within the enclosure to ensure that the error microphones and secondary sources are not placed there. As nodes are locations of minimum pressure, placing a sensor at this location means that a mode will not be sensed; similarly placing a secondary source at a node of a mode means that the mode cannot be excited. In a rectangular enclosure of low modal density, anti-nodes exist in each corner of the enclosure. Computer simulations showed that at resonance and with error sensors located where the primary sound field is a maximum, sound level reductions using squared pressure minimisation at these error sensors were similar to those using global potential energy minimisation.

Global control in a sound field with high modal densities has proved difficult using a pressure squared cost function. However, with a large number of control sources or with the primary and control sources separated by less than half a wavelength, global control can be achieved. Experimental work by Elliott et al. (1987) showed that there can be an overall increase in the level of the sound field when attempting to minimise the noise at a frequency corresponding to an anti-resonance. Controlling anti-resonance frequencies is considerably more difficult as a result of many modes contributing to the sound field compared to resonance frequencies where a single mode dominates the response. Elliott et al's experimental work confirmed that there are significant sound reductions at resonance frequencies with the error microphones located at anti-nodes of the sound field. Their conclusion was that active noise control is most successful in enclosed resonant fields with low modal density.

Elliott and Nelson (1987), realising that global control within a diffuse acoustic environment is difficult (and sometimes impossible), examined the spatial extent of localised zones of control around single error sensors. They found that active control of a diffuse sound field results in localised zones of attenuation in the shape of a sphere with a diameter of a tenth of a wavelength within which the reduction is greater than 10dB. Global control was only achieved when controlling a sound field of low modal density.

Bullmore et al. (1990) used the theory developed previously (Nelson et al., 1987a, Bullmore et al., 1987 and Elliott et al., 1987) to conduct theoretical studies into actively controlling propeller induced aircraft cabin noise. These theoretical studies involved modelling a BAe78 aircraft fuselage structural response as a finite, isotropic cylindrical thin shell with a floor and the cabin acoustic response as a hard walled cylindrical cavity. The study attempted to control the first and second harmonic of the propeller blade pass frequency. For this, the control system consisted of 16 loudspeaker control sources and 32 error sensors positioned in a plane at the average height of a passengers head. The authors realised that global control of this sound field would not be possible without a considerable increase in the number of error sensors and control sources. Instead they decided to restrict the region of control to a single plane. Average

control results were 14 dB for the first harmonic and 4 dB for the second harmonic over the plane. This control also produced localised zones of attenuation at error sensors of up to 35 dB.

Johansson et al. (1999) investigated experimentally the performance of a twin-reference control system to attenuate noise from two propellers being transmitted into an aircraft fuselage. The level of control achieved was assessed in a plane corresponding to average head height. With the two propellers syncrohronised 18 dB of attenuation of the blade pass frequency was recorded. With the propellers unsyncrohronised attenuation of 3-6 dB was achieved.

Guo et al. (2002) studied the performance of local and global active control systems within rooms. This work analysed the effect of control and primary source location as well as damping on the performance of a global control system. Many of the outcomes of this study agreed with the earlier work of Nelson et al. (1987b) and Bullmore et al. (1987). They found that the location of the primary source has a large effect on the level of global control achieved and that the distance between the control and primary sources must be less than half a wavelength to achieve global control as suggested by Bullmore et al. (1987). Increasing the amount of damping in the room resulted in a decrease in the level of attenuation achieved.

2.1.2 Active Structural Acoustic Control (ASAC)

Global control has also been attempted using Active Structural Acoustic Control (ASAC) which is a combination of active noise and active vibration control. ASAC can be achieved by reducing the amplitudes of vibrations modes which are efficient radiators or by rearranging (or restructuring) modes so they radiate less efficiently. This control method has been researched and developed by a number of authors, Fuller and Jones (1987), Fuller et al. (1989b), Fuller et al. (1991), Snyder and Hansen (1991a), Thomas et al. (1993a), Bullmore et al. (1987), Maillard and Fuller (1998) and Guigou et al. (1996). The concept of radiation modes (explained in detail in Section 2.1.2.1) is used to decompose the structural vibration such that each radiation

mode is orthogonal with respect to the radiated sound field. Shaped polyvinylidene fluoride materials, commonly called shaped sensors have also been developed to sense only radiation modes (refer to Section 2.1.2.2).

The development of ASAC began with Fuller and Jones (1987) when they suggested that because the interior noise of an aircraft is directly coupled to the fuselage vibration, global control of the aircraft interior sound field can be achieved by controlling the fuselage vibration. This was tested in a finite unstiffened aluminium cylinder with capped ends, representative of a simplified aircraft fuselage. The interior noise disturbance produced by the propellers was simulated using a single monopole source and control was supplied by a single vibration actuator. Experiments produced global attenuation of 10 to 20 dB in interior noise. These good results were obtained because, in this particular example, only one structural mode coupled well with the acoustic interior and therefore only one control source was required. The authors stated that for every structural mode that is well coupled with one or more interior acoustic modes, an independent control source is required. Clearly then, this method will only be effective for sound fields with low modal density. These preliminary findings were supported by additional work by Jones and Fuller (1989). The experimental set up was similar to that used in the experiments conducted earlier by Fuller and Jones (1987) except that two external acoustic sources and two control actuators were used. Using the dual control sources produced an attenuation of 30 dB at resonance.

Fuller et al. (1989b) applied ASAC to sound transmission through an elastic circular plate with accelerometers used as error sensors instead of microphones which were used in their earlier work (Fuller and Jones, 1987 and Jones and Fuller, 1989). In this case, the use of accelerometers as error sensors led to reduced control performance compared to microphones as error sensors, showing that minimising structural vibration does not necessarily lead to a reduction in the transmitted sound. This was an important result since it led to the development of the radiation mode concept for use in active noise control.

Fuller et al. (1991) and Snyder and Hansen (1991a) described the mechanisms associated with

the control of structural vibration, *modal suppression* and *modal restructuring* . *Modal suppression* can control only the modes that couple well with the sound field while the remaining modes are left uncontrolled. However in most cases, the number of structural modes controlled is equal to the number of actuators used. *Modal restructuring,* sometimes called *modal rearranging,* occurs when the structural vibration distribution is modified in terms of the relative vibration phase distribution over the structure, to reduce the radiation efficiency. This can sometimes lead to an increase in overall structural vibration levels.

Snyder and Hansen (1991a) investigated the effect that control source location has on the two ASAC mechanisms. In this case ASAC was applied to a rectangular panel mounted in an infinite baffle radiating into free space with a single control source. It was concluded from this work that the location of the vibration control source determined which mechanism of structural control was invoked and hence the level of control achieved.

Rossetti and Norris (1996) used a deHavilland DASH-7 fuselage section to experimentally compare the performance of structural and acoustic sensors and control actuators in an active noise control system. Their analysis considered the physical mechanism responsible for the noise. Comparing structural and acoustic actuators demonstrated that below 70Hz the structural actuators performed at least 10 dB better than the acoustic actuator because at low frequencies the structural/acoustic coupling dominates the acoustic response. Between 70 and 200 Hz the performance associated with the two different actuator types converges. Above 200 Hz the acoustic actuators performed better than the structural system as acoustic modes begin to dominate the acoustic response.

Sun et al. (1996) developed distributed piezoelectric actuators to globally reduce the interior noise and structural vibrations of a uniform cylindrical shell with rigid end caps, which was used as a simplified model of an aircraft fuselage. Two distributed piezoelectric actuators were designed based on the structural-acoustic coupling properties of the system. Simulated and experimental results showed that these actuators were capable of reducing the tonal shell structural vibrations and the interior noise at the same time.

Thomas et al. (1993a) based their work on the analytical aircraft fuselage model used by Bullmore et al. (1987) and examined the effectiveness of using a cost function proportional to the total kinetic energy in the cylindrical shell. They found it difficult to obtain notable reductions in the vibrational energy at the fundamental blade pass frequency because a large number of modes that contribute significantly to the interior acoustic field are excited at this frequency. They also noted that an impractical number of secondary sources are required to obtain a significant global reduction. In the companion paper, Thomas et al. (1993b) minimised total acoustic potential energy within the cylinder and achieved considerable reductions using very few secondary sources. The authors attributed this improvement to very specific structural acoustic coupling.

Maillard and Fuller (1998) compared two methods of sound radiation control from a baffled rectangular plate using structural sensing techniques. Their first approach, Discrete Structural Acoustic Sensing (DSAS) uses an accelerometer array, the outputs of which were individually weighted and summed together to estimate the far-field radiated pressure in a given direction. Their second approach, Discrete Structural Volume Acceleration Sensing (DSVAS), is a simplification of the first in which the individual accelerometer signals are summed to get an estimate of the net volume acceleration of the structure. Guigou et al. (1996) showed in a letter to the editor that the net volume velocity of a planar structure radiating to the free field is equivalent to the far field pressure in a direction normal to the structure. Hence, as DSVAS is an estimate of the net volume acceleration of the structure, minimising it will minimise the far field pressure.

2.1.2.1 Radiation Modes

Traditionally, ASAC was employed in an attempt to control the sound radiated from a vibrating structure by reducing the overall amplitude of structural vibration or by modifying it in such a way as to make it less efficient. However, reducing the amplitude of the dominant structural vibration mode, or even the overall structural vibration, does not guarantee a reduction in

radiated sound (Fuller et al., 1989a). This occurs because structural modes do not radiate independently, as the radiated sound due to one structural mode can interfere with that radiated by other structural modes. A solution to this problem is to decompose the structural vibration into radiation modes which are orthogonal with respect to the radiated sound field and therefore radiate independently.

Borgiotti (1990) and Cunefare (1991) were the first to develop a formulation to describe structural vibration in terms of radiation modes. Radiation modes are made up of differing contributions of normal structural modes, with the relative contributions of each structural mode to a particular radiation mode being weakly frequency dependent. As a result, the radiation mode shape is also weakly frequency dependent. The amplitudes of particular radiation modes may be used as error signals for an active control system designed to reduce the sound radiated by a structure. As the radiation modes are orthogonal with respect to the radiated sound field, reducing the amplitudes of any one radiation mode is guaranteed to reduce the radiated sound.

Borgotti calculated free space radiation modes in the development of a modal representation for radiated acoustic power. Cunefare used the natural vibration modes of a beam as components of the radiation modes. Elliott and Johnson (1993) extended the work of Borgotti and Cunefare to develop a method for actively controlling the sound power radiated by a simply supported beam and a simply supported plate using radiation modal amplitudes as control system error signals. Elliott and Johnson (1993) found that at low frequencies only one radiation mode contributed significantly to the far field radiation. The velocity distribution of this radiation mode was uniform across the surface of the structure and its amplitude was proportional to the volume velocity of the structure. Cunefare and Currey (1994) explored the use of radiation modes to describe the vibration response of a baffled beam. Cazzolato (1999) and Snyder et al. (1993) developed the theory to describe the structural vibrations responsible for sound transmission into an enclosure in terms of radiation modes.

2.1.2.2 Shaped Sensors

The development of shaped sensors began with Lee and Moon (1990) when they successfully showed that polyvinylidene fluoride (PVDF) film could be shaped to produce voltage outputs proportional only to specific vibration modes. PVDF is sensitive to induced strain and therefore its sensitivity is proportional to the second derivative of the out-of-plane displacement (mode shape). The work presented by Lee and Moon (1990) demonstrated experimentally that shaped PVDF could measure specific vibration modes of one dimensional plates and beams. This research was extended by Burke and Hubbard (1991) who applied the sensor theory to rectangular plates with arbitrary boundary conditions. Sullivan et al. (1999) extended the sensor theory to sensors with arbitrary spatial distributions. Clark and Fuller (1991), Clark and Fuller (1992a), Clark and Fuller (1992b) used uniform strips of PVDF to minimise the radiation from plates.

A number of researchers have achieved large reductions in radiated sound power through the minimisation of total volume velocity. In Section 2.1.2, it was described how Maillard and Fuller (1998) demonstrated that radiation modes can be measured using discretely weighted sensors. Rex and Elliott (1992) have shown that the discrete sensors can be replaced by continuous sensors. They also extended the ideas of Lee and Moon (1990) and developed the concept of a Quadratically-Weighted Strain-Integrating Sensor (QWSIS). The QWSIS is designed to have a quadratically varying spatial weighting so that the sensor output is proportional to the spatial integral of the out-of-plane displacement over the sensor length. This is in fact a volume displacement sensor which is proportional to volume velocity at a given frequency“. Johnson and Elliott (1993), using the QWSIS theory, showed that the volume velocity of a two-dimensional structure can be measured by covering the whole structure with PVDF and quadratically weighting the sensitivity or the thickness. Charette et al. (1995) and Charette et al. (1998) successfully designed shaped PVDF volume velocity sensors for a clamped plate. The design was based on experimentally measured mode shapes and therefore the design technique can be applied to any two dimensional structure.

Shaped sensors have not only been used to sense structural modes. There has also been some success in sensing the radiation modes of structures using shaped strain sensors. Snyder and Tanaka (1995) and Tanaka et al. (1996) investigated the use of shaped PVDF to sense the radiation modes of a simply supported plate . Realising that two dimensional sensors were impractical, they developed a one-dimensional method of sensing two dimensional radiation modes. Tanaka et al. (1996) developed a procedure to determine the number of one-dimensional sensors and to establish their location required to sense the radiation mode.

Work by Cazzolato and Hansen (1997, 1998) investigated the use of radiation modes to actively control sound transmission through a curved panel into a coupled enclosure and into a cylindrical enclosure. The sound transmission into the rectangular curved panel-cavity system was controlled using PVDF shaped sensors to sense the first two radiation modes. Experiments showed that although small errors in the shape of the PVDF sensors resulted in 'leak through' of undesired modes, the PVDF sensors still out performed discrete sensors. They also showed that these sensors were able to reduce the convergence time of the controller and increase the controller stability when compared to traditional active noise control techniques.

In Cazzolato and Hansen's (1998) work, structural vibration of the stiffened cylinder was decomposed into radiation modes and the effectiveness of using shaped sensors as error sensors was considered. Their work addressed issues of the practical implementation of shaped PVDF, which showed that a small number of continuous sensors demonstrated a superior performance to traditional structural and acoustic error sensing techniques.

2.2 Local control

Olson and May (1953) developed the "Electronic sound absorber" to attenuate low frequency noise using feedback control. The paper suggests that the sound absorber would be effective in aeroplanes, automobiles, trains and individual locations near noise emitting machinery. They

found that the electronic sound absorber could reduce the sound pressure level by 10 to 25 dB in the vicinity of the error sensor which was located adjacent to the control loudspeaker.

Having identified the difficulty in achieving global control within enclosures, many researchers have considered the concept of local control where the aim is to produce localised zones of attenuation. This means that occupants within the enclosures can have the noise they are exposed to attenuated without the need to control the sound within the entire enclosure. The acoustic conditions necessary to produce local zones of quiet near error sensors have been investigated by a number of researchers over the years.

Ross (1980) used a point monopole secondary source to cancel a plane wave primary sound field. This study showed that at low frequencies the "zone of quiet" was a shell shape that surrounded the error sensors. As the frequency increased the size of the "zone of quiet" rapidly decreased. Subsequent studies (Elliott et al., 1988; Joseph et al., 1994) also found that the size of the zone of quiet was dependent on frequency; however they quantified the relationship. They found that in a diffuse field the diameter of the "zone of quiet" (defined as a reduction of 10 dB or more) is limited to approximately a tenth of the wavelength, clearly showing that local control is only an efficient method of active noise control at low frequencies.

Joseph et al. (1994) presented a very interesting paper titled "Near field zones of quiet" in which the generation of zones of quiet within the near field of the control speakers is considered. The idea presented was to develop a local active noise control system which could be used in the headrest of seats within cars and aircraft where the error microphone is located in the near field of the control source. The size of the zones of quiet, which incorporated a minimum of 10 dB attenuation, was quantified in the near and far field as follows:

$$\begin{aligned} \textbf{Near field}: 2r \approx 0.63 r_o \quad & kr_o \ll 1 \\ \textbf{Far field}: 2r \approx 0.1\lambda \quad & kr_o > 1 \end{aligned} \tag{2.3}$$

where r is the radius of the zone of quiet, r_o is the distance between the error microphone and

the control source, λ is the wavelength and k is the wavenumber. The size of the near field zone of quiet is independent of frequency. In the far field the size of the quiet zone is inversely proportional to frequency. Theoretical and experimental zones presented were in agreement and were not dissimilar to the results presented by Elliott et al. (1988) in which the error sensor was located in the far field of the secondary source.

David and Elliott (1994) presented a study of local active control with the error microphone located both on and off-axis of the secondary source at a number of frequencies. Results presented for the error microphone located both on and off axis indicate very similar spatial patterns up to frequencies of 1 kHz, with the boundary of the zone of quiet of 10 dB reduction resembling a ring with the control source at the centre. This suggests that for low frequency control, the error microphone could be located away from the intended location of the zone of quiet and still achieve the same attenuation as if the error microphone was at that zone. Above 1 kHz the spatial regions of sound control for the on and off axis case are considerably different but in both cases the region of quiet decreases with increasing frequency. Rafaely et al. (1997) showed that zones of quiet are larger at low frequencies than at high frequencies and at 500 Hz the zone of quiet is too small to be useful (50mm) in a diffuse field.

Elliott and Garcia-Bonito (1995) and Garcia-Bonito and Elliott (1995b) investigated pressure and pressure gradient control to increase the spatial extent of a localised zone of attenuation. This work will be discussed in Section 2.3 and therefore only briefly reviewed here as the aim of the paper was to produce local control. Controlling energy density increased the size of the zone of quiet from a sphere of diameter one tenth of wavelength to a "cylinder with rounded ends, which has length of about $\lambda/2$ and a diameter of about $\lambda/10$" (page 571). Energy density control was compared with the control achieved using two microphones, with the pressure at each microphone controlled using two independent control sources. The spatial zone of quiet was the same as achieved using energy density control at certain separation distances between the microphones up to 0.3λ. Elliott and Garcia-Bonito (1995) showed that at a separation distance of 0.5λ, the application of control results in two spheres of 10 dB or

greater attenuation each 0.1λ. Miyoshi et al. (1994) also examined the effect of inter-element spacing between error microphones and the number of error microphones. They defined the relationship between the level of attenuation and the spacing between the error microphones.

The effect that a rigid sphere has on localised zones of quiet at high and low frequencies was explored by Garcia-Bonito and Elliott (1995b). They illustrated that the presence of the sphere distorted the zone of quiet but this was generally of benefit as the zone of quiet extended and "attached" to the sphere. As the sphere is an approximate model of a head, it is clearly beneficial for the zone of quiet to extend to the rigid sphere. This effect was demonstrated both analytically and experimentally. Garcia-Bonito et al. (1997a) investigated the zone of quiet generated in the presence of reflecting surfaces, including a rigid sphere, a wall, a two wall edge and a corner. This work found that the 10 dB zone of quiet was extended in the presence of these reflecting surfaces compared with no surface.

The performance of a local control system was analysed in a lightly and heavily damped room by Guo et al. (2002). In a real-time control scenario they found that the size of the localised greater than 10 dB zone of quiet was dependent on the level of room damping in a non-diffuse environment. In a lightly damped enclosure (with an average absorption coefficient of 0.06) the zone of quiet was approximately a tenth of a wavelength. However, as the level of damping increased, to an average absorption coefficient of 0.3, so did the zone of quiet to around a seventh of a wavelength.

Local control has been shown to be effective at generating localised zones of quiet centred around an error sensor and many authors have suggested this as a method for achieving sound control for people within enclosed spaces such as aeroplanes and cars. The one significant disadvantage with local control is the interference of the error sensor with the free movement of the people experiencing the noise control.

2.3 Energy Density

Energy density is defined as the sum of acoustic kinetic energy density and acoustic potential energy density, which is measured experimentally as particle velocity and pressure respectively. The particle velocity may be measured with two microphones using the finite difference technique.

During the 1990's, a considerable amount of research was performed on the development of energy density as an error signal, which has a distinct advantage over squared pressure, as the dependence on the location of the error sensors is reduced. This is because there are fewer nodal surfaces in an energy density field than in a pressure field (Sommerfeldt et al., 1995). To achieve maximum attenuation using a pressure squared cost function, the error sensors must be placed at local maxima (anti-node); other error sensor locations will result in considerably reduced attenuation.

Sommerfeldt and Nashif (1991) compared the performance of energy density, potential energy and squared pressure as error criteria in a one dimensional enclosure. This work confirmed that the performance of the energy density cost function is independent of location while the control of squared pressure is highly dependent on location. Nashif and Sommerfeldt (1992) and Sommerfeldt and Parkins (1994) also investigated the effectiveness of minimising energy density in a one dimensional enclosure. Their work showed that minimising energy density resulted in significantly larger zones of attenuation than obtained by minimising squared pressure.

Sommerfeldt et al. (1995) and Parkins (1998) extended this work to a three dimensional enclosure. A three axis energy density sensor was built using 6 electret microphones mounted in a wooden sphere. The attenuation achieved by minimising acoustic energy density at discrete locations, pressure squared and global potential energy were compared. Global potential energy was determined by integrating the squared pressure over the volume of the enclosure. Global potential energy is impractical for experimental implementation due to the number of sensors

required to adequately measure it. However it may be used to provide a theoretical estimate of the optimal performance. In this particular study, the control source and sensor locations were arbitrary since the focus of the work was to compare the extent of global sound pressure control achieved using various control implementations. The control strategies were assessed at two frequencies and in both cases the error sensor location, when controlling squared acoustic pressure, was at a nodal plane of the dominant mode of the enclosure, causing an increase in sound pressure level within the enclosure. Confirming their previous work, the authors found that when energy density is controlled, global minimisation is achieved regardless of error sensor location. This work showed both experimentally and numerically that energy density control is able to produce significant global control, in scenarios where squared pressure control is not.

Cazzolato (1999) and Cazzolato and Hansen (2003) used a simplified three axis energy density sensor which used only four microphones instead of six. Their work found that the four microphone sensor was sufficient for active noise control of an enclosed energy density field. Energy density control in enclosures with low modal density was found to produce global control. In a high modal density environment, the region of control produced was not global but much larger than that achieved using pressure control at a point.

Parkins et al. (1999) investigated the effect of sensor location in a three dimensional enclosure in terms of the probability of locating an error sensor on a nodal plane. They looked at the probability that an error sensor would be located within a nodal volume for both pressure and energy density control. They showed that the probability of randomly locating an error sensor within a nodal volume is always less for energy density control than for squared pressure. At least four pressure sensors randomly located in space are required to match the performance of one energy density sensor which contains a minimum of four microphones in a tetrahedral configuration. The pressure sensors are located throughout the three dimensional enclosure which presents its own problems of wiring and interference with people in the case of a practical example such as an aircraft cabin.

Park and Sommerfeldt (1997) showed that minimising energy density produced improved global attenuation of broadband noise in a one-dimensional enclosure, more than did minimising squared pressure at one location. Parkins et al. (2000a) observed the attenuation achieved using an energy density active control system to minimise narrow band and broadband noise within a three-dimensional enclosure. Maximum attenuations of 14.4 dB and 3.8 dB were achieved in narrow band and broadband experiments respectively. This work highlighted that while control of energy density is very effective at controlling single frequencies within an enclosure it is not so effective at broadband control.

Elliott and Garcia-Bonito (1995) applied energy density control to a pure tone diffuse field by cancelling pressure and pressure gradient along a single axis, thus enlarging the zone of quiet produced when compared to that achieved when cancelling pressure at a single point. Cancelling only pressure, produces a 10 dB zone of quiet in the form of a sphere of diameter of one-tenth of a wavelength. However, when minimising energy density the zone of quiet becomes larger, with the 10 dB or greater zone of quiet in the shape of a cylinder with rounded ends of length about half a wavelength and diameter of about one-tenth of a wavelength orientated along the microphone axis.

2.4 Sound Intensity

Sound intensity is defined as the rate of energy flow per unit area transmitted in a specified direction. Sound intensity has been considered by a number of researchers as a cost function for active noise control. Active intensity exists where there is a net flow of energy away from the source and this occurs in the far field of a source. Reactive intensity occurs when there is no net flow of energy and energy oscillates locally. Reactive intensity occurs in the near field of sound sources and in reactive sound fields (Fahy, 1995). There needs to be a net flow of energy for sound intensity to be an effective cost function and for this reason, the use of sound intensity as a cost function for active noise control within an enclosure has been unsuccessful.

However, sound intensity sensing has proved successful in the free field (Qui and Hansen, 1997, Qui et al., 1998, Berry et al., 1999 and Koehler, 2001). Sound intensity is a signed quantity and this can cause problems when utilising active intensity sensors (Sommerfeldt and Nashif, 1994).

Sommerfeldt and Nashif (1994) discussed the need for the acoustic intensity to be a positive definite function as if it is not, an unstable control result can result. This is an important consideration as acoustic intensity is not always positive definite. To ensure the function is positive definite, consideration needs to be given to the physical arrangement of the control system. Alternatively, the cost function could be the square of acoustic intensity. Swanson (1994) used a simulation to examine the performance of an acoustic intensity error sensor in a circular duct. The results showed that the use of the intensity cost function produced attenuation of approximately 10 dB from three tones while the use of a pressure squared cost function was only able to attenuate one tone.

Reichard et al. (1995) performed experiments in a nearly closed circular duct with an intensity sensor using frequency domain filtered-x feedforward control. The intensity sensor was located downstream of the control source, where reductions in the pressure field of up to 20 dB were reported. Kang and Kim (1997) reported on an experiment which examined the performance of an intensity cost function versus a pressure squared cost function in the control of sound radiated from an open ended tube. Their experiments showed that the sound intensity cost function out-performed the pressure squared cost function in terms of attenuation of the exterior sound field. However, there has been little work on the use of sound intensity error sensors for active control within enclosed sound fields because the reactive sound intensity dominates the reverberant sound field, making control difficult.

The minimisation of active intensity has proved more efficient in the control of free field radiation. Qui and Hansen (1997), Qui et al. (1998), Berry et al. (1999) and Koehler (2001) have investigated using an intensity cost function to control free field sound radiation. An advantage of sound intensity is that far field energy can be estimated using measurements in the near

field. Berry et al. (1999) examined the use of active intensity sensors in the near field of a vibrating plate which was radiating energy into a free field. They found that as sound intensity is a signed quantity, it limited its performance in an active noise control system. They also reported that for near field sound intensity sensing, a large number of sensors are required for successful control.

2.5 Errors in cost functions incorporating spatial derivatives of pressure

The most common method of sound intensity measurement is the two microphone technique which uses the two microphone signals to estimate the pressure gradient and the pressure at the midpoint between them to calculate the sound intensity. Many forms of error exist as a result of using this technique, such as inherent errors due to finite separation of the microphones, and instrumentation errors due to phase and sensitivity mismatch between microphone elements. The errors associated with the measurement of acoustic intensity have been investigated by a number of authors and a book detailing much of this work has been published by Fahy (1995). Fahy (1995) presented analytical expressions for the influence that these errors have on the accuracy of the sound intensity measurement. Sound intensity is very sensitive to errors in phase between the two sensors.

Parkins (1998), Cazzolato (1999), Parkins et al. (2000b), Cazzolato and Hansen (2000b) and Cazzolato and Hansen (2000a) analysed the effect that the inherent and experimental errors have on the measurement of energy density using the two microphone technique. Both a one dimensional and a three dimensional energy density sensor were investigated in a one-dimensional reactive sound field and in a plane progressive sound field. Energy density is more tolerant to these errors than sound intensity because energy density is calculated from the addition of pressure squared and velocity squared while sound intensity is the product of

the two quantities.

More recently, Ghan et al. (2002, 2003) derived a expression for the estimation of the time-averaged energy density in the frequency domain and analysed the statistical errors associated with this expression. They found that the normalised random error depends on the number of averages and not on the characteristics of the sound field being measured.

2.6 Active Headsets

For people working within noisy environments the traditional method of noise control is to wear passive headsets. However, these are only effective in the mid to high frequency range. Consequently, a number of researchers have investigated the use of active headsets to attenuate the low frequency noise. There are currently a number of active headsets commercially available. Some of the problems associated with the effectiveness of these headsets are air leaks around the edges of the headset and instability caused by transient, high level sounds. The use of active headsets is a technique for providing personal noise control.

An adaptive feedforward active headset was considered by Pan et al. (1995). Their active headset consisted of an externally mounted reference microphone, an error microphone located near the control speaker and an observer microphone located where the entrance to the ear canal would be. They attempted to control broadband noise over a frequency range of 40 to 750 Hz. While attenuation at the error microphone ranged from a minimum of 10 dB to a maximum of 35 dB at various frequencies, the attenuation recorded at the entrance to the ear canal was considerably lower above 150 Hz. Attenuation was achieved up to 400 Hz at the observer microphone and above this frequency an increase in sound pressure level was recorded. The observer microphone was located only 30 mm from the error microphone. So although notable reductions were recorded at the error microphone, the wearer of the headset may not observe a notable reduction in the disturbance.

Bao and Pan (1996) considered the use of adaptive feedback control in active headsets and they compared the performance against that of a feedforward headset. The feedback controller was found to be less robust than the feedforward headset and the use of the feedback headset resulted in much lower levels of attenuation compared to the feedforward controller. However, they claim that feedback control copes better with the head movement of the wearer.

Brammer et al. (1997) used multi-rate sampling in an attempt to reduce the delay in a digital system and therefore improve broadband control using feedforward active headsets. This study showed good levels of broadband control of replayed helicopter noise. Johansson and Winberg (1997) also investigated the use of active headsets to control helicopter noise. In this case the disturbance was broadband in nature but contained tonal components, a result of the blade pass frequency and its harmonics. To control this disturbance, a hybrid active headset consisting of digital feedforward and an analog feedback controller was developed. The feedforward controller targeted the tonal components of the disturbance while the feedback controller was designed for broadband control. Results presented in this paper showed the low frequency tonal components were attenuated by up to 23 dB by the feedforward controller and the feedback controller produced attenuation of the disturbance from 0 to 400 Hz of around 20 dB across the spectrum.

Rafaely (2001) presented an overview of active headset research in his Inter-Noise 2001 paper. He identified issues influencing the performance for both feedback and feedforward active headsets. In feedforward controlled active headsets, the reference microphone and the error microphone are only a few centimeters apart and hence the total electronic delay may exceed the acoustic delay. The acoustic delay is a result of the reference microphone being mounted externally on the headset. It is not possible to shorten the electronic delay sufficiently, the application of the feedforward controller may be limited to the band-limited or tonal disturbances.

In a recent paper, Rafaely and Jones (2002) presented a study on the performance of a hybrid feedback/feedforward active headset for broadband control. Rafaely and Jones (2002) com-

pared the performance of the headsets in a direct and in a reverberant field with the headset in different positions relative to the loudspeaker generating the disturbance.

The performance of the hybrid headset in the direct field was found to be dependent on the position of the headset with respect to the loudspeaker. The position only affected the feedforward component of the headset. When the headset moved off axis from the loudspeaker or the reference microphone was on the opposite side of the head to the loudspeaker, the performance of the feedforward part of the hybrid controller was greatly affected. This was due to the increase in the acoustic delay between the reference and error microphone, and as other authors have found, this affects the performance of a feedforward controller. The path of the disturbance propagation has no effect on the performance of the feedback component of the hybrid headset as the feedback controller requires no information about the disturbance outside of the headset.

Controlling a broadband disturbance (200-900 Hz) in a reverberant field, the relative position of the headset had little effect on control achieved. This result is not unexpected as in a reverberant field there should be no directivity. Decreasing the bandwidth of the disturbance from 700 Hz to 300 Hz greatly improved the performance of the feedforward controller in both sound fields but most notably in the direct field, therefore highlighting that the performance is less affected by acoustic delay when the disturbance is predictable or narrow band in nature. This work did show that the use of a hybrid controller active headset improves broadband control performance when compared to simply employing a feedback controller.

2.7 Virtual Sensors

Creating local zones of quiet around the error sensor means that for an observer within the enclosure to experience any reduction in the sound pressure level, the error sensor needs to be located at the observer's ear and this may restrict their movement (Elliott and David, 1992). A

solution to this problem would be to move the error sensor away from the observer's ear while maintaining the local zone of quiet at the ear. This is the concept of virtual sensing. Elliott and David (1992), Garcia-Bonito et al. (1996), Garcia-Bonito et al. (1997b) and Rafaely et al. (1999) investigated the use of virtual microphones to produce a local zone of quiet around a human ear. The theory developed in these papers was based upon a known (previously measured) acoustic transfer function between a permanent remote microphone and a microphone temporarily placed at the position of the human ear. This model assumes that the transfer function between the physical microphone and the virtual microphone and the location of the intended zone of quiet do not change with time. Also, this virtual microphone method assumes that the primary field pressure measured at the virtual location is equal to the pressure at the location of the permanent microphone. This assumption will only hold at low frequencies and in the free field where the spatial rate of change of the pressure is low. Another problem with this model is that the algorithm cannot be adjusted easily to accommodate head movement or the addition of new control sources.

Rafaely et al. (1997) showed that using the virtual microphone (technique developed by Elliott and David, 1992) can project the zone of attenuation away from the error sensor to a desired location. Their work illustrated an increase in attenuation of about 6 dB using a virtual microphone versus a traditional remote error sensor.

The Elliott and David method was very effective at projecting the zone of quiet away from the error sensor to the virtual location at low frequencies; however the performance deteriorated at high frequencies (Garcia-Bonito et al., 1997b). Garcia-Bonito et al. (1997b) and Garcia-Bonito and Elliott (1995b) investigated the effect of having a person's head next to the virtual location as would be the case in a practical implementation. They found that having the rigid sphere next to the virtual location improved the performance of the virtual sensor at high frequencies. They attributed this to the fact that at the surface of the rigid sphere, the pressure gradient is zero and therefore the primary and secondary fields are more spatially uniform near the rigid sphere. This is essentially energy density control.

Roure and Albarrazin (1999) used the same technique as described by Garcia-Bonito et al. (1996) and investigated the performance of the algorithm in a test room built to simulate an aeroplane interior. They identified that successful implementation of the transfer function virtual microphone depends upon the accuracy of the transfer functions prior to control. The transfer functions may vary with time as the temperature can fluctuate and the frequency can shift. Brothanek and Jiricek (2002) used the transfer function method to create zones of quiet around a head simulator. This work looked at the performance of the virtual sensor using broadband noise from 100 to 900 Hz. As would be expected, the virtual sensors were not effective at higher frequencies where the wavelength is shorter than at low frequencies. They found the virtual sensors to be effective over a frequency range from 100 to 500 Hz, although maximum attenuation was achieved at the error sensor and not at the observer's ear (virtual location).

Tseng and Elliott (2002) investigated the performance of the transfer function virtual error sensing technique in a feedback real-time control scenario. This work highlighted the many difficulties in the real-time implementation of the transfer function method, namely controller stability and modelling of the transfer functions of both the physical and virtual system. Real-time control achieved a maximum of 6 dB attenuation at the virtual location.

Cazzolato (1999) suggested an alternative virtual microphone formulation utilising forward wave prediction theory with two and three microphone arrays to predict the sound pressure level at the observer location. He also suggested using the forward prediction theory to create a virtual energy density sensor. Kestell (2000), Kestell et al. (2000, 2001b), Kestell and Hansen (2001) and Kestell et al. (2001a) explored the performance of these forward-difference virtual microphones in a free field, in a one dimensional waveguide and within a mock aircraft cabin. The two microphone array used a first-order prediction method and the three microphone array used a second-order prediction. The investigation into the performance of the forward-difference virtual microphone was carried out using an analytical model of the free field and the one dimensional waveguide sound fields and experimentally measured transfer functions

in both the free and reactive field. Control was simulated using quadratic optimisation. The results obtained using the experimental transfer function showed a notable degradation in the level of control achieved compared to the control results obtained using the analytical model of the sound field. While the use of the experimental transfer functions instead of the analytical model should result in some small decrease in performance due to the presence of some experimental error but not of the order reported by Kestell (2000). It is thought the cause of the discrepancy between the level of control achieved in the two examples was due to experimental error in the measurement of the transfer function such as spectral leakage. However, their work did find that the first-order virtual microphone was a more robust algorithm than the second-order virtual microphone as it resulted in greater levels of attenuation at the virtual location. It appeared that the second-order virtual microphone was more sensitive to short wavelength extraneous noise. The virtual energy density sensor produced a broader region of control when compared with virtual pressure control, which produced high levels of attenuation over a very small region. Real-time control using the virtual sensors was never attempted.

2.8 Conclusions from the Literature Review

To date there has been considerable research on the active control of interior sound fields, with the aim of attenuating engine noise radiated into cabins of heavy mining vehicles or propeller noise radiated into light aircraft cabins to provide a safe and more comfortable environment for people working within these spaces. The first studies attempted to control the noise throughout the enclosure using a pressure squared cost function which found that to achieve notable global attenuation, a large number of control sources and error sensors are required and their location is often restricted due to difficulties in observing the primary field. Consequently, global control systems are complex, expensive and often impractical. Realising the difficulty of achieving global control, alternative cost functions and control techniques to control interior noise have been developed. Control using an energy density cost function has shown promising results,

as this method overcomes the observability problems experienced with a squared pressure cost function. When used for local control, energy density also produces much broader zones of attenuation than achieved using a squared pressure cost function. The use of active intensity sensing in active noise control has been investigated mainly to control free field radiation of sound from a vibrating structure and not for control of interior sound fields. Although active sound intensity sensing can produce higher levels of attenuation than using a squared pressure cost function, it requires a large number of sensors and, as sound intensity is a signed quantity, active control does not always result in attenuation of the disturbance.

Methods of Active Structural Acoustic Control (ASAC) have sparked interest from a number of researchers in recent years and thus much effort has been invested in its development. ASAC generally involves attaching sensors and or actuators to a noise radiating structure to sense and control the structural vibrations. While this method can produce global control, the installation of these systems may not be possible in all enclosures due to space restrictions, and attaching sensors to the structure may compromise its integrity.

The use of active headsets is another method for producing personal sound control for occupants of an enclosed space. Active headsets provide both low and mid-frequency control. However, the headsets need to be very well maintained to produce prolonged and continuous hearing protection as any air gaps will severely degrade their performance.

In many cases, local control may be the only way to achieve sound attenuation for occupants within the enclosures. In fact global control may not even be required as occupants within light aircraft, mining cabins and other similar enclosures remain seated and therefore in the same location. Thus localised zones of control will only be required over a relatively small spatial region. Using a traditional cost function such as squared pressure will result in significant attenuation but the zone of quiet will be very small such that, for the occupant to observe any reduction, the error sensor would need to be located at their ear. This is clearly an unacceptable solution as it would impede the free movement of the occupant's head.

Virtual error sensing is a relatively new method for producing localised zones of attenuation, while avoiding the problem of head movement, by projecting the zone of quiet away from the error sensors to a desired location such as a person's ear. This desired location is called the virtual location. The zone of quiet is created by predicting the sound pressure level at the virtual location and using that as the error signal to be minimised. The first virtual microphone developed used a 'transfer function' method to predict the sound pressure level at the remote location and this method has been extensively researched. The problem with this method is that it cannot adjust for changing acoustic conditions and changes in the distance between the virtual location and the error sensors. Research using forward-difference virtual microphones has been limited to date. There has been no research on their performance in a real-time control scenario or on the effect that experimental errors have on their prediction performance. The small amount of research performed on these virtual microphones to date identified their susceptibility to corruption of their prediction accuracy due to short wavelength extraneous noise. Therefore there still exists considerable scope to investigate, understand and develop these forward-difference virtual sensors into robust error sensors suitable for practical control systems.

Chapter 3

One-dimensional Waveguide Experiments

3.1 Introduction

In this chapter the performance of the linear and quadratic prediction algorithms are examined for a one-dimensional waveguide. A long narrow duct has been used to approximate such a system. The cross sectional dimensions were considerably smaller than the acoustic wavelength to eliminate cross modes, thus ensuring a simple sound field. Within this environment, the forward-difference virtual microphone formulations (discussed in Section 3.2.1) were analysed using an analytical model, post-processed experimental data and in a real-time control scenario.

In his thesis Kestell (2000), presented a performance evaluation of the forward-difference virtual microphones in a one-dimensional waveguide. This evaluation was conducted with simulated control using an analytical model as well as experimentally measured transfer functions. From the results presented it is clear that there was a notable degradation in performance between the control achieved using the analytical model and the control using the measured transfer functions. This could indicate that there was experimental error in the measurement of the transfer functions or it could be a deficiency in the forward-difference virtual microphone

formulation. Using the experimental procedure described by Kestell, the experiments were repeated here with special attention paid to the measurement of the transfer functions. The aim of repeating this work was to determine if the poor control results were a product of poor data acquisition or the virtual microphone formulation. In addition to repeating Kestell's work, the performance evaluation has been extended to include real-time control, since Kestell's (2000) work focused on post-processed control (using measured transfer functions) and analytical comparisons.

3.2 Theory

The theory used to complete the analytical and experimental work presented in this chapter is summarised in this section.

3.2.1 Virtual Microphone Formulation

In this section, prediction algorithms for the forward-difference virtual microphones are derived. At low frequencies, when the distance between the transducers making up the virtual sensor is much less than a wavelength, the spatial rate of change of pressure is low and therefore predictable (Cazzolato, 1999) . Hence, by fitting a straight or curved line between the pressure measured at microphones, p_1, p_3 and p_5 at fixed locations (see Figures 3.1 and 3.2), the pressure p_v, at a remote location can be estimated. This nomenclature for the microphones has been chosen to maintain consistency with theory developed in later chapters.

3.2.1.1 Linear Prediction Virtual Microphone

The linear equation for predicting the complex sound pressure at any location, x is:

$$p(x) = ax + b \tag{3.1}$$

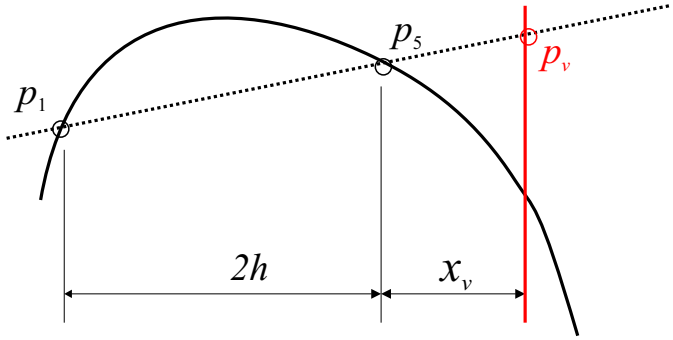

Figure 3.1: Schematic of the linear forward-difference extrapolation where the black curved line represents the true pressure field and the straight line represents the linear estimate.

where $p(x)$ is the pressure at a given spatial location x, a is the gradient and b is a constant. This equation may be applied to a system of two microphones, separated by $2h$ as shown in Figure 3.1 where the black curved line indicates the true pressure field.

The matrix form of Equation (3.1) can be written as:

$$\begin{bmatrix} p_1 \\ p_5 \end{bmatrix} = \begin{bmatrix} -2h & 1 \\ 0 & 1 \end{bmatrix} \begin{bmatrix} a \\ b \end{bmatrix} \tag{3.2}$$

where p_5 is at $x = 0$ and $p_1$is at $x = -2h$. Equation (3.2) can be written as

$$\mathbf{p}_2 = \mathbf{H}_2\mathbf{a}_2 \tag{3.3}$$

where $\mathbf{p}_2 = \begin{bmatrix} p_1 \\ p_5 \end{bmatrix}$, $\mathbf{H}_2 = \begin{bmatrix} -2h & 1 \\ 0 & 1 \end{bmatrix}$ and $\mathbf{a}_2 = \begin{bmatrix} a \\ b \end{bmatrix}$.

Since the pressures at microphones 1 and 5 are known, the coefficients, $\mathbf{a}_2$, may be calculated by taking the inverse of Equation 3.3 as follows

$$\mathbf{a}_2 = \mathbf{H}_2^{-1}\mathbf{p}_2 \tag{3.4}$$

where

$$\mathbf{H}_2^{-1} = \frac{1}{2}\begin{bmatrix} \frac{-1}{h} & \frac{1}{h} \\ 0 & 2 \end{bmatrix} \tag{3.5}$$

Therefore the pressure at some virtual location x_v is found using Equation (3.4):

$$p_v = \begin{bmatrix} x_v & 1 \end{bmatrix}\begin{bmatrix} a \\ b \end{bmatrix} = \mathbf{x}\mathbf{H}_2^{-1}\mathbf{p}_2 \tag{3.6}$$

Substituting Equation (3.5) into Equation (3.6) yields the equation for predicting the pressure at some distance x_v from the microphone array:

$$p_v = \begin{bmatrix} \frac{x_v}{h} & 1 \end{bmatrix}\begin{bmatrix} -0.5 & 0.5 \\ 0 & 1 \end{bmatrix}\begin{bmatrix} p_1 \\ p_5 \end{bmatrix} \tag{3.7}$$

3.2.1.2 Quadratic Prediction Virtual Microphone

The quadratic prediction virtual microphone uses a three equi-spaced microphone array spanning $2h$. A second-order polynomial may be fitted to the measured microphone pressures (see Figure 3.2) as follows:

$$p(x) = ax^2 + bx + c \tag{3.8}$$

where $p(x)$ is the pressure at a given spatial location x and a, b and c are coefficients of the polynomial.

With p_5 and p_1 located in the same positions as in Section 3.2.1.1 and p_3 located at $x = -h$, the following relationship can be derived:

$$\begin{bmatrix} p_1 \\ p_3 \\ p_5 \end{bmatrix} = \begin{bmatrix} (-2h)^2 & -2h & 1 \\ (-h)^2 & -h & 1 \\ 0 & 0 & 1 \end{bmatrix}\begin{bmatrix} a \\ b \\ c \end{bmatrix} \tag{3.9}$$

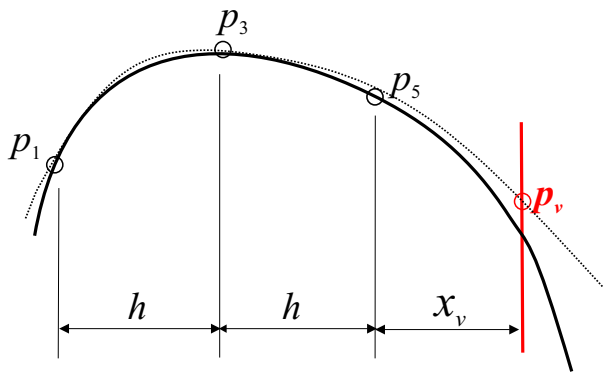

Figure 3.2: Schematic of quadratic forward-difference virtual microphones

This equation can be written as follows:

$$\mathbf{p}_3 = \mathbf{H}_3\mathbf{a}_3 \tag{3.10}$$

The coefficients are found by inverting the matrix $\mathbf{H}_3$; that is

$$\mathbf{a}_3 = \mathbf{H}_3^{-1}\mathbf{p}_3 \tag{3.11}$$

where

$$\mathbf{H}_3^{-1} = \frac{1}{2}\begin{bmatrix} \frac{1}{h^2} & \frac{-2}{h^2} & \frac{1}{h^2} \\ \frac{1}{h} & \frac{-4}{h} & \frac{3}{h} \\ 0 & 0 & 2 \end{bmatrix} \tag{3.12}$$

The complex pressure at a given point p_v using the quadratic prediction method is calculated using the following equation

$$p_v = \begin{bmatrix} x_v^2 & x_v & 1 \end{bmatrix}\begin{bmatrix} a \\ b \\ c \end{bmatrix} = \mathbf{x}\mathbf{H}_3^{-1}\mathbf{p}_3 \tag{3.13}$$

where,

$$\mathbf{x} = \begin{bmatrix} \left(\frac{x_v}{h}\right)^2 & \left(\frac{x_v}{h}\right) & 1 \end{bmatrix}, \mathbf{H}_3^{-1} = \begin{bmatrix} 0.5 & -1 & 0.5 \\ 0.5 & -2 & 1.5 \\ 0 & 0 & 1 \end{bmatrix}, \mathbf{p}_3 = \begin{bmatrix} p_1 \\ p_3 \\ p_5 \end{bmatrix}$$

3.2.2 Modelling of sound field within a rigid walled enclosure

The theory to model the acoustic sound field in rigid walled enclosures is presented here from Nelson and Elliott (1992). The modal model was used for the simulations.

The acoustic mode shapes (eigenfunctions), $\psi_{n,m,o}(x,y,z)$ within a rigid walled enclosure are given by:

$$\psi_{n,m,o}(x,y,z) = \sqrt{\varepsilon_n \varepsilon_m \varepsilon_o} \cos\frac{n\pi x}{L_x} \cos\frac{m\pi y}{L_y} \cos\frac{o\pi z}{L_z} \tag{3.14}$$

where L_x, L_y and L_z are the dimensions of the enclosure in the x, y and z co-ordinate directions and n, m and o denotes the modal indices. The normalisation factors, ε_n, ε_m and ε_o are defined as:

$$\varepsilon_{n,m,o} = \begin{cases} 1 & n,m,o \neq 0 \\ 2 & n,m,o = 0 \end{cases} \tag{3.15}$$

The eigenvalue, $k^2_{n,m,o}$ within a rigid walled enclosure is:

$$k^2_{n,m,o} = \left[\frac{n\pi}{L_x}\right]^2 + \left[\frac{m\pi}{L_y}\right]^2 + \left[\frac{o\pi}{L_z}\right]^2 \tag{3.16}$$

A special type of enclosure is one for which the dimensions in one direction are much greater than in the other two directions. This is commonly known as a duct (see Figure 3.3).

A plane wave is characterised as having the same amplitude and phase across the progressing wave front which is normal to the direction of wave propagation. Plane waves will propagate

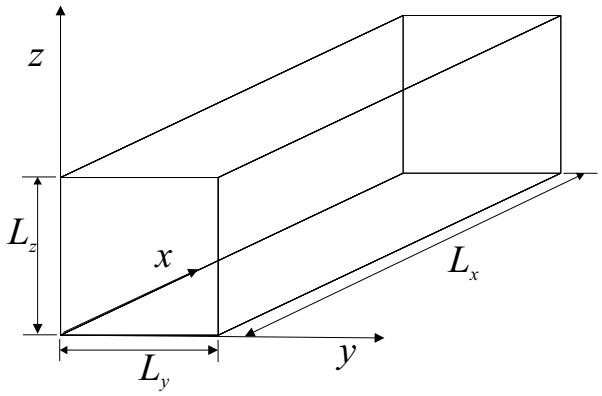

Figure 3.3: Co-ordinate system of an enclosure

unattenuated but higher-order modes will only propagate if the frequency of excitation is above cut-on. Munjal (1987) defines the cut-on frequency by

$$f > \frac{c}{2}\left\{\left(\frac{m}{L_y}\right)^2 + \left(\frac{o}{L_z}\right)^2\right\}^{\frac{1}{2}} \tag{3.17}$$

If the frequency of excitation is below cut-on the higher-order modes will decay exponentially with increasing distance from the source.

3.2.3 Quadratic Optimisation

Quadratic optimisation is commonly used when modelling active noise control systems to determine optimum secondary source strengths and the maximum achievable reduction in the controlled cost function, assuming the availability of an ideal controller. This method was used to simulate control using both an analytical model and experimentally measured transfer functions between the secondary source and the error sensors. For minimising the sum of squared pressures, at a number of locations the cost function may be written as:

$$J = \mathbf{p}^H\mathbf{p} \tag{3.18}$$

where $\mathbf{p}$ is a vector representing the total acoustic pressure at several sensors and H indicates a Hermitian transpose. The total pressure vector is given by

$$\mathbf{p} = \mathbf{p}_p + \mathbf{Z}\mathbf{q} \tag{3.19}$$

where $\mathbf{p}_p$ is the primary or uncontrolled pressure, $\mathbf{Z}$ is the transfer impedence matrix representing the relationship between the pressure measured at the error sensor and the control source strength and $\mathbf{q}$ is the secondary source control strength vector representing the control source volume velocities. Therefore by substituting Equation (3.19) into Equation (3.18) the cost function takes the form of the Hermitian quadratic form as:

$$J = \mathbf{q}^H\mathbf{Z}^H\mathbf{Z}\mathbf{q} + \mathbf{q}^H\mathbf{Z}^H\mathbf{p}_p + \mathbf{p}_p^H\mathbf{Z}\mathbf{q} + constant \tag{3.20}$$

If the matrix $\mathbf{Z}^H\mathbf{Z}$ is positive definite then the cost function J can be minimised with a unique value of the secondary source strength vector (Bullmore et al. (1987)). The unique value of the secondary source strength can be calculated using:

$$\mathbf{q} = -[\mathbf{Z}^H\mathbf{Z}]^{-1}\mathbf{Z}^H\mathbf{p}_p \tag{3.21}$$

3.3 The Experimental System

The one dimensional waveguide used for the experiments was a long narrow duct with dimensions of 4.83m x 0.205m x 0.205m. A primary noise source was located at one end and the control source 0.5m from the other end (see Figure 3.4). Two scenarios were investigated: rigidly terminated end caps and damped end caps. The rigidly terminated duct had a resonance quality factor of approximately 50. Adding the acoustically absorbent material to one end re-

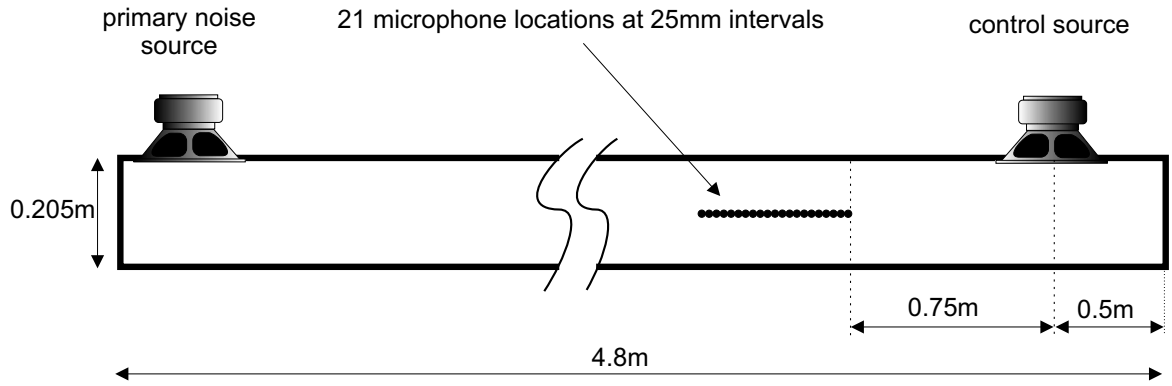

Figure 3.4: Schematic system representation of the one-dimensional waveguide (after Kestell (2000))

duced this to approximately 10. These are the same experimental conditions as used by Kestell (2000). The performance of the virtual algorithms was analysed at an acoustic resonance and anti-resonance. The natural frequency of the *n*th mode is given by (Kuttruff, 2000)

$$f_n = \frac{cn}{2L_x} \tag{3.22}$$

where c is the speed of sound in air and L_x is the length of the duct. The resonance frequency used for the tests was 248 Hz which corresponds to the natural frequency of the 7th axial mode. In the experiments the resonance frequency of the 7th axial mode was found to be 247 Hz. The anti-resonance frequency was 265 Hz, lying between the 7th and 8th axial mode. These frequencies were selected because they were below the duct cut-on frequency and the wavelengths of these modes were large compared with the spacing between the microphones. The level of control achieved was examined over a 0.5 m length extending from the closest microphone at $h = 25$mm intervals (see Figure 3.4). The virtual microphone algorithms have been tested at four separation distances. The separation distance is the distance between the closest element of the microphone array (p_5) and the virtual microphone location. The separation distances investigated are h, $2h$, $3h$ and $4h$. At 247 Hz, $h = 0.018\lambda$ and at 265 Hz, $h = 0.019\lambda$. Note that $h = 25$mm.

The Nyquist limit for spatial aliasing is given by (Bendat and Piersol (1971))

$$\lambda_{min} = 2 \triangle x \tag{3.23}$$

where λ_{min} is the minimum wavelength. Wavelengths smaller than λ_{min} will result in spatial aliasing. $\triangle x$ is the spacing between sensors, which in this case equals $2h$. For this experimental system $\lambda_{min} = 0.1$m which corresponds to a maximum frequency of 3409Hz. This corresponds to $n = 96$, hence, spatial aliasing will be negligible at the frequencies selected for this analysis.

3.4 Experimental Method

3.4.1 Simulated Control

The performance of the two virtual microphone formulations were initially tested using a MATLAB simulation. The acoustic sound field was simulated using the theory outlined in Section 3.2.2 and control was implemented using quadratic optimisation as explained in Section 3.2.3. In an effort to reflect the results of real-time control, a 1% error in magnitude was introduced to limit the attenuation to 40 dB. Without this limit the theoretical attenuation due to application of control would be infinite. The first 25 modes were considered in the MATLAB model. The inclusion of more than 25 modes in the calculation of the model of the acoustic sound field as this was all that was required to achieve convergence of the sound field.

3.4.2 Post-processed Control

Post-processed control was implemented computationally using experimentally measured transfer functions and quadratic optimisation. Transfer functions were measured between the pri-

mary source location and each of the 21 microphone locations (see Figure 3.4) and also between each microphone and control source combination. The measurement of the transfer functions was carried out using the Hewlett Packard Dynamic Signal Analyser 35665A. The sources were excited with broadband noise over a frequency range of 0 to 400 Hz. A FFT bandwidth of 0.5 Hz was used with a sampling rate of 1024 Hz with 2048 samples. Parameters such as bandwidth and sampling rate for these experiments were selected to minimise the experimental error in the measurement of the transfer functions. The transfer functions were also measured using tonal excitation, by driving the sources with a sinusoidal signal at the chosen resonance and anti-resonance frequencies. The tonal transfer functions were also measured because a possible source of the experimental error from the broadband transfer functions was resolution bias errors and using a tonal source should eliminate the error. The traversing microphone used at each measurement location was mounted on a cable wrapped around a pulley at each end of the duct with a ruler secured to the top of the duct to ensure accurate placement of the microphone with a maximum spatial error of 0.5mm, see Figures 3.5 and 3.6.

3.4.3 Real-time Control

Real-time control was implemented using the Causal Systems EZ-ANC II adaptive feedforward controller. For these experiments, the normalised convergence coefficient was 0.01 and the sample rate was 2756 Hz. The gradient descent algorithm used for feedforward control was a Filtered-x LMS algorithm. The cancellation path modelling was performed off-line with random noise and a 1024 tap FIR filter. The specifications of the EZ-ANC II can be found in Snyder et al. (2000).

The experimental configuration is illustrated in the block diagram presented in Figure 3.7. A microphone array was constructed using electret microphones as shown in Figure 3.8. As shown in Figure 3.7, the microphones were connected to a microphone amplifier, the output of

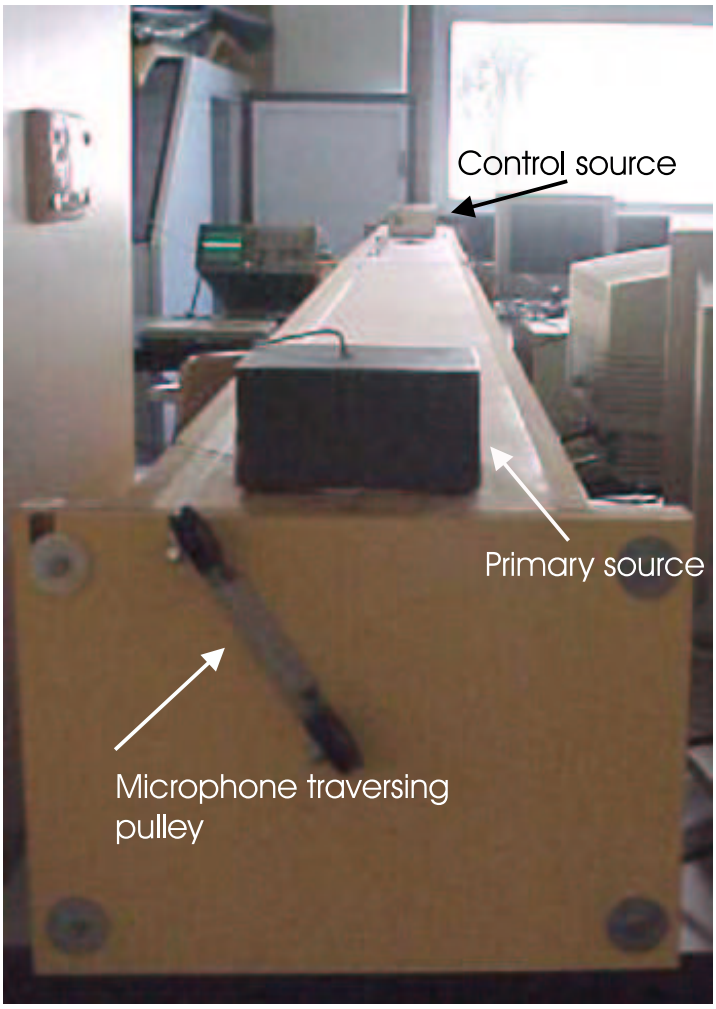

Figure 3.5: Photograph of one-dimensional waveguide

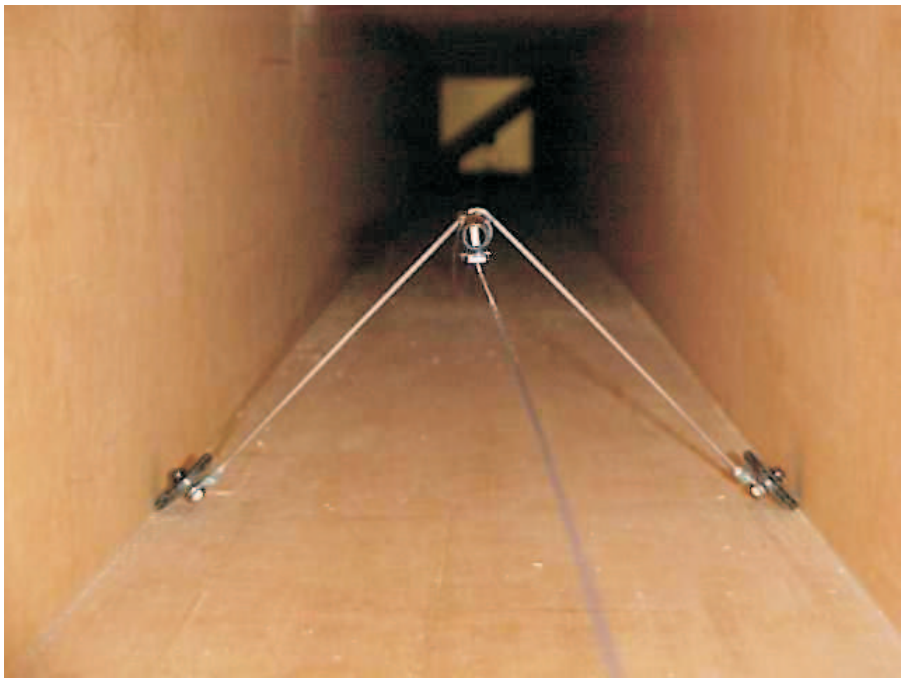

Figure 3.6: Photograph of microphone traverse within the one-dimensional waveguide

which was then input to the EZ-ANC II. The disturbance signal was created using the source signal from the Hewlett Packard Dynamic Signal Analyser 35665A. This was fed into a power amplifier and also provided the reference signal for the controller. The control output from the control was amplified before driving the controller speaker. The fixed weights for the virtual microphone were calculated using the equations in Section 3.2.1 and each microphone signal from the microphone array was weighted and summed within the EZ-ANC II software to create the error signal, which was the predicted pressure at the virtual location. As an illustration, a screen dump of the EZ-ANC II user interface is presented in Figure 3.9 showing the microphone weighting tool. The individual microphone weightings are defined within the Signal Definitions window of the EZ-ANC II software as shown in Figure 3.9. The microphone mounted on the traverse used in the post-processed transfer function measurements was used to manually scan a line in the region of interest to record the sound attenuation provided by the control system.

The microphones used in the array were phase and sensitivity matched to within $\pm 1^{\circ}$ and

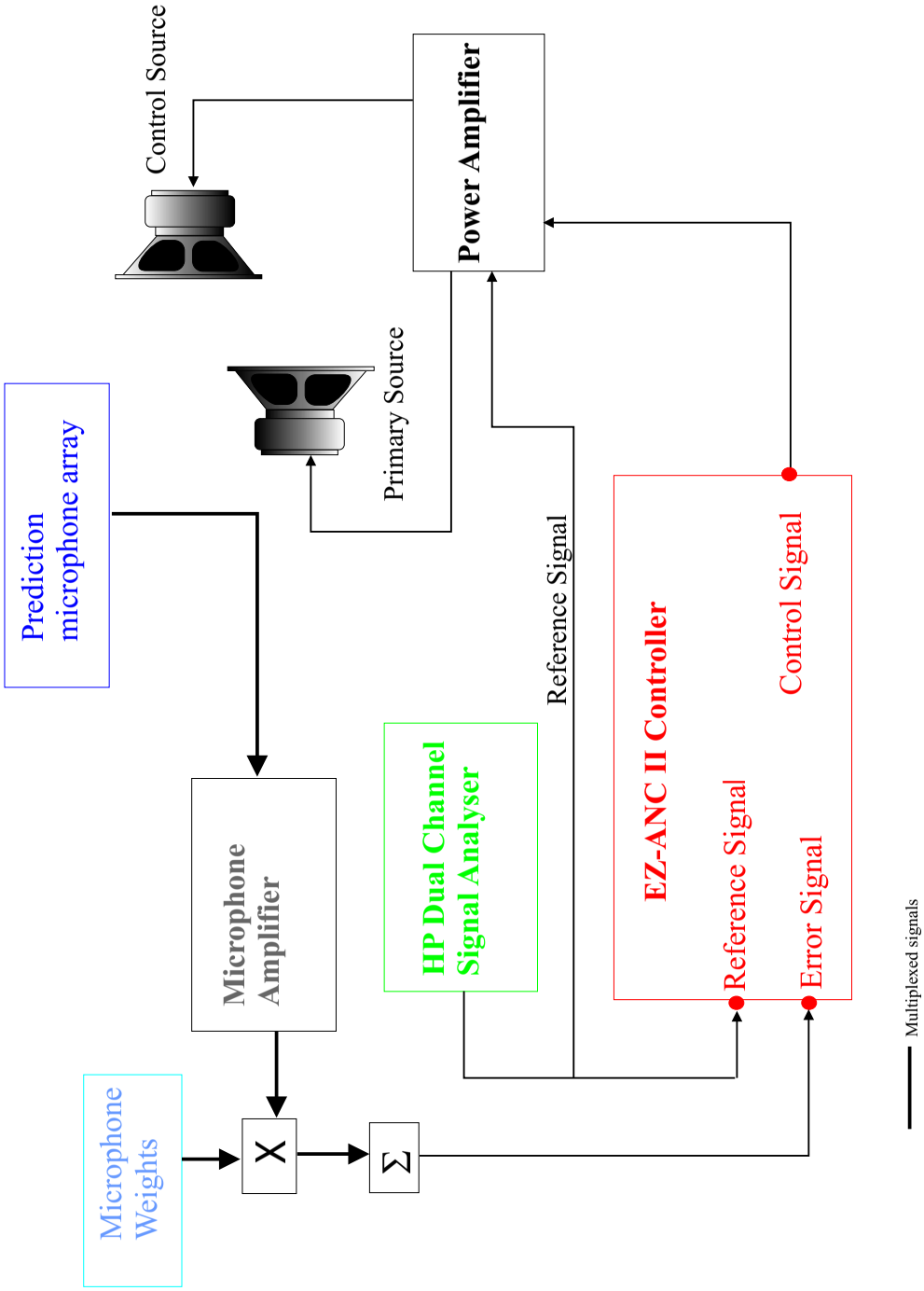

Figure 3.7: Schematic of the measured and control set-up

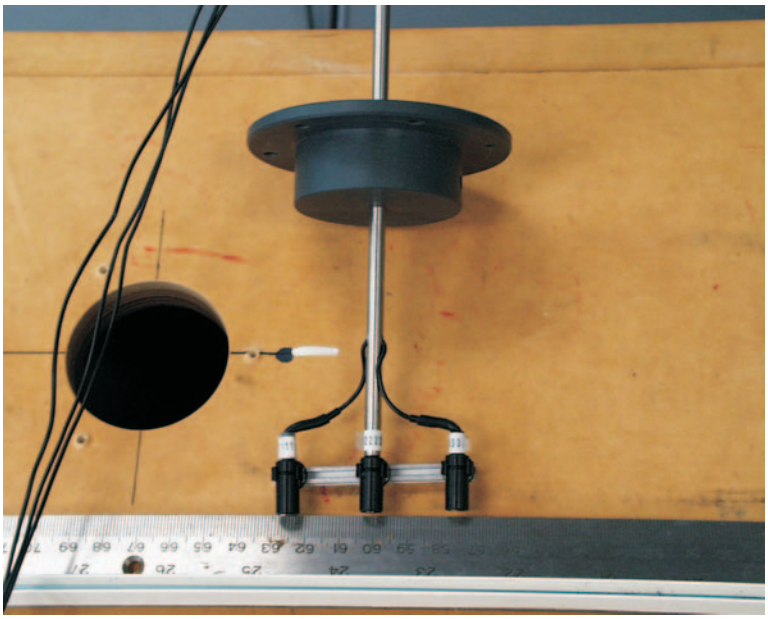

Figure 3.8: Photograph of the microphone array used in the real-time experiments

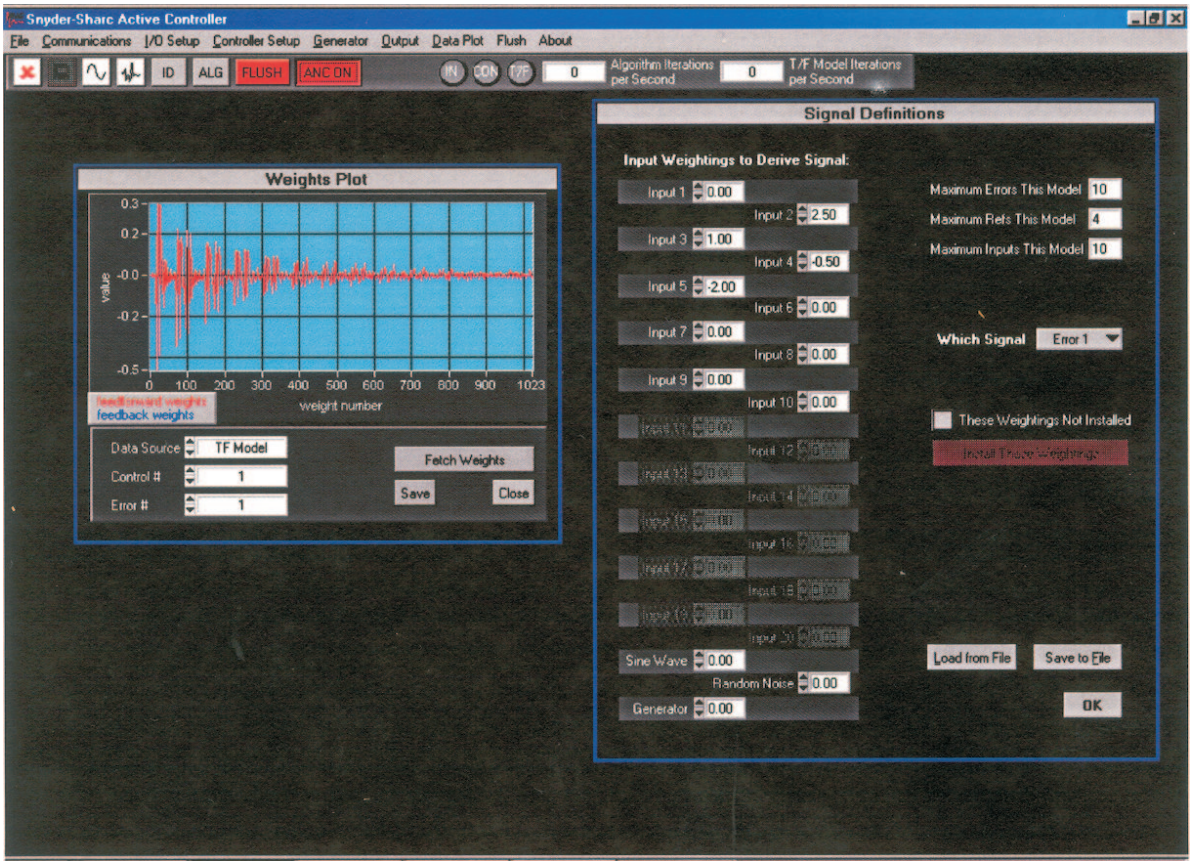

Figure 3.9: Implementation of the microphone weighting in the EZ-ANC II software

± 0.5dB. This matching was performed in a standing wave tube as shown in Figure 3.10. A plate was constructed to position a number of microphones at the end of the tube in the same vertical plane. The source was then driven with broadband noise to below the cut-on frequency to ensure that only plane waves propagated. Transfer functions between each microphone located in the tube were measured and the ones with the closest matching phases and sensitivity were selected. As the microphones were not perfectly matched, the extent of the importance of phase and sensitivity matching on the accuracy of the prediction could be observed.

Figure 3.10: Photograph of the experimental set-up to select phase and sensitivity matched microphones

3.5 Results for Rigidly Terminated Duct

3.5.1 Resonance

3.5.1.1 Linear Virtual Microphone

Figure 3.11 shows the results obtained when controlling an acoustic resonance in a long, narrow, rigidly-terminated duct. These figures show the primary or uncontrolled sound field amplitude as a thick line at the top of the figure. The controlled sound fields are represented by the other curves with the vertical lines indicating the location of the prediction microphone array and the solid circles indicating the virtual locations. Figures 3.11(a), (b), (c) and (d) show a comparison of the performance of the four control evaluation methods using the linear virtual microphone. Purely analytical control shows an attenuation of approximately 40 dB at all separation distances. The amount of control was limited to 40 dB due to the artificial 1% error applied to the calculated optimal control source strengths. In this idealised environment the linear virtual microphone is able to accurately predict the sound pressure at all virtual locations. Analytical control predictions using measured transfer functions between the error sensor and control source locations as well as between the error sensor and primary source locations are referred to as “post-processed tonal control” when a tonal signal was used to measure the transfer functions and “post-processed broadband control” when a broadband random noise signal was used to measure the transfer functions. Post-processed tonal control, post-processed broadband control and the real-time control all show a decrease in attenuation as the separation distance between the transducers and the observer location is increased to $4h$. Control using the tonal experimental transfer function compares more favourably to the theory than the other experimental examples with 37 dB attenuation at an observer/sensor separation distance of $4h$. The post-processed control using broadband transfer function data performed the worst of the four control examples with 19 dB of attenuation at $4h$, while real-time control achieved an attenuation of 25 dB at $4h$. Note that h is 25mm.

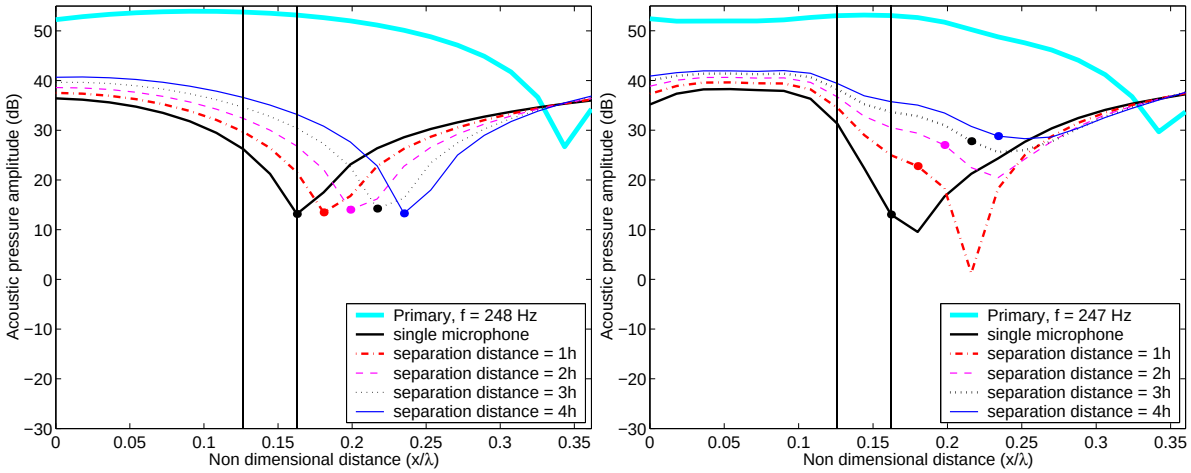

(a) Analytical model

(b) Post-processed experimental control using broadband noise to measure the transfer functions

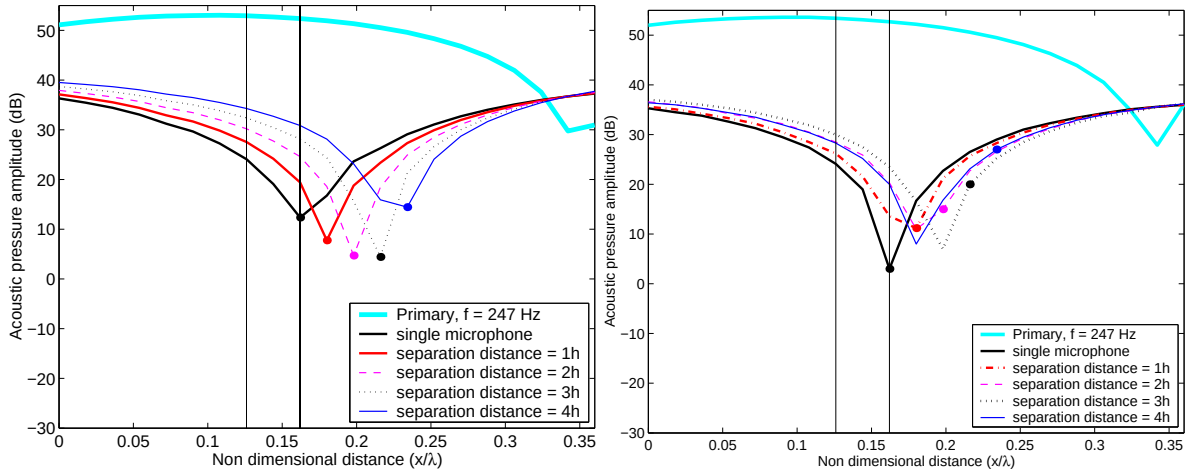

(c) Post-processed experimental control using tonal noise to measure the transfer functions

(d) Real-time

Figure 3.11: Uncontrolled and controlled sound pressure amplitudes along a rigidly terminated duct at an acoustic resonance using linear virtual microphone. The vertical lines represent the location of the microphone array and the filled circles represent the location of the virtual microphone.

Unlike the post-processed data, which used a single microphone to measure the transfer functions, the real-time measurements used a minimum of two microphones to predict the pressure at the virtual location. Sensitivity and phase mismatch between the sensors used in real-time experiments limited the performance. Errors in the positioning of the prediction sensors may have also affected the prediction accuracy. Therefore the performance of the post-processed broadband transfer functions should theoretically be superior to the real-time control results. It can therefore be concluded that the performance of the control obtained using post-processed transfer function measurements obtained with broadband noise is affected by errors associated with the use of the Fast Fourier Transform (FFT) used to calculate the frequency response functions. These errors are greatest when the coherence is low, occurring at resonances and anti-resonances. The poor coherence at anti-resonances is a result of low signal to noise ratio. It can be seen that the coherence is lowest at resonance which is due to resolution bias errors. Attempts were made to minimise these by using a Hanning window and a large number of points in the FFT (2048). Unfortunately some errors was still present. More points in the FFT would have been used, but the HP spectrum analyser used to collect the data was restricted to a maximum of 2048 points. Using tonal noise to measure the transfer functions eliminates the low coherence caused by marginal errors in the spectral density estimate; consequently resulting in higher levels of predicted attenuation as a result of active noise control, for all separation distances.

Figure 3.12 illustrates how increasing the number of points in the FFT will greatly reduce the extent of the resolution bias errors . These figures are of the simulated complex transfer function and the corresponding coherence for the one-dimensional waveguide using a 2048 point FFT (Figure 3.12(a)) and a 8192 point FFT (Figure 3.12(b)). It is evident from these figures that increasing the number of points from 2048 to 8192 greatly improves the coherence of the transfer function because with the frequency resolution is greatly increased. With a coarse frequency resolution the transfer function at the centre frequency of the measurement band is effectively an average over the bandwidth. Thus when the frequency resolution is increased

a more accurate estimation of the transfer function results (Bendat and Piersol (1993)). Or considering it in the time domain, the buffer length is much longer and thus the sound field has decayed completely prior to the buffer being full.

In order to justify the use of virtual microphones, it is important to determine if the virtual microphone formulations produce higher levels of attenuation compared to that offered by a single microphone located at p_5, shown by a solid black line in Figure 3.11. In the case of the analytical model, the post-processed tonal control and real-time control, the linear virtual microphone out-performs the single microphone at all separation distances. Post-processed control using broadband transfer functions is out-performed by the single closest microphone at all separation distances.

3.5.1.2 Quadratic Virtual Microphone

Figure 3.13 illustrates the performance of the quadratic virtual microphone for the four different control strategies. The analytical model shows an attenuation of 40 dB for all separation distances. Note that this is an artificial limit imposed to simulate the expected limitations of a real-time controller. Similar to the linear virtual microphone, real-time control also achieves greater attenuation than post-processed control using broadband transfer function data for all separation distances, which reflects the effect that resolution bias errors has on the accuracy of the data used for post-processed control. Employing real-time control at a separation distance of $4h$ results in 22 dB attenuation, compared with 20 dB achieved using post-processed control with broadband transfer functions. Control using post-processed tonal transfer function data was much better than that achieved by the other two experimental control examples with 33 dB attenuation at $4h$ where h is 25mm.

The effect of experimental errors on the performance of the quadratic algorithm is highlighted when comparing the results with the attenuation achieved using the single remote microphone. Control using a single microphone located at p_5 achieves much higher levels of attenuation

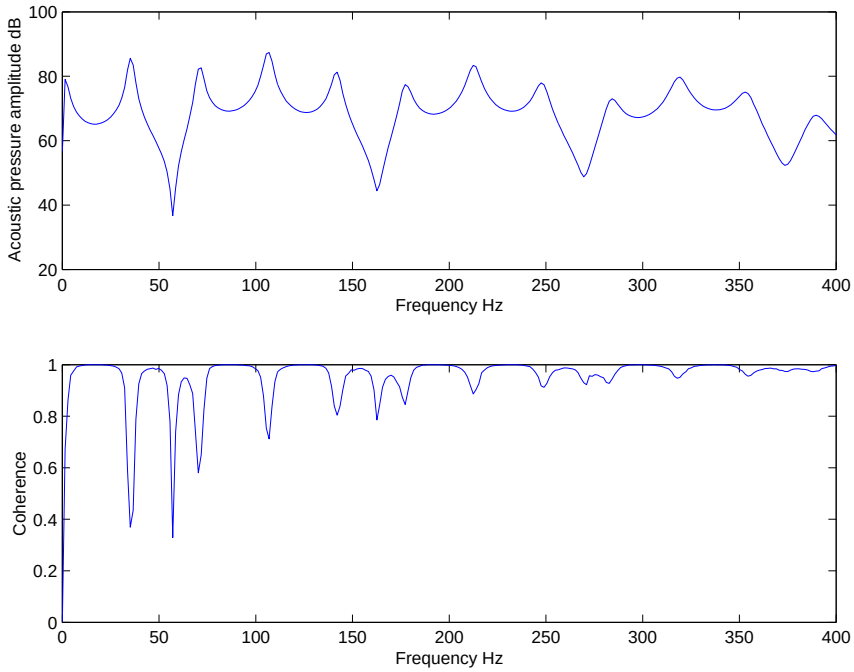

(a) 2048 point FFT

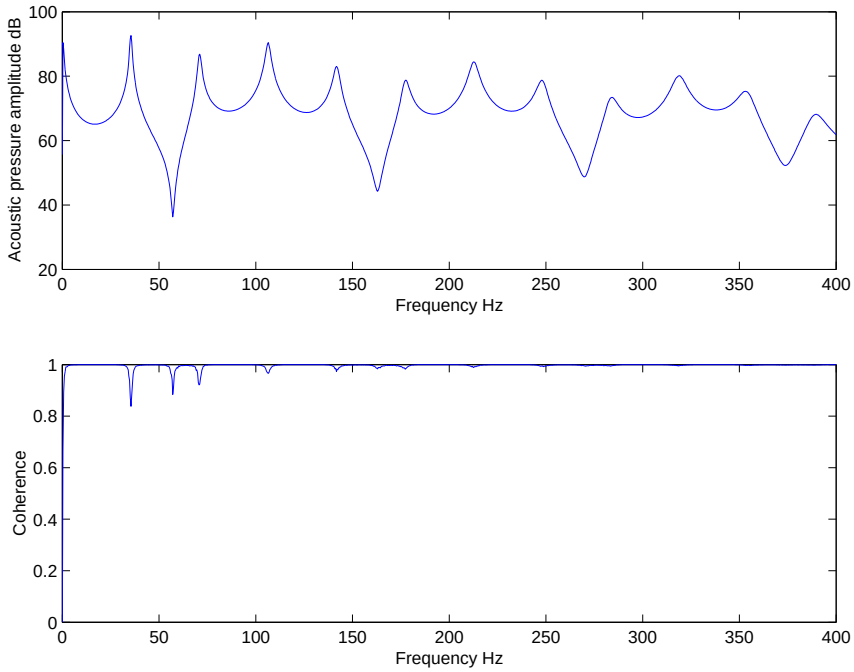

(b) 8192 point FFT

Figure 3.12: Example of the affect the number of points in the FFT has on the coherence due to resolution bias errors

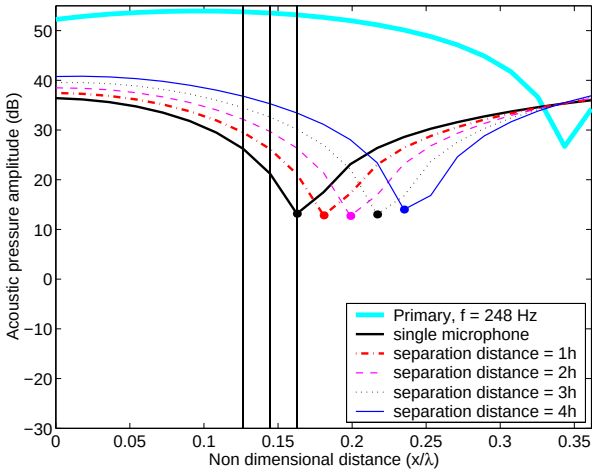

(a) Analytical model

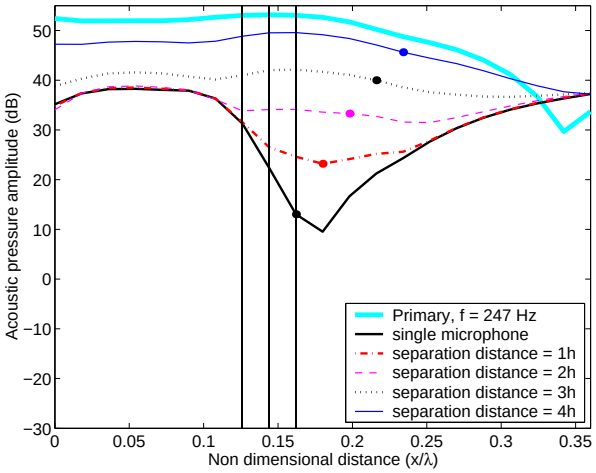

(b) Post-processed experimental control using broadband noise for the transfer function measurements

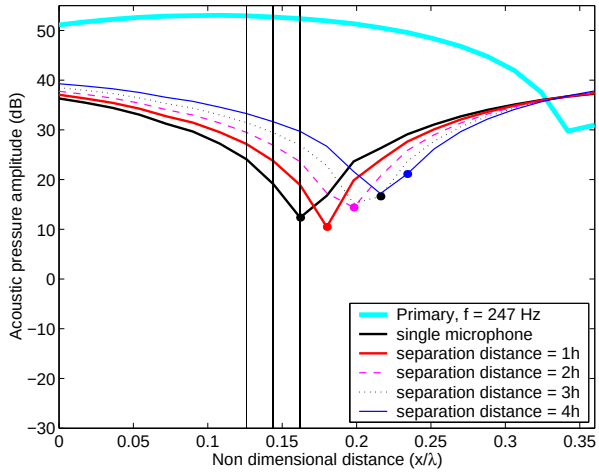

(c) Post-processed experimental control using tonal noise for the transfer function measurements

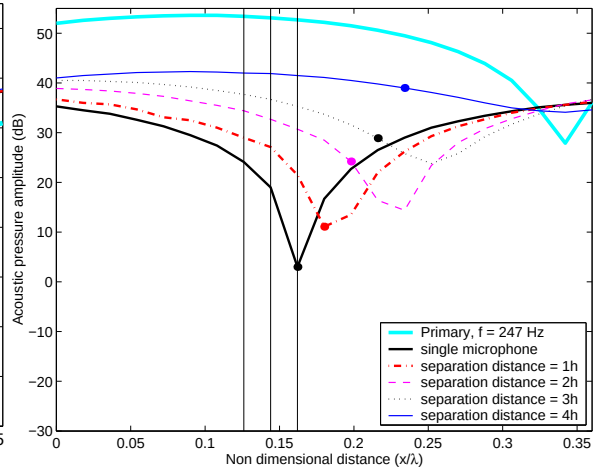

(d) Real-time

Figure 3.13: Uncontrolled and controlled sound pressure amplitudes along a rigidly terminated duct at an acoustic resonance using quadratic virtual microphones. The vertical lines represent the location of the microphone array and the filled circles represent the location of the virtual microphone.

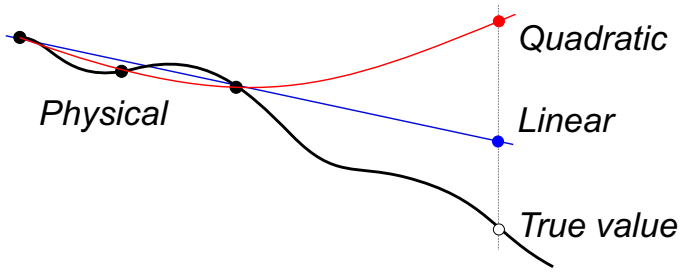

Figure 3.14: Prediction errors in the presence of short wavelength spatial pressure variations (after Kestell (2000))

over most separation distances than was achieved with control using the quadratic virtual microphone in real-time and broadband post-processed control. Therefore no advantage is obtained using the quadratic virtual microphone compared with the conventional single remote microphone.

Comparing the quadratic virtual microphone control examples with the corresponding linear control examples shows that the linear algorithm out-performs the quadratic algorithm with the exception of the analytical models. This is a result of the presence of experimental errors, inherent errors and short wavelength spatial variations in the experimental data (see Figure 3.14) as suggested by Kestell (2000). Consequently, quadratic predictions are less accurate than the linear estimates when using physical data. The quadratic virtual microphone real-time experiment used three microphones. Matching both phase and magnitude sensitivities for all three microphones was very difficult and consequently the pressure estimate at the virtual location was degraded, compared with the linear virtual microphone.

3.5.2 Anti-resonance

3.5.2.1 Linear Virtual Microphone

In Figure 3.15, the results obtained when controlling an anti-resonance (at 265 Hz) in the same rigidly-terminated, long, narrow duct using a linear virtual microphone are presented. At an

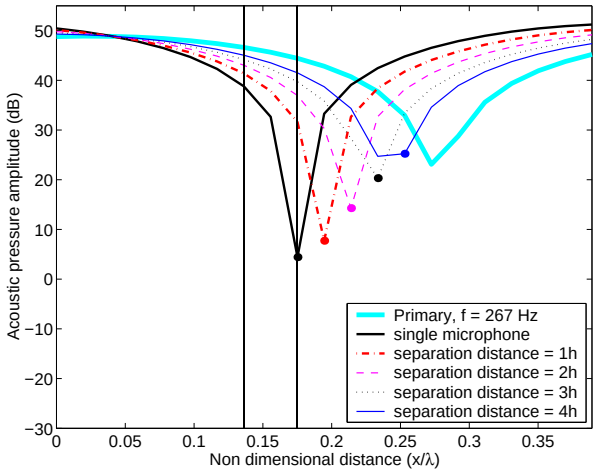

(a) Analytical model

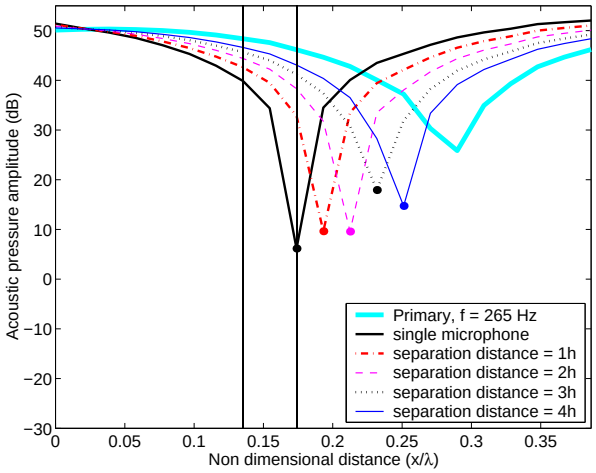

(b) Post-processed experimental control using broadband noise for the transfer function measurements

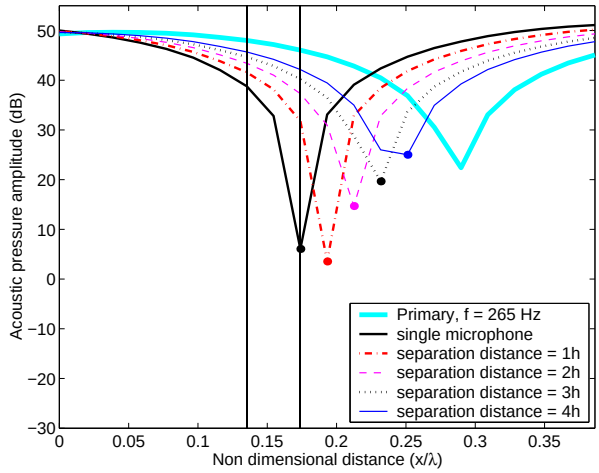

(c) Post-processed experimental control using tonal noise for the transfer function measurements

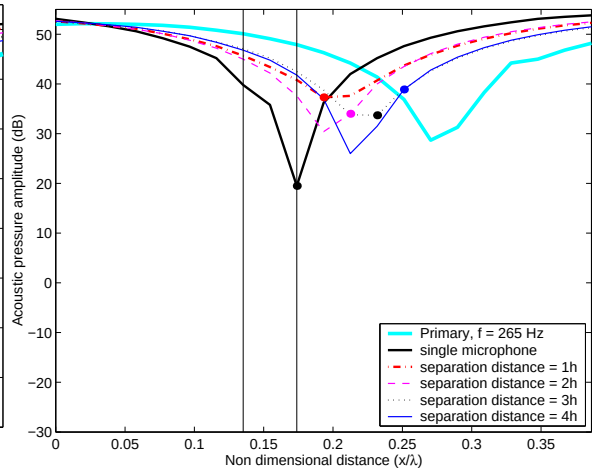

(d) Real-time

Figure 3.15: Uncontrolled and controlled sound pressure amplitudes along a rigidly terminated duct at an acoustic anti-resonance using linear virtual microphones. The vertical lines represent the location of the microphone array and the filled circles represent the location of the virtual microphone.

off-resonance condition, the level of control is significantly reduced when controlling at a location remote from the microphones because several modes dominate the response. This is evident in Figure 3.15(a) where the simulated level of control produced is much reduced compared with the corresponding resonance example. In this case, post-processed experimental control using broadband transfer function data out performs real-time control because the frequency response data are less affected by resolution bias errors at an anti-resonance frequency (see Figure 3.12). Figure 3.15(b) shows that at a separation distance of $4h$ an attenuation of 14 dB is achieved using broadband transfer function measurements. Figure 3.15(c) displays control results obtained using post-processed transfer function data measured using a tonal signal. This figure indicates that there is no improvement in this control field when using tonal measurements compared to that achieved using transfer functions measured with broadband noise. This confirms that there is not a significant level of resolution bias errors at this frequency to adversely affect the level of control achieved.

Real-time control resulted in a gain of 2 dB of the primary field at $4h$ as can be seen in Figure 3.15(d) although at smaller separation distances significant attenuations were achieved. At the anti-resonance, the real-time control performance is partly limited by the strength of the signal, since there is a lower signal to noise ratio (compared to the resonance example) at this frequency. More importantly, it is also limited by the sensitivity and phase mismatch between the transducers, which affects the accuracy of the prediction algorithm, in contrast to the post-processed data that were obtained using the same microphone for all of the measurements.
The linear virtual microphone out-performs the single microphone located at p_5 in all four control strategies at all separation distances.

3.5.2.2 Quadratic Virtual Microphone

Figure 3.16 shows the results for the quadratic virtual microphone for the four control scenarios. Figure 3.16(a) illustrates the performance of the quadratic virtual microphone using simulated control of an anti-resonance. These results are quite erratic. Figures 3.16(b) and

(c) show the post-processed control results using broadband excitation and tonal excitation respectively to obtain the transfer function data. Comparing the results displayed in these two figures again confirms that at an acoustic anti-resonance, the effect of resolution bias errors is significantly reduced, as the level of attenuation achieved in each of these examples is almost identical. At a separation distance of $4h$, both post-processed control examples obtained an attenuation of approximately 10 dB. In comparison, real-time control produced a gain of 5 dB at $4h$ when compared to the uncontrolled sound field. As discussed previously, this poor performance was a result of both poor signal to noise ratio at the anti-resonance frequency (limited by dynamic range of the controller) and transducer sensitivity and phase mismatch problems.

Although the quadratic virtual microphone out-performs the conventional control method of a single microphone at all separation distances, the virtual microphone does not necessarily result in an attenuation of the primary sound field.

The linear prediction algorithm out-performs the quadratic algorithm in the post-processed control and real-time control examples, confirming that the quadratic prediction algorithm is prone to corruption from short wavelength extraneous noise and other experimental errors.

3.6 Results for a Duct with Absorptive Ends

Sound absorbing material was added to the one-dimensional waveguide to observe the impact that increased damping has on the virtual microphone algorithms. The addition of the sound absorbing material reduced the value of the resonance quality factor from 50 to 10.

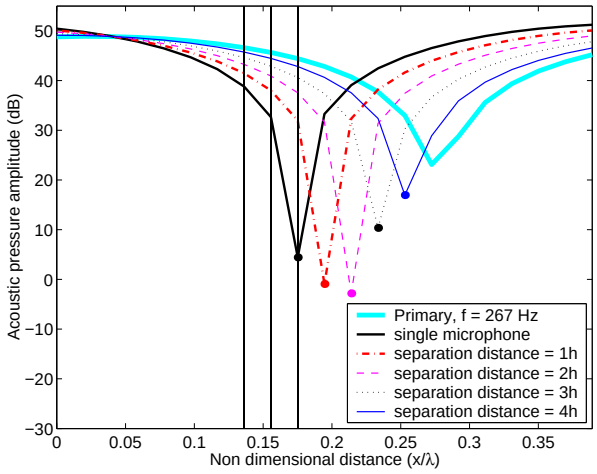

(a) Analytical model

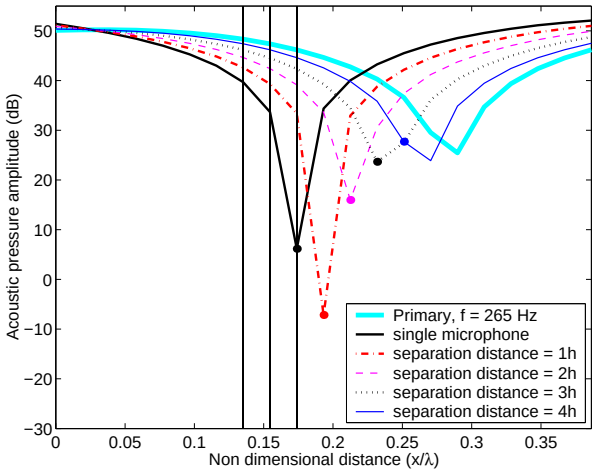

(b) Post-processed experimental control using broadband noise for the transfer function measurements

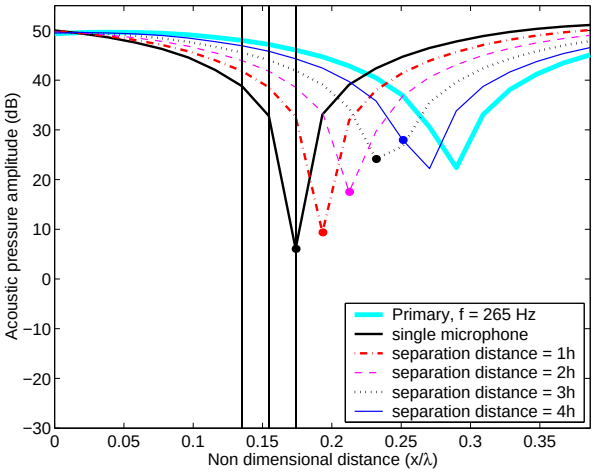

(c) Post-processed control using tonal noise for the transfer function measurements

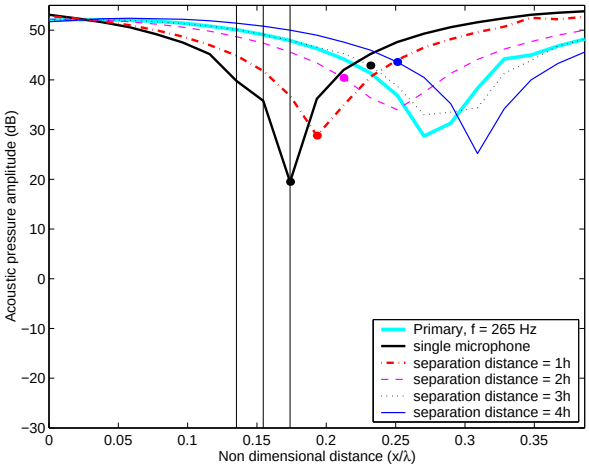

(d) Real-time

Figure 3.16: Uncontrolled and controlled sound pressure amplitudes along a rigidly terminated duct at an acoustic anti-resonance using quadratic virtual microphones. The vertical lines represent the location of the microphone array and the filled circles represent the location of the virtual microphone.

3.6.1 Resonance

3.6.1.1 Linear Virtual Microphone

This section discusses the results obtained using the linear virtual microphone algorithms in a long narrow duct with absorptive ends at resonance. Figure 3.17 shows the results for the linear virtual microphone at resonance. Figure 3.17(a) shows the control profile obtained using the analytical model. This figure shows 40 dB of attenuation at the separation distances of 0h and h decreasing to 22 dB at a separation distance of 4h. Figure 3.17(b) shows a significant decrease in the level of control achieved using broadband transfer function data when compared to Figure 3.17(a). The results obtained using tonal transfer function data are comparable to those obtained using the analytical model as seen in Figure 3.17(c). While the tonal results still out-perform the broadband results it can be seen that the broadband results are less affected by resolution bias errors than the rigid duct example due to the reduction in reverberation time within the duct and therefore the resolution bias errors. With the decrease in the value of Q from 50 to 10, the resonant peaks become much broader and therefore the extent of the resolution bias errors is significantly reduced. This effect is illustrated in Figure 3.18. The analytical model of the damped duct was used and simulated complex transfer functions and coherence were plotted for the duct with broadband excitation using 2048 point FFT and 8192 FFT as was done for the rigid duct. Figure 3.18(a) shows the frequency response and coherence for the 2048 point FFT. Comparing this figure with Figure 3.12(a) for the rigid duct shows that the coherence is significantly improved for the case of the damped duct. This indicates that for the same number of FFT points, the resolution bias errors in the damped duct measurement is reduced. With much broader resonant peaks the number of points required to accurately calculate the FFT are reduced. The controlled sound field plots using the post processed broadband experimental data indicate this with more comparable levels of control with the real-time control.

The real-time control results presented in Figure 3.17(d) indicate a decrease in the level of

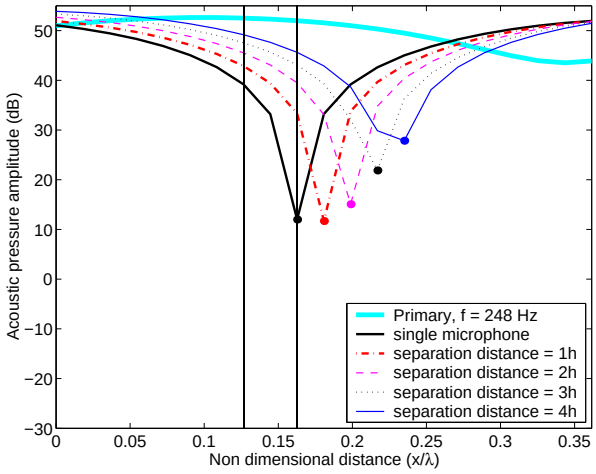

(a) Analytical model

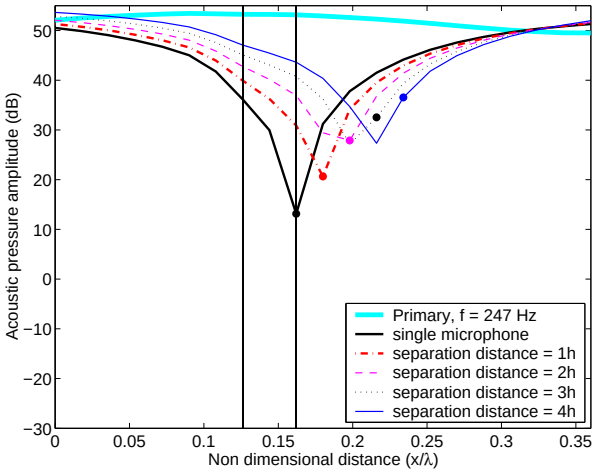

(b) Post-processed experimental control using broadband noise for the transfer function measurements

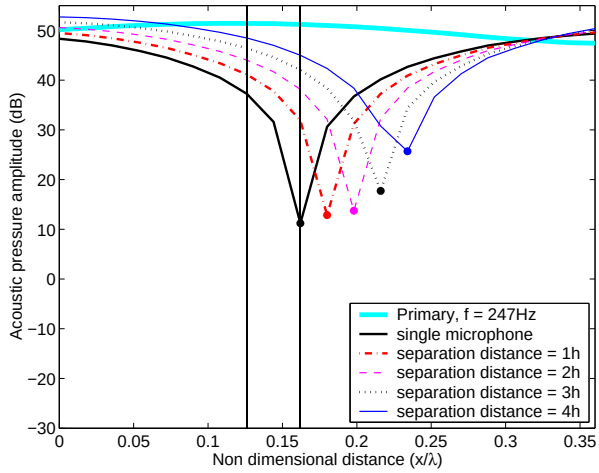

(c) Post-processed experimental control using tonal noise for the transfer function measurements

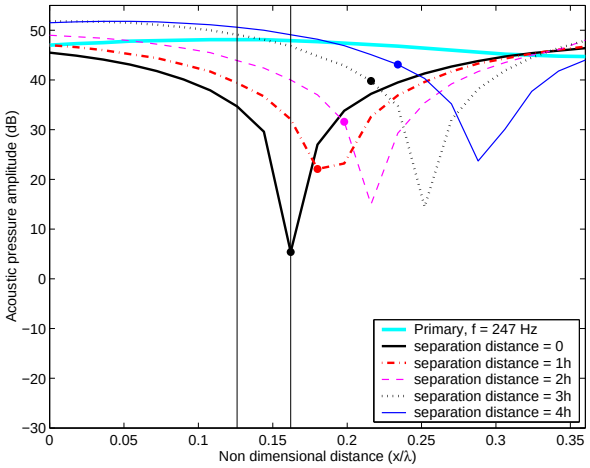

(d) Real-time

Figure 3.17: Uncontrolled and controlled sound pressure amplitudes along a duct with absorptive ends at an acoustic resonance using linear virtual microphones. The vertical lines represent the location of the microphone array and the filled circles represent the location of the virtual microphone.

attenuation compared to the other three examples. The zone of maximum attenuation is shifted from the virtual location, indicating that there is phase and sensitivity mismatch between the sensors.

3.6.1.2 Quadratic Virtual Microphone

Figure 3.19 illustrates the results for the quadratic virtual microphone controlling an acoustic resonance in a duct with absorptive ends. The results of control using the analytical model are shown in Figure 3.19(a), with a 40 dB reduction up to a separation distance of $2h$, which slightly decreases to 30 dB at $4h$. This decrease in attenuation is a result of inaccurate prediction of the pressure at the virtual location at large separation distances. Figure 3.19(b) also shows a decrease in the level of control due to resolution bias errors when using the broadband transfer function data . It is clear from these results that there is still a small degree of resolution bias errors present, which corrupts the prediction accuracy of the quadratic virtual microphone algorithm. Eliminating the effect of resolution through the use of tonal transfer function data results in a significantly higher level of control with a 20 dB increase in the level of attenuation at $4h$. The effect of this small amount of resolution bias errors highlights the susceptibility of the quadratic virtual microphone to experimental errors. The real-time control results shown in Figure 3.19(d) indicate that the level of attenuation decreases from 40 dB at $0h$ to 10 dB at $4h$.

As with the previous examples it can be clearly seen when comparing the results that the linear virtual microphone out-performs the quadratic when physical data is used. This again illustrates the quadratic algorithm's susceptibility to the corruption of accuracy as a result of experimental errors.

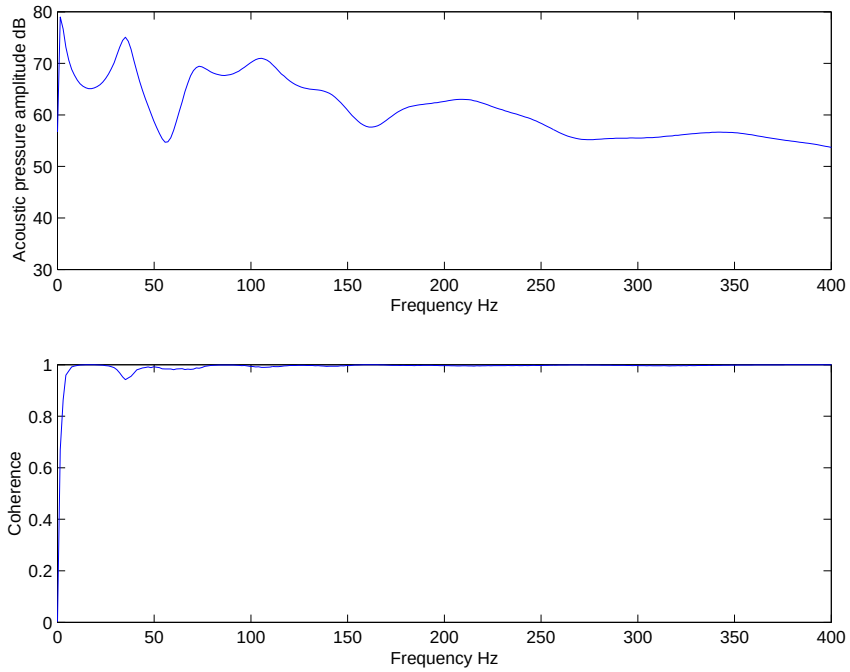

(a) 2048 point FFT

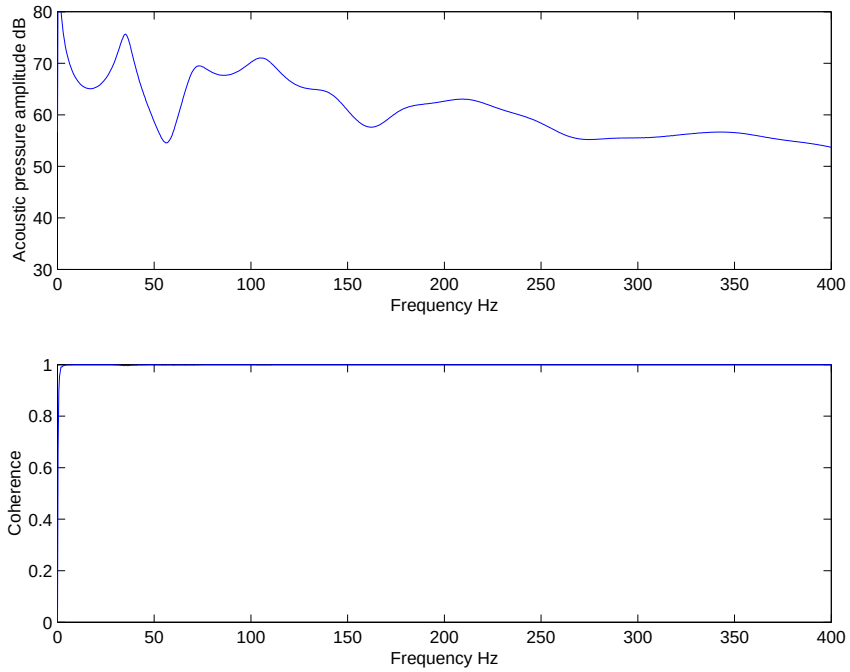

(b) 8192 point FFT

Figure 3.18: Example of the affect the number of points on the FFT has on the coherence due to resolution bias errors

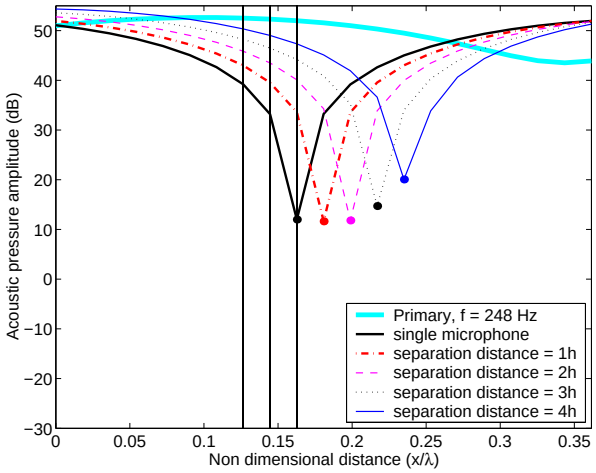

(a) Analytical model

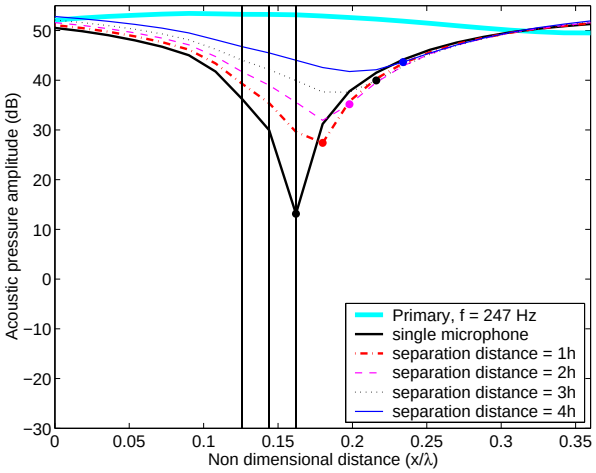

(b) Post-processed experimental control using broadband noise for the transfer function measurements

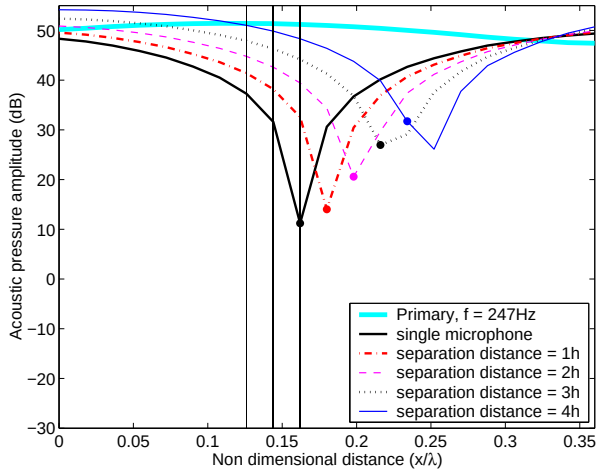

(c) Post-processed experimental control using tonal noise for the transfer function measurements

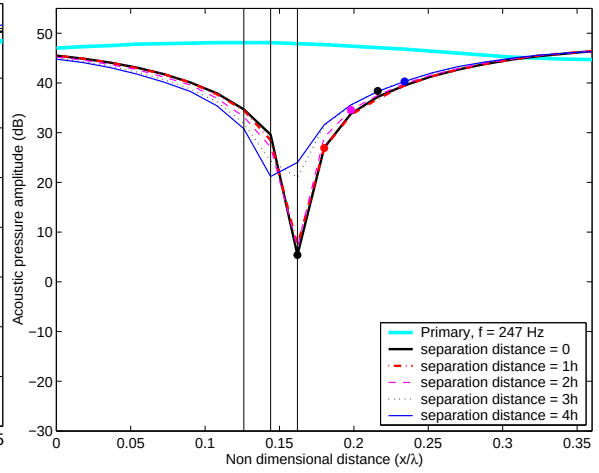

(d) Real-time

Figure 3.19: Uncontrolled and controlled sound pressure amplitudes along a duct with absorptive ends at an acoustic resonance using quadratic virtual microphones. The vertical lines represent the location of the microphone array and the filled circles represent the location of the virtual microphone.

3.6.2 Anti-resonance

3.6.2.1 Linear Virtual Microphone

In Figure 3.20 the performance of the linear virtual microphone using different control strategies for the anti-resonant example is compared. The results for the analytical model presented in Figure 3.20(a) again illustrate the reduction in the degree of attenuation compared to the resonance example. The results for the two post-processed control examples presented in Figures 3.20(b) and (c) indicate that the problem of resolution bias errors does not occur and this is evident because the control profiles for both examples are very similar. The absence of spectral resolution bias errors in the control example with broadband transfer function measurements is due to the damping from the absorptive ends of the duct and that the frequency being controlled is an anti-resonance. The results for real-time control are presented in 3.20(d). This control profile displays a similar trend to that produced in the resonance example. For separation distances larger than h, the zone of maximum attenuation does not occur at the virtual location, which is an indication of phase and sensitivity errors between microphone elements.

3.6.2.2 Quadratic Virtual Microphone

Figure 3.21 shows the control profiles achieved using a quadratic virtual microphone to control an acoustic anti-resonance in a damped one-dimensional waveguide. The results of the analytical model presented in Figure 3.21(a) again highlight the superior performance of the quadratic algorithm in this error free environment. Considering the two post-processed control examples presented in Figures 3.21(b) and (c), it can again be seen that resolution bias errors is absent in this case. However, the experimental errors are still present to a small extent as the control using tonal data produces slightly superior control profiles than achieved using broadband data. Finally, the real-time control results are shown in Figure 3.21(d). This results again show the effect of phase and sensitivity mismatch between the microphones on

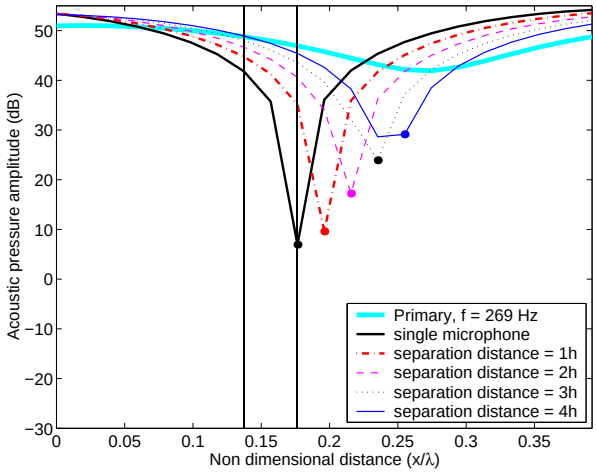

(a) Analytical model

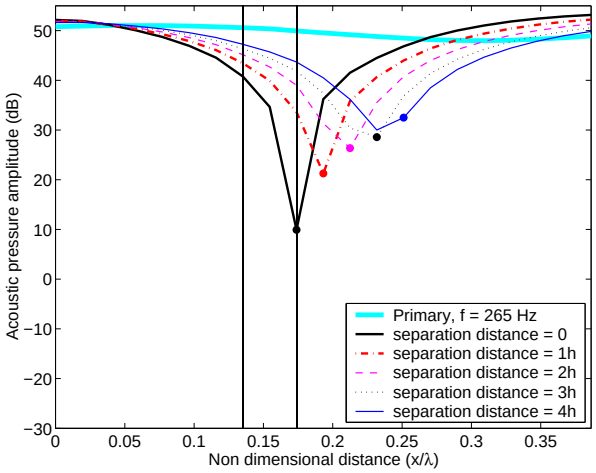

(b) Post-processed experimental control using broadband noise for the transfer function measurements

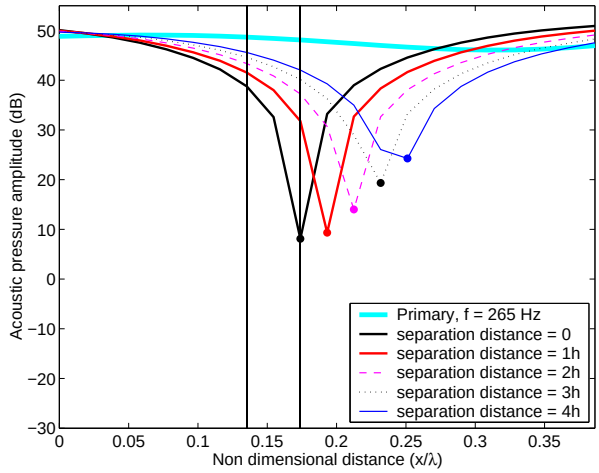

(c) Post-processed experimental control using tonal noise for the transfer function measurements

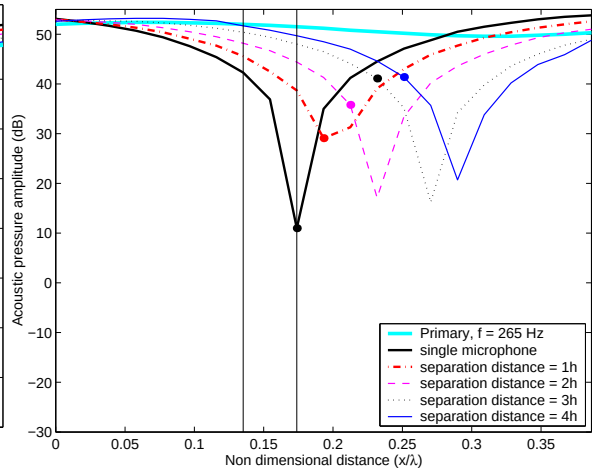

(d) Real-time

Figure 3.20: Uncontrolled and controlled sound pressure amplitudes along a duct with absorptive ends at an anti-acoustic resonance using linear virtual microphones. The vertical lines represent the location of the microphone array and the filled circles represent the location of the virtual microphone.

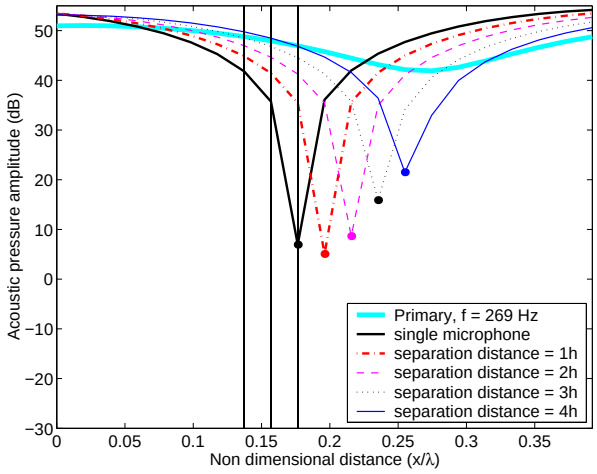

(a) Analytical model

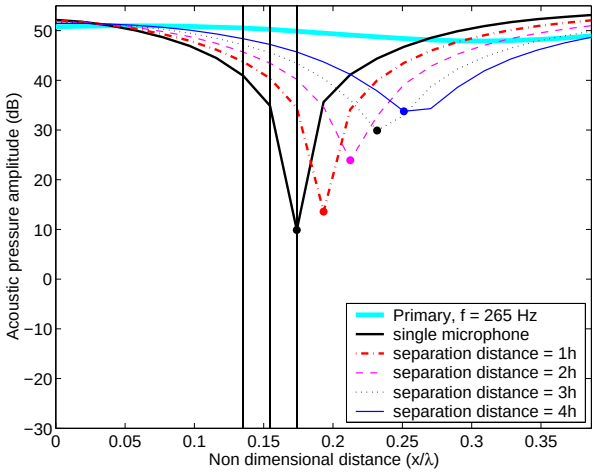

(b) Post-processed experimental control using broadband noise for the transfer function measurement

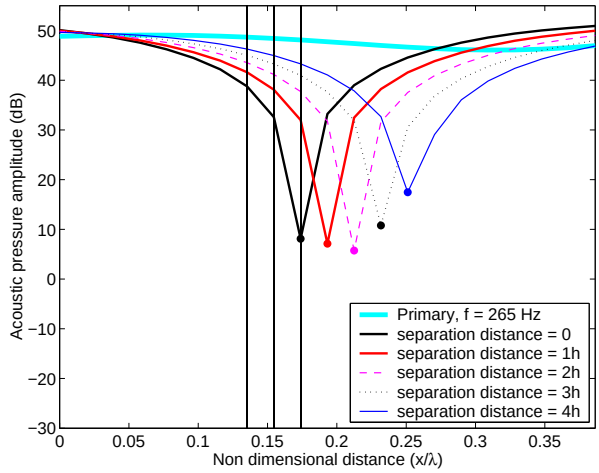

(c) Post-processed experimental control using tonal noise for the transfer function measurement

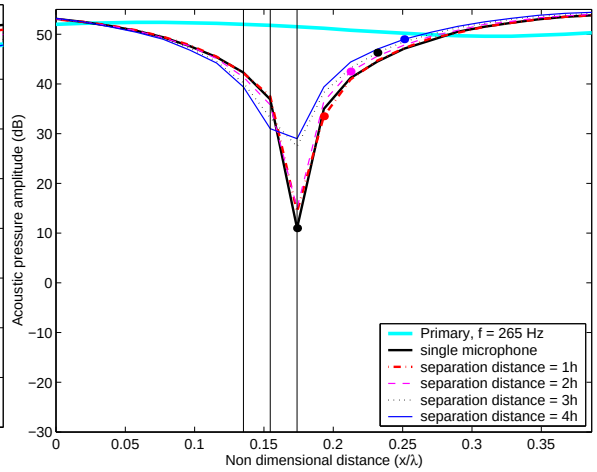

(d) Real-time

Figure 3.21: Uncontrolled and controlled sound pressure amplitudes along a duct with absorptive ends at an anti-resonance using quadratic virtual microphones. The vertical lines represent the location of the microphone array and the filled circles represent the location of the virtual microphone.

the prediction accuracy of the quadratic algorithm. The effect of phase and sensitivity on the prediction accuracy of the quadratic algorithm is covered in detail in Chapter 6.

3.7 Conclusion

The performance of two forward-difference prediction virtual algorithms using real-time control in a long, narrow duct has been evaluated. The results presented in this chapter suggest the forward-difference virtual microphones can predict the pressure at a location remote from that of the prediction microphones and therefore produce localised zones of sound attenuation at the virtual location.

One of the aims of this work was to ascertain the reason for the poor control results produced using post-processed transfer functions presented by Kestell (2000). The control results presented here indicate that Kestell's poor control results using the forward difference virtual microphones was a product of erroneous experimental data due to resolution bias errors and not a product of the virtual microphone formulation. The results presented here showed that control with the broadband transfer functions produced the lowest levels of attenuation of all the control examples. The use of tonal transfer functions for simulated control resulted in a significant increase in the attenuation achieved at the virtual location. This result indicates that the deficient performance of control using broadband transfer functions is a result of resolution bias errors. The real-time control results presented also out-performed the control produced using broadband transfer functions. This was not expected as the implementation of real-time control should introduce more experimental error than was present in the simulated control. These errors include the limitation of the accuracy of the real-time controller and the use of a number of microphones to predict the pressure at the virtual location, with phase and sensitivity mismatch errors between microphones.

The post-processed control results using broadband transfer functions highlights the importance of selecting the appropriate measurement method in order to minimise experimental

errors. Also selecting the most appropriate measurement for the post-processed control will give a more accurate estimation of the results to expect when real-time control is attempted. Hence the measurements of broadband transfer functions in a lightly damped enclosure can result in resolution bias errors as the resonant peaks are narrow. Resolution bias errors result in poor coherence at the resonant frequency which produces poor attenuation in the virtual microphone simulations. However, with absorptive ends on the duct causing the resonant peaks to be significantly broader, bias errors was found to be considerably reduced. This is evident in the results presented here as the control profiles achieved using the virtual microphone algorithms were comparable to those achieved using the tonal transfer function measurements in the duct with absorptive ends.

In practice, the performance of real-time control is influenced by phase and sensitivity mismatch between the prediction transducers. Thus accurate system calibration and transducer selection is important. When the location of the maximum zone of attenuation shifts from the virtual location, it is an indication of the presence of phase and sensitivity mismatch. The effect of these errors is assessed thoroughly in Chapter 4.

Comparing the performance of the linear and the quadratic virtual microphone algorithms, it was clear in the three control examples which involved experimental data, that the linear virtual microphone out-performed the quadratic virtual microphone. It is thought that the performance of the quadratic virtual microphone is very sensitive to experimental errors and short wavelength extraneous noise.

To develop more accurate virtual microphone algorithms, the concept of higher-order virtual microphones was considered. These virtual microphones use an over-constrained forward-difference algorithm to predict the sound pressure at the virtual location. The algorithm is over-constrained because additional microphones are added to the prediction array while still using the first and second order algorithms. These higher-order virtual microphones are designed to filter out short wavelength extraneous noise and hence result in a more accurate prediction at the virtual location. Higher-order virtual microphones will be discussed in Chapter 5.

Chapter 4

Error Analysis

As with sound intensity and energy density measurement, the prediction of remote sound pressure using an array of microphones results in three sources of errors; namely, finite separation errors, diffraction and interference effects at microphones, and instrumentation errors such as phase and gain mismatch between the microphone elements. Fahy (1995) presented a study on the affect of these errors on sound intensity measurements. Cazzolato (1999), drawing heavily on Fahy's work, analysed the errors in the measurement of acoustic energy density for one-dimensional sound fields using both the two microphone technique and the three dimensional error sensor he developed. This chapter presents a study of how these errors affect the virtual microphone algorithms, using as a basis the work of Fahy (1995) and Cazzolato (1999). The following errors are considered in a reactive field and a plane wave field:

- inherent
- phase
- sensitivity.

4.1 Finite Separation Errors

Finite separation (inherent) errors are not a result of measurement or instrumentation performance but a result of the type of field under investigation and the orientation of the probe within the field (Fahy, 1995). The pressure between two points in space separated by h is given by:

$$\begin{aligned} p(x+(x-x_v),t) &= p(x,t)+(x-x_v)p^{(1)}(x,t)+((x-x_v)^2/2)p^{(2)}(x,t) \\ &\quad +((x-x_v)^3/6)p^{(3)}(x,t)+\ldots+((x-x_v)^n/n!)p^n(x,t)+\ldots \end{aligned} \tag{4.1}$$

where $p(x,t)$ has arbitrary time dependence, $p^n(x,t)$ denotes the nth derivative of p with respect to x at any time t (Fahy, 1995) and x_v.

4.1.1 Linear Virtual Microphone

The linear virtual microphone consists of a two element array, with each element separated by $2h$. The configuration of this virtual sensor is presented schematically in Figure 4.1. The sound pressure measured at microphones p_1 and p_5 is used to predict the pressure at the virtual microphone located at x_v.

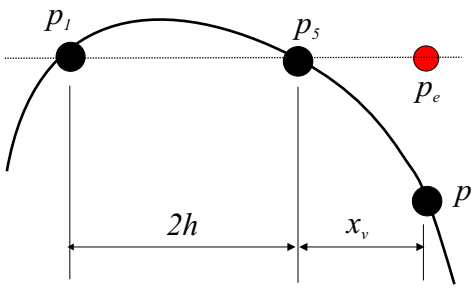

Figure 4.1: Illustration of the estimation of pressure at the virtual location using a linear prediction algorithm.

The two microphone linear prediction algorithm is:

$$p_e = \begin{bmatrix} \left(\frac{x_v}{h}\right) & 1 \end{bmatrix} \begin{bmatrix} -0.5 & 0.5 \\ 0 & 1 \end{bmatrix} \begin{bmatrix} p_1 \\ p_5 \end{bmatrix} \tag{4.2}$$

where

$$p_1 = p(x - x_v - 2h) \tag{4.3}$$

$$p_5 = p(x - x_v) \tag{4.4}$$

where x_v is the separation distance between the physical transducers and the virtual location.

The normalised error in the estimate of p is given by:

$$e(p) = \frac{p_e - p}{p} \tag{4.5}$$

where p is the exact measurement of the pressure.

4.1.2 Quadratic Virtual Microphone

For the quadratic virtual microphone a three element array is used and in this case each element is separated by h. This virtual microphone estimates the sound pressure level using a second-order prediction algorithm at some distance, x_v from the outer most microphone, p_5 as indicated in Figure 4.2.

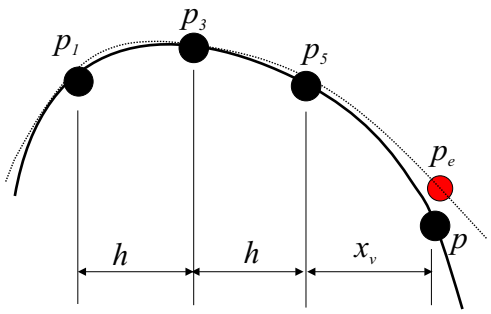

Figure 4.2: Illustration of the estimation of pressure at the virtual location using a quadratic prediction algorithm.

The three microphone quadratic prediction algorithm is:

$$p_e = \begin{bmatrix} \left(\frac{x_v}{h}\right)^2 & \frac{x_v}{h} & 1 \end{bmatrix} \begin{bmatrix} 0.5 & -1.0 & 0.5 \\ 0.5 & -2.0 & 1.5 \\ 0 & 0 & 1.0 \end{bmatrix} \begin{bmatrix} p_1 \\ p_3 \\ p_5 \end{bmatrix} \tag{4.6}$$

where

$$p_5 = p(x - x_v) \tag{4.7}$$

$$p_3 = p(x - x_v - h) \tag{4.8}$$

$$p_1 = p(x - x_v - 2h) \tag{4.9}$$

The normalised error in the estimate of p is calculated using Equation (4.5).

4.1.3 One-dimensional Reactive Sound Field

The real pressure fluctuation in a one-dimensional reactive sound field can be written as $p(x,t) = \Re\{p(x)e^{j\omega t}\}$ where $p(x) = P_o e^{jkx}$. Therefore the pressure and pressure gradients are given by:

$$p = P_o \cos(kx) \tag{4.10}$$

$$p^{(1)} = -kP_o \sin(kx) \tag{4.11}$$

$$p^{(2)} = -k^2 P_o \cos(kx), = -k^2 P \tag{4.12}$$

$$p^{(3)} = k^3 P_o \sin(kx), = -k^3 P^{(1)} \tag{4.13}$$

$$p^{(4)} = k^4 P_o \cos(kx) = k^4 P \tag{4.14}$$

4.1.3.1 Linear Virtual Microphone

Inherent errors are a result of the finite sum and finite difference approximations used to estimate the sound pressure level at the virtual location. The inherent errors presented here are for the linear virtual microphone at all separation distances. These equations are derived in Appendix A.

For a separation distance between the closest element of the microphone array (p_5) and the virtual microphone location of h ($x_v = h$), the normalised error is given by:

$$e(p_h) = \frac{3h^2k^2}{2} - \frac{13h^4k^4}{8} + 2h^3k^3 \tan(kx) \tag{4.15}$$

For a separation distance between the closest element of the microphone array (p_5) and the virtual microphone location of $2h$ the normalised error is:

$$e(p_{2h}) = 4h^2k^2 - \frac{28h^4k^4}{3} + 8h^3k^3 \tan(kx) \tag{4.16}$$

For a separation distance between the closest element of the microphone array (p_5) and the virtual microphone location of $3h$ the normalised error is:

$$e(p_{3h}) = \frac{15h^2k^2}{2} - \frac{245h^4k^4}{8} + 20h^3k^3 \tan(kx) \tag{4.17}$$

For a separation distance between the closest element of the microphone array (p_5) and the

virtual microphone location of $4h$ the normalised error is:

$$e(p_{4h}) = 12h^2k^2 - 76h^4k^4 + 40h^3k^3\tan(kx) \tag{4.18}$$

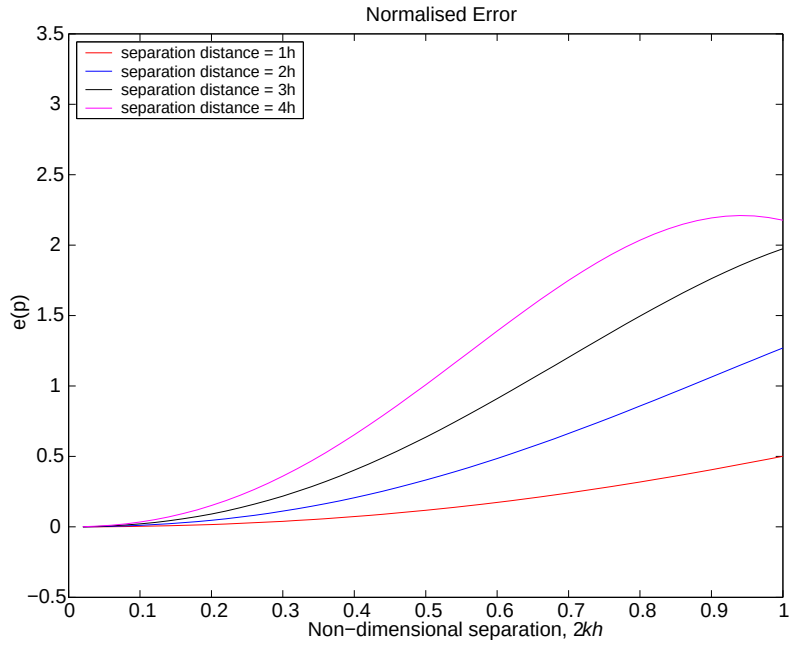

Figure 4.3: Inherent errors of the linear virtual microphone as a function of the non-dimensional separation distance (2kh) for a reactive one-dimensional sound field with $x/L = 1/4$.

The inherent error for the two element linear virtual microphone is plotted against the non-dimensional separation, $2kh$ in Figure 4.3. Since the error is dependent upon the location of the sensors, it was necessary to select a particular location within the duct to evaluate the error. For this case a normalised location, $x/L = 1/4$ was selected which represents the ratio of the distance from the primary source to the sensor location x to cavity length L. This is the same location as was used by Cazzolato (1999). From this figure it can be seen that as expected, the inherent error increases with increasing separation distance. This is consistent with the behaviour of the inherent errors that occur in sound intensity and energy density measurements.

4.1.3.2 Quadratic Virtual Microphone

The normalised pressure error due to finite separation when using the quadratic virtual microphone was calculated using the same procedure as described in Section 4.1.3.1 and is derived in Appendix A.

For a separation distance of h ($x_v = h$), the normalised error at location x in the field is:

$$e(p_h) = \frac{3h^4k^4}{2} + h^3k^3\tan(kx) \tag{4.19}$$

For a separation distance of $2h$ the normalised error is:

$$e(p_{2h}) = 9h^4k^4 + 4h^3k^3\tan(kx) \tag{4.20}$$

For a separation distance of $3h$ the normalised error is:

$$e(p_{3h}) = 30h^4k^4 + 10h^3k^3\tan(kx) \tag{4.21}$$

For a separation distance of $4h$ the normalised error is:

$$e(p_{4h}) = 75h^4k^4 + 20h^3k^3\tan(kx) \tag{4.22}$$

From these equations it can be concluded that the minimum error will occur at $kx = n\pi$ and the error will become infinite at $kx = (2n+1)\pi/2$.

As with the linear virtual microphone the inherent error for the quadratic virtual microphone at all separation distances is plotted against non-dimensional separation distance in Figure 4.4 again at a position corresponding to $x/L = 1/4$. The inherent error increases markedly with increasing separation distance. Comparing this figure with Figure 4.3, it can be seen that at high frequencies (large kh) the inherent errors in the quadratic estimate are significantly larger than the linear virtual microphone inherent errors. However, at lower frequencies (small kh)

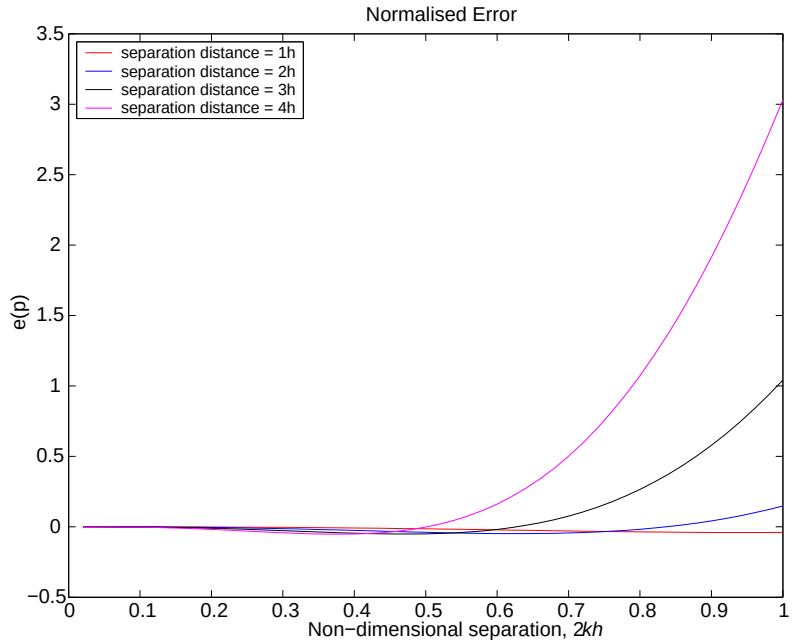

Figure 4.4: Inherent errors of the quadratic virtual microphone as a function of the non-dimensional separation distance (2kh) for a reactive one-dimensional sound field with $x/L = 1/4$.

the inherent errors in the quadratic estimate are smaller than the linear estimate inherent errors.

4.1.4 Plane progressive wave

A plane progressive wave is a good approximation to a free field, which represents a completely different type of sound field to the reactive sound field. A plane wave can be defined as:

$$p(x,t) = \Re\left\{P_o e^{j\omega t - jkx}\right\} \tag{4.23}$$

The pressure and pressure gradients of the idealised model of this sound field are given by:

$$P = P_o e^{-jkx} \tag{4.24}$$

$$P^{(1)} = -jkP \tag{4.25}$$

$$P^{(2)} = -k^2 P \tag{4.26}$$

$$P^{(3)} = -k^2 P^{(1)} = jk^3 P \tag{4.27}$$

$$P^{(4)} = k^4 P \tag{4.28}$$

4.1.4.1 Linear Virtual Microphone

The normalised errors for the virtual pressure at all separation distances using a linear virtual microphone are derived in Appendix A and presented below. The configuration of the virtual microphone array is the same as was presented in Figure 4.1.

$$e(p_h) = \frac{3}{2}h^2k^2 + 2jh^3k^3 - \frac{13}{8}h^4k^4 \tag{4.29}$$

$$e(p_{2h}) = 4h^2k^2 + 8jh^3k^3 - \frac{28h^4k^4}{3} \tag{4.30}$$

$$e(p_{3h}) = \frac{15}{2}h^2k^2 + 20jh^3k^3 - 30.625h^4k^4 \tag{4.31}$$

$$e(p_{4h}) = 12h^2k^2 + 40jh^3k^3 - 76h^4k^4 \tag{4.32}$$

The above equations indicate that as expected, the error in the prediction of the sound pressure level in a plane progressive field is independent of the position of the sensors in the field. The inherent error of a linear virtual microphone in a plane wave is plotted against non-dimensional separation distance, $2kh$ in Figure 4.5. Figure 4.5 shows that the influence of the inherent errors increases with increasing frequency.

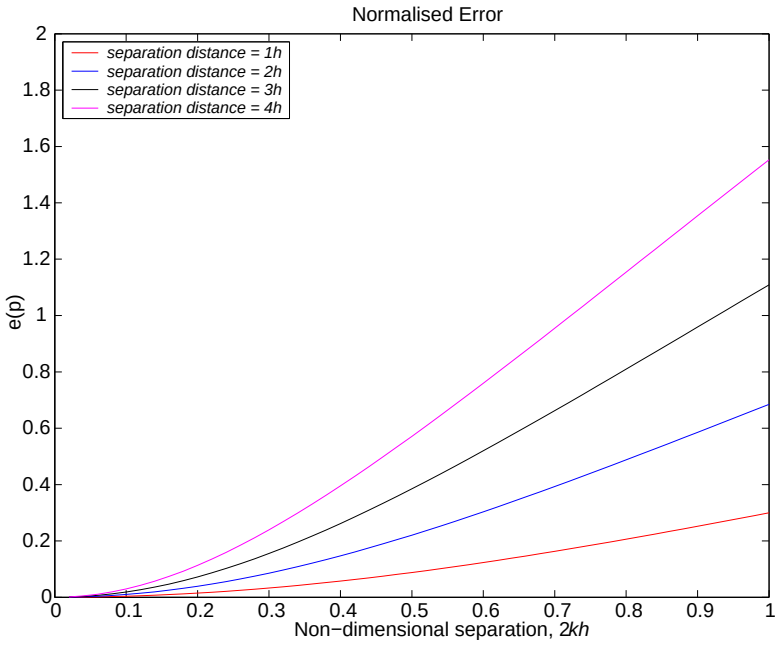

Figure 4.5: Inherent errors of the linear virtual microphone as a function of the non-dimensional separation distance (2kh) for a plane progressive wave.

4.1.4.2 Quadratic Virtual Microphone

In this section the normalised error for the virtual pressure using a three element quadratic virtual microphone (described in Section 4.1.2) in a plane progressive wave is presented. The normalised error in the pressure estimate at various virtual locations is given by:

$$e(p_h) = -jh^3k^3 + \frac{3h^4k^4}{2} \tag{4.33}$$

$$e(p_{2h}) = -4jh^3k^3 + 9h^4k^4 \tag{4.34}$$

$$e(p_{3h}) = -10jh^3k^3 + 30h^4k^4 \tag{4.35}$$

$$e(p_{4h}) = -20jh^3k^3 + 75h^4k^4 \tag{4.36}$$

As with the linear virtual microphones in a plane progressive wave, the above equations indicate that the inherent error of the quadratic virtual microphone is independent of its position

in the sound field. Figure 4.6 presents the inherent error for the quadratic virtual microphone in plane wave conditions plotted against non-dimensional separation distance. Comparing the inherent error for the linear and quadratic virtual microphone it can be seen that for small microphone separation distances up to $2h$, the use of the quadratic virtual microphone results in smaller values of inherent error. However, for the larger separation distances the quadratic virtual microphone produces higher levels of inherent error than the linear virtual microphone.

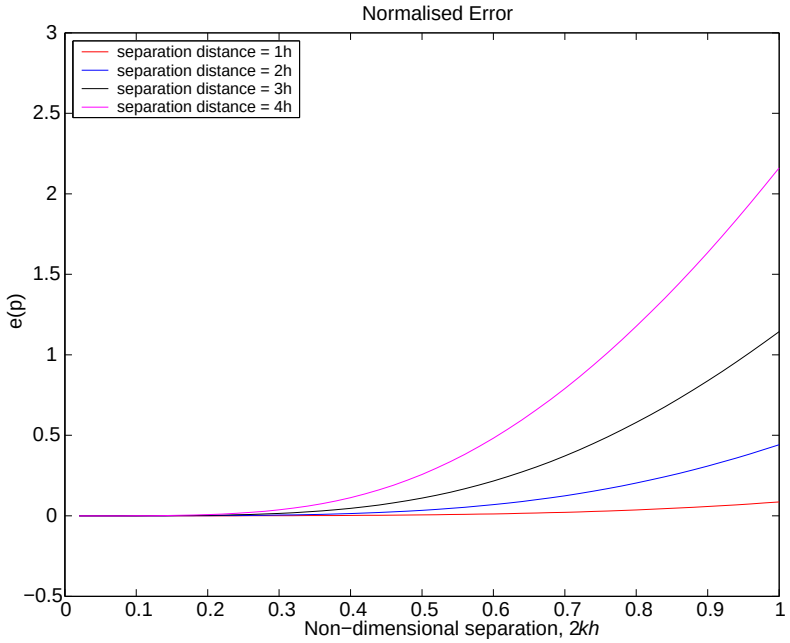

Figure 4.6: Inherent errors of the quadratic virtual microphone as a function of the non-dimensional separation distance (2kh) for a plane progressive wave.

4.2 Phase Mismatch Errors

For the case of simple harmonic fields, the pressure responses of two microphones with a phase mismatch of $2\phi_s$ are given by the products of the true pressures with $e^{\pm j\phi_s}$, that is

$$\hat{p}_1(x,t) = p_1(x,t)e^{j\phi_s} \tag{4.37}$$

$$\hat{p}_5(x,t) = p_5(x,t)e^{-j\phi_s} \tag{4.38}$$

The effect of phase mismatch errors depends upon relative magnitudes of the phase mismatch and the actual phase difference of the sound pressure at the sensor locations. The actual phase difference between the two measured sound pressures will depend upon the type of sound field, as well as the location and orientation of the transducers within the sound field (Fahy, 1995). The actual phase difference between the transducers is $2kh$ where $2h$ is the transducer separation distance.

4.2.1 One-dimensional Reactive Sound Field

4.2.1.1 Linear Virtual Microphone

Using the expression for a stationary reactive sound field, the true pressures measured at microphones p_1 and p_5 are

$$\widehat{p_1} = P_o(\cos(k(x - x_v - 2h))\cos(\omega t + \phi_s)) \tag{4.39}$$

$$\widehat{p_5} = P_o(\cos(k(x - x_v))\cos(\omega t - \phi_s)) \tag{4.40}$$

where the ^ represents the pressure response with the phase mismatch. Substituting Equations (4.39) and (4.40) into Equation (4.2) the pressure estimate with phase error can be calculated as:

$$\widehat{p_e} = \begin{bmatrix} \left(\frac{x_v}{h}\right) & 1 \end{bmatrix} \begin{bmatrix} -0.5 & 0.5 \\ 0 & 1 \end{bmatrix} \begin{bmatrix} \widehat{p_1} \\ \widehat{p_5} \end{bmatrix} \tag{4.41}$$

Using Equation (4.5), the normalised error for the pressure estimate for various separation distances is given by:

$$e(\widehat{p_h}) = e(p_h) + \phi_s j \sec(kx)(-1.5\cos(kx - kh) - 0.5\cos(kx - 3kh)) \tag{4.42}$$

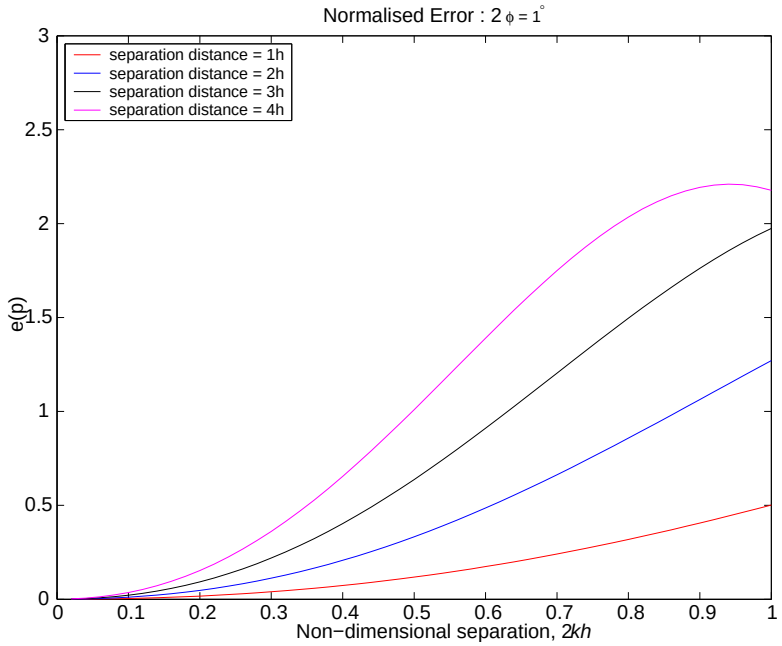

Figure 4.7: Normalised error in pressure at the virtual location using a linear virtual microphone in a one-dimensional reactive sound field with phase mismatch as a function of non-dimensional separation distance (2kh) with $x/L = 1/4$.

$$e(\widehat{p}_{2h}) = e(p_{2h}) + \phi_s j \sec(kx)(-2\cos(kx-2kh) - \cos(kx-4kh)) \tag{4.43}$$

$$e(\widehat{p}_{3h}) = e(p_{3h}) + \phi_s j \sec(kx)(-2.5\cos(kx-3kh) - 1.5\cos(kx-5kh)) \tag{4.44}$$

$$e(\widehat{p}_{4h}) = e(p_{4h}) + \phi_s j \sec(kx)(-3\cos(kx-4kh) - 2\cos(kx-6kh)) \tag{4.45}$$

where $e(p_h)$, $e(p_{2h})$, $e(p_{3h})$ and $e(p_{4h})$ is the inherent error derived from Section 4.1.3.1 for the separation distances of h, $2h$, $3h$ and $4h$ respectively.

In Figure 4.7 the normalised error in the pressure estimate at the virtual location with a phase error of $2\phi_s = 1^\circ$ is plotted against the non-dimensional separation distance. This figure does not show a notable increase in the normalised error when compared to the inherent error plotted in Figure 4.3.

To determine the effect that larger phase mismatches would have on the normalised error, phase mismatches ranging between $\pm 4^\circ$ were sequentially applied to each microphone in increments of 1° and the normalised error was calculated at a separation distance of $4h$ for every possible

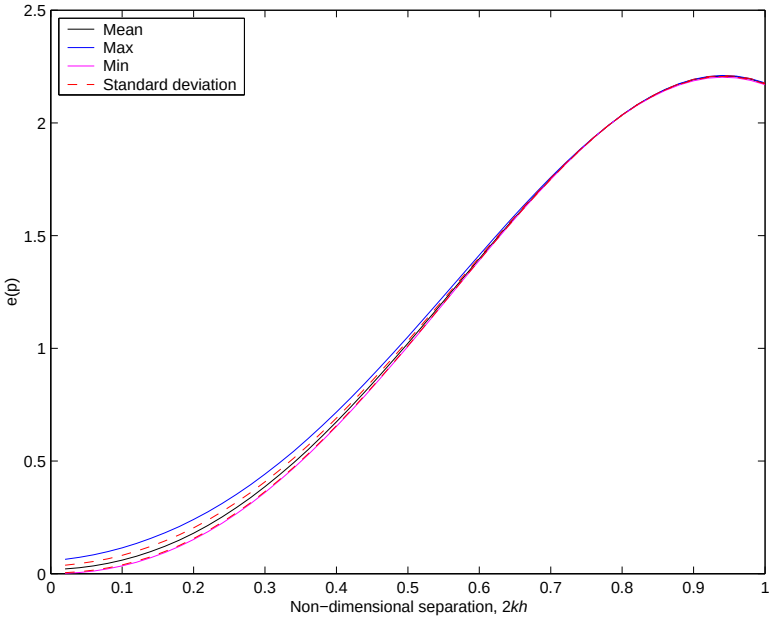

Figure 4.8: Normalised statistical error in virtual pressure at a separation distance of 4h using a linear prediction with the phase error (ϕ_s) varying $\pm 4°$.

combination. The mean, maximum, minimum and standard deviation was calculated from the normalised error and the result is plotted in Figure 4.8. The maximum mismatch applied across the two microphones is 8°. This figure indicates that this phase mismatch has a small impact on the normalised error at low frequencies.

4.2.1.2 Quadratic Virtual Microphone

The equations for pressure measured for quadratic virtual sensing at the three microphones with phase errors are given by:

$$\widehat{p}_1 = P_o(\cos(k(x-x_v))\cos(\omega t+\phi_s)) \tag{4.46}$$

$$\widehat{p}_3 = P_o\cos(k(x-x_v-h)\cos(\omega t) \tag{4.47}$$

$$\widehat{p}_5 = P_o(\cos(k(x-x_v-2h))\cos(\omega t-\phi_s)) \tag{4.48}$$

The above equations indicate that microphone three has no additional phase mismatch and microphones one and five have the same mismatch as for the linear virtual microphone case. Sharing the error equally over the two other microphones simplifies the error analysis. The estimated pressure at the virtual location with the above phase mismatch, using a second-order prediction method is given by:

$$p_e = \begin{bmatrix} \left(\frac{x_v}{h}\right)^2 & \frac{x_v}{h} & 1 \end{bmatrix} \begin{bmatrix} 0.5 & -1.0 & 0.5 \\ 0.5 & -2.0 & 1.5 \\ 0 & 0 & 1 \end{bmatrix} \begin{bmatrix} \widehat{p}_1 \\ \widehat{p}_3 \\ \widehat{p}_5 \end{bmatrix} \tag{4.49}$$

and the normalised error is calculated using Equation (4.3) and is given by:

$$e(\widehat{p}_h) = e(p_h) + j\phi_s \sec(kx)(3\cos(kx-kh) - \cos(kx-3kh)) \tag{4.50}$$

$$e(\widehat{p}_{2h}) = e(p_{2h}) + j\phi_s \sec(kx)(6\cos(kx-2kh) - 3\cos(kx-4kh)) \tag{4.51}$$

$$e(\widehat{p}_{3h}) = e(p_{3h}) + j\phi_s \sec(kx)(10\cos(kx-3kh) - 6\cos(kx-5kh)) \tag{4.52}$$

$$e(\widehat{p}_{4h}) = e(p_{4h}) + j\phi_s \sec(kx)(15\cos(kx-4kh) - 10\cos(kx-6kh)) \tag{4.53}$$

where $e(p_h), e(p_{2h}), e(p_{3h})$ and $e(p_{4h})$ is the normalised inherent error in a one-dimensional sound field presented in Section 4.1.3.2 for separation distance h, $2h$, $3h$ and $4h$ respectively.

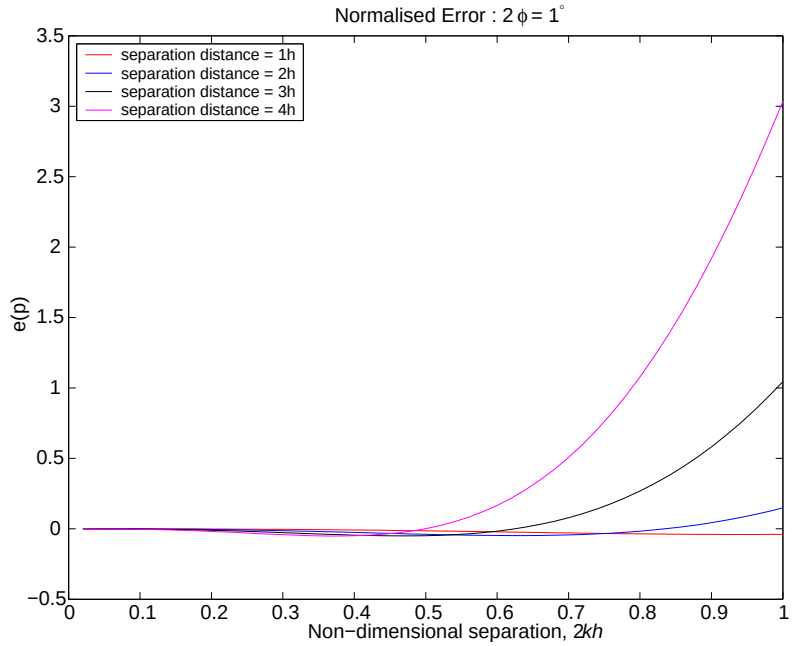

Figure 4.9: Normalised error in pressure at the virtual location using a quadratic virtual microphone in a one-dimensional reactive sound field with phase mismatch as a function of non-dimensional separation distance (2kh) with $x/L = 1/4$.

Figure 4.9 presents the normalised error in the pressure estimate with phase error of $2\phi_s = 1^\circ$ for the quadratic virtual microphones plotted against non-dimensional separation distance. Comparing this figure with Figure 4.4, it can be seen that this amount of phase error does not increase the normalised error above the inherent error.

Figure 4.10 shows the statistical analysis results for the quadratic virtual microphone with phase mismatch applied to only the two outermost microphones (1 and 5) and also to all three microphones. Figure 4.10(a) presents the results for phase mismatch of $\pm 4^\circ$ applied sequentially at increments of 1° to only the outermost microphones, such that the amount of phase error applied is the same as for the linear prediction case presented in Section 4.2.1.1. Comparing the results in Figure 4.10 with the linear results presented in Figure 4.8, it can be seen that with the quadratic virtual microphone the effect of this error is more significant. The phase mismatch was also applied to all three prediction microphones. Phase mismatch of $\pm 4^\circ$ was applied sequentially in increments of 1° to all three microphones and at a separation distance

of $4h$ the normalised error was calculated for all possible combinations of phase mismatch. Figure 4.10(b) shows the results with phase mismatch applied to all three microphones and this has a notable effect on the maximum normalised error. This is the more realistic case, as in practice phase mismatch would exist in all three microphones. These results confirm previous experimental results presented in Chapter 3, which indicates that the performance of the quadratic virtual microphones is degraded as a result of experimental errors.

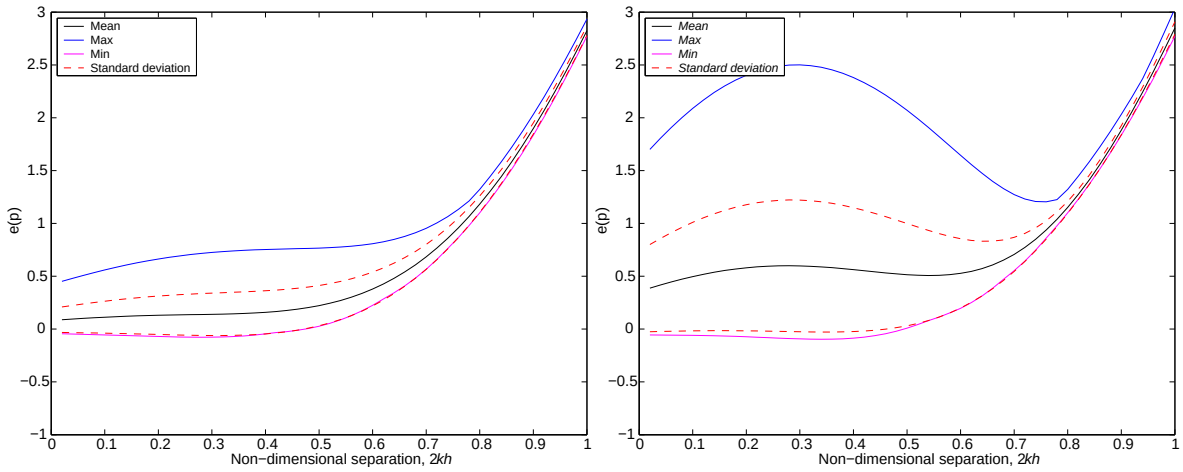

(a) Error applied to microphones 1 and 5 *(b) Error applied to all three microphones*

Figure 4.10: Normalised statistical error in virtual pressure at a separation distance of $4h$ using a quadratic prediction with the phase error (ϕ_s) varying $\pm 4°$.

4.2.2 Plane Progressive Wave

4.2.2.1 Linear Virtual Microphone

For a plane progressive wave, the phase mismatch is equivalent to modifying the sensor spacing, hence, $k\hat{h} = kh - \phi_s$. Therefore, the normalised error for the linear virtual microphone with phase mismatch in a plane progressive wave at all separation distances is given by:

$$e(p_h) = \frac{3}{2}\hat{h}^2k^2 + 2j\hat{h}^3k^3 - \frac{13}{8}\hat{h}^4k^4 \tag{4.54}$$

$$e(p_{2h}) = 4\widehat{h}^2k^2 + 8j\widehat{h}^3k^3 - \frac{28\widehat{h}^4k^4}{3} \tag{4.55}$$

$$e(p_{3h}) = \frac{15}{2}\widehat{h}^2k^2 + 20j\widehat{h}^3k^3 - \frac{245}{8}h^4k^4 \tag{4.56}$$

$$e(p_{4h}) = 12\widehat{h}^2k^2 + 40j\widehat{h}^3k^3 - 76\widehat{h}^4k^4 \tag{4.57}$$

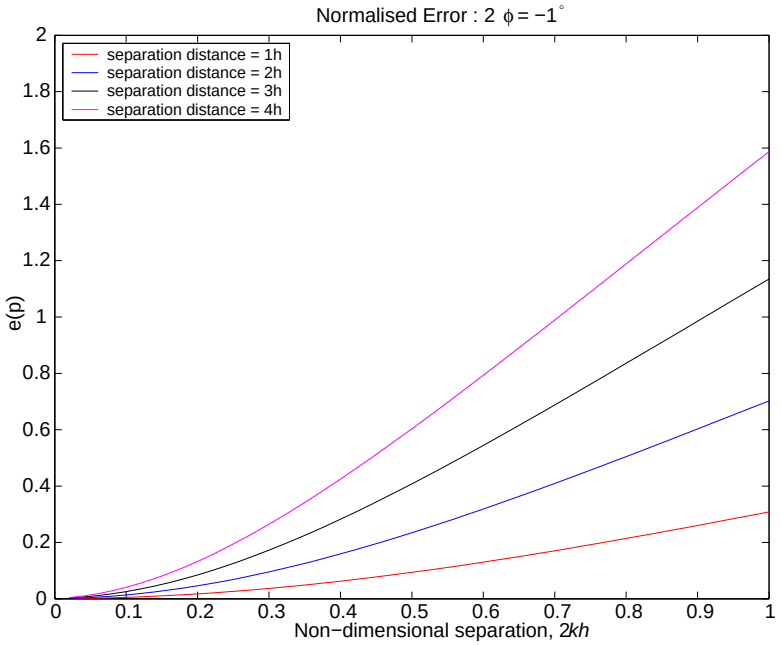

Figure 4.11: Normalised error in pressure at the virtual location using a linear virtual microphone in a plane progressive wave with phase mismatch as a function of non-dimensional separation distance (2kh).

Figure 4.11 presents the normalised error in virtual pressure using a linear virtual microphone plotted against non-dimensional separation distance with a phase error of $2\phi_s = 1°$.

The normalised statistical error for the linear virtual microphone at a separation distance of $4h$ with varying phase mismatch between $\pm 4°$ is presented in Figure 4.12. The process for calculating the statistical error was the same as described in Section 4.2.1.1. This figure indicates that the effect of this error is consistent over the entire frequency range.

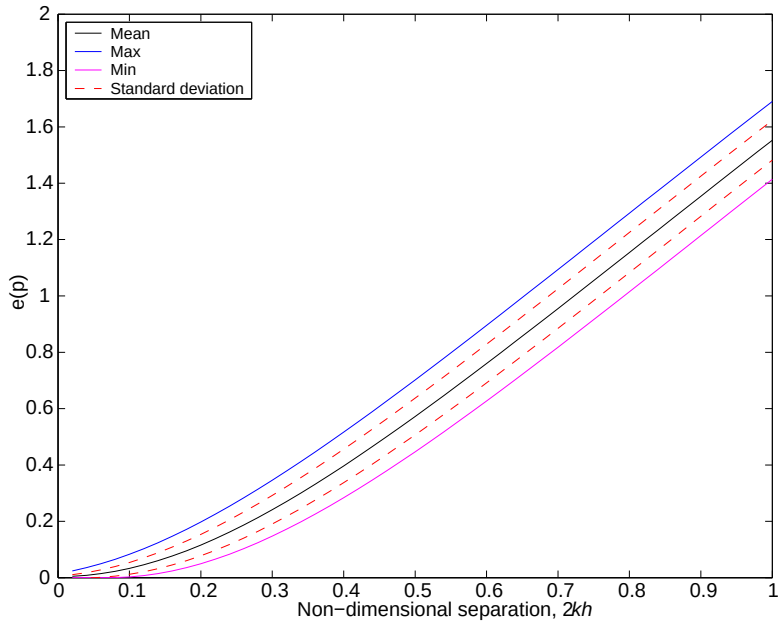

Figure 4.12: Normalised statistical error in virtual pressure at a separation distance of 4h using a linear prediction with the phase error (ϕ_s) varying between $\pm 4°$

4.2.2.2 Quadratic Virtual Microphone

The analytical equations for the quadratic virtual microphone with phase error in a one-dimensional plane progressive wave environment are difficult to derive. This is because in a plane progressive wave, the phase mismatch is equivalent to modifying the sensor spacing and while the modification of the separation distance between the two outermost microphones is known, the modification of the central microphone location relative to the others is not known. Thus analytical equations for the quadratic virtual microphone normalised error as a result of phase mismatch in plane wave conditions will not be derived. The normalised error for the quadratic virtual microphone with phase mismatch in plane wave conditions was calculated numerically and is presented in Figure 4.13.

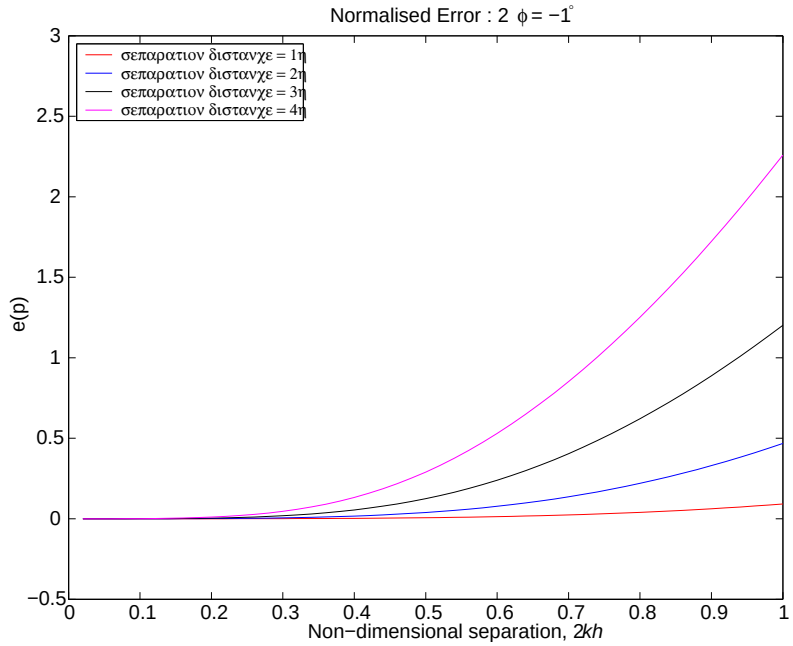

Figure 4.13: Normalised error in pressure at the virtual location using a quadratic virtual microphone in a plane progressive wave with phase mismatch as a function of non-dimensional separation distance (2kh).

The normalised statistical error for the quadratic virtual microphone with varying phase mismatch ranging between $\pm 4°$ applied to only the outermost microphones and all microphones is presented in Figure 4.14(a) and (b) respectively. The procedure to calculate the statistical error was outlined in Section 4.2.1.1. Figure 4.14(a) highlights the sensitivity of the quadratic prediction algorithms to experimental errors. Introducing additional phase mismatch by applying a phase error to the central microphone greatly increases the error as shown in Figure 4.14(b). These figures again illustrate the susceptibility of the quadratic virtual microphone to phase errors.

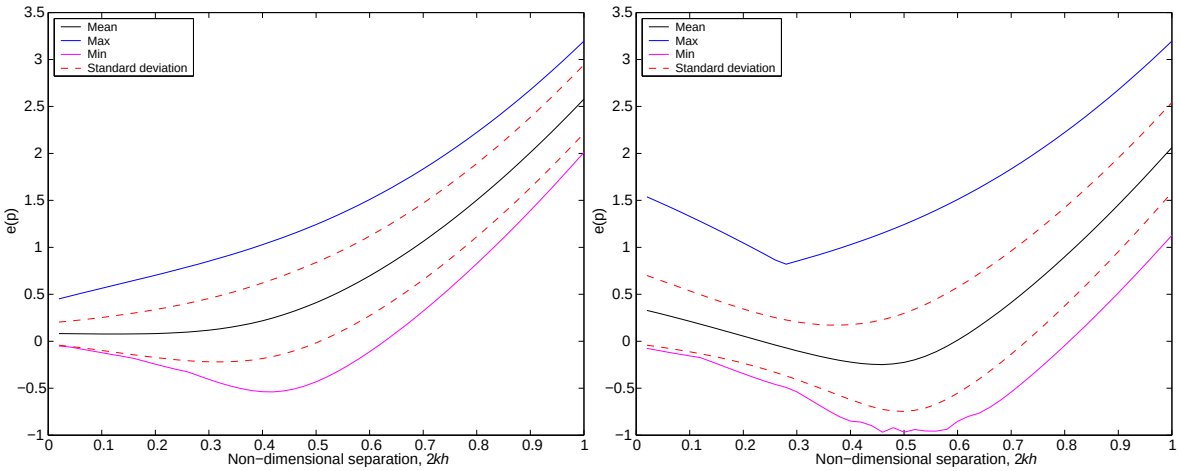

(a) Error applied to microphones 1 and 5 *(b) Error applied to all microphones*

Figure 4.14: Normalised statistical error in virtual pressure at a separation distance of 4h using a quadratic prediction with the phase error (ϕ_s) varying between $\pm 4°$

4.3 Sensitivity Errors

Sensitivity differences between microphone elements may effect that the accuracy of the pressure estimation at the virtual location. The pressure sum and difference are altered in both phase and magnitude by sensitivity mismatch (Fahy, 1995).

4.3.1 One-dimensional Reactive Sound Field

The error arising from sensitivity mismatches in a one-dimensional reactive sound field has been calculated and is presented below.

4.3.1.1 Linear Virtual Microphone

Let the sensitivity difference between the two transducers be $\pm T$ such that the ratio of the sensitivities is given by $(1+T)/(1-T) \approx 1+2T$ for small T. Therefore the pressures at the

two microphones are given by:

$$\widetilde{p}_1 = p_1(x,t)(1-T) \tag{4.58}$$

$$\widetilde{p}_5 = p_5(x,t)(1+T) \tag{4.59}$$

where for the stationary reactive sound field, the pressure is given by:

$$p(x,t) = \Re\{p(x)e^{j\omega t}\} \tag{4.60}$$

The analytical equations for the errors arising from the sensitivity mismatch $\pm T$, using a linear virtual microphone for separation distances from h to $4h$ are given by

$$e(\widetilde{p}_h) = e(p_h) + T\sec(kx)(1.5\cos(kx-kh) + 0.5\cos(kx-3kh)) \tag{4.61}$$

$$e(\widetilde{p}_{2h}) = e(p_{2h}) + T\sec(kx)(2\cos(kx-2kh) + \cos(kx-4kh)) \tag{4.62}$$

$$e(\widetilde{p}_{3h}) = e(p_{3h}) + T\sec(kx)(2.5\cos(kx-3kh) + 1.5\cos(kx-5kh)) \tag{4.63}$$

$$e(\widetilde{p}_{4h}) = e(p_{4h}) + T\sec(kx)(3\cos(kx-4kh) + 2\cos(kx-6kh)) \tag{4.64}$$

The derivation of these equations is presented in Appendix A. Figure 4.15 shows the normalised error in pressure at the virtual location in a one-dimensional reactive sound field with a sensitivity mismatch as a function of non-dimensional separation distance for a linear virtual microphone. This figure shows that with a sensitivity error of 1% the inherent error due to the finite separation of the transducers dominates the error, as there is no notable difference between this figure and the normalised error shown in Figure 4.3.

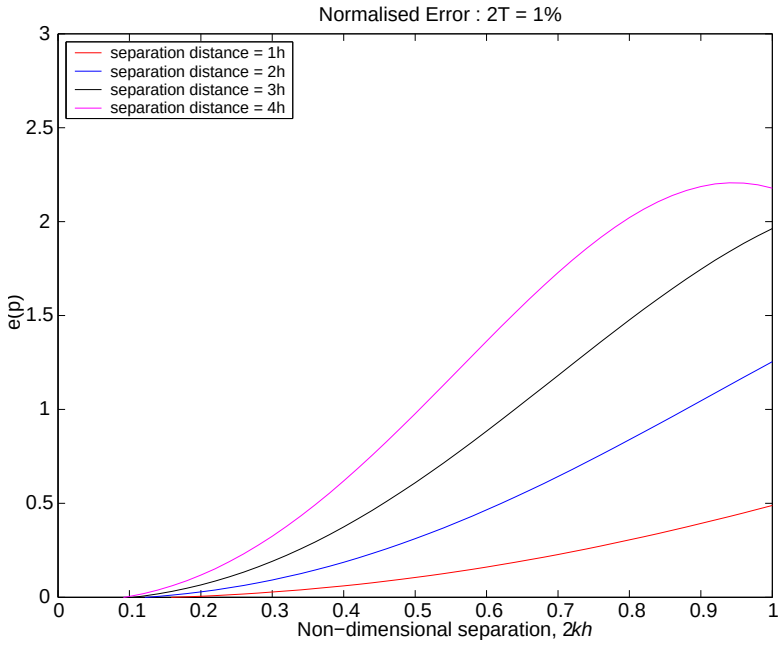

Figure 4.15: Normalised error in pressure at the virtual location using a linear virtual microphone in a one-dimensional reactive sound field with sensitivity mismatch as a function of non-dimensional separation distance (2kh) with $x/L = 1/4$.

To observe the effect of larger sensitivity mismatches, the normalised error was calculated for sensitivity mismatch between $\pm 6\%$ in steps of 1% and the normalised error was calculated for all possible combinations of sensitivity mismatch. From the calculated normalised error the statistical measures of mean, maximum, minimum and standard deviation were calculated. Figure 4.16 presents the normalised statistical error for a linear virtual microphone in a reactive sound field with sensitivity mismatch (T) varying between $\pm 6\%$ which represents a tolerance of 0.5dB.

4.3.1.2 Quadratic Virtual Microphone

The sensitivity mismatch across the three microphones is $\pm T$ with microphones one and three having a $-T$ and $+T$ mismatch respectively.

$$\widetilde{p}_1 = p_1(x,t)(1-T) \tag{4.65}$$

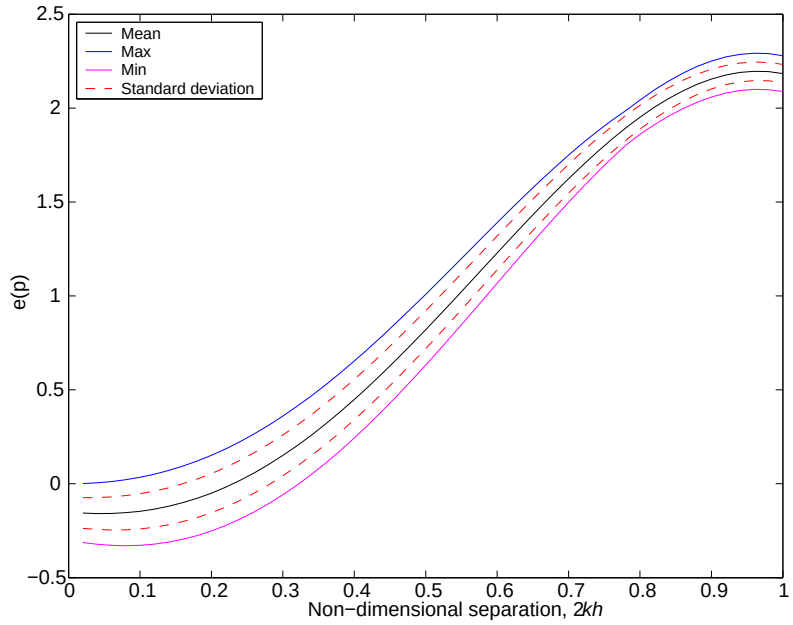

Figure 4.16: Normalised statistical error in virtual pressure at a separation distance of 4h using a linear prediction with sensitivity error (T) varying ±6%.

$$\widetilde{p}_3 = p_3(x,t) \tag{4.66}$$

$$\widetilde{p}_5 = p_5(x,t)(1+T) \tag{4.67}$$

As with the case for phase mismatch the central microphone in the array (microphone three) has no sensitivity mismatch to simplify the derivation of the analytical expressions.

By substituting Equation (4.65-4.67) into Equation (4.6) it is possible to calculate the normalised error for pressure for separation distances from h to $4h$. The normalised error for pressure for a microphone sensitivity error for all separation distances is given by:

$$e(\widetilde{p}_h) = e(p_h) + T\sec(kx)(3\cos(kx-kh) - \cos(kx-3kh)) \tag{4.68}$$

$$e(\widetilde{p}_{2h}) = e(p_{2h}) + T\sec(kx)(6\cos(kx-2kh) - 3\cos(kx-4kh)) \tag{4.69}$$

$$e(\widetilde{p}_{3h}) = e(p_{3h}) + T\sec(kx)(10\cos(kx-3kh) - 6\cos(kx-5kh)) \tag{4.70}$$

$$e(\widetilde{p}_{4h}) = e(p_{4h}) + T\sec(kx)(10\cos(kx-4kh) - 6\cos(kx-6kh)) \tag{4.71}$$

The normalised error in virtual pressure prediction with a sensitivity mismatch of $2T = 1\%$ is plotted against the non-dimensional separation distance in Figure 4.17 at a non-dimensional position of $x/L = 1/4$.

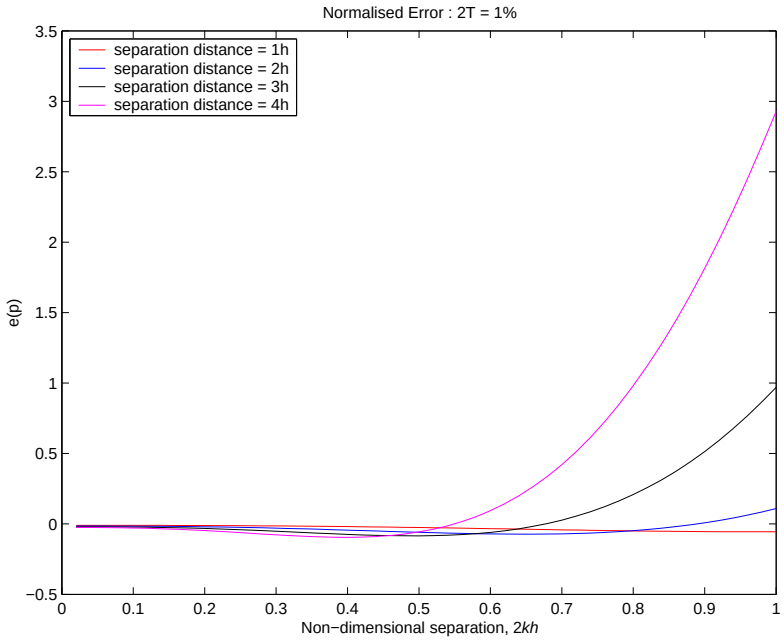

Figure 4.17: Normalised error in pressure at the virtual location using a quadratic virtual microphone in a one-dimensional reactive sound field with phase mismatch as a function of non-dimensional separation distance (2kh) with $x/L = 1/4$.

Figure 4.18 shows the normalised statistical error for the quadratic virtual microphone with a sensitivity mismatch, T, of between -8% and 8% in a reactive sound field at separation distance of $4h$. The normalised statistical error was calculated using the method outlined in Section 4.2.1.1. Figure 4.18(a) shows the statistical error with a sensitivity mismatch only, applied to the two outermost microphones such that the amount of error applied is equal to that applied to the linear microphone. Thus comparing Figure 4.16 with Figure 4.18(a), it can be seen that the sensitivity mismatch results in larger errors for the quadratic virtual microphone than for the linear virtual microphone. This was also seen for phase mismatch and thus also confirms previous experimental results which suggested that the quadratic microphone was more susceptible to these errors. Figure 4.18(b) shows the normalised statistical errors with sensitivity errors applied to all three microphones in the prediction array which was calculated

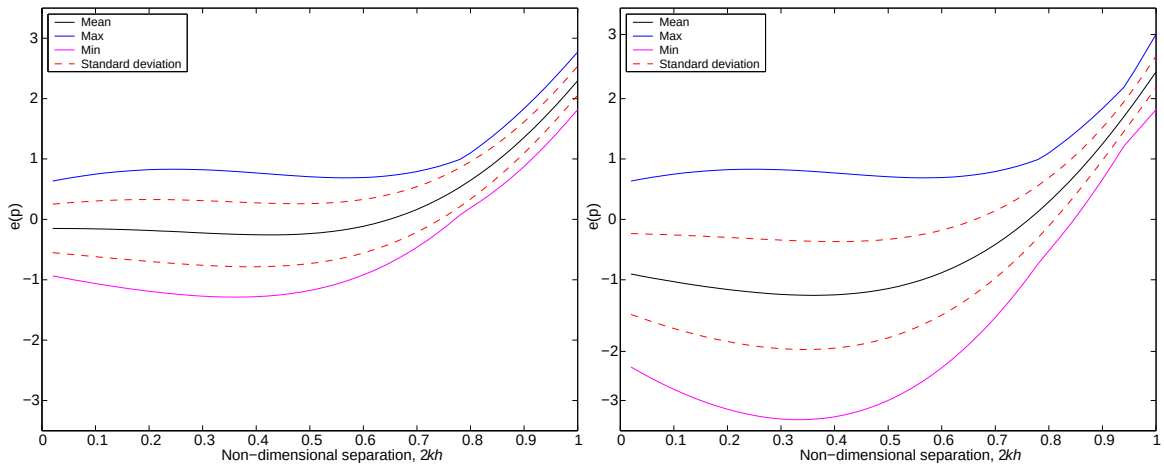

Figure 4.18: Normalised statistical error in virtual pressure at a separation distance of 4h using quadratic prediction with sensitivity error (T) varying between $\pm 6\%$ *at* $x/L = 1/4$.

using the method outlined in Section 4.2.1.2. This is a more realistic situation than with the mismatch only present on the two outer microphones as in experiments it is likely that each microphone will have some amount of sensitivity mismatch. The sensitivity mismatch was applied across each of the three microphones as follows:

$$\widetilde{p}_1 = p_1(x,t)(1-T), \qquad \widetilde{p}_3 = p_3(x,t)(1+T), \qquad \widetilde{p}_5 = p_5(x,t)(1+T) \tag{4.72}$$

Figure 4.18(b) shows that in this case the normalised error has significantly increased.

4.3.2 Plane Progressive Wave

4.3.2.1 Linear Virtual microphone

In this case, the normalised error is equal to the inherent normalised error from Section 4.1.4.1 plus an additional term due to the sensitivity error. The derivation for these equations is presented in Appendix A.

$$e(\widetilde{p}_h) = e(p_h) + T(1 + 3jhk + 3h^2k^2 - \frac{5}{2}jh^3k^3 + \frac{7}{4}h^4k^4) \tag{4.73}$$

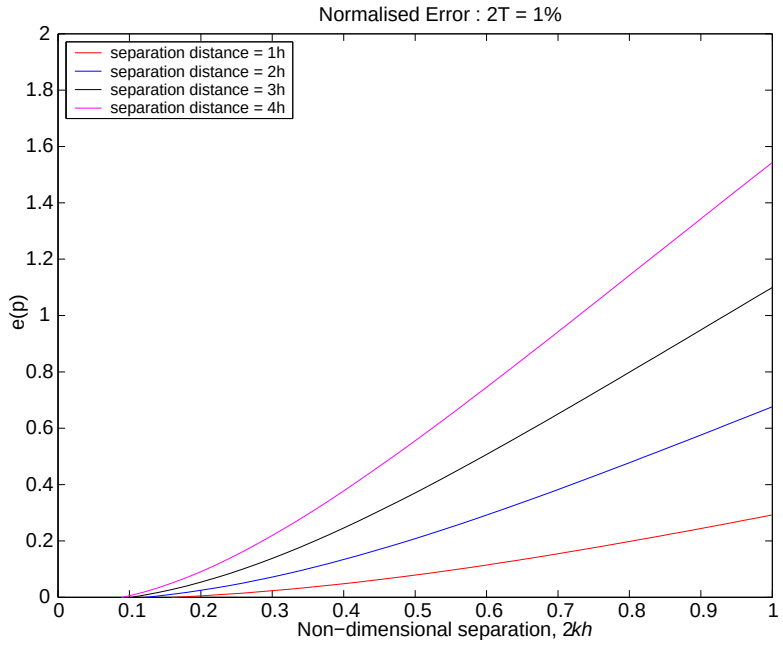

Figure 4.19: Normalised error in pressure at the virtual location using a linear virtual microphone in a plane progressive wave with sensitivity mismatch as a function of non-dimensional separation distance (2kh).

$$e(\widetilde{p}_{2h}) = e(p_{2h}) + T(2 + 8jhk - 12h^2k^2 - \frac{40}{3}jh^3k^3 + 12h^4k^4) \tag{4.74}$$

$$e(\widetilde{p}_{3h}) = e(p_{3h}) + T(3 + 15jhk - 30h^2k^2 - \frac{85}{2}jh^3k^3 + \frac{95}{2}h^4k^4) \tag{4.75}$$

$$e(\widetilde{p}_{4h}) = e(p_{4h}) + T(4 + 24jhk - 60h^2k^2 - 104jh^3k^3 + 140h^4k^4) \tag{4.76}$$

Figure 4.19 presents the normalised error with a sensitivity mismatch of $2T = 1\%$ for the linear virtual microphone plotted against non-dimensional separation distance. As was found for the other examples of sensitivity mismatch, this amount of sensitivity mismatch does not increase the normalised error significantly above the inherent error.

Figure 4.20 presents the normalised statistical error for the linear virtual microphone in plane wave conditions with varying sensitivity mismatch of -6% to 6%.

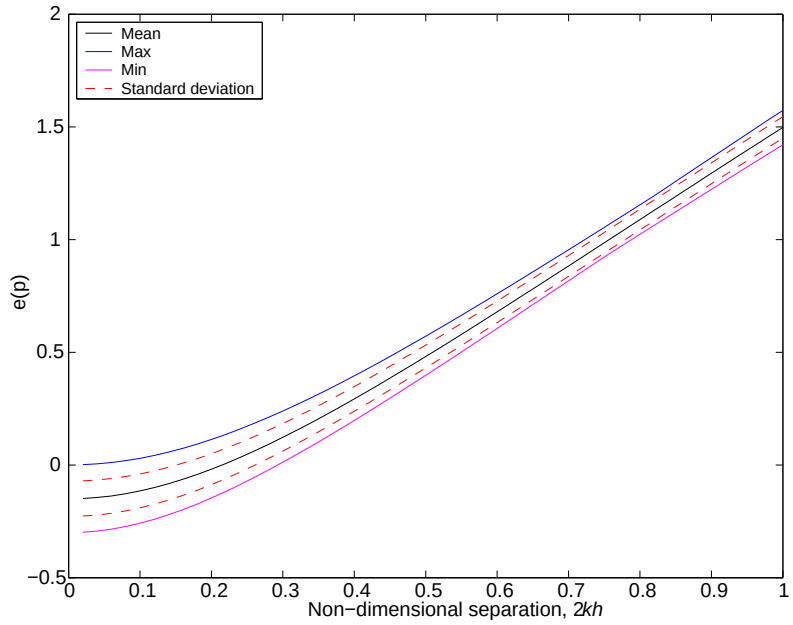

Figure 4.20: Normalised statistical error in virtual pressure at a separation distance 4h using a linear prediction with the sensitivity error (T) varying between $\pm 6\%$.

4.3.2.2 Quadratic Virtual Microphone

The sensitivity mismatch for the error analysis for a plane wave is the same as for the one-dimensional reactive sound field. Thus across the three microphones the sensitivity mismatch is $\pm T$ with microphones one and five having a $-T$ and $+T$ mismatch respectively. The pressure at the three microphones is given by:

$$\widetilde{p}_1 = p_1(x,t)(1-T), \qquad \widetilde{p}_3 = p_3(x,t), \qquad \widetilde{p}_5 = p_5(x,t)(1+T) \tag{4.77}$$

The central microphone in the array (microphone three) has no sensitivity mismatch, so as to simplify the derivation of the analytical expressions. The analytical expressions for the normalised error with the quadratic virtual microphone incorporating sensitivity mismatch between transducers in a plane progressive wave for all separation distances is presented below:

$$e(\widetilde{p}_h) = e(p_h) + T(1 + 3h^2k^2 + 4jh^3k^3 - \frac{13h^4k^4}{4}) \tag{4.78}$$

$$e(\widetilde{p}_{2h}) = e(p_{2h}) + T(2 + 12h^2k^2 + 24jh^3k^3 - 28h^4k^4) \tag{4.79}$$

$$e(\widetilde{p}_{3h}) = e(p_{3h}) + T(3 + 30h^2k^2 + 80jh^3k^3 - \frac{245h^4k^4}{2}) \tag{4.80}$$

$$e(\widetilde{p}_{4h}) = e(p_{4h}) + T(4 + 60h^2k^2 + 200jh^3k^3 - 380h^4k^4) \tag{4.81}$$

Figure 4.21 presents normalised errors in virtual pressure using a quadratic virtual microphone in plane wave conditions in the presence of sensitivity mismatch between transducers plotted against non-dimensional separation distance. Once again a 1% error in transducer sensitivity does not significantly degrade the normalised error in virtual pressure.

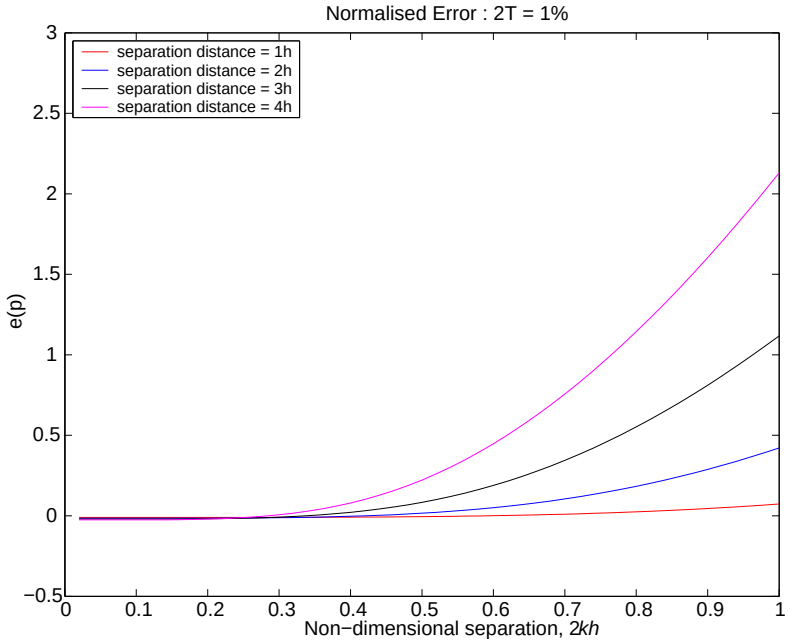

Figure 4.21: Normalised error in pressure at the virtual location using a quadratic virtual microphone in a plane progressive wave with sensitivity mismatch as a function of non-dimensional separation distance (2kh).

Figure 4.22 presents the normalised statistical error for the quadratic virtual microphone at $4h$ with a sensitivity mismatch. The results for the case with the sensitivity mismatch applied to the two outermost microphones of the prediction array are presented in Figure 4.22(a). The sensitivity mismatch, T, applied to each microphone was between $\pm 6\%$ which is the same as the error applied to the linear virtual microphone in increments of 1%. Comparing the results

from the linear virtual microphone with sensitivity mismatch (see Figure 4.20) with Figure 4.22(a), it can be seen that using the quadratic virtual microphone results in larger values of normalised error. Figure 4.22(b) shows the normalised statistical error for the quadratic virtual microphone with sensitivity mismatch applied to all three microphones (using Equation (4.72)) in the prediction array, which results in considerably larger normalised error compared to that shown in Figure 4.22(a). This result is not surprising considering the results presented earlier in this chapter and again highlights the intolerance of the quadratic virtual microphone to experimental errors.

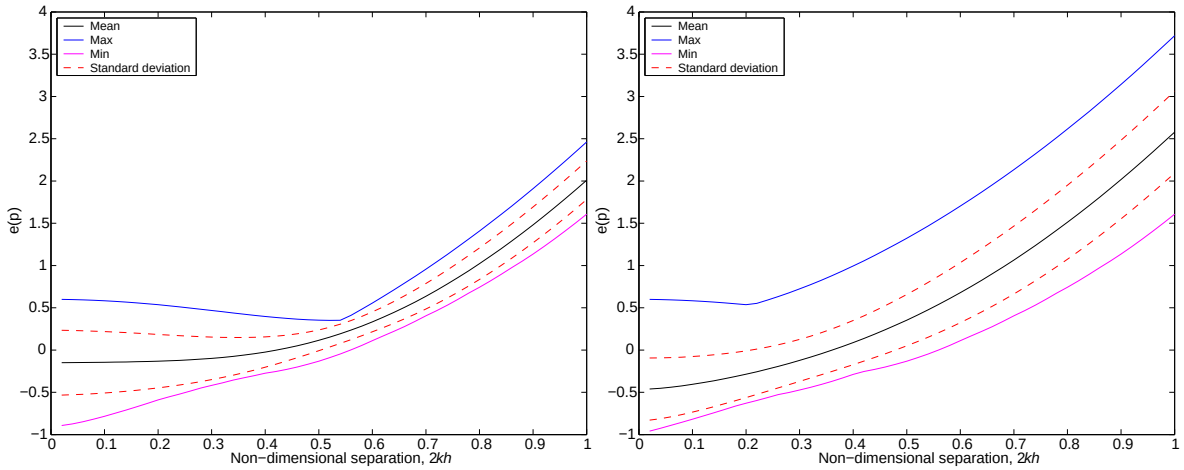

(a) Error applied to microphones 1 and 5 *(b) Error applied to all microphones*

Figure 4.22: Normalised statistical error in virtual pressure at a separation distance of 4h using quadratic prediction with sensitivity error (T) ranging between ±6%.

4.4 Discussion

Results presented here indicate that the quadratic virtual microphone is in fact more susceptible to phase and sensitivity errors than the linear virtual microphone. The effect of a combination of these errors has not been assessed here but the combined affect of the errors needs to be less than 10% for active noise control to be effective and ideally less than 1%. A 10% error in the prediction of the remote pressure level restricts the maximum attenuation achievable

to 20 dB. The errors presented here are considerably less than the errors presented for sound intensity and energy density by Fahy (1995) and Cazzolato (1999) respectively. This is not a surprising result when the formulations of sound intensity and energy density are considered. Sound intensity is calculated using the product of pressure and particle velocity; therefore any phase or sensitivity errors will have a considerable affect on the calculation of sound intensity. Energy density is calculated through the addition of the squared pressure and particle velocity; therefore errors in the magnitude of the pressure and particle velocity will affect the energy density measurement. The calculation of the pressure at the virtual location is the sum of the weighted pressure measured at each microphone in the array. Therefore it is obvious the errors in phase and sensitivity will not have a large effect on the pressure estimate but clearly this error still impacts the performance of the active noise control system.

4.5 Conclusions

This chapter presented an error analysis for linear and quadratic virtual microphones in a reactive one-dimensional sound field and in a plane wave field. The type of errors assessed here were inherent errors due to the finite separation of the transducers, as well as errors due to phase and sensitivity mismatch between the transducers for which analytical expressions were derived. The error analysis was performed to determine if the poor experimental results obtained in Chapter 3 using the quadratic virtual microphone in particular was due to the phase and sensitivity mismatch between the prediction microphones. The study found that the quadratic virtual microphone was affected by the phase and sensitivity errors much more than the linear virtual microphone.

The effect of the simultaneous combination of all errors on the accuracy of the virtual microphone formulation was not investigated in this case as the aim of this investigation was to analyse the effect of each error had upon the virtual microphone formulation. Also the errors combine in a complicated manner and are not just additive and therefore performing this type

of error analysis on the combination of errors would be very time consuming and beyond the scope of this thesis.

Chapter 5

Higher-order Virtual Microphone

5.1 Introduction

The results presented in Chapter 3 identified some of the problems with the forward difference prediction method; namely the hypothesised susceptibility of quadratic prediction to short wavelength extraneous noise. Increasing the order of the prediction algorithm from linear to quadratic was shown to decrease the prediction accuracy of the virtual algorithm in Chapter 3. For this reason, it is thought that further increasing the order of the prediction above a second-order polynomial will also not result in an improvement in the prediction accuracy. In an attempt to improve the prediction accuracy of the forward-difference algorithm, additional microphone elements have been incorporated into the array while still using the linear or quadratic prediction. The effect of this modification to the array is the subject of this chapter. Increasing the number of elements in the array while retaining the order of the prediction algorithm creates an over-constrained system of equations, the intention of which is to spatially filter out the short wavelength extraneous noise that was postulated to be the cause of the poor performance of the quadratic virtual microphone. From this point on, the ordinary (or not over-constrained) virtual microphones will be called lower-order virtual microphones and the over-constrained virtual microphones will be called higher-order virtual microphones.

The performance of the higher-order virtual microphones using real-time control was investigated in the one-dimensional waveguide introduced in Chapter 3 where the performance of simulated control, post-processed control and real-time control was compared. Post-processed control can be a useful tool in an initial investigation of a new control technique; however, the results in Chapter 3 indicated that the performance of post-processed control is affected by errors that do not occur when using real-time control. Since the real-time implementation of the forward-difference virtual microphones is very simple, there is no need to initially test the formulation using computer simulations or post-processed control. Hence this chapter will only present real-time control results for higher-order virtual microphone microphones and a comparison of the level of attenuation achieved will be compared with that of the lower-order virtual microphones. The performance of the higher-order virtual microphone was also investigated in the free field and compared against the performance of the lower-order virtual microphones. The free field performance investigation was performed using analytical simulations and experimental real-time control. Analytical control results have been presented to complete the picture of the forward-difference virtual microphone's performance in the free field, as no analytical control results have been presented so far. The real-time experiments were conducted in the anechoic chamber located at The University of Adelaide. These results will be presented at the end of the chapter, as first the derivations of the higher-order virtual microphone equations will be presented.

5.2 Higher-order Virtual Microphone Formulation

5.2.1 Three Microphone Linear Prediction

A three-element microphone array, equi-spaced over a total distance of $2h$ is shown in Figure 5.1. If the extrapolation estimate is based upon a straight line fitted to the microphone output signal versus the microphone spatial location for three microphones, the problem is over-

constrained with three simultaneous equations and only two unknowns.

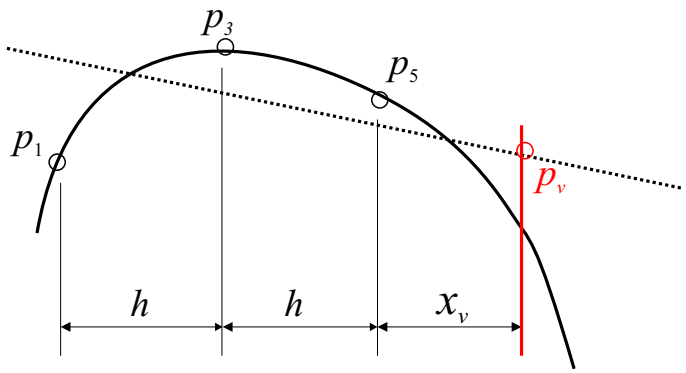

Figure 5.1: Schematic of three microphone linear prediction

Using a least squares approximation (Press et al., 1992), the following weighting equation for three microphones is derived:

$$p(x) = ax + b \tag{5.1}$$

Equation 5.1 may be applied to a system of three microphones, each separated by h, with microphone 5 located at $x = 0h$, microphone 3 located at $x = -h$ and microphone 1 located at $x = -2h$. Therefore the matrix form of Equation 5.1 can be written as:

$$\begin{bmatrix} p_1 \\ p_3 \\ p_5 \end{bmatrix} = \begin{bmatrix} -2h & 1 \\ -h & 1 \\ 0 & 1 \end{bmatrix} \begin{bmatrix} a \\ b \end{bmatrix} \tag{5.2}$$

Equation (5.2) can be rewritten as:

$$\mathbf{p}_3 = \mathbf{H}_{3o}\mathbf{a}_{2o} \tag{5.3}$$

where $\mathbf{p}_3 = \begin{bmatrix} p_1 \\ p_3 \\ p_5 \end{bmatrix}$, $\mathbf{H}_{3o} = \begin{bmatrix} -2h & 1 \\ -h & 1 \\ 0 & 1 \end{bmatrix}$ and $\mathbf{a}_{2o} = \begin{bmatrix} a \\ b \end{bmatrix}$.

$\mathbf{H}_{3o}$ is the matrix of polynomial coefficients for the three microphone system, $\mathbf{p}_3$ is the vector containing the sound pressure measured at the three microphone locations.The subscript 3 refers to the number of microphones used in the prediction, the subscript *o* refers to the over-constrained algorithm and the subscript 2 refers to the order of the prediction.

Therefore the coefficients of the linear relationship are given by:

$$\mathbf{a}_{2o} = \mathbf{H}_{3o}^{-1}\mathbf{p}_3 \tag{5.4}$$

The pressure at point x_v remote to the three sensing microphones can be found using Equations (5.4) and (5.2), and is given by:

$$p_v = \begin{bmatrix} x_v & 1 \end{bmatrix} \begin{bmatrix} a \\ b \end{bmatrix} = \mathbf{x}\mathbf{H}_{3o}^{-1}\mathbf{p}_3 \tag{5.5}$$

Clearly as $\mathbf{H}_{3o}$ is not square, the inverse requires a pseudo inverse which is calculated using the least squares method as follows:

$$\mathbf{H}_{3o}^{-1} = \left(\mathbf{H}_{3o}^T\mathbf{H}_{3o}\right)^{-1}\mathbf{H}_{3o}^T \tag{5.6}$$

Therefore,

$$\mathbf{H}_{3o}^{-1} = \frac{1}{6}\begin{bmatrix} -\frac{3}{h} & 0 & \frac{3}{h} \\ -1 & 2 & 5 \end{bmatrix} \tag{5.7}$$

Substituting Equation (5.7) into Equation (5.5) produces an equation for estimating the sound pressure at the virtual location using a three microphone array with a linear approximation given by:

$$p_v = \frac{1}{6}\begin{bmatrix} \frac{x_v}{h} & 1 \end{bmatrix}\begin{bmatrix} -3 & 0 & 3 \\ -1 & 2 & 5 \end{bmatrix}\begin{bmatrix} p_1 \\ p_3 \\ p_5 \end{bmatrix} \tag{5.8}$$

5.2.2 Five Microphone Linear Prediction

The same procedure can be applied to a five microphone linear prediction system as shown in Figure 5.2, spanning $2h$, with a microphone element inter-spacing of $h/2$. This also results in a system that is over constrained.

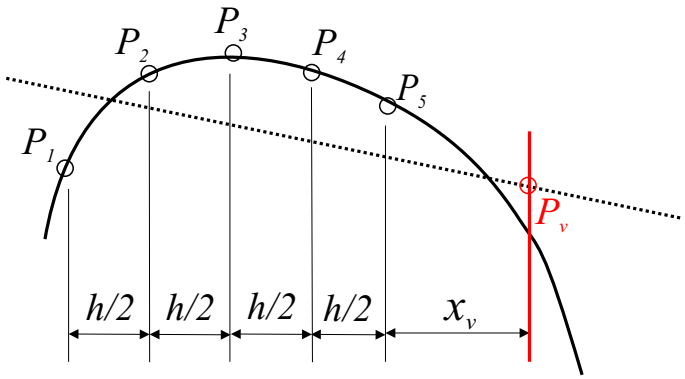

Figure 5.2: Schematic of five microphone linear prediction

The pressure response at the five microphones can be related to the straight line fit by the following relationship,

$$\begin{bmatrix} p_1 \\ p_2 \\ p_3 \\ p_4 \\ p_5 \end{bmatrix} = \begin{bmatrix} -2h & 1 \\ -\frac{3h}{2} & 1 \\ -h & 1 \\ -\frac{h}{2} & 1 \\ 0 & 1 \end{bmatrix}\begin{bmatrix} a \\ b \end{bmatrix} \tag{5.9}$$

Using the method outline above, the pseudo-inverse of the second matrix in Equation (5.9) can be found and therefore the linear prediction equation for a five microphone array is given by:

$$p_v = \frac{1}{5}\begin{bmatrix} \frac{x}{h} & 1 \end{bmatrix}\begin{bmatrix} -2 & -1 & 0 & 1 & 2 \\ 3 & 2 & 1 & 0 & -1 \end{bmatrix}\begin{bmatrix} p_1 \\ p_2 \\ p_3 \\ p_4 \\ p_5 \end{bmatrix} \tag{5.10}$$

5.2.3 Five Microphone Quadratic Prediction

Rather than fitting a straight line through the microphone elements, a quadratic function can be used to provide a second-order polynomial prediction (see Figure 5.3). The equation for a second-order polynomial is:

$$p(x) = ax^2 + bx + c \tag{5.11}$$

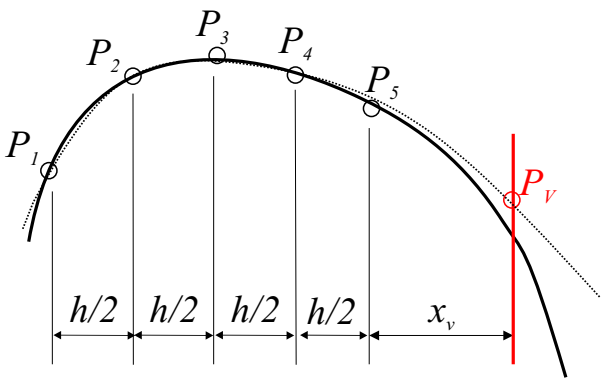

Figure 5.3: Schematic of five microphone quadratic prediction

Therefore with the five microphones located $h/2$ apart, the above equation can be rewritten as

follows

$$\begin{bmatrix} p_1 \\ p_2 \\ p_3 \\ p_4 \\ p_5 \end{bmatrix} = \begin{bmatrix} (-2h)^2 & -2h & 1 \\ \left(-\frac{3h}{2}\right)^2 & -\frac{3h}{2} & 1 \\ (-h)^2 & -h & 1 \\ \left(-\frac{h}{2}\right)^2 & -\frac{h}{2} & 1 \\ 0 & 0 & 1 \end{bmatrix} \begin{bmatrix} a \\ b \\ c \end{bmatrix} \tag{5.12}$$

Using the derivation from Section 5.2.1, the equation for predicting the sound pressure level at some virtual location, x_v, using a quadratic estimate is

$$p_v = \frac{1}{35} \begin{bmatrix} \left(\frac{x_v}{h}\right)^2 & \frac{x_v}{h} & 1 \end{bmatrix} \begin{bmatrix} 20 & -10 & -20 & -10 & 20 \\ -54 & 13 & 40 & -27 & -26 \\ 31 & 9 & -3 & -5 & 3 \end{bmatrix} \begin{bmatrix} p_1 \\ p_2 \\ p_3 \\ p_4 \\ p_5 \end{bmatrix} \tag{5.13}$$

5.3 One-dimensional Waveguide

The higher-order virtual microphone formulations derived in the preceding section, were utilised to predict the virtual sound pressure in a real-time control scenario in a one-dimensional waveguide with both rigidly terminated and absorptive end caps. In this section the control profiles for the higher-order virtual microphones will be presented at an acoustic resonance and at an acoustic anti-resonance. The resonance frequency corresponds to the seventh axial mode and the anti-resonance frequency lies between the eight and ninth axial modes. Also, the levels of attenuation achieved using the higher-order virtual microphones will be compared with the attenuation achieved using the lower-order virtual microphones.

5.3.1 Experimental Configuration

The experimental configuration and test procedure used to determine the real-time performance of the higher-order virtual microphones was the same as was detailed in Chapter 3. The microphone array was, however, extended to incorporate five microphones (see Figure 5.4). These microphones were phase and sensitivity matched to within $\pm 1^\circ$ and ± 0.5dB as outlined in Chapter 3.

Figure 5.4: Photograph of the extended microphone array (with five elements) used in higher-order virtual microphone real-time experiments

5.3.2 Results for a Rigidly Terminated Duct

5.3.2.1 Resonance

Figure 5.5 shows the results for the three higher-order virtual microphones controlling the 7th axial mode of the waveguide at 247 Hz as was done in Chapter 3. These figures show the primary or uncontrolled sound field as a thick line at the top of the figure. The controlled

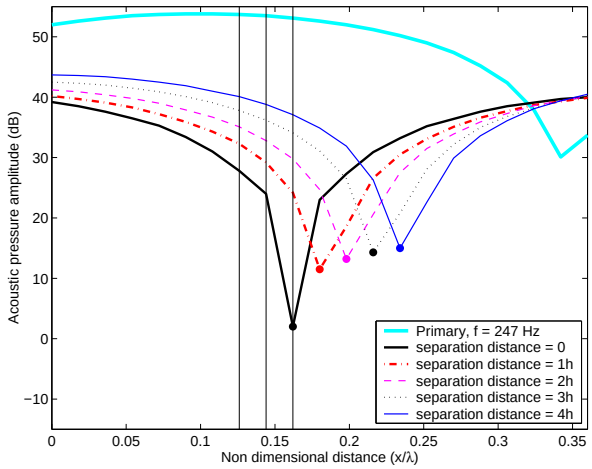

(a) Three microphone array using linear prediction

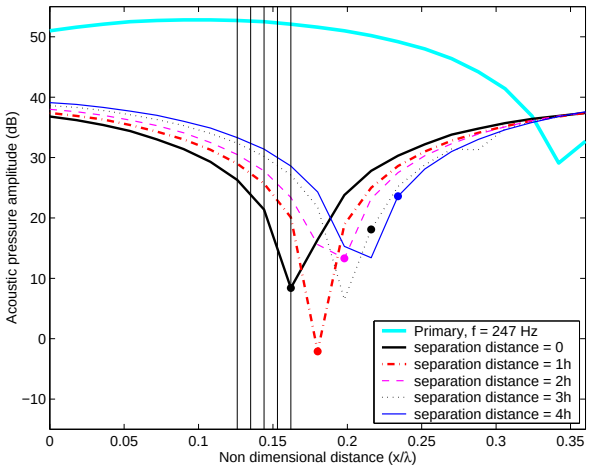

(b) Five microphone array using linear prediction

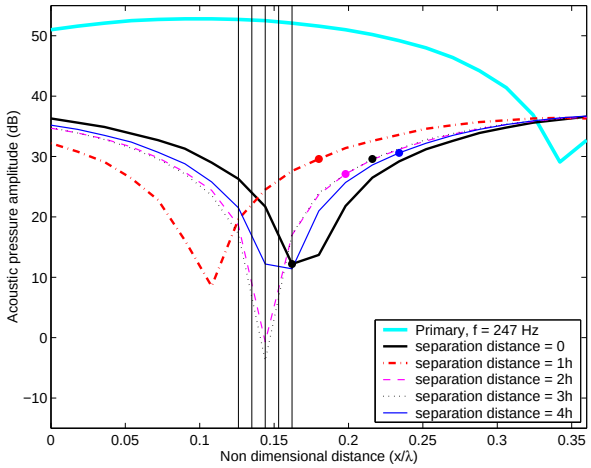

(c) Five microphone array using quadratic prediction

Figure 5.5: Results of real-time control of an acoustic resonance in a rigid duct using higher-order virtual microphones. The vertical lines represent the location of the microphone array. The filled circles indicate the location of the virtual microphone.

sound fields are the other curves with the vertical lines indicating the location of the prediction microphone array and the solid circles indicating the virtual locations. The results for the three microphone linear prediction are shown in Figure 5.5(a). This figure indicates a high level of attenuation at the virtual location for all separation distances. As can be seen from Figure 5.5(b) the results for the five microphone array, using linear prediction, does not show the same good results produced using the three-element linear virtual microphone, with the zone of maximum attenuation occurring away from the virtual location when the separation distances are larger than 2h. This indicates that the prediction accuracy of the five microphone system was affected by phase and sensitivity mismatch since the zone of maximum attenuation does not occur at the virtual location for the separation distances of 3h and 4h. This figure also shows that at a separation distance of h there is a higher level of attenuation than at 0h; this is a result of phase and sensitivity mismatch between microphone elements, which often results in decreased levels of attenuation at the virtual location; however, the converse is also possible and a high level of attenuation has been the result here. Figure 5.6 illustrates this effect. Figure 5.5(c) shows the control profiles obtained using the five microphone array with the quadratic prediction algorithm. The prediction accuracy of this virtual microphone is clearly affected by phase and sensitivity mismatch between microphone elements with the maximum zone of attenuation (zone of quiet) not occurring at the virtual location except for at a separation distance of 0h.

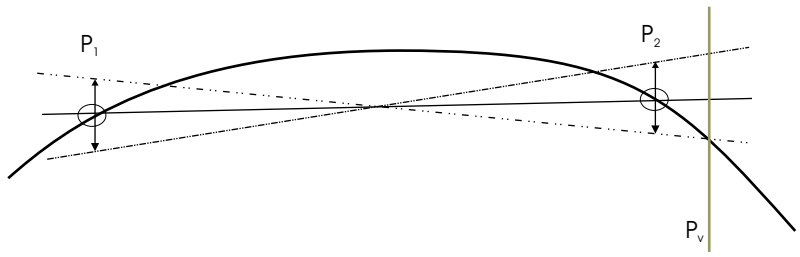

Figure 5.6: An illustration of the effect of phase or sensitivity mismatch on prediction accuracy. Curved line indicates the true pressure field. The arrowed lines indicate the potential amplitude error due to sensitivity and phase mismatch. The straight lines are the bounds of the linear prediction.

The objective of developing higher-order virtual microphones was to achieve higher levels of

attenuation at the virtual location compared with the levels of attenuation achieved with the lower order virtual microphones. Therefore a comparison between the attenuation achieved with the lower and higher-order virtual microphones is shown graphically in Figure 5.7. This shows that the linear prediction algorithm out-performs the quadratic prediction algorithm regardless of the number of microphones used in the microphone array.

For the case of the quadratic prediction algorithm, adding the extra microphone elements (thus creating a five-element array) decreases the prediction accuracy when compared to the three microphone quadratic prediction array. This is most likely because the introduction of additional microphone elements introduces additional phase and sensitivity mismatch errors. The effect of the additional microphones on the prediction accuracy of the virtual microphone algorithms is examined in detail in Chapter 6. Figure 5.7 shows that a single microphone located at p_5 out-performs the five-element array with quadratic prediction at all separation distances and the quadratic algorithm with a three microphone array for separation distance greater than h.

The three-element linear prediction virtual microphones produce the most accurate pressure prediction at the virtual location (except for at a separation distance of h where the five-element linear virtual microphone is superior) resulting in the highest levels of attenuation. Figure 5.7 clearly demonstrates the linear algorithm's superiority in terms of prediction accuracy over the quadratic algorithm. The five-element linear virtual microphone also achieves higher levels of attenuation than the three and five-element higher-order quadratic virtual microphones and the two-element linear virtual microphone. Figure 5.7 illustrates the poor performance of the five-element quadratic virtual microphone, which achieves the lowest levels of attenuation when compared to the other virtual microphones and the single remote microphone at all separation distances. This again highlights the susceptibility of the quadratic prediction algorithm to experimental errors as previously discussed.

Another important measure of performance in localised control is the size of the zone of quiet. In this resonance example, the size of the zone in which the attenuation is greater than 10

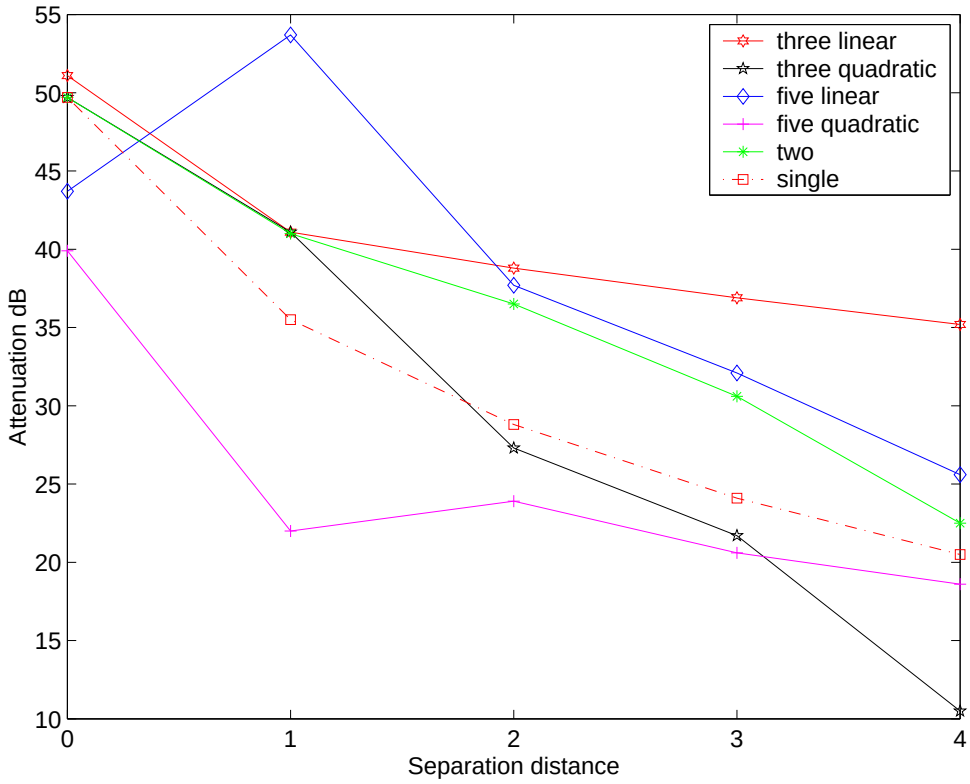

Figure 5.7: Comparison of attenuation between all virtual microphone formulations when controlling an acoustic resonance in a rigid, one-dimensional waveguide.

dB is examined. The linear prediction virtual microphones (Figures 5.5(a) and (b)) produced, on average, a zone of quiet centred around the virtual microphone with a radius of 0.27λ except for separation distances of $3h$ and $4h$ for the five-element linear virtual microphone. This a quite a large zone of quiet, almost 0.4m at 247 Hz. The zone of quiet does reduce in size slightly with increasing separation distance of the virtual microphone location from the physical array, but this may be due to the proximity of the virtual microphone to a pressure node in the primary sound field. As a node is a location of minimum sound pressure, it is impossible to produce significant attenuation there. The quadratic virtual microphone using five sensors produced similar sized zones of quiet, which were not centred around the virtual microphone.

5.3.2.2 Anti-resonance

Figure 5.8 shows the results for the three and five microphone higher-order virtual sensors when controlling an acoustic anti-resonance in a rigid duct. In this case of controlling an acoustic anti-resonance (Figure 5.8(a)) the level of attenuation achieved is significantly reduced for the three microphone linear prediction when compared with the resonance example. As in the resonance case, the zone of maximum attenuation occurs at the virtual location. Figure 5.8(b) shows the control profile achieved when controlling an acoustic anti-resonance using a linear prediction with a five microphone array. The features of this figure are also very similar to the previous resonance example, with the zone of attenuation occurring at the virtual location up to a separation distance of $2h$ and a very high level of attenuation was recorded at a separation distance of h. The pattern continues for the separation distance of $3h$ and $4h$ where the zone of maximum attenuation shifts from the virtual location. The explanation for the very high level of attenuation at a separation distance of h was outlined in Section 5.3.2.1 with the aid of Figure 5.6. The inherent phase and sensitivity mismatch between microphone elements has been shown to have either an adverse or beneficial affect on the prediction accuracy. The results presented in Figure 5.8(c) indicate that the quadratic prediction algorithm again proves

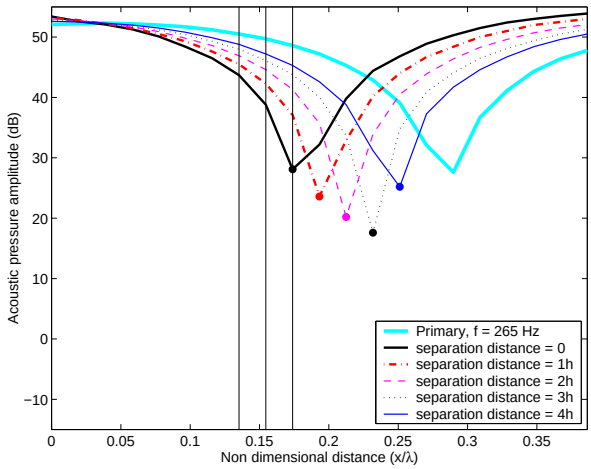

(a) Three micorphone array using linear prediction

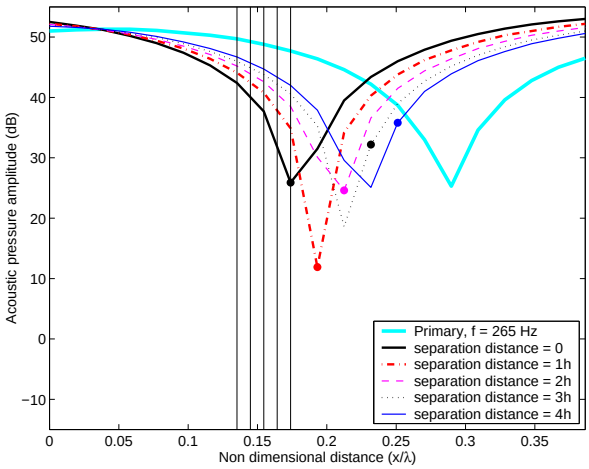

(b) Five microphone array using linear prediction

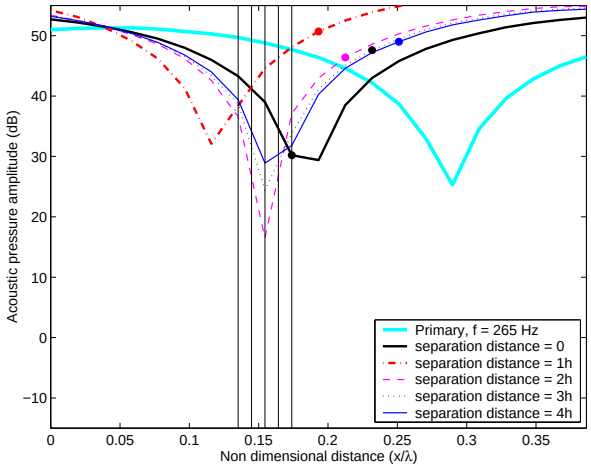

(c) Five microphone array using quadratic prediction

Figure 5.8: Results of real-time control of an acoustic anti-resonance in a rigid duct using higher-order virtual microphones

to be a poor estimator of the pressure at the virtual location. This figure shows that for all separation distances except 0h, the application of control results in an increase of the sound pressure level at the virtual location.

Figure 5.9 compares and summarises the attenuation achieved by all of the virtual microphone formulations when controlling an anti-resonance in a rigid one-dimensional waveguide. The five microphone array, using a quadratic prediction algorithm, is again clearly the worst performer, resulting in less attenuation than when using a single microphone located at p_5, the microphone closest to the virtual location. As discussed previously increasing the number of microphones used in the quadratic prediction introduces additional phase and sensitivity mismatch errors which degrade the prediction accuracy. As with the resonance example, the linear prediction using three and five microphone arrays are consistently the most accurate.

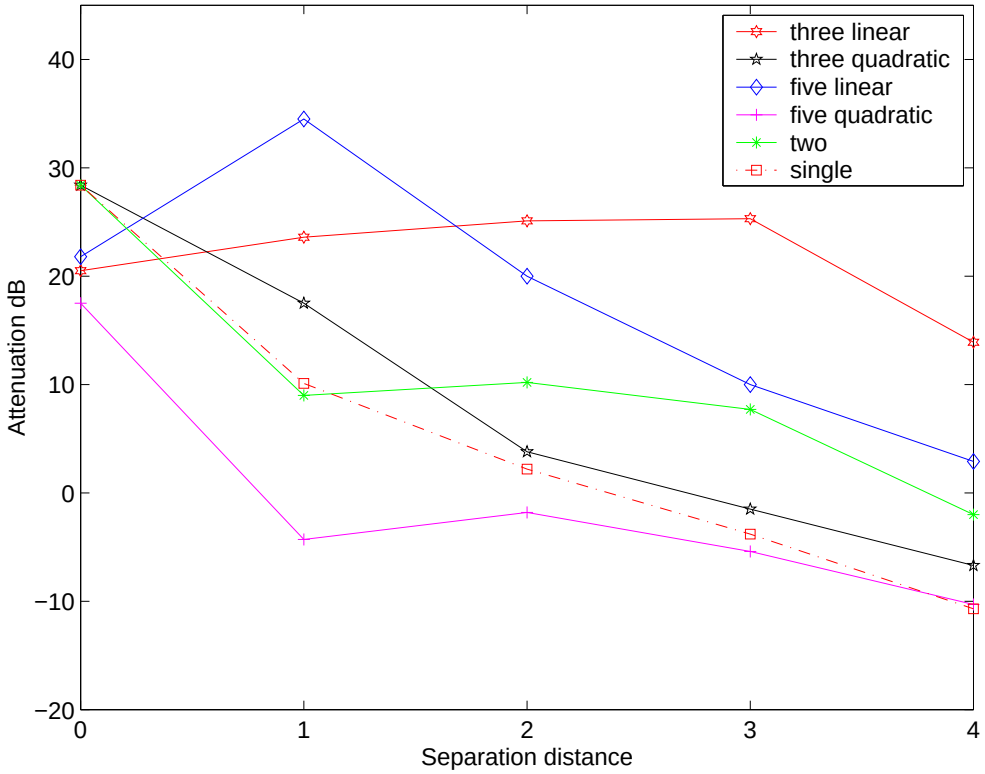

Figure 5.9: Comparison of attenuation between all virtual microphone formulations when controlling an acoustic anti-resonance in a rigid, one-dimensional waveguide.

For this example, the radius of the zone of quiet for attenuation greater than 10 dB is 0.05λ.

The size of this zone of quiet is considerably smaller than is achieved when controlling an acoustic resonance as the potential for attenuation is reduced when controlling an acoustic anti-resonance. In addition, the microphone array and the virtual microphone are located close to a pressure node in the primary sound field and therefore it is likely that if the microphones were positioned further away from the node, a larger zone of quiet would result. Figure 5.8(c) again illustrates that the size of the zone of quiet produced using the higher-order quadratic virtual microphone is similar to that achieved using the linear virtual microphones but control is not at the virtual location.

5.3.3 Results for Duct with Absorptive Ends

5.3.3.1 Resonance

Figure 5.10 shows the results obtained when controlling an acoustic resonance in a one-dimensional waveguide with absorptive ends. The control profile obtained using a three-element linear prediction array is shown in Figure 5.10(a). This figure shows that up to a separation distance of $2h$, the zone of maximum attenuation occurs at the virtual location. At the larger separation distances, the accuracy of the pressure prediction is once again affected by phase and sensitivity mismatch and therefore the zone of maximum attenuation shifts away from the virtual location. The five-element linear prediction virtual microphone produced the results shown in Figure 5.10(b). This figure indicates that increasing the number of microphones in the prediction array results in a decrease in the level of attenuation achieved at the virtual location when compared to the three microphone case. This is a result of the additional elements in the array introducing additional errors due to phase and sensitivity mismatch between the elements. Figure 5.10(c) displays the results achieved using a five-element quadratic prediction array. It can be seen from this figure that the prediction accuracy is greatly reduced using the quadratic algorithm.

Figure 5.11 shows a comparison of the attenuation achieved using all the virtual microphone

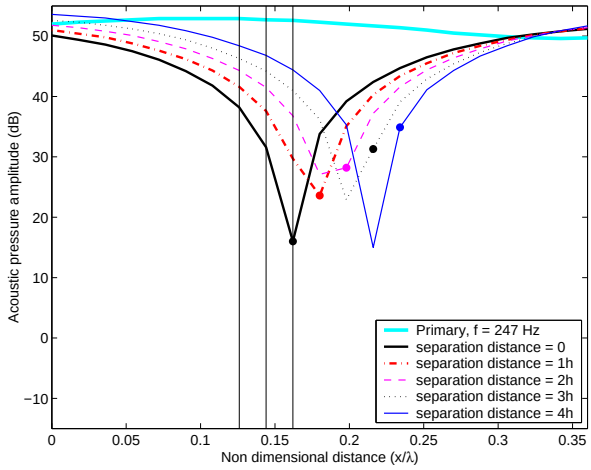

(a) Three microphone using linear prediction

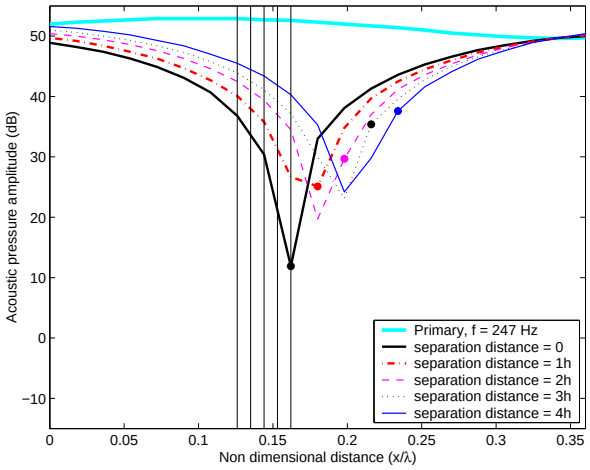

(b) Five microphone using linear prediction

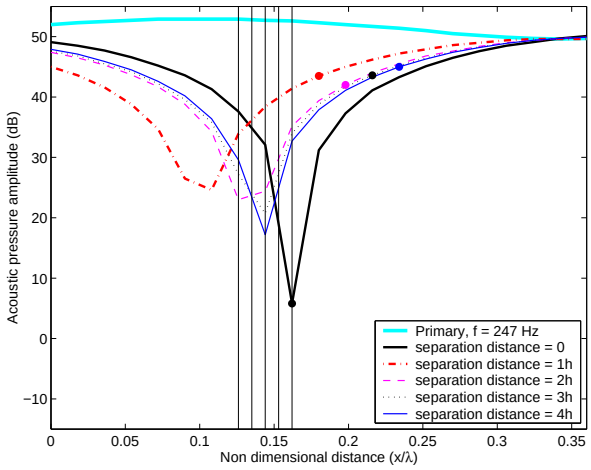

(c) Five microphone using quadratic prediction

Figure 5.10: Results of real-time control of an acoustic resonance in a duct with absorptive ends using higher-order virtual microphones

formulations at all separation distances. This figure once again demonstrates (as in Sections 5.3.2.1 and 5.3.2.2) that the three and five-element linear prediction microphone arrays are the most accurate methods and that the five-element quadratic prediction array is the least accurate of the virtual microphone formulations. It is also apparent that in this sound field, the single remote microphone produces greater levels of attenuation than both the quadratic virtual microphone formulations.

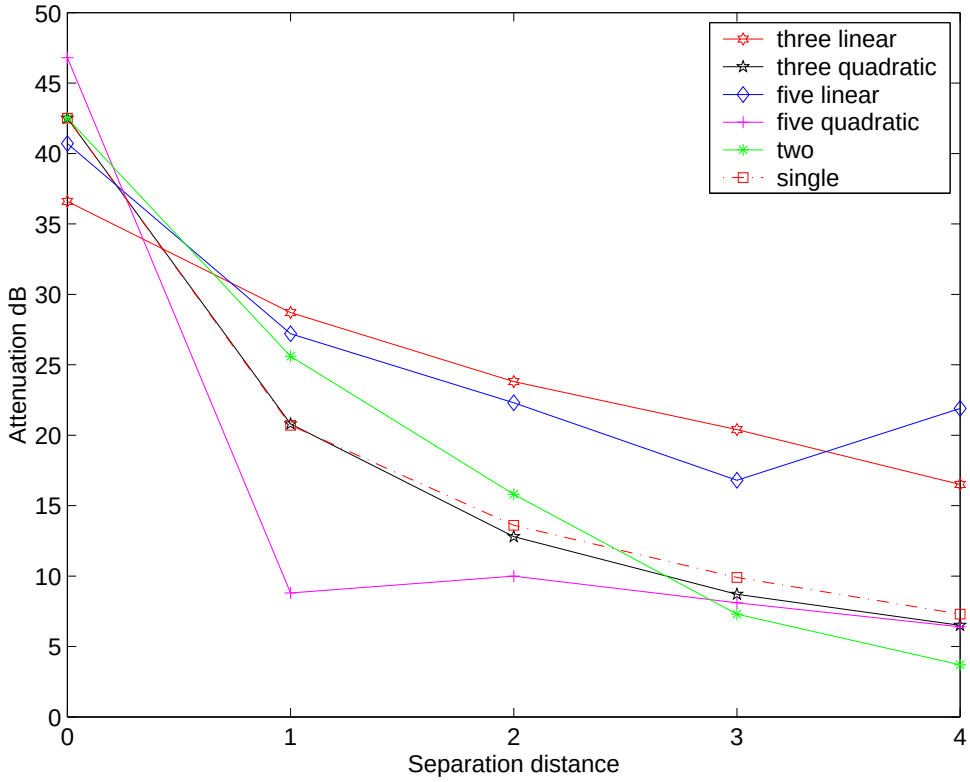

Figure 5.11: Comparison of attenuation between all virtual microphone formulations when controlling an acoustic resonance in a one-dimensional waveguide with absorptive ends.

The spatial extent of the zone of quiet, at an acoustic resonance in a duct with absorptive ends, is similar to the results previously discussed. Both higher-order linear virtual microphones achieve a 10 dB zone of quiet of approximately 0.1λ in size. The quadratic virtual microphone, using the five-element array, does not produce zones of quiet centred around the virtual microphone.

5.3.3.2 Anti-resonance

This section presents the results obtained when controlling an acoustic anti-resonance in a damped one-dimensional waveguide using the three virtual microphone formulations (Figure 5.12). Figure 5.12(a) demonstrates a very similar control profile to that shown in Figure 5.10(a), which shows the results obtained using a three-element array with a linear prediction

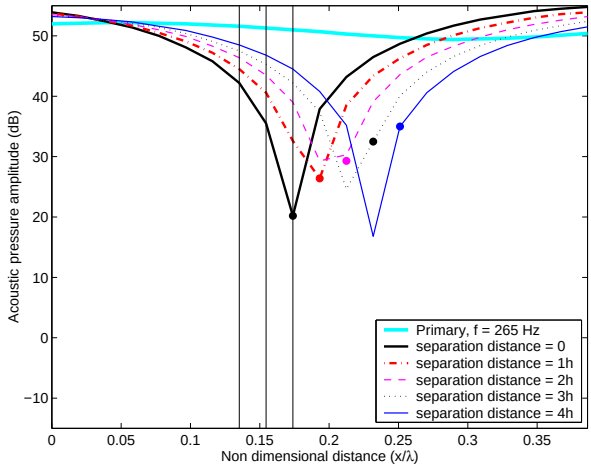

(a) Three microphone using linear prediction

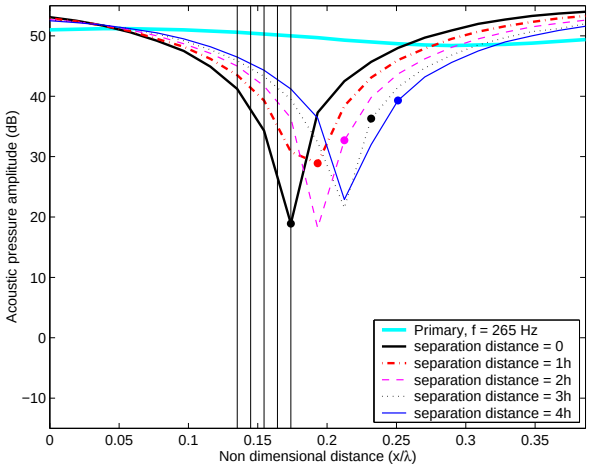

(b) Five microphone using linear prediction

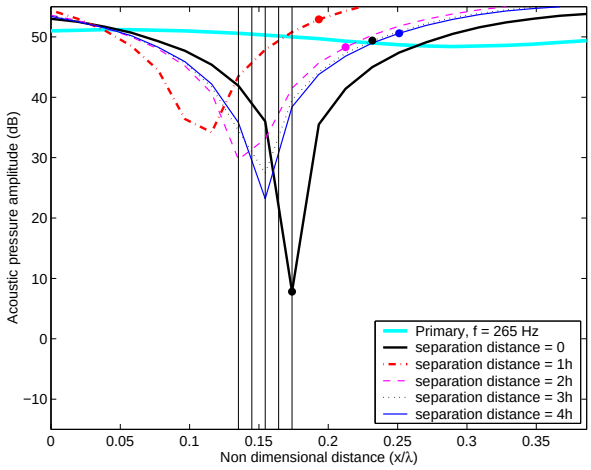

(c) Five microphone using quadratic prediction

Figure 5.12: Results of real-time control of an acoustic anti-resonance in a duct with absorptive ends using higher-order virtual microphones

algorithm. As with the resonance example the zone of attenuation attenuation is centred at the virtual location up to a separation distance of $2h$. Figure 5.12(b) shows the control profile obtained using a five microphone array with a linear prediction algorithm. These results also demonstrate a similar profile to that obtained in the resonance example. As with all the previous examples the quadratic prediction algorithm, Figure 5.12(c) indicates that this algorithm is highly susceptible to errors, resulting in low levels of attenuation.

Figure 5.13 shows the attenuation comparison for all control methods. This figure again highlights that the higher-order linear algorithm results in the highest levels of attenuation while the higher-order quadratic algorithm results in the lowest levels of attenuation. The attenuation achieved using a single microphone located at p_5 is comparable with that achieved using the three microphone quadratic prediction. The single microphone control results indicate that this method is more accurate than using the five microphone quadratic prediction algorithm. The higher-order virtual microphone using linear prediction offers a slight increase in the level of attenuation achieved compared to using the two-microphone array with linear prediction.

The spatial extent of the 10 dB zone of quiet produced using the linear virtual microphones is approximately 0.07λ. As with the other quadratic prediction examples the 10 dB zone of quiet for quadratic prediction is around 0.06λ in size but is not centred around the virtual location.

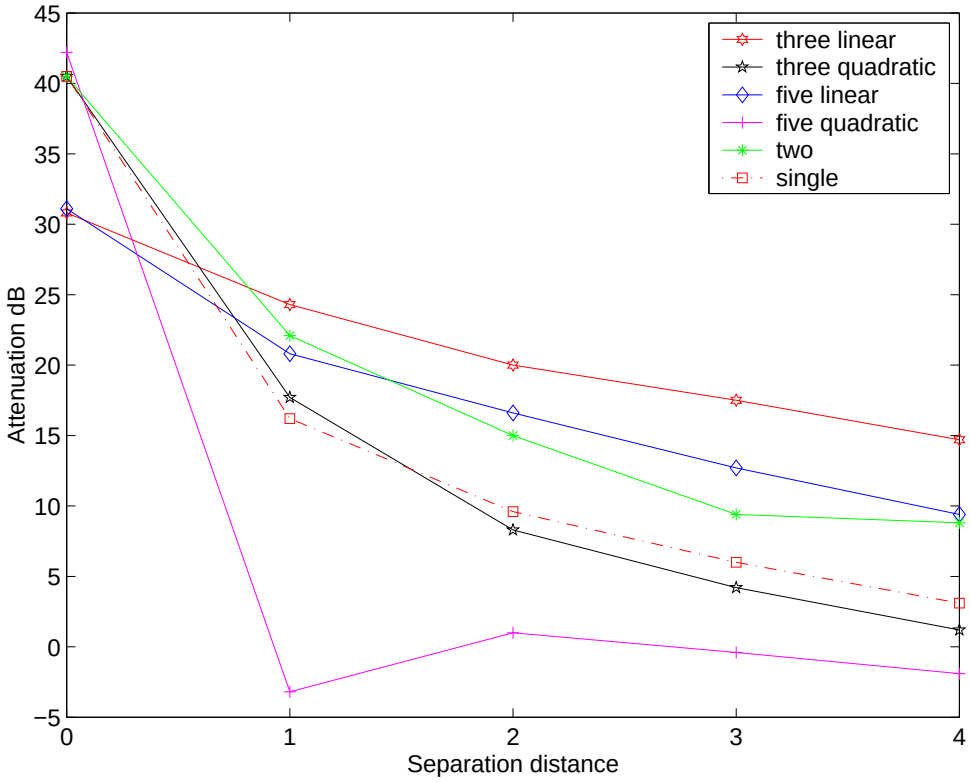

Figure 5.13: Comparison of attenuation between all virtual microphone formulations when controlling an acoustic anti-resonance in a one-dimensional waveguide with absorptive ends.

5.3.4 Discussion

In this section the performance of the higher-order virtual microphone was assessed and compared to the performance of the ordinary virtual microphones in the reactive environment of a one-dimensional waveguide. The use of linear prediction in the higher-order microphone arrays improved the prediction accuracy when compared to the two-element linear prediction virtual microphone (lower-order virtual microphone). In general, the three microphone linear prediction algorithm consistently achieved the highest level of attenuation. Therefore it can be concluded that the use of the three-element linear virtual microphone will improve the prediction accuracy compared to the lower order virtual microphones. For the linear prediction algorithm, increasing the number of prediction microphones from three to five does not offer any significant increase in the level of control achieved. In some cases the five-element lin-

ear virtual microphone out-performs the lower-order virtual microphones, but not in all cases. This result suggests that incorporating extra microphone elements introduces more experimental errors in the form of phase and sensitivity mismatch between the microphone elements and hence reduces the prediction accuracy of the algorithm compared to the three-element higher-order virtual microphone.

Increasing the number of microphones in the quadratic prediction algorithm results in a decrease in the level of attenuation achieved due to the introduction of more errors in the form of phase and sensitivity mismatch between the microphone elements. This result again highlights the susceptibility of the quadratic algorithms to experimental errors. In fact the higher-order quadratic virtual microphone often produced less attenuation at the virtual location than was achieved using conventional control with a single remote microphone. While the higher-order linear prediction virtual microphone is able to compensate for the phase and sensitivity mismatch better than the quadratic method, it is still susceptible to these errors.

5.4 Free Field

This section presents the results of simulated and experimental real-time control using the higher-order forward-difference virtual microphones in the free field and are compared with results for the lower-order virtual microphones. The results of the analytical control in the free field are presented to give a complete picture of the expected performance of the forward-difference virtual microphones.

5.4.1 Experimental Set-up

The real-time control experiments had an identical set-up to the experiments conducted by Kestell (2000). In the anechoic chamber, a 150 mm diameter loudspeaker (with an enclosed back) acted as the primary source and a similar control source speaker was positioned 4.5 m

apart at opposite ends of the chamber. The controlled sound field was analysed along a 0.5 m length at 25 mm increments (see Fig 5.14). The experiments and simulations were conducted at two single frequencies; namely 200 Hz and 400 Hz.

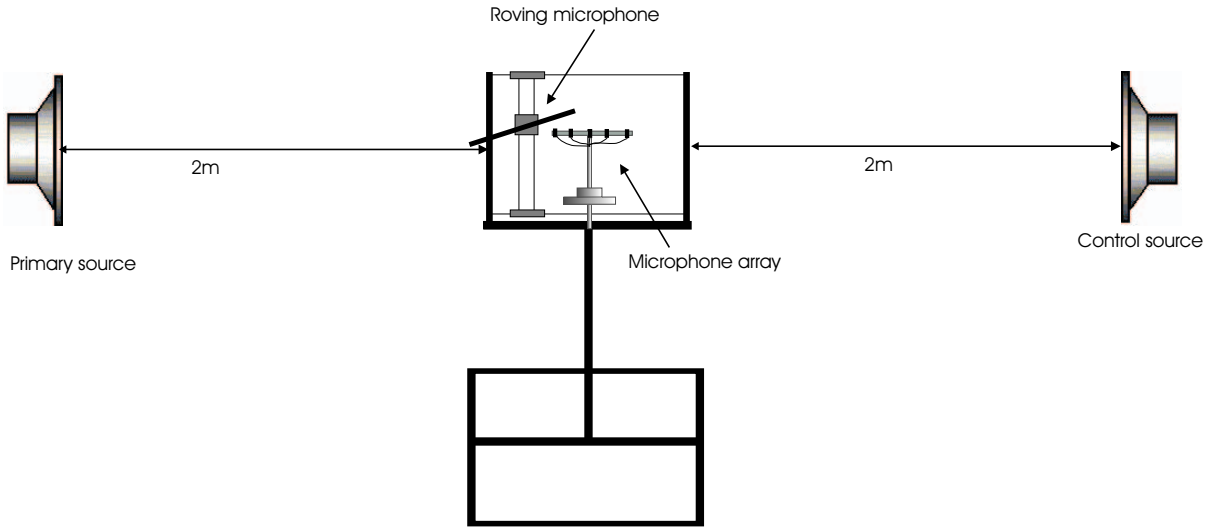

Figure 5.14: Schematic of experimental set-up for free field experiments

5.4.1.1 Control Simulation

A MATLAB simulation was written incorporating the physical set-up described above. The sound field was simulated with the primary and control sources modelled as point monopoles with a spherical pressure amplitude radiation pattern (Hansen and Snyder, 1997) which is defined as follows:

$$p_r = \frac{j\omega\rho_o q e^{-jkr}}{4\pi r} \tag{5.14}$$

where p is the pressure amplitude measured at a distance r from the source, ω is the rotational frequency, ρ_o is the air density, q is the source strength and k is the wavenumber. The cost functions were minimised using quadratic optimisation explained in Chapter 3.

5.4.2 Real-time control

These real-time experiments were carried out using a similar procedure as for the one dimensional waveguide experiments explained in Section 3.4.3. The only difference was that the microphone used to observe the controlled sound field was moved using a stepper motor driving a microphone traverse. The microphone traverse with the stepper motor is shown in Figure 5.15(a), and Figure 5.15(b) shows a photo of the control source, the microphone array and the roving microphone in the anechoic chamber. The roving microphone was used to record the level of attenuation achieved over the 0.5 m region of interest. Real-time control was implemented with the EZ-ANC II feedforward controller. The normalised convergence coefficient was 0.01 and the sample rate for the controller was 5513 Hz. The cancellation path modelling was performed off-line with random noise excitation and a 1024 tap FIR filter. The taps for the free field were too long but the taps were kept the same length for all real-time experiments. However, the length of taps will not effect the results of the real-time control.

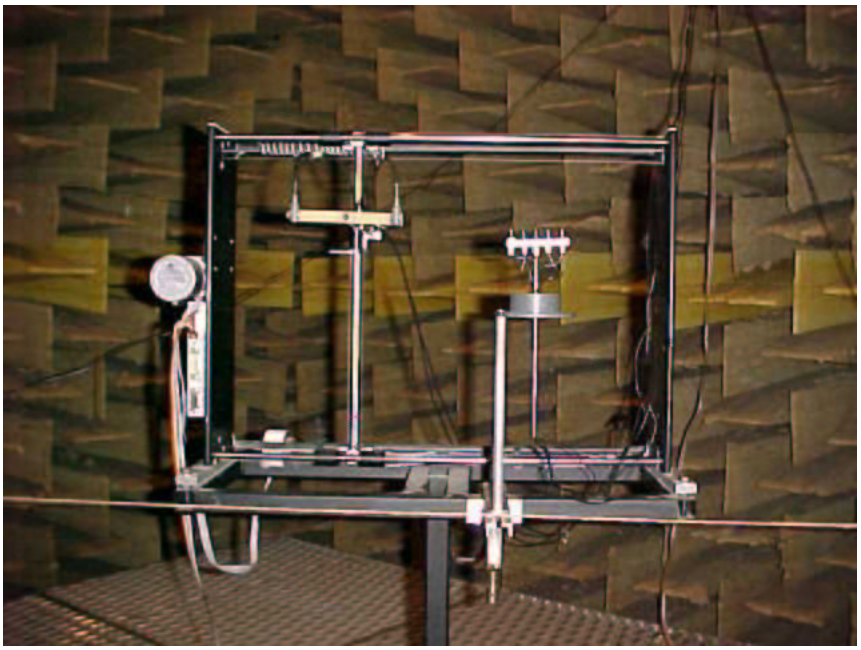

(a) Microphone traverse

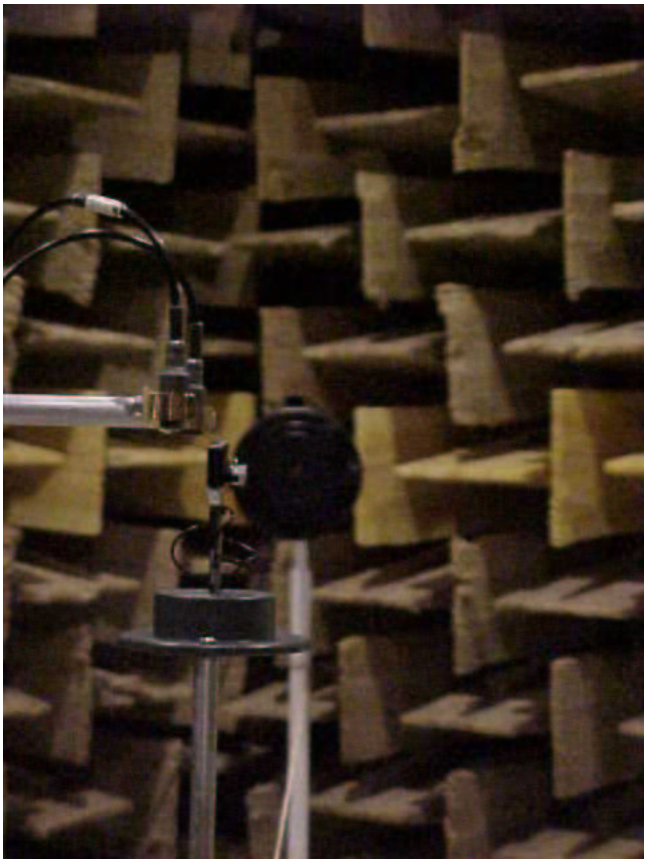

(b) Control speaker, microphone array and roving microphone

Figure 5.15: Experimental setup of equipment in the anechoic chamber

5.4.3 Results for a 200 Hz Sinusoidal Tone in a Free Field

5.4.3.1 Linear Virtual Microphone

The simulated and real time control profiles that were produced when controlling a 200 Hz, tone using linear prediction virtual microphones, are presented in Figure 5.16. Figures 5.16(a), (c) and (e) illustrate the results using two, three and five microphone arrays respectively and simulated control. These figures are identical which suggests that, as there was no experimental errors present in the simulation, increasing the number of microphones cannot improve the prediction accuracy.

Figure 5.17(a) shows the spatial decay of the primary acoustic pressure field from the source to furthest observation point. In addition to the primary field, the pressure gradient and the curvature of the primary field are shown. Figure 5.17(b) is a plot of the pressure, pressure gradient and curvature of the primary field over only the 0.5m region of interest. From this figure it can clearly be seen why increasing the number of elements in the linear array does not change the control profile in the case of simulated control, as the pressure gradient could be accurately predicted using a microphone array containing only two elements.

The real-time control results are presented in Figure 5.16(b), (d) and (f). The results obtained using the two-microphone linear virtual microphone in a real-time control scenario is shown in Figure 5.16(b). An attenuation of 35.8 dB is produced at $0h$ and as the separation distance increases the attenuation decreases to 12 dB at $4h$. Figure 5.16(d) presents the results obtained using the three-microphone linear prediction virtual microphone. This virtual sensing method produces more consistent levels of attenuation across all separation distances with 28 dB attenuation achieved at $0h$ and 17.4 dB at $4h$. Figure 5.16(e) indicates that using the five-microphone linear prediction array in the free field produces quite erratic results. This result would suggest that increasing the number of elements in the prediction array increases the experimental errors as a result of phase and sensitivity mismatch between the elements.

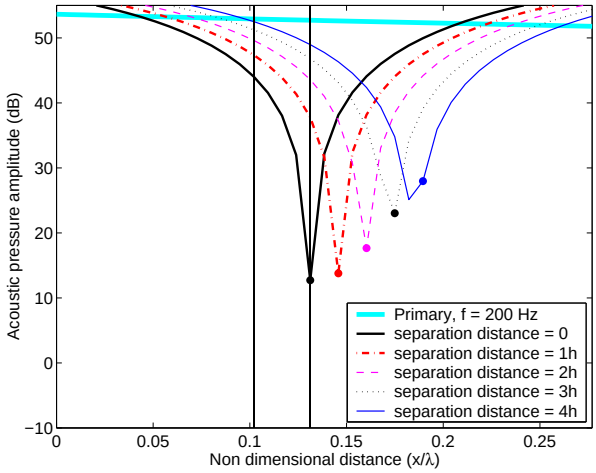

(a) Simulated control - two microphone array

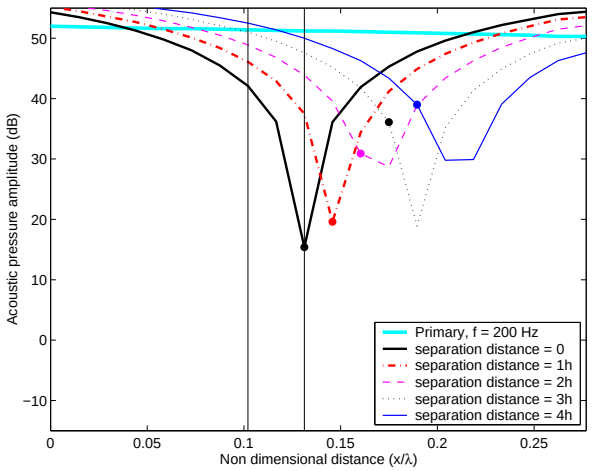

(b) Real-time control - two microphone array

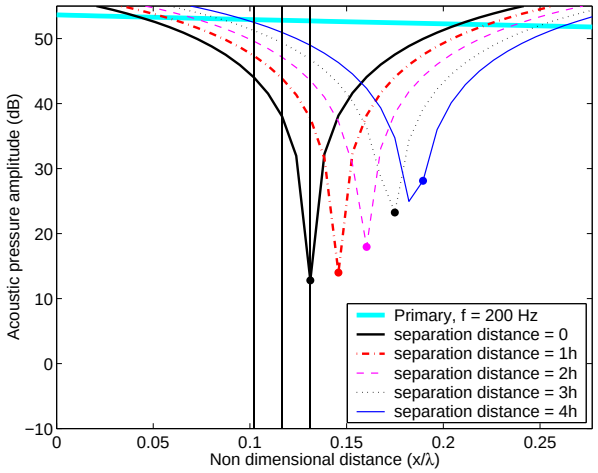

(c) Simulated control - three microphone array

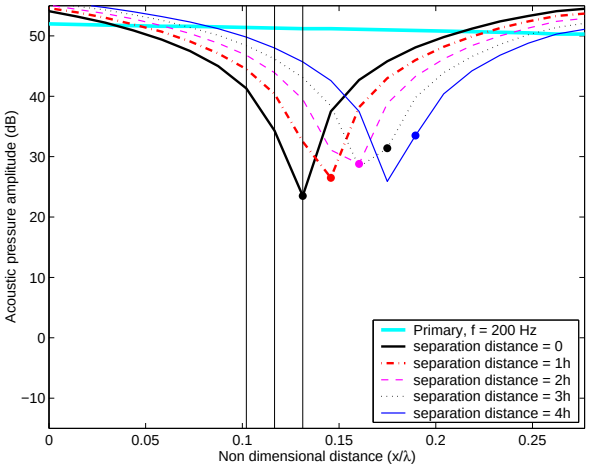

(d) Real-time control - three microphone array

Figure 5.16: Results of control (simulated and real-time) of a 200 Hz tone in a free field using linear virtual microphones.

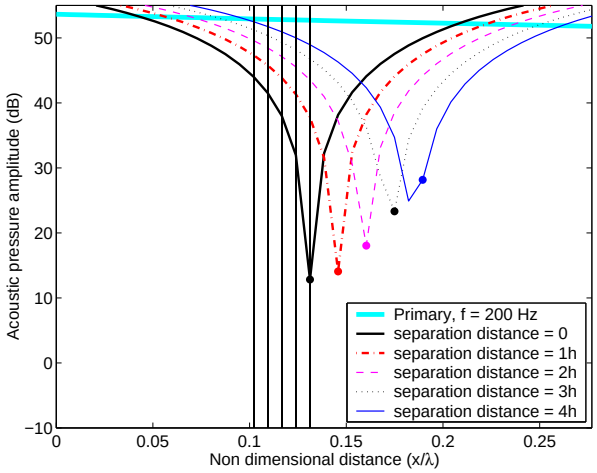

(e) Simulated control - five microphone array

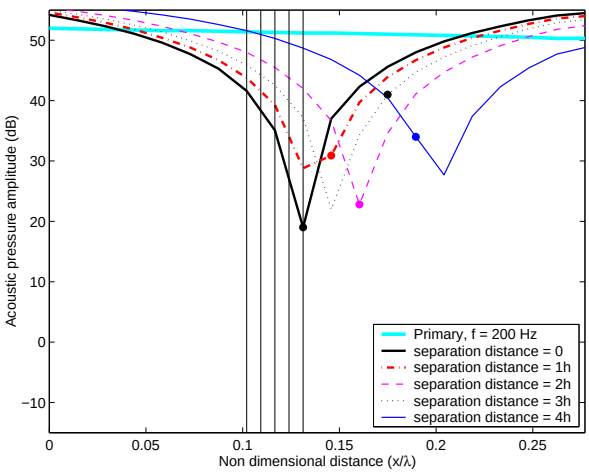

(f) Real-time control - five microphone array

Figure 5.16: cont.. Results of control (simulated and real-time) of a 200 Hz tone in a free field using linear virtual microphones.

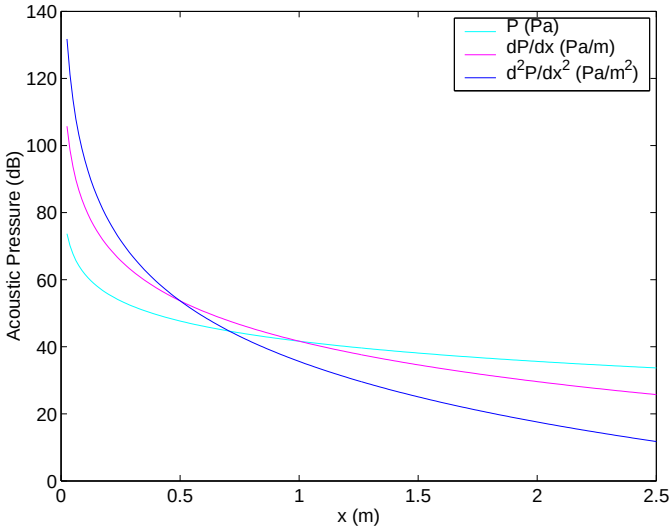

(a) From source to outermost point in the region of interest

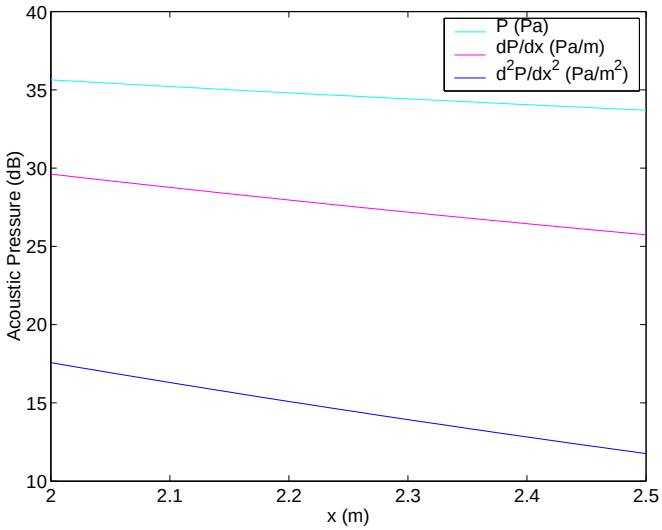

(b) Region of interest

Figure 5.17: Spatial decay of the 200 Hz primary sound field, the gradient and the curvature.

5.4.3.2 Quadratic Virtual Microphone

Figure 5.18 presents the results obtained when controlling a 200 Hz tone using quadratic virtual microphones using both simulated and experimental real-time control. Once again, increasing

the number of elements from three to five in the quadratic prediction has no effect on the control achieved in the simulation as illustrated in Figures 5.18(a) and (c). The quadratic virtual microphone predicts the rate of change of the pressure gradient (or curvature) in order to estimate the pressure at the virtual location. From Figures 5.17(a) and (b) it can be seen that a three-element array can provide enough information to accurately predict the curvature and thus increasing the elements in the array to five will not improve the prediction. The real-time control results obtained using the three and five-microphone arrays are presented in Figures 5.18(b) and (d) respectively. These figures are very similar in that they both exhibit a poor level of control for all separation distances greater than 0h. Clearly, even in the free field the accuracy of the quadratic algorithm is highly prone to corruption as a result of experimental errors.

Comparing the performance of the linear and the quadratic virtual microphones in simulations illustrates once again that the quadratic prediction algorithm is more accurate in the absence of errors. The real-time control results are quite different however, with all the linear virtual microphones out-performing the quadratic formulations. For example, the three-element linear prediction virtual microphone achieves 17.4 dB at 4h, while the three microphone quadratic prediction virtual microphone achieves just 1 dB attenuation.

5.4.4 Results for a 400 Hz Sinusoidal Tone in a Free Field

5.4.4.1 Linear Virtual Microphone

The results of control using linear virtual microphones to control a 400 Hz tonal sound field are presented here. The simulated control results using the two, three and five-microphone arrays are presented in Figure 5.19(a), (c) and (e) respectively. As was found when controlling at 200 Hz, these figures are identical. They show that the sound pressure reduction is approximately

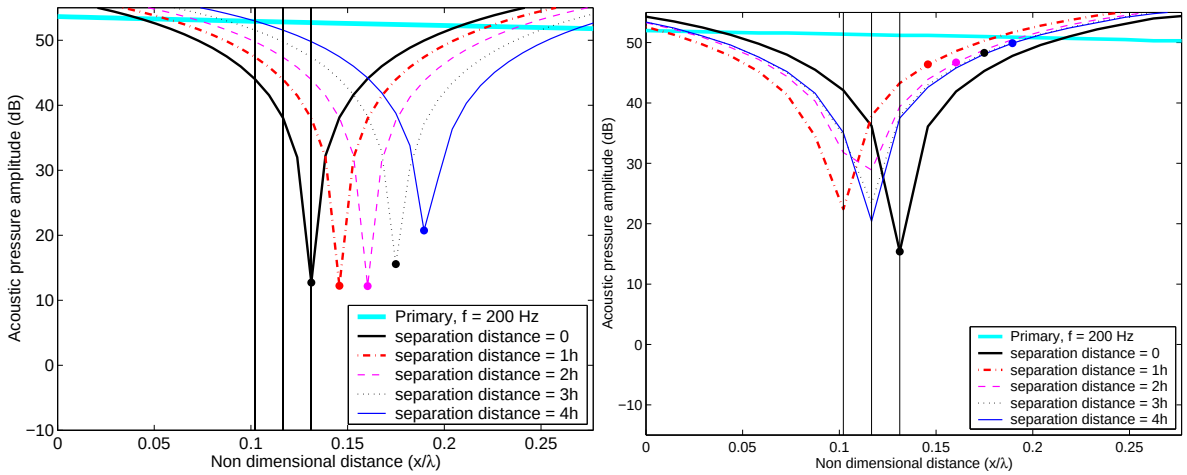

(a) Simulated control - three microphone array *(b) Real-time control - three microphone array*

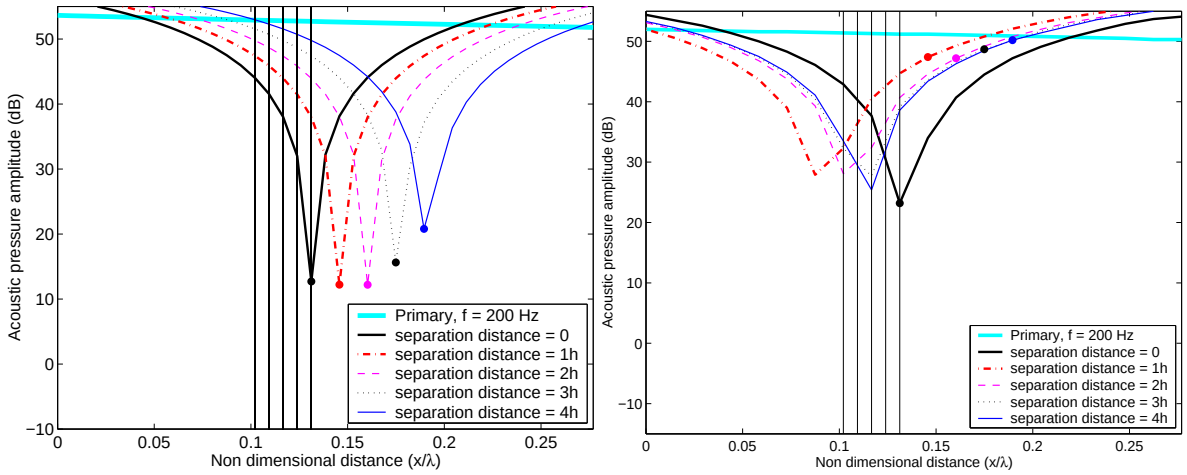

(c) Simulated control - five microphone array *(d) Real-time control - five microphone array*

Figure 5.18: Results of control (simulated and real-time) of a 200 Hz tone in the free field using quadratic virtual microphones.

40 dB at $0h$ and at a separation distance of $4h$ the attenuation is only approximately 12 dB. The control profiles presented in Figure 5.19(b) for the two-element virtual microphone shows very high levels of attenuation are achieved at all separation distances in a real-time control scenario. Comparing this control profile with that achieved controlling a 200 Hz tone, it can be seen that the attenuation achieved controlling a 400 Hz tone is far superior. The real-time results using the three-element linear virtual microphone at 400 Hz (see Figure 5.19(d)) are not consistent with the control achieved at 200 Hz. At 200 Hz, the control achieved is fairly constant across all separation distances and the zone of quiet is centred around the virtual location. This suggests that the ratio of the minimum element spacing to the wavelength is important. Figure 5.19(e) presents the control achievable using a five-element linear virtual microphone to control a 400 Hz tone. As observed previously, the achievable reduction in sound pressure level is considerably less when the number of elements in the prediction array is increased to five.

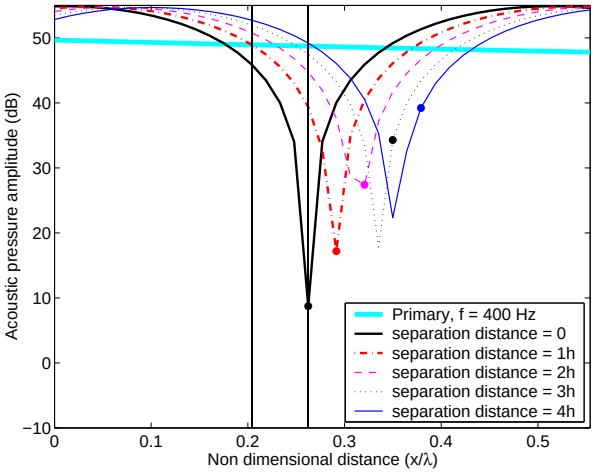

(a) Simulated control - two microphone array

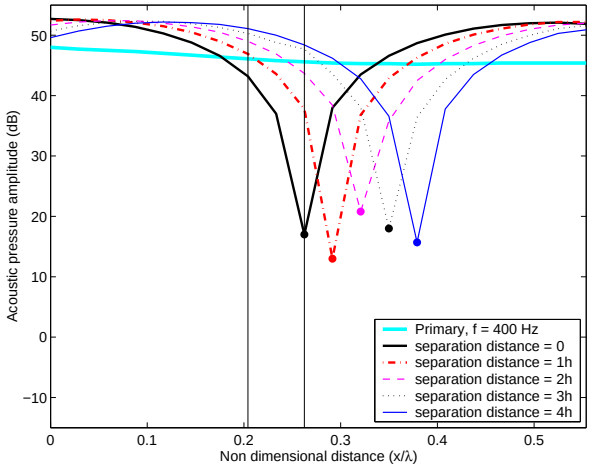

(b) Real-time control - two microphone array

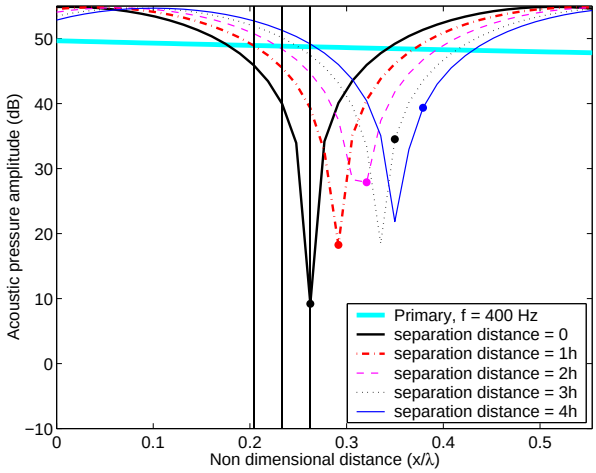

(c) Simulated control - three microphone array

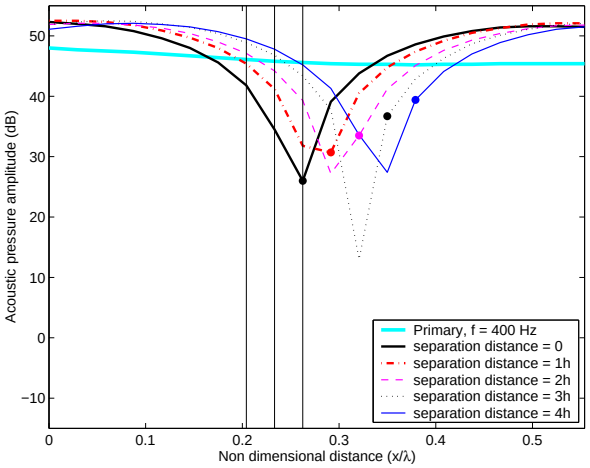

(d) Real-time control - three microphone array

Figure 5.19: Results of control (simulated and real-time) of a 400 Hz tone in a free field using linear virtual microphones.

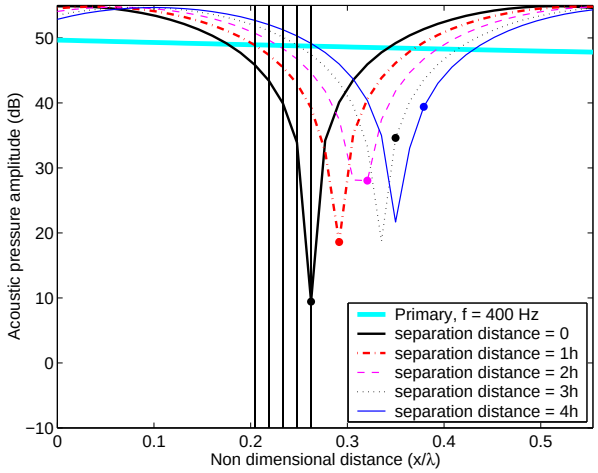

(e) Simulated control - five microphone array

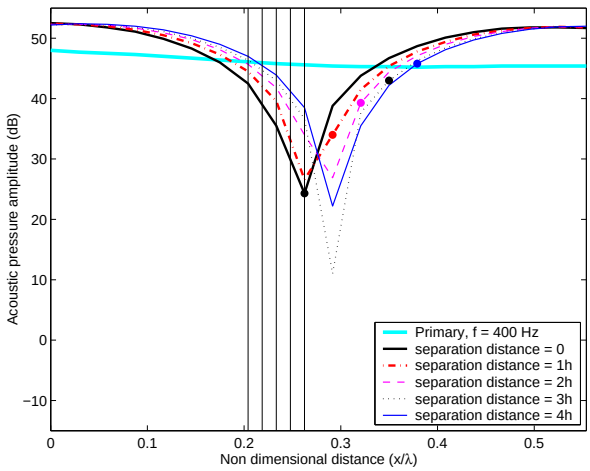

(f) Real-time control - five microphone array

Figure 5.19: cont.. Results of control (simulated and real-time) of a 400 Hz tone in a free field using linear virtual microphones.

5.4.4.2 Quadratic Virtual Microphone

The results obtained using quadratic virtual microphones to control a 400 Hz tone are illustrated in Figure 5.20 in a simulated environment and real-time control experiments. Figures 5.20(a) and (c) present simulated control results using quadratic virtual microphones. The use of these virtual microphones produced 40 dB attenuation at 0h separation distance, decreasing to 18 dB at 4h.

Figures 5.20(b) and (d) again illustrate the poor control achieved when using the quadratic virtual microphones in a real environment with real-time control. Using this virtual microphone offers no practical advantage over the conventional remotely placed microphone. Figure 5.20(d) shows that increasing the number of elements in the prediction array results in no improvement in the performance.

Comparing the sound pressure reduction achieved with the linear virtual microphone versus the quadratic virtual microphone, shows that once again the linear prediction is the superior prediction algorithm in an experimental situation. The linear virtual microphone increases the

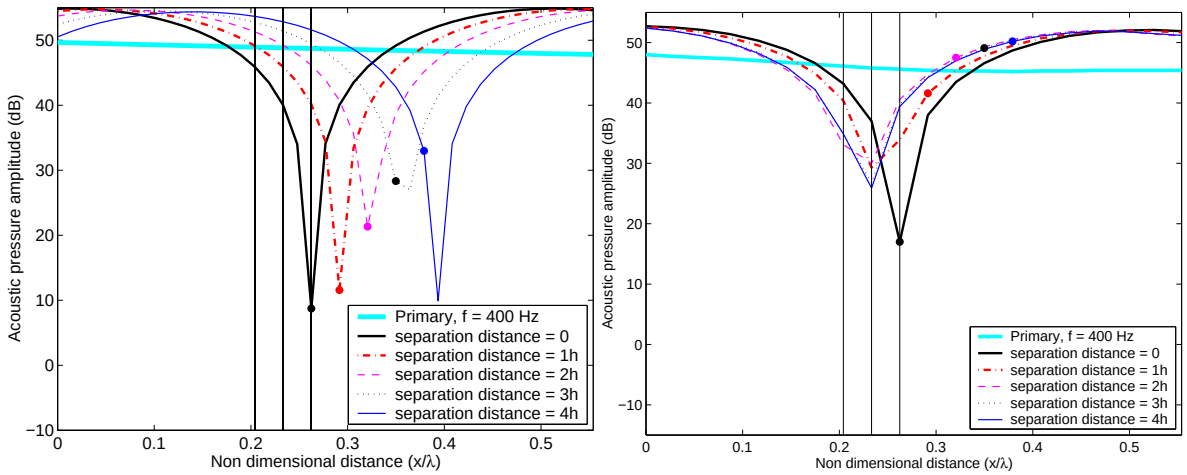

(a) Simulated control - three element array *(b) Real-time control - three microphone array*

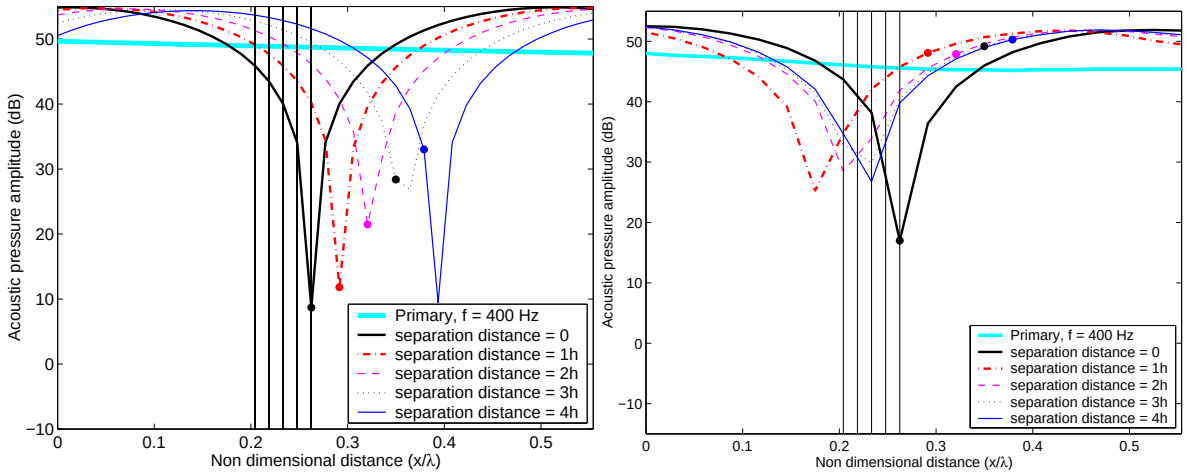

(c) Simulated control - five element array *(d) Real-time control - five microphone array*

Figure 5.20: Results of control (simulated and real-time) of a 400 Hz tone in a free field using the quadratic virtual microphones

attenuation achieved at the virtual location when compared to the conventional single microphone while the quadratic virtual microphone does not.

5.4.5 Discussion

Five different virtual microphone formulations have been evaluated for active local control in a free field. When the zone of maximum attenuation is centred around the virtual location, the spatial extent of the localised zones of quiet with greater than 10 dB of attenuation is one fifth of a wavelength. For the case of the quadratic virtual microphone, the spatial extent of the zone of quiet is still one fifth of a wavelength but it is not centred around the virtual location. From the results presented here, the virtual microphone technique shows promise as a tool to create a localised zone of attenuation. Confirming previous results from the reactive sound field, it can be seen that the quadratic virtual microphone performs best in the simulated control scenario, while for real-time control in experiments, the linear virtual microphone was clearly a better predictor of the remote sound pressure level.

An interesting result was produced when using the two and three-element linear virtual microphone in a real-time control scenario. When controlling a 200 Hz tone the three-microphone linear prediction produces the highest attenuation levels across all separation distances. However, the same virtual microphone performs rather poorly when controlling a 400 Hz tone compared to the two element linear virtual microphone. This result could suggest a relationship between wavelength and inter-element spacing but this result presents no pattern and with decreasing wavelength (increasing frequency) one would expect smaller inter-element spacing to be more effective. At different frequencies the phase and magnitude errors could change and this would effect the prediction accuracy of the virtual microphones.

The two and three-element linear virtual microphones produce the highest and most consistent levels of attenuation compared to the other virtual microphone formulations. The use of the five-element linear virtual microphone decreases the level of attenuation achieved suggesting

that increasing the number of microphone introduces more experimental error through instrumentation calibration errors. The smaller inter-element spacing may also be a source of error. It is possible that phase mismatch between the microphones is larger than the actual phase change over the region of the microphone array.

5.5 Conclusion

In this chapter higher-order virtual microphone formulations were derived and the results from the implementation of these higher-order virtual microphones in a real-time control scenario were presented. The aim of developing these higher-order virtual microphones was to improve the prediction accuracy of the virtual algorithms by spatially filtering short wavelength extraneous noise.

In the reactive sound field of a one-dimensional waveguide, the performance of the higher-order virtual microphones was assessed in a real-time control scenario and compared against the performance of the lower-order virtual microphones. These results showed that the use of the three-element linear virtual microphone resulted in significantly higher levels of attenuation when compared to the attenuation achieved using the lower-order virtual microphones. The use of the five-element linear virtual microphone, in general, did result in higher levels of attenuation than the lower order virtual microphones but not in all cases. This suggests that the phase and sensitivity mismatch does affect the performance of the higher-order virtual microphones. The performance of the quadratic higher-order virtual microphone using a five-element array was poor, in many cases resulting in less attenuation than was achieved using the single remote microphone. The quadratic virtual microphone, lower and higher-order, has proved to be the most susceptible to experimental error especially phase and sensitivity mismatch.

The performance of the higher-order virtual microphones was also assessed in the free field using both numerical simulations and experimental real-time control. In simulated control

the quadratic virtual microphones produced the highest levels of attenuation at all separation distances compared to the linear virtual microphones. However, using real-time control the linear virtual microphone out-performed the quadratic virtual microphone. The linear virtual microphones using two and three-element arrays performed better than the five-element linear virtual microphone. Again this has been attributed to the effect of the extra experimental error introduced through the incorporation of the additional microphones. The two element linear virtual microphone produces the highest levels of attenuation when controlling a 400 Hz tone while the three-element linear virtual microphone achieves the highest levels of attenuation when controlling a 200 Hz tone. Further investigation of the effect of the inter-element spacing could form the basis of future work.

While the linear higher-order virtual microphones does improve on the performance of the lower-order virtual microphones, its performance is still affected by phase and sensitivity mismatch. A possible method of compensating for these errors is to use an adaptive LMS algorithm to determine the optimal microphone weights in the presence of all the physical errors. The effectiveness of this adaptive virtual microphone will be investigated in the Chapter 6.

Chapter 6

Adaptive LMS Algorithm

6.1 Introduction

Traditionally in active noise control applications, the adaptive Least Mean Square (LMS) algorithm has been used to calculate the optimal control signals. The adaptive LMS algorithm can also be used to calculate the physical microphone weights to obtain an estimate for the sound pressure at the virtual location. The LMS algorithm should therefore calculate the optimum weights that will account for the sensitivity, phase and position errors which adversely affect the accuracy of the pressure estimate at the virtual location when using fixed weight virtual microphones. The optimal microphone weights are determined with a microphone placed at the intended location of the virtual microphone and using the array of microphones (as for the forward-difference virtual microphones) and the LMS algorithm, the microphone weights are adapted until they predict the sound pressure measured by the microphone at the virtual location. The weights may then be fixed and the microphone removed. This method differs from the virtual microphone developed by Elliott and David (1992). Their method uses a microphone temporarily located at the intended location of the virtual microphone and a single permanent remote microphone. Transfer functions are measured between the permanent microphone and the control source and between the microphone at the virtual microphone location

and the control source. Once the transfer functions have been measured the microphone at the virtual location is removed. Then assuming that the primary field at the virtual microphone and the permanent remote microphone is equal and using the measured transfer functions, an equation can be obtained for predicting the pressure at the virtual microphone. The adaptive virtual microphone makes no assumptions about the nature of the primary field.

The performance of the adaptive virtual microphone was assessed using a SIMULINK numerical simulation and using real-time control in the one dimensional waveguide that was introduced in earlier chapters. The SIMULINK simulation was used to analyse the capability of the LMS algorithm to compensate for the sensitivity, phase and position errors in three acoustic models. The three models have increasing numbers of modes included, with the first model included just the first four axial modes and the second model including the first 23 axial modes. The final model included 125 modes. Real-time control was also implemented on an experimental rig using the adaptive virtual microphones and these results are also presented. Further, the attenuation resulting from real-time control using the adaptive virtual microphone was compared with the control results of the fixed weight virtual microphones.

6.2 The Least Mean Square Algorithm

The LMS algorithm with leakage is (Hansen and Snyder (1997))

$$\mathbf{w}(k+1) = \mathbf{w}(k)(1-\alpha\mu) + 2\mu e(k)\mathbf{x}(k) \tag{6.1}$$

where $\mathbf{w}$ is the vector of microphone weights, k is the iteration number, α is the leakage coefficient, μ is the convergence coefficient, e is the error signal at time k, namely the difference between the desired and estimated signal, and $\mathbf{x}$ is the input signal at time k. The input signal vector consists of input values prior to and at the current time sample k. The number of values in the input vector is equal to the number of weights in the FIR filter and the weight vector.

6.3 SIMULINK Modelling

The SIMULINK model used to investigate the adaptive LMS virtual microphone is shown in Figure 6.1.

The first block on the far left of the SIMULINK model is a source producing *Band Limited White Noise*. The system was excited with broadband noise, the frequency of which was dependent upon the acoustic system being investigated, approximately ten times the maximum frequency of interest in the acoustic system under investigation.

6.3.1 The Duct Model

The block labelled *Duct Model* in Figure 6.1 is a mask representing the subsystem containing the acoustic model of the one-dimensional waveguide. This mask (or subsystem model) makes the SIMULINK model easier to understand and of a manageable size. The subsystem represented by the mask is shown in Figure 6.2. Using MATLAB, the state space equations which represent the acoustic response at each microphone, including the virtual microphone were calculated. This information was then loaded into the SIMULINK model using the state space blocks which are labelled *mic 1* through to *mic 5* in Figure 6.2. The acoustic response at the virtual location was not a part of the *Duct Model*, but a separate block in the main SIMULINK model (Figure 6.1).

Within this subsystem blocks are included to enable phase and sensitivity mismatch to be incorporated into the system. Sensitivity mismatch is incorporated into the model by adjusting the gain. Phase mismatch between microphone elements is modelled by modifying the location of poles of the frequency response of the microphone. Position errors are applied within the MATLAB program. The microphone signals are then used in both the fixed weight and the adaptive algorithm systems. The magnitude and implementation of these errors will be discussed in Section 6.3.4.

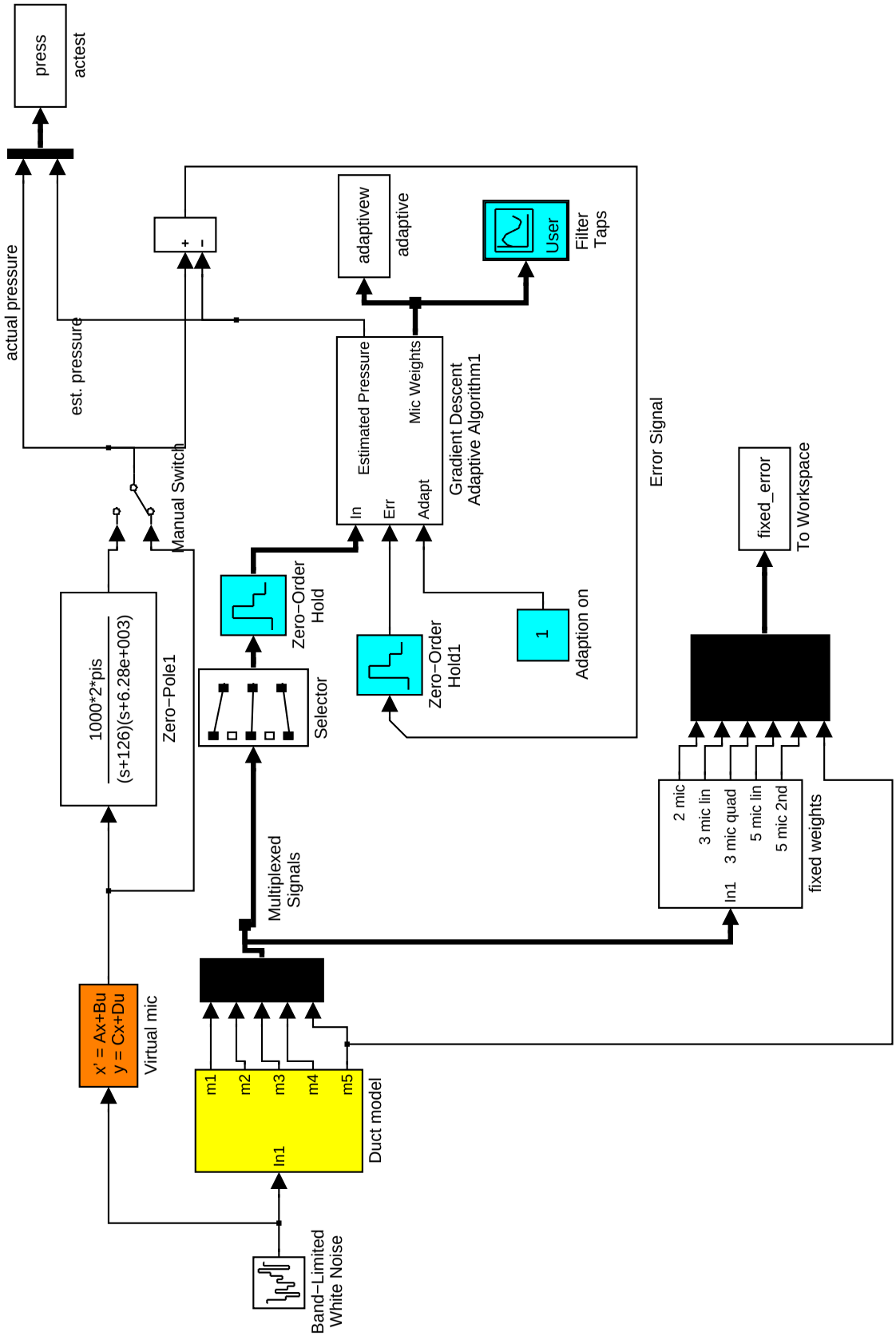

Figure 6.1: SIMULINK model

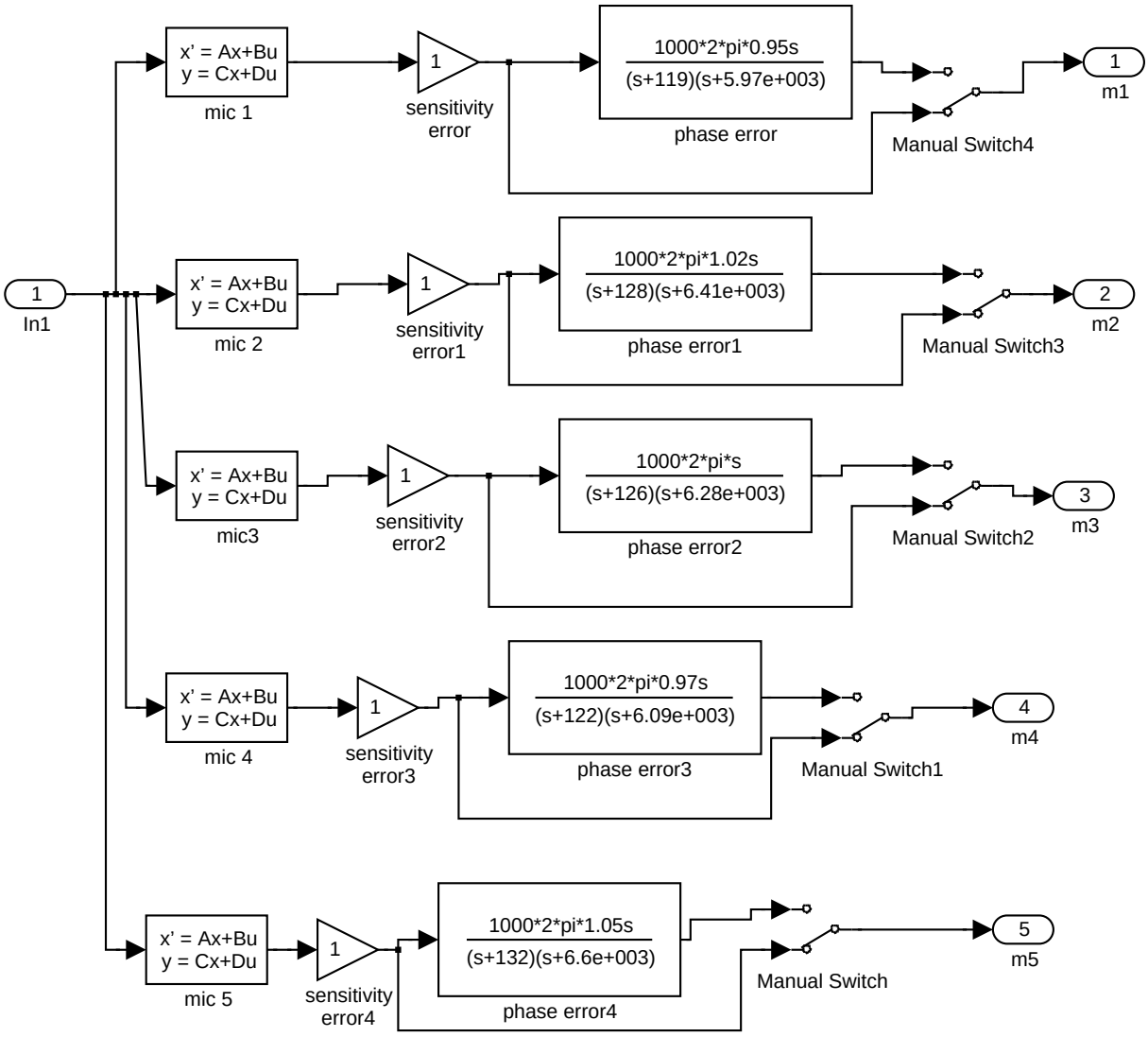

Figure 6.2: The duct acoustic model subsystem

6.3.2 Optimal Weight System

In the adaptive system, the multiplexed signals from the *Duct Model* were passed through a selector block (Figure 6.1) so the required number of microphones could be selected depending on the number of elements in the prediction array. The microphone signals were fed into the *Gradient Descent Algorithm* block as the input. The convergence coefficient was initially set to $\mu = 0.25$ and decreased logarithmically down to $\mu = 0.0025$ over the time of the simulation. Gradually decreasing the convergence coefficient resulted in rapid convergence and accurate estimation of the microphone weights. The estimated pressure was then calculated for a given set of microphone weights and the error signal was calculated from the difference between the estimated pressure and the actual pressure calculated at the desired virtual microphone location (see Figure 6.1). This error signal was then fed into the adaptive algorithm. The microphone weights were adjusted and then the process was repeated, thus, reducing the magnitude of the error signal. Once convergence was achieved, and the adaption essentially halted with $\mu = 0.0025$, the actual pressure and the final estimate of the pressure was transferred to the MATLAB work-space and the normalised root mean square error (NRMS) was calculated as a measure of the accuracy of the pressure estimate at the virtual location. The normalised root mean squared error is defined as:

$$NRMS = \sqrt{\frac{\sum |y_{est} - y|^2}{\sum |y|^2}} \tag{6.2}$$

where y_{est} is the estimated pressure and y is the actual pressure.

6.3.3 The Fixed Weight System

The fixed weights subsystem from Figure 6.1 is shown in full in Figure 6.3. The input signals for this model were the multiplexed signals from the *Duct Model*. A selector block was used

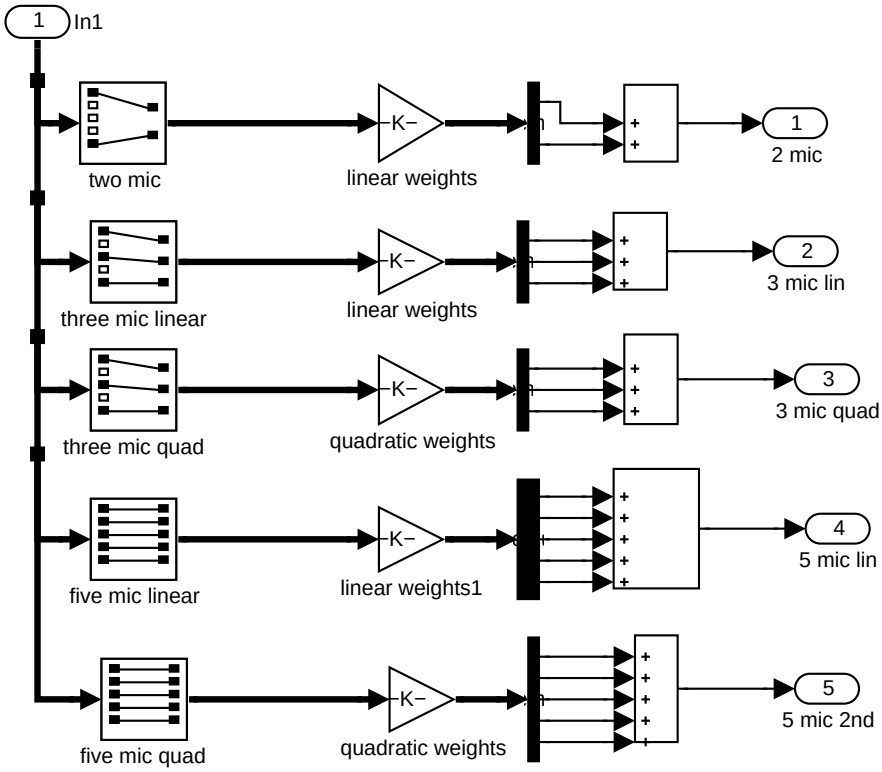

Figure 6.3: The fixed weight (forward difference) subsystem

to select the required microphone signals for each of the different fixed weight virtual microphones. These signals were then weighted and summed to estimate the pressure at the virtual location for all of the forward difference prediction algorithms. The results transferred to the MATLAB workspace and the NRMS error was subsequently calculated.

6.3.4 The Errors

Phase, sensitivity and position errors were incorporated into the model to determine the effect that each individual error and the combination of all three errors had on the prediction accuracy of the forward-difference virtual microphones, and to determine the ability of the adaptive virtual microphone to compensate for these errors. The sensitivity and position errors are summarised in Table 6.1. The phase error is not included in Table 6.1 because the phase

mismatch is dependent on the frequency. The phase mismatch was modelled in SIMULINK by modifying the location of the low and high frequency poles. The response of the microphone was modelled using the following equation

$$G(s) = \frac{\omega_2 s}{(s+\omega_1)(s+\omega_2)} \tag{6.3}$$

where $s = -\omega_1$ for the low frequency pole and $s = -\omega_2$ is the high frequency pole. For this model the low frequency pole was set at 20 Hz and the high frequency pole was set to 1 kHz. The poles of each of the five microphones were each modified by: 0.95, 1.02, 1, 0.97 and 1.05. A frequency response plot of the modelled microphone response with and without the phase error is presented in Figure 6.4.

Microphone	Error	
	Sensitivity	Position
1	+0.2dB	+2.5mm
2	+0.1dB	+1.25mm
3	0	0
4	-0.1dB	-2.5mm
5	-0.2dB	-1.25mm

Table 6.1: Summary of errors incorporated in Simulink model

6.3.5 Acoustic Models

In addition to incorporating phase, sensitivity and position errors, the number of modes included in the model was varied to determine the effect of the higher-order modes on the prediction accuracy. Three acoustic environments were analysed. The first included the first four axial modes which includes frequencies from 0 to 142 Hz (see Table 6.2), with the upper limit corresponding to the natural frequency of the fourth mode. A Bode plot of the acoustic model is presented in Figure 6.5. The second model, which includes the first 23 axial modes, including frequencies from 0 to 817 Hz is also summarised in Table 6.2. The final model includes

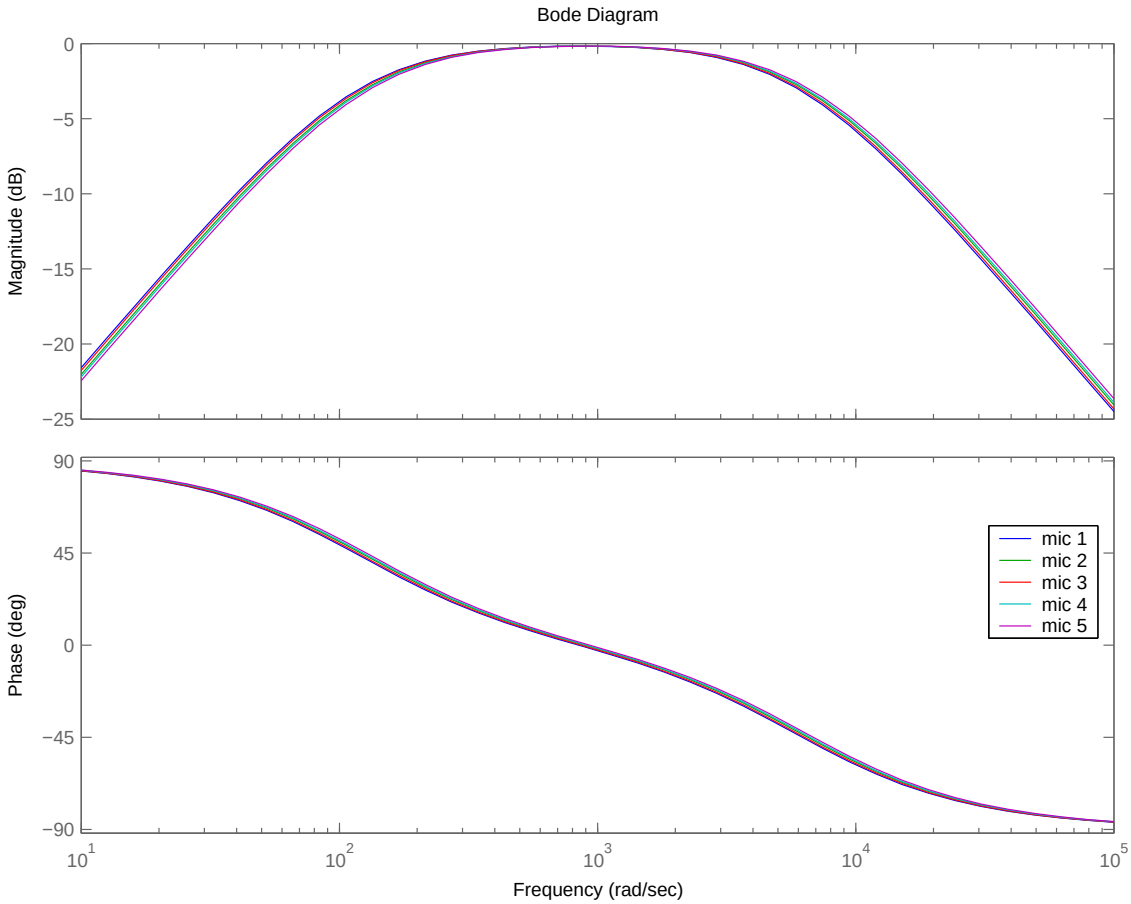

Figure 6.4: Frequency response of the modelled microphone response with phase mismatch

every combination of the modal indices from 0 to 4 in each orthogonal direction, with a total of 125 modes up to a maximum natural frequency of 4735 Hz. The construction of this model in this way means that some information about the axial sound field has been lost but to include all the axial modes up to the 4,4,4 mode would mean including 1000 modes in the model. It is not possible to include this number of modes in Simulink as the model will become ill-conditioned and unstable. The intention of this model was to observe the effect of cross modes on the prediction performance. The pressure was only predicted at a separation distance of $4h$. To perform the following analysis at all separation distances would be far too laborious and the general patterns of performance can be seen from this one example.

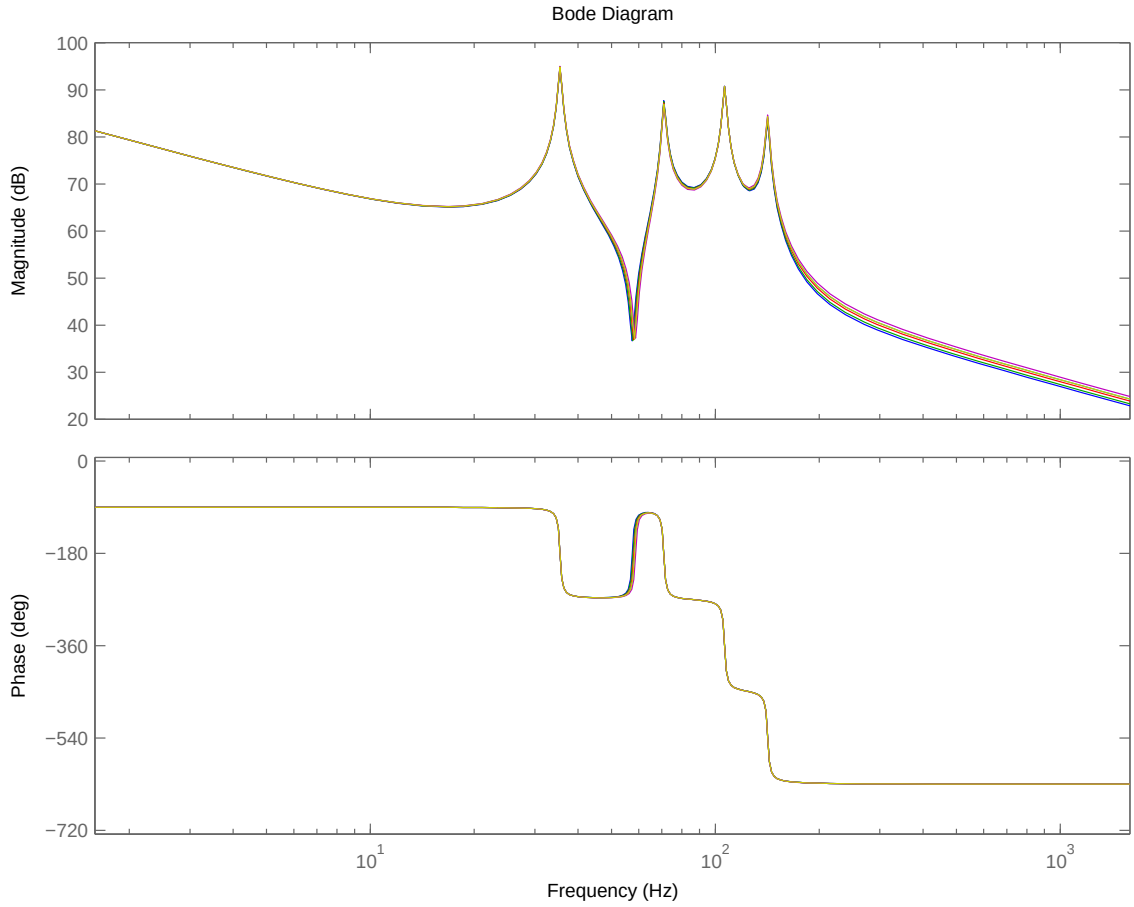

Figure 6.5: Bode plot of the acoustic duct model including first four axial modes

n	*m*	*o*	Frequency Hz
1	0	0	35.5
2	0	0	71.0
3	0	0	106.5
4	0	0	142.0
5	0	0	177.5
6	0	0	213.0
7	0	0	248.5
8	0	0	284.5
9	0	0	319.6
10	0	0	355.0
11	0	0	390.6
12	0	0	426.1
13	0	0	461.6
14	0	0	497.1
15	0	0	532.6
16	0	0	568.1
17	0	0	603.6
18	0	0	639.1
19	0	0	674.6
20	0	0	710.1
21	0	0	745.6
22	0	0	781.2
23	0	0	816.7
0	0	1	836.6
0	1	0	836.6
1	0	1	837.3

Table 6.2: Natural frequencies of the first 26 modes of the one-dimensional waveguide

6.4 Results from SIMULINK Modelling

6.4.1 No Errors Present

This section presents the simulation results in an error free environment for the three acoustic models. In other words all microphones were perfectly phase and amplitude matched and were located with perfect accuracy.

6.4.1.1 Acoustic Model - the first four axial modes

Table 6.3 displays the results for all forward difference and adaptive virtual microphones predicting at a location at a distance of 4*h* from the closest microphone in an error free environment.

Number of microphones	Sensor Type	Weights					NRMS error
		1	2	3	4	5	
two	linear	2	-	-	-	3	0.017
	adaptive	-1.991	-	-	-	2.98	0.014
three	linear	-2.17	-	0.33	-	2.83	0.017
	quadratic	10	-	-24	-	15	0.001
	adaptive	-1.95	-	-0.002	-	2.96	0.014
five	linear	-1.8	-0.8	0.2	1.2	2.2	0.017
	quadratic	12.2	-7.8	-13.8	-5.8	16.2	0.001
	adaptive	-1.59	-0.86	0.03	1.09	2.32	0.014
one	single	-	-	-	-	1	0.102

Table 6.3: The optimal weights and the normalised RMS error for both the optimal and fixed weight virtual sensors with no errors present for an acoustic model containing the first four axial modes for a separation distance of 4*h*

The following observations can be made from the results presented in Table 6.3:

- All of the virtual microphone formulations, both adaptive and linear, are almost an order of magnitude better than a conventional single remote microphone.

- The quadratic prediction algorithm is more accurate than the linear algorithm in an error free environment, thus confirming earlier simulation results.
- The adaptive weights for the two, three and five microphone cases closely approximate the linear weights.

6.4.1.2 Acoustic Model - the first 23 axial modes

Table 6.4 presents the adaptive weights and NRMS error for the linear, quadratic and adaptive virtual microphones.

Number of microphones	Sensor Type	Weights					NRMS error
		1	2	3	4	5	
two	linear	2	-	-	-	3	0.155
	adaptive	-1.54	-	-	-	2.47	0.144
three	linear	-2.17	-	0.33	-	2.83	0.156
	quadratic	10	-	-24	-	15	0.076
	adaptive	8.37	-	-19.7	-	12.3	0.042
five	linear	-1.8	-0.8	0.2	1.2	2.2	0.158
	quadratic	12.2	-7.8	-13.8	-5.8	16.2	0.077
	adaptive	9.66	-5.84	-11.01	-4.9	13.12	0.042
one	single	-	-	-	-	1	0.215

Table 6.4: The optimal weights and the normalised RMS error for the optimal and fixed weight virtual sensors with no errors present for an acoustic model containing the first 23 axial modes

The following comments can be made with respect to Table 6.4:

- The adaptive weights offers the best pressure estimate at the virtual location.
- All virtual microphone formulations out-perform the single remote microphone.
- The adaptive weights are a closer approximation to the quadratic weights than the linear weights.
- The quadratic prediction algorithm is more accurate than the linear algorithm.

- Increasing the number of axial modes excited, clearly degrades the prediction performance of both virtual microphone formulations when compared to the model including the first four axial modes.

6.4.1.3 Acoustic Model - cross modes

The results for the acoustic model incorporating cross modes with no sensitivity, phase or position errors are presented in Table 6.5.

Number of microphones	Sensor Type	Weights					NRMS error
		1	2	3	4	5	
two	linear	2	-	-	-	3	0.023
	adaptive	-1.85	-	-	-	2.85	0.012
three	linear	-2.17	-	0.33	-	2.83	0.023
	quadratic	10	-	-24	-	15	0.005
	adaptive	-0.84	-	-2.07	-	3.91	0.011
five	linear	-1.8	-0.8	0.2	1.2	2.2	0.023
	quadratic	12.2	-7.8	-13.8	-5.8	16.2	0.005
	adaptive	-0.46	-1.36	-1.04	0.51	3.35	0.012
one	single	-	-	-	-	1	0.152

Table 6.5: The optimal weights and the normalised RMS error for the optimal and fixed weight virtual sensors with no errors present for an acoustic model containing the first four modes in each orthogonal direction

From Table 6.5 the following observations can be summarised:

- The magnitude of the error is considerably smaller than for the 23 axial modes case. This is because the number of longitudinal modes used in the simulation have been reduced.
- The quadratic prediction results in much smaller errors than the linear prediction.

6.4.2 Phase Errors

The phase error described in Section 6.3 was applied to the virtual microphone array and the effect that this error has on the prediction accuracy of the virtual sensors is discussed below.

6.4.2.1 Acoustic Model - the first four axial modes

Table 6.6 summarises the results obtained using adaptive, linear and quadratic virtual microphones with phase mismatch present between the transducers in an acoustic sound field containing the first four axial modes.

Number of microphones	Sensor Type	Weights					NRMS error
		1	2	3	4	5	
two	linear	2	-	-	-	3	0.099
	adaptive	-1.58	-	-	-	2.56	0.093
three	linear	-2.17	-	0.33	-	2.83	0.099
	quadratic	10	-	-24	-	15	0.103
	adaptive	-1.62	-	0.1	-	2.50	0.094
five	linear	-1.8	-0.8	0.2	1.2	2.2	0.061
	quadratic	12.2	-7.8	-13.8	-5.8	16.2	0.095
	adaptive	-1.02	-2.14	0.08	2.75	1.30	0.016
one	single	-	-	-	-	1	0.214

Table 6.6: The optimal weights and the normalised RMS error for the optimal and fixed weight virtual sensors with phase errors present for an acoustic model containing the first four axial modes

The following observations can be made from the results presented in Table 6.6:

- The adaptive weights improve the pressure estimate compared to the fixed weights but are unable to completely compensate for the introduced error. This is not surprising given that adjusting the gain of the microphones cannot compensate for phase.
- The quadratic prediction algorithm is most affected by the phase mismatch as it shows the largest increase in NRMS error when compared to the “no errors” case. This is consistent with results presented in previous chapters.
- For both the fixed weight and adaptive virtual microphones, increasing the number of microphones improves the prediction accuracy.

6.4.2.2 Acoustic Model - the first 23 axial modes

Table 6.7 summarises the results for the first 23 axial modes model with phase errors.

Number of microphones	Sensor Type	Weights					NRMS error
		1	2	3	4	5	
two	linear	2	-	-	-	3	0.3120
	adaptive	-1.52	-	-	-	2.35	0.268
three	linear	-2.17	-	0.33	-	2.83	0.323
	quadratic	10	-	-24	-	15	0.178
	adaptive	7.81	-	-18.48	-	11.64	0.13
five	linear	-1.8	-0.8	0.2	1.2	2.2	0.311
	quadratic	12.2	-7.8	-13.8	-5.8	16.2	0.187
	adaptive	8.59	-5.87	-10.60	-1.15	9.99	0.113
one	single	-	-	-	-	1	0.436

Table 6.7: The optimal weights and the normalised RMS error for the optimal and fixed weight virtual sensors with phase errors present for an acoustic model containing the first 23 axial modes

The following comments can be made with respect to the results presented in Table 6.7:

- Once again the adaptive weights improve the pressure estimate compared to the fixed weight virtual sensors
- The adaptive microphone weights for three and five microphone arrays approximate the quadratic fixed weights.
- All virtual microphone methods out-perform conventional control using a single remote microphone.
- Quadratic prediction is more accurate than linear prediction and this result is contrary to the other results presented where the linear algorithm is more accurate than the quadratic algorithm. The adaptive weights in this case approximate the weights of the quadratic prediction algorithm suggesting that this is a special case where the presence of the phase errors results in a more accurate quadratic prediction.

6.4.2.3 Acoustic Model - cross modes

The results for the acoustic model incorporating cross modes with phase errors are presented in Table 6.8.

Number of microphones	Sensor Type	Weights					NRMS error
		1	2	3	4	5	
two	linear	2	-	-	-	3	0.116
	adaptive	-1.32	-	-	-	2.32	0.084
three	linear	-2.17	-	0.33	-	2.83	0.116
	quadratic	10	-	-24	-	15	0.135
	adaptive	-2.55	-	2.42	-	1.13	0.084
five	linear	-1.8	-0.8	0.2	1.2	2.2	0.073
	quadratic	12.2	-7.8	-13.8	-5.8	16.2	0.132
	adaptive	-0.8275	-2.20	-0.231	2.6889	1.55	0.015
one	single	-	-	-	-	1	0.173

Table 6.8: The optimal weights and the normalised RMS error for the optimal and fixed weight virtual sensors with phase errors present for an acoustic model containing the first four modes in each axis

The following observations can be made from the results presented in Table 6.8:

- The adaptive algorithm weights offer a significant improvement in performance compared to the fixed weight virtual microphones.
- The quadratic prediction is adversely affected by the phase errors and therefore the linear prediction algorithm is a more accurate method for predicting the sound pressure level at the virtual location.
- The virtual microphones all out-performed the single remote microphone.

6.4.3 Sensitivity Errors

In a method of presentation similar to Section 6.4.2, this section assesses the effect of the sensitivity mismatch between microphones with respect to the prediction accuracy of the fixed

weight virtual microphones and ability of the adaptive virtual microphone to compensate for the errors. The sensitivity mismatch applied to each microphone within the prediction array is detailed in Table 6.1.

6.4.3.1 Acoustic Model - the first four axial modes

Table 6.9 summarises the results for the forward-difference and adaptive virtual microphone with sensitivity errors present in an acoustic environment with the first four axial modes excited.

Number of microphones	Sensor Type	Weights					NRMS error
		1	2	3	4	5	
two	linear	2	-	-	-	3	0.108
	adaptive	-2.03	-	-	-	2.93	0.014
three	linear	-2.17	-	0.33	-	2.83	0.108
	quadratic	10	-	-24	-	15	0.101
	adaptive	-1.96	-	-0.087	-	2.94	0.014
five	linear	-1.8	-0.8	0.2	1.2	2.2	0.069
	quadratic	12.2	-7.8	-13.8	-5.8	16.2	0.064
	adaptive	-1.57	0.92	0.06	1.05	2.57	0.014
one	single	-	-	-	-	1	0.102

Table 6.9: The optimal weights and the normalised RMS error for the optimal and fixed weight virtual sensors with sensitivity errors present for an acoustic model containing the first four axial modes

The following remarks may be made about the results presented in Table 6.9:

- Adaptive virtual microphone weights result in a more accurate estimation of the pressure at the virtual location than the fixed weight virtual microphones.
- Comparing these results with the “no errors” case (Table 6.3), it can be seen that the adaptive algorithm is able to completely compensate for the sensitivity errors, whereas the fixed weight algorithm error is significantly increased.

6.4.3.2 Acoustic Model - the first 23 axial modes

The results for inclusion of the sensitivity error in the model containing the first 23 axial modes are presented in Table 6.10.

Number of microphones	Sensor Type	Weights					NRMS error
		1	2	3	4	5	
two	linear	2	-	-	-	3	0.202
	adaptive	-1.57	-	-	-	2.42	0.144
three	linear	-2.17	-	0.33	-	2.83	0.203
	quadratic	10	-	-24	-	15	0.139
	adaptive	8.54	-	-19.67	-	12.05	0.042
five	linear	-1.8	-0.8	0.2	1.2	2.2	0.181
	quadratic	12.2	-7.8	-13.8	-5.8	16.2	0.121
	adaptive	9.81	-5.7	-11.0	-5.09	12.92	0.042
one	single	-	-	-	-	1	0.239

Table 6.10: The optimal weights and the normalised RMS error for the optimal and fixed weight virtual sensors with sensitivity errors present for an acoustic model containing the first 23 axial modes

The main observations are outlined below from the results presented in Table 6.10:

- As with the acoustic model with the first four axial modes, the adaptive algorithm is able to completely compensate for the sensitivity mismatch introduced into the system, while the errors for the fixed weight virtual microphones were in general significantly increased.
- In the presence of the sensitivity errors, the quadratic prediction still out-performs the linear prediction.
- The adaptive weights approximate the quadratic fixed weights for the three and five microphone arrays.

6.4.3.3 Acoustic Model - cross modes

Table 6.11 displays the results for all fixed weight and adaptive virtual microphones predicting the sound pressure level at a separation distance of $4h$ in the presence of sensitivity errors.

Number of microphones	Sensor Type	Weights					NRMS error
		1	2	3	4	5	
two	linear	2	-	-	-	3	0.1
	adaptive	-1.89	-	-	-	2.80	0.012
three	linear	-2.17	-	0.33	-	2.83	0.099
	quadratic	10	-	-24	-	15	0.106
	adaptive	-0.82	-	-2.13	-	3.85	0.011
five	linear	-1.8	-0.8	0.2	1.2	2.2	0.067
	quadratic	12.2	-7.8	-13.8	-5.8	16.2	0.081
	adaptive	-0.43	-1.37	-1.06	0.46	3.34	0.012
one	single	-	-	-	-	1	0.204

Table 6.11: The optimal weights and the normalised RMS error for the optimal and fixed weight virtual sensors with sensitivity errors present for an acoustic model containing the first four modes in each orthogonal direction

Reviewing Table 6.11 results in the following observations:

- The linear prediction virtual sensors results in a better pressure estimate than using the quadratic virtual microphone. This indicates that quadratic estimates are more sensitive to cross modes than are linear estimates. This is not at all surprising given the results presented in previous chapters indicated that the linear virtual microphone out performed the quadratic virtual microphone.
- The adaptive virtual sensor employing two, three or five microphones demonstrates an ability to completely compensate for sensitivity errors.

6.4.4 Position Errors

Position errors applied to the elements in the virtual microphone arrays were designed to reflect the errors that might occur during real-time experiments. It was difficult to know exactly the positions of the acoustic centres of the microphones and therefore they were just estimated. The position errors incorporated in the model are detailed in Table 6.1.

6.4.4.1 Acoustic Model - first four axial modes

The results for the acoustic model incorporating the first four axial modes with position errors are presented in Table 6.12.

Number of microphones	Sensor Type	Weights					NRMS error
		1	2	3	4	5	
two	linear	2	-	-	-	3	0.016
	adaptive	-1.89	-	-	-	3.17	0.014
three	linear	-2.17	-	0.33	-	2.83	0.016
	quadratic	10	-	24	-	15	0.088
	adaptive	-2.13	-	-0.02	-	3.09	0.014
five	linear	-1.8	-0.8	0.2	1.2	2.2	0.017
	quadratic	12.2	-7.8	-13.8	-5.8	16.2	0.018
	adaptive	-1.77	0.92	0.06	1.05	2.57	0.014
one	single	-	-	-	-	1	0.104

Table 6.12: The optimal weights and the normalised RMS error for the optimal and fixed weight virtual sensors with position errors present for an acoustic model containing the first four axial modes

From these results the following observations can be made:

- Comparing these results with the same acoustic model with “no errors” present it can be seen that the accuracy of the fixed weight linear algorithm is unaffected by position errors.
- The accuracy of the quadratic algorithm is significantly affected by the position errors.

- The adaptive virtual microphone is able to completely compensate for the position errors.
- All virtual microphone formulations provide a significantly better pressure estimate at the virtual location than the single remote microphone.

6.4.4.2 Acoustic Model - the first 23 axial modes

Table 6.13 displays the results for all fixed weight and adaptive virtual microphones predicting the sound pressure level at a separation distance of $4h$ in the presence of position errors.

Number of microphones	Sensor Type	Weights					NRMS error
		1	2	3	4	5	
two	linear	2	-	-	-	3	0.150
	adaptive	-1.55	-	-	-	2.48	0.139
three	linear	-2.17	-	0.33	-	2.83	0.151
	quadratic	10	-	-24	-	15	0.163
	adaptive	10.25	-	-20.1	-	11.75	0.041
five	linear	-1.8	-0.8	0.2	1.2	2.2	0.150
	quadratic	12.2	-7.8	-13.8	-5.8	16.2	0.188
	adaptive	9.73	-4.36	-10.03	-7.44	13.09	0.040
one	single	-	-	-	-	1	0.218

Table 6.13: The optimal weights and the normalised RMS error for the optimal and fixed weight virtual sensors with position errors present for an acoustic model containing the first 23 axial modes

Reviewing the results presented in Table 6.13 the following comments can be made:

- The adaptive virtual microphone is able to completely compensate for the position errors.
- The presence of the position errors has no effect on the accuracy of the linear virtual microphones.
- The prediction accuracy of the quadratic virtual microphone is again greatly affected by the introduced position errors.

6.4.4.3 Acoustic Model - cross modes

Table 6.14 presents the results achieved when predicting the sound pressure level at a separation distance of $4h$ in the presence of position errors.

Number of microphones	Sensor Type	Weights					NRMS error
		1	2	3	4	5	
two	linear	2	-	-	-	3	0.011
	adaptive	-2.04	-	-	-	3.03	0.012
three	linear	-2.17	-	0.33	-	2.83	0.012
	quadratic	10	-	-24	-	15	0.022
	adaptive	1.07	-	-1.92	-	3.98	0.012
five	linear	-1.8	-0.8	0.2	1.2	2.2	0.014
	quadratic	12.2	-7.8	-13.8	-5.8	16.2	0.042
	adaptive	-0.68	-1.34	-0.92	0.36	3.57	0.012
one	single	-	-	-	-	1	0.217

Table 6.14: The optimal weights and the normalised RMS error for the optimal and fixed weight virtual sensors with position errors present for an acoustic model containing the first four modes in each orthogonal direction

From these results the ensuing comments may be made:

- As in the other examples, the adaptive virtual sensors are able to completely compensate for the position errors.
- The linear prediction accuracy is better than the quadratic prediction.
- The normalised RMS error is slightly smaller for this case compared to the “no errors” case.
- All results are the same as for the model containing the first 23 axial modes, except the errors are much smaller in this model than for the case where all plane wave modes up to cut-on are excited.

6.4.5 All Errors Present

In this final example all the errors presented in Table 6.1 were incorporated into the simulation and the normalised RMS error in the prediction accuracy at a separation distance of $4h$ was calculated along with the optimum microphone weights.

6.4.5.1 Acoustic Model - first four axial modes

Table 6.15 displays the results for all forward-difference and adaptive virtual microphones predicting at a location at a distance of $4h$ from the closest microphone with all errors present.

Number of microphones	Sensor Type	Weights					NRMS error
		1	2	3	4	5	
two	linear	2	-	-	-	3	0.016
	adaptive	-2.18	-	-	-	3.17	0.014
three	linear	-2.17	-	0.33	-	2.83	0.133
	quadratic	10	-	-24	-	15	0.128
	adaptive	-1.24	-	-0.95	-	3.09	0.098
five	linear	-1.8	-0.8	0.2	1.2	2.2	0.086
	quadratic	12.2	-7.8	-13.8	-5.8	16.2	0.110
	adaptive	-1.06	-2.55	0.08	2.98	1.53	0.016
one	single	-	-	-	-	1	0.154

Table 6.15: The optimal weights and the normalised RMS error for the optimal and fixed weight virtual sensors with all errors present for an acoustic model containing the first four axial modes

The following comments may be made in regard to Table 6.15:

- The quadratic virtual microphone error is very large, in fact, almost 100 times larger than the error in a noise free environment in one case.
- The adaptive virtual microphone is clearly the best predictor of the pressure at the virtual location.
- Increasing the number of microphones over two in the adaptive virtual microphone formulations offers no improvement in prediction accuracy.

6.4.5.2 Acoustic Model - first 23 axial modes

The results for all virtual microphones in an acoustic environment incorporating the first 23 axial modes with all errors present is displayed in Table 6.16.

Number of microphones	Sensor Type	Weights					NRMS error
		1	2	3	4	5	
two	linear	2	-	-	-	3	0.364
	adaptive	-2.18	-	-	-	3.17	0.2649
three	linear	-2.17	-	0.33	-	2.83	0.367
	quadratic	10	-	-24	-	15	0.33
	adaptive	8.96	-	-19.0	-	10.98	0.115
five	linear	-1.8	-0.8	0.2	1.2	2.2	0.33
	quadratic	12.2	-7.8	-13.8	-5.8	16.2	0.33
	adaptive	9.68	-5.89	-10.12	-2.73	10.03	0.117
one	single	-	-	-	-	1	0.446

Table 6.16: The optimal weights and the normalised RMS error for the optimal and fixed weight virtual sensors with all errors present for an acoustic model containing the first 23 axial modes

The results in Table 6.16 shows that:

- The errors for this model are very large in fact the largest of all the models.
- The adaptive virtual microphone achieves the best pressure estimate at the virtual location.
- The adaptive weights approximate the quadratic fixed weights.

6.4.5.3 Acoustic Model - cross modes

Table 6.17 displays the results for all forward-difference and adaptive virtual microphones predicting at a separation distance of $4h$ with all errors present.

Number of microphones	Sensor Type	Weights					NRMS error
		1	2	3	4	5	
two	linear	2	-	-	-	3	0.143
	adaptive	-1.44	-	-	-	2.37	0.088
three	linear	-2.17	-	0.33	-	2.83	0.146
	quadratic	10	-	-24	-	15	0.19
	adaptive	-11.07	-	-1.92	-	3.98	0.086
five	linear	-1.8	-0.8	0.2	1.2	2.2	0.089
	quadratic	12.2	-7.8	-13.8	-5.8	16.2	0.186
	adaptive	-0.97	-2.56	-0.13	2.95	1.67	0.015
one	single	-	-	-	-	1	0.169

Table 6.17: The optimal weights and the normalised RMS error for the optimal and fixed weight virtual sensors with all errors present for an acoustic model containing the first four modes in each orthogonal direction

From the results presented in Table 6.17 the following comments can be made:

- Both the quadratic virtual microphone formulations result in larger errors than obtained using the single remote microphone.
- The accuracy of the quadratic virtual microphone is most affected by the presence of the simulated errors.
- The adaptive virtual microphone offers the best estimate of the pressure at the virtual location for the two, three and five microphone cases.

6.4.6 The Effect of Wavelength on Adaptive Weights

An interesting outcome from the simulation results presented here was that for the model that included 23 modes, the adaptive weights for the three and five microphone arrays approximated the weights for the quadratic virtual microphone. However, for the other two acoustic models the adaptive weights approximated the linear fixed weights. This result implies that the magnitude of the wavelength in the axial direction influences the order of the adaptive

weights needed to obtain the best pressure estimate at the virtual location. This idea was investigated further. Initially, it was considered that a number of factors could affect the order of the adapted weights. These factors were:

- The separation distance between the microphone array and the virtual location
- The inter-element sensor spacing.

It was found that while increasing the separation distance changed the magnitude of the weights it did not affect the order of the optimum weights.

It was found that the relationship between the sensor spacing and the wavelength determined the order of the weights. Using an array of three microphones, various sensor spacings were used with increasing numbers of modes included in the simulation. The spacings investigated were: an inter-element spacings of $h/4$, $h/2$, h and $2h$. Figure 6.6 illustrates the results of this work and the legend for this figure indicates the number of modes included in each model in that all axial modes up to $x,0,0$ are included. For example in Figure 6.6(a) the red line shows the microphone weights for the first axial mode and the green line shows the microphone weights for a model including all axial mode up to the sixth axial mode. Figure 6.6(a) shows the microphone weights for an inter-element spacing of $2h$ predicting at a separation distance of $8h$ with increasing numbers of modes. It can be seen from Figure 6.6(a) that microphone weights change from linear to quadratic with the inclusion of the third axial mode. Figure 6.6(b) presents the results for an inter-element spacing of h with the virtual location at $4h$. The weights become quadratic at the sixth axial mode. Figure 6.6(c) illustrates the relationship between a decreasing wavelength and the order of the adaptive microphone weights. For this example an inter-element separation of $h/2$ was used with a separation distance of $2h$. Finally, a separation distance of h and an inter-element spacing of $h/4$ was examined. These results are presented in Figure 6.6(d). From this figure it can be seen that the microphone weights become quadratic with the incorporation of the nineteenth axial mode. To determine

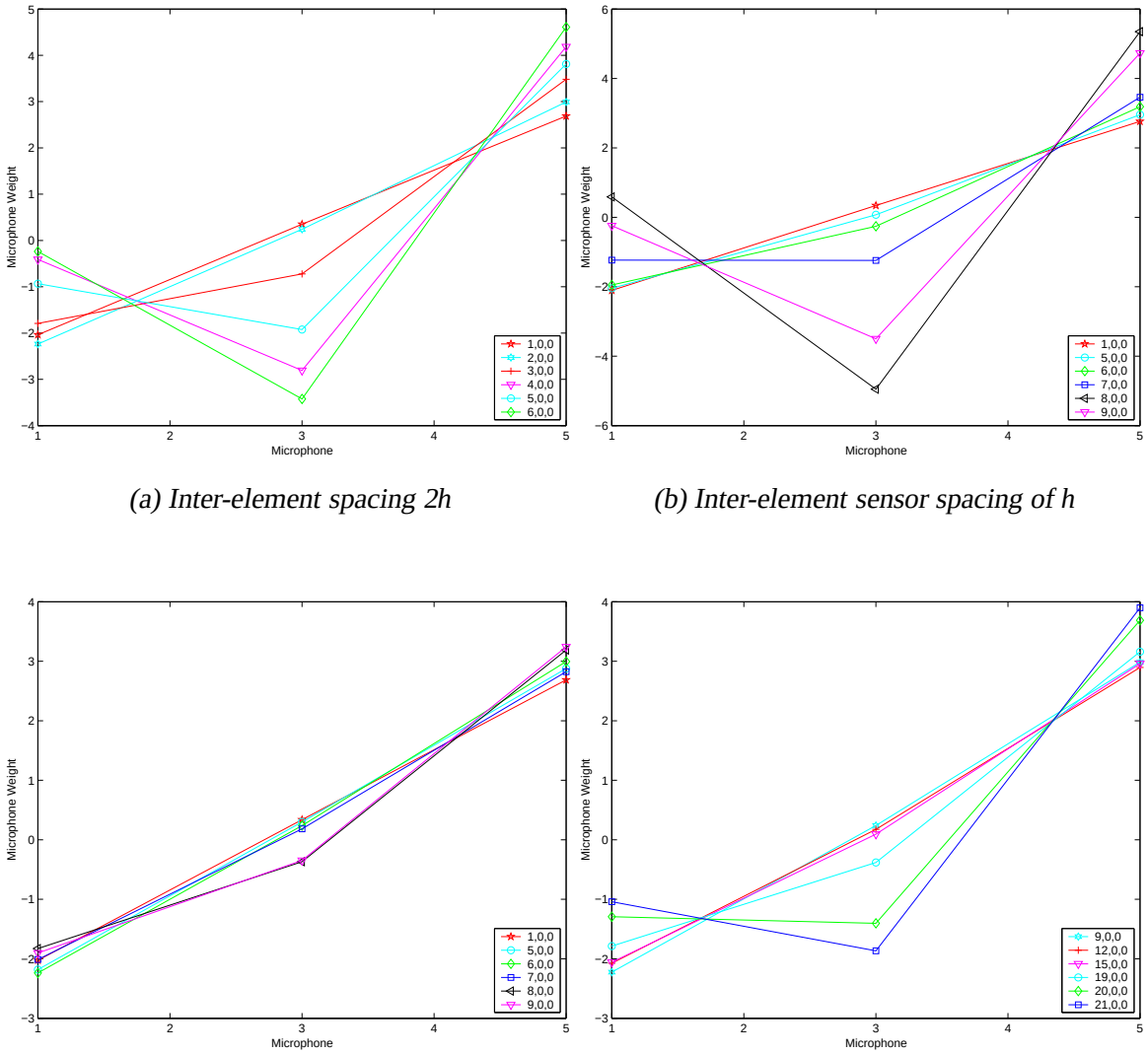

(a) Inter-element spacing 2h

(b) Inter-element sensor spacing of h

(c) Inter-element sensor of h/2

(d) Inter-element spacing - h/4

Figure 6.6: The effect of wavelength on optimum microphone weights to achieve the best pressure estimate at the virtual location. Each line represents an acoustic model including all axial modes up to $x, 0, 0$.

the relationship between wavelength and inter-element spacing, the wavelength is normalised to the inter-element spacing.

$$\begin{aligned} \text{spacing} - 2h &\quad \tfrac{\lambda}{2h} = 64.4\,(\lambda = 3.22\text{m}) \\ \text{spacing} - h &\quad \tfrac{\lambda}{h} = 64.4\,(\lambda = 1.61\text{m}) \\ \text{spacing} - h/2 &\quad \tfrac{\lambda}{h/2} = 96.8\,(\lambda = 1.21\text{m}) \\ \text{spacing} - h/4 &\quad \tfrac{\lambda}{h/4} = 81.4\,(\lambda = 0.51\text{m}) \end{aligned} \tag{6.4}$$

From the normalised wavelength presented above, it is difficult to draw any conclusive patterns as to the frequency at which the order of the adaptive weights changes from linear to quadratic.

6.4.7 Summary

This work investigated the effect that phase, sensitivity and position errors have on the accuracy of the pressure estimate at the virtual location using the forward-difference virtual microphones, and the ability of the adaptive virtual sensors to compensate for these errors and therefore produce a better pressure estimate at the virtual location. The errors were incorporated into the model individually to determine the effect that each error had on the algorithms and then all errors were included together to provide a more accurate representation of actual experimental conditions. Three acoustic models were used in these simulations with different numbers of included modes to determine the effect that higher-order modes had on the prediction accuracy.

The results of the simulations confirmed many of the results of the experimental work presented in previous chapters. The quadratic prediction algorithm was the most accurate system in an error free environment; however with errors incorporated into the models the accuracy was significantly affected. For the “no errors” case, the quadratic virtual microphones produced a better estimate of pressure at the virtual location than using the adaptive virtual microphones. Error surfaces can be quite complicated and may contain localised areas of sub-

optimal minima. So it is possible the adaptive weights for the “no errors” case converged to a sub-optimal result. This could be remedied by modifying the convergence coefficient or by allowing the adaption to run longer.

Irrespective of the acoustic environment, the adaptive LMS virtual microphones improved the pressure estimate at the virtual location. The adaptive algorithm was able to completely compensate for sensitivity and position errors. The algorithm was only able to partly compensate for phase errors. The adaptive algorithm attempts to compensate for the phase error by adjusting the weights of each microphone in the prediction array. Clearly, modifying the weights applied to the individual microphone signals will not enable complete compensation for errors in phase as it can for errors in sensitivity and position.

In most cases increasing the number of microphones, up to five, used in the adaptive virtual microphone decreased the normalised RMS error.

6.5 Experiments using Real-time Control and the LMS algorithm

Real-time experiments were conducted in the one dimensional waveguide (described in Chapter 3) using the LMS adaptive algorithm. The performance of the adaptive algorithm was investigated using the two, three and five microphone arrays at both resonance and anti-resonance frequencies in both a lightly damped and moderately damped duct.

6.5.1 Experimental Procedure

The procedure for carrying out the experiments was very similar to that used for the experiments in the one-dimensional waveguide presented in earlier chapters. A schematic of the

experimental equipment and set-up is shown in Figure 6.7. The adaptive weights were calculated using the LMS algorithm model built in SIMULINK (see Figure 6.8) and then downloaded onto the dSpace DS1104 board. The parameters of the adaptive algorithm were modified using Control Desk software. The user interface of the Control Desk software is shown in Figure 6.9. The software allowed the value of the convergence coefficient to be modified, the adaption of the microphone weights viewed and the final weights recorded. A broadband noise source over a frequency range from 0 to 400 Hz was used for the adaptation. The sample rate was 4 kHz. The convergence coefficient was modified during the operation of the adaptive algorithm. The convergence coefficient with an initial value of 0.5 was gradually decreased to 0 as the weights converged. No leakage was required in this experiment. With the optimal weights determined, the adaptation process was stopped and the weights recorded. Real-time control was then performed using the same method as outlined for the open loop control, that is, when the weights were fixed to the value determined using the procedure outlined above, an EZ-ANC II electronic control system was used to control the sound field using the virtual microphone signal as an error signal.

6.5.2 Results for the Rigidly Terminated Duct

In this section the performance of the LMS adaptive algorithm is assessed in a rigidly terminated duct at an acoustic resonance and anti-resonance. The resonance frequency selected corresponded to the natural frequency of the 7th axial mode and the anti-resonance frequency was in between 7th and 8th axial modes.

6.5.2.1 Resonance

Figure 6.10 shows the results obtained using the microphone weights determined with the adaptive LMS algorithm. The most striking feature of these results is that the zone of maximum attenuation occurs at the virtual location for all separation distances. This indicates

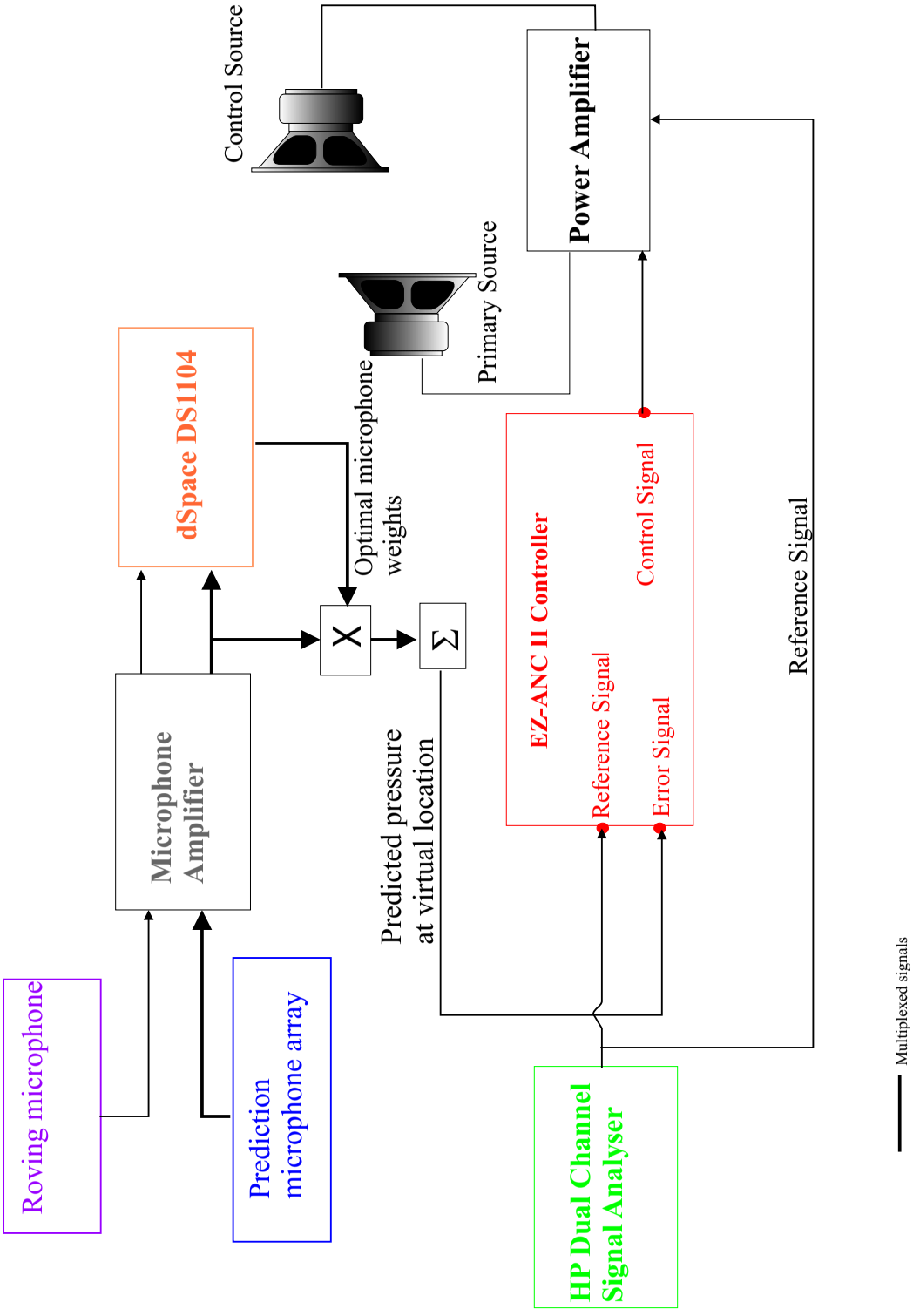

Figure 6.7: Schematic of experimental set-up

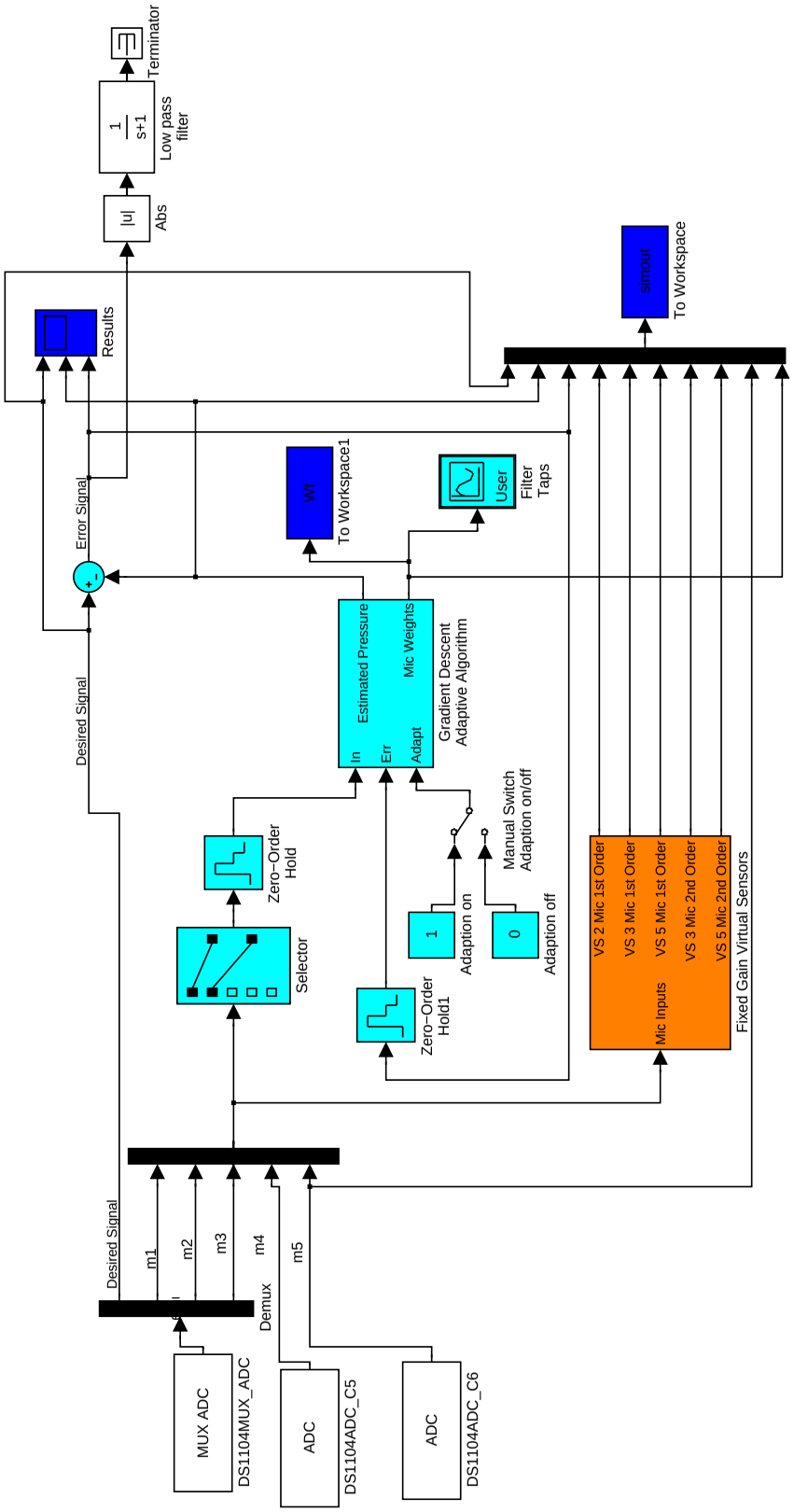

Figure 6.8: Simulink model used in real-time experiments

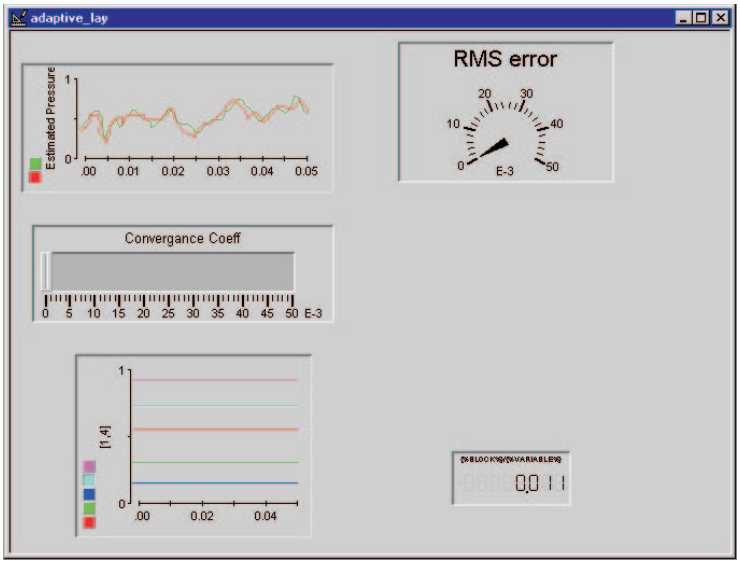

Figure 6.9: Control desk user interface

that the adaptive weights are able to compensate for the phase, location and sensitivity mismatch that occurs between the microphone elements. Figure 6.10(a) shows the control profiles obtained using a two microphone array and the adaptive algorithm. This figure indicates a very high level of attenuation is achieved at all separation distances. Figure 6.10(b) shows the results obtained using a three microphone array with adaptive weights. While this figure indicates a high level of attenuation at all separation distances, the two microphone array produces a slightly higher level of control. The results for the five-element array using optimal weights are shown in Figure 6.10(c). As before this figure shows that a high level of attenuation is realised at all separation distances. However, comparing this figure with figures (b) and (c), it can be seen that increasing the number of microphones beyond two in an adaption process does not improve the level of control realised at the virtual location.

In Figure 6.11 the performance of the fixed weight higher-order virtual microphones is compared with the results of the adaptive virtual microphones. This figure highlights the improved performance of the adaptive virtual microphones especially when using a two microphone array. The excellent performance of the two-element adaptive virtual microphone can be highlighted by comparing its performance with that of the three-element linear virtual microphone

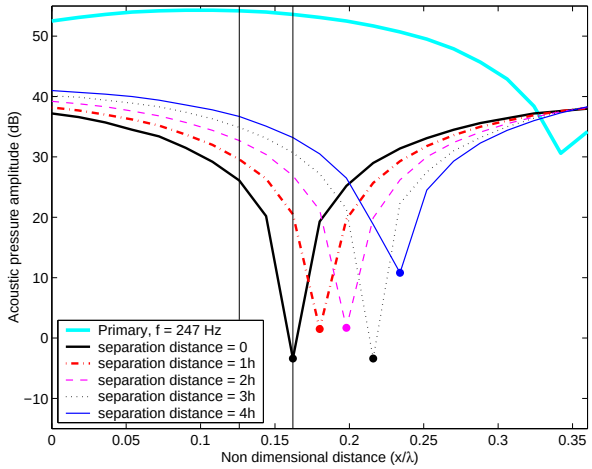

(a) Two microphone

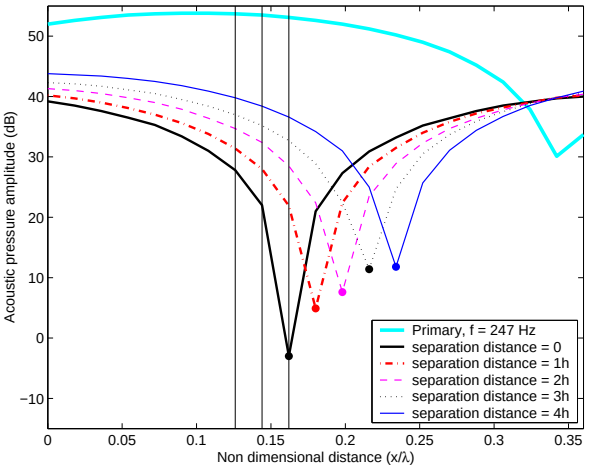

(b) Three microphone

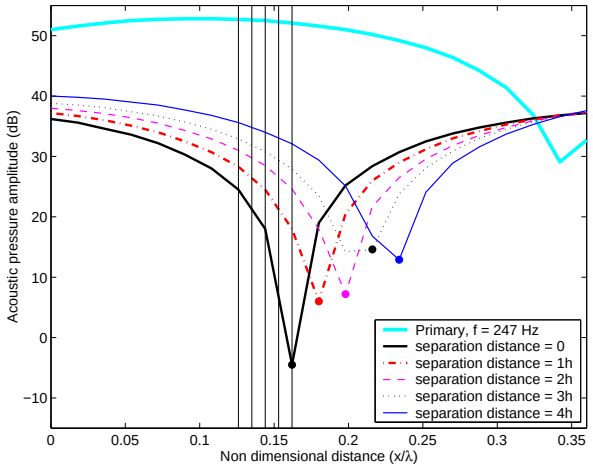

(c) Five microphone

Figure 6.10: Results of real-time control of an acoustic resonance in a rigid duct using adaptive virtual microphones

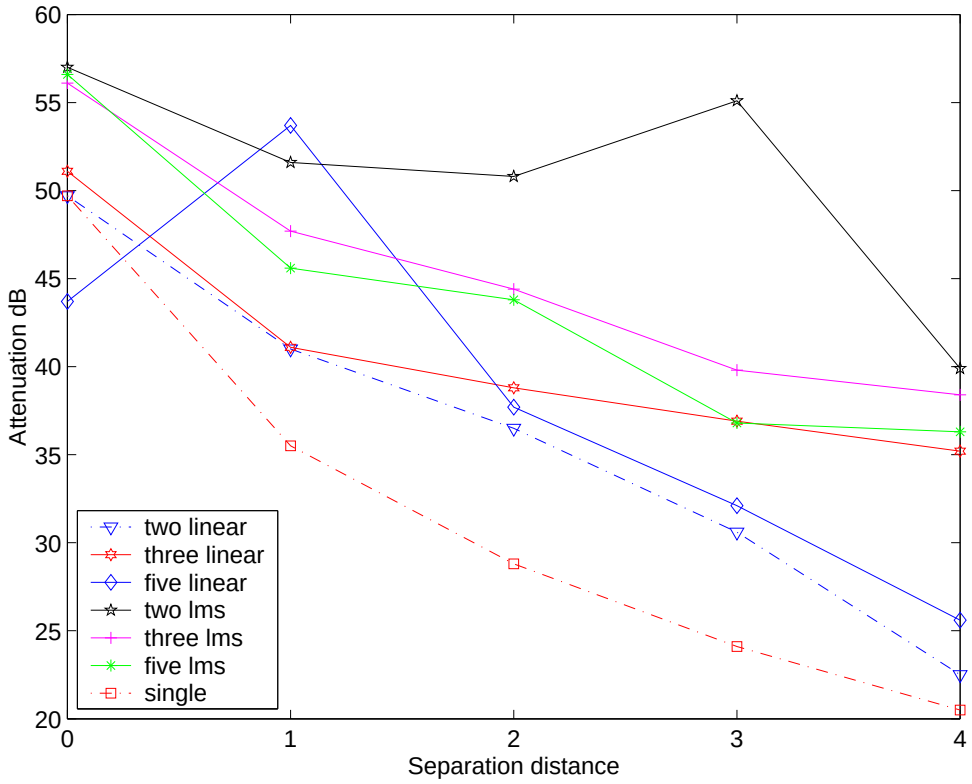

Figure 6.11: A comparison of real-time attenuation achieved using adaptive and linear virtual microphones controlling an acoustic resonance in a rigid duct.

(best of the fixed weight virtual sensors). The figure shows a marked improvement in the level of attenuation achieved for these two virtual sensors. For example: at a separation distance of $3h$, the two-element adaptive virtual microphone produces 24.5 dB additional attenuation compared to the two-element linear virtual microphones.

In addition to the increased level of attenuation achieved, the spatial extent of the 10 dB zone of quiet should also be considered. It is important to know if the zone of quiet produced is of a practical size. The spatial extent of a 10 dB zone of quiet is determined in accordance with the previous chapters (see Chapter 5). The average size of the zone of quiet is 0.27λ, which is the same as for the fixed weights.

Table 6.18 presents the optimum adaptive microphone weights for the rigid one-dimensional waveguide.

		Weights				
	Separation distance	1	2	3	4	5
Two microphone	$0h$	-0.26	-	-	-	0.87
	$1h$	-0.19	-	-	-	1.31
	$2h$	-0.76	-	-	-	1.75
	$3h$	-1.07	-	-	-	2.07
	$4h$	-1.47	-	-	-	2.31
Three microphone	$0h$	-0.84	-	-0.09	-	1.2
	$1h$	-1.1	-	0.6	-	0.94
	$2h$	-1.29	-	1.26	-	0.64
	$3h$	-1.49	-	1.72	-	0.45
	$4h$	-1.79	-	2.06	-	0.36
Five microphone	$0h$	-0.97	-0.25	0.18	0.78	0.86
	$1h$	-1.4	-0.25	0.97	0.78	0.93
	$2h$	-1.69	-0.35	1.75	0.26	1.07
	$3h$	-2.05	-0.46	2.47	-0.13	1.39
	$4h$	-2.36	2.85	-0.39	-0.34	1.52

Table 6.18: Adaptive weights for lightly damped duct

6.5.2.2 Anti-resonance

Figure 6.12 shows the results for the adaptive virtual microphones when controlling an acoustic anti-resonance in a one-dimensional waveguide. Figure 6.12(a) displays the control profile

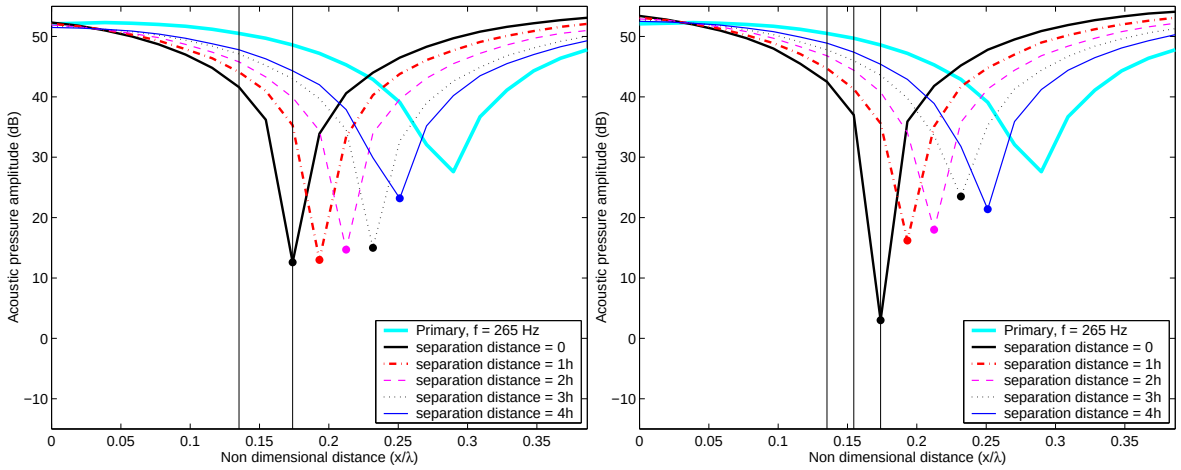

(a) Two microphone *(b) Three microphone*

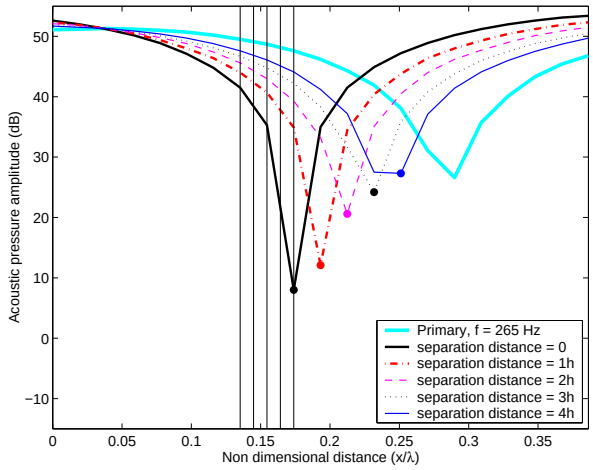

(c) Five microphone

Figure 6.12: Results of real-time control of an acoustic anti-resonance in a rigid duct using adaptive virtual microphones.

achieved using the two-element adaptive virtual microphone. This figure shows that a high level of attenuation is realised at all separation distances. The results for the three-element adaptive virtual microphone are shown in Figure 6.12(b). These results indicate that the adap-

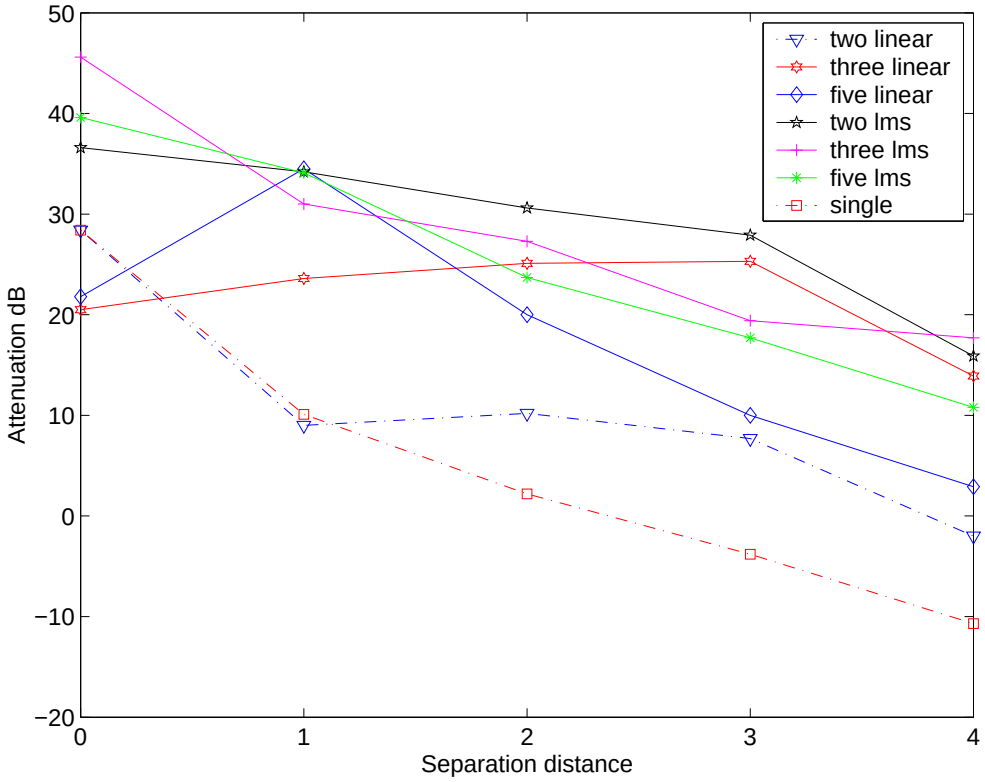

Figure 6.13: A comparison of real-time attenuation achieved using adaptive and linear fixed weight virtual microphones when controlling an acoustic anti-resonance in a rigid duct.

tive weights provided a good estimate of the sound pressure at the virtual location and therefore active control was successful. The control results using a five-element adaptive virtual microphone are presented in Figure 6.12(c). This figure indicates that while the maximum zone of attenuation is centred at the virtual location for all separation distances, the level of attenuation decreases markedly with increasing separation distance.

As before, the attenuation achieved at all separation distances using the adaptive virtual microphone at the anti-resonance frequency is compared with the linear forward-difference virtual microphones in Figure 6.13. This figure shows that the two-element adaptive virtual microphone is superior in this acoustic environment. In general the adaptive virtual microphones produce higher levels of attenuation, although the difference in performance between the two types of virtual sensors is not as distinctive as in the resonance example. At an anti-resonance frequency the potential for attenuation is reduced as many modes contribute to the sound field

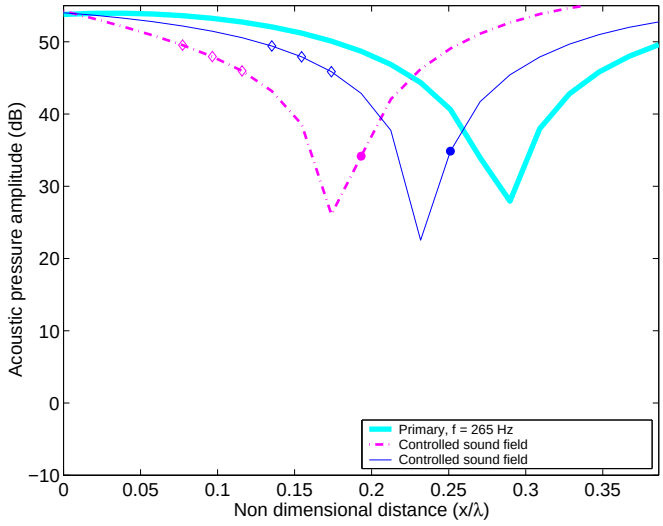

Figure 6.14: Illustration of the effect proximity of pressure node to the size of the zone of quiet. The blue line shows how the level of attenuation is affected by the proximity of the pressure node. The pink dotted line shows the control profile achieved at a larger distance from the pressure node.

rather than being dominated by a single mode as occurs at a resonance. Hence, control of an acoustic anti-resonance does not result in as much attenuation as the control of an acoustic resonance.

The spatial extent of the 10 dB zone of quiet centred around the virtual location was found to be approximately 0.05λ. This represents a very small zone of localised control. However, the size is limited by the close proximity of the virtual location to a pressure node. If the virtual location was located further from a node a larger zone of quiet should be produced. Figure 6.14 shows the control achieved using a three element linear prediction method at a separation distance of $4h$ at varying distances from the pressure node. In both cases the controlled sound field has a similar profile but the one furthest from the node results in a higher level of attenuation. This figure has been produced using simulated control in a one-dimensional waveguide.

6.5.3 Results for a Duct with Absorptive Ends

The investigation of the adaptive virtual microphone in a rigidly terminated duct presented in Section 6.5.2 was repeated for a duct with absorptive end terminations. As with the rigid duct

example, the performance of the adaptive virtual microphone was investigated at a resonance and an anti-resonance frequency.

6.5.3.1 Resonance

The results for the resonance case are presented in Figure 6.15. The noise reduction achieved using the two microphone adaptive virtual sensor is shown in Figure 6.15(a). This figure

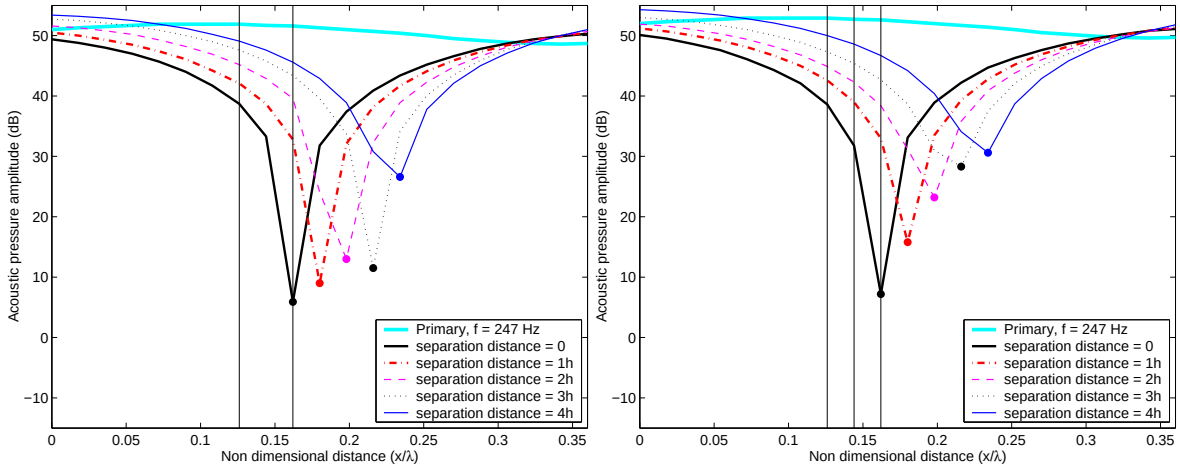

(a) Two microphone *(b) Three microphone*

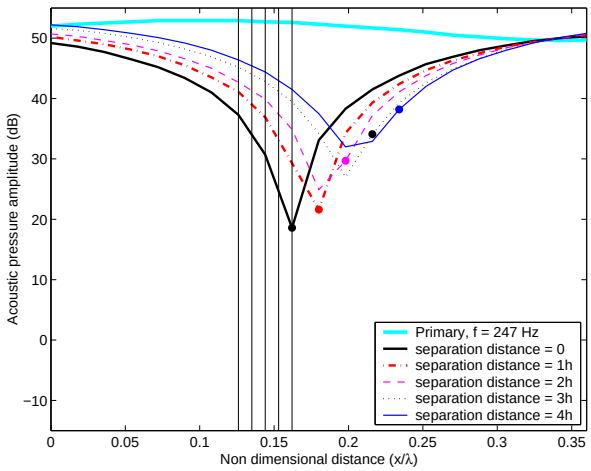

(c) Five microphones

Figure 6.15: Results of real-time control of an acoustic resonance in a duct with absorptive ends using an adaptive virtual microphone.

indicates that a two microphone array produces an accurate estimate of the sound pressure at the virtual location up to a separation distance of 3h. At a separation distance of 4h, the prediction accuracy seems to be reduced, with an almost 20 dB reduction in the amount of attenuation achieved at the virtual location compared with the other separation distances. The three element adaptive virtual sensor achieves an attenuation of 45 dB at 0h which decreases to 20 dB at a separation distance of 4h (see Figure 6.15(b)). The results presented in Figure 6.15(c) again illustrate that adding additional elements over two in the adaptive virtual sensor results in a reduction in the level of attenuation realised.

As with the other examples, the level of attenuation achieved using linear fixed weight virtual microphones is compared with the adaptive virtual sensors in Figure 6.16. This figure again shows that the two-element adaptive sensor is the superior virtual error sensor for all separation distances. The five-element adaptive sensors achieves a similar level of attenuation as the higher-order virtual sensors. These results suggest that the five-element adaption is unable to completely compensate for the experimental errors that corrupt the prediction accuracy.

The localised 10 dB zone of quiet was found to be 0.1λ. For the duct with absorptive ends the size of the zone of quiet is much smaller than in a lightly damped duct at resonance. The potential for noise reduction is significantly reduced in a damped acoustic environment as several modes contribute to the total acoustic response, even at resonance.

Table 6.19 displays the adaptive microphone weights for two, three and five-element arrays at all separation distances in a long narrow duct with absorptive ends.

6.5.3.2 Anti-resonance

Figure 6.17 presents the control profiles achieved using the adaptive virtual microphones to control an acoustic anti-resonance in a one-dimensional waveguide with absorptive ends. Figure 6.17(a) shows results typical of the two-element adaptive virtual microphone; that is, very high levels of attenuation up to a separation distance of 4h, at which point the attenuation

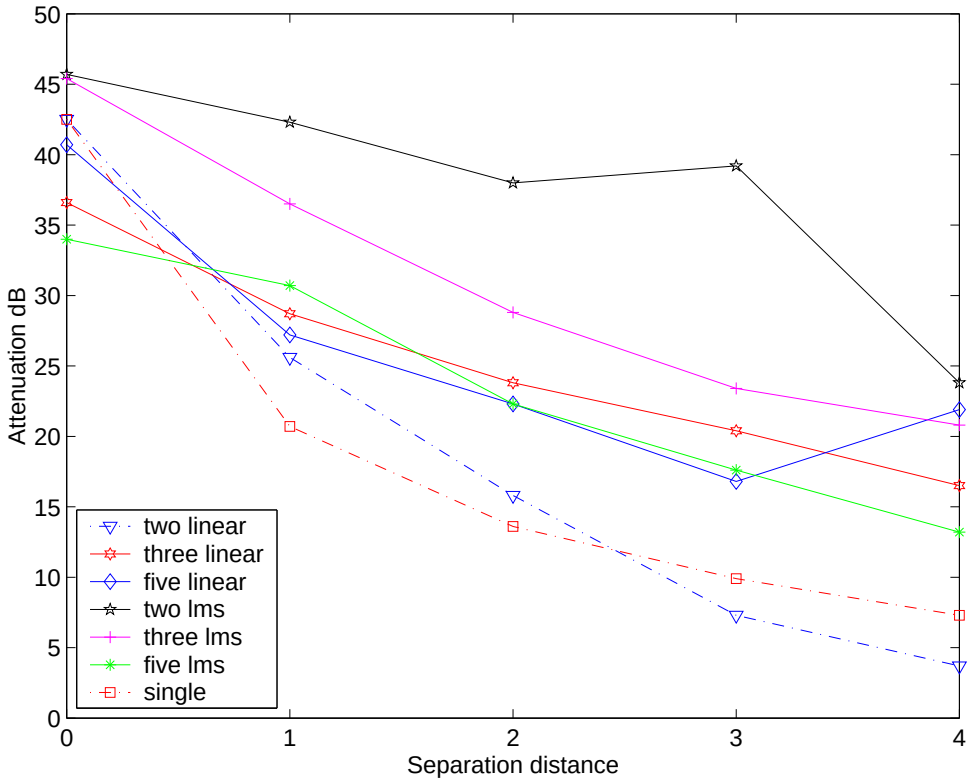

Figure 6.16: A comparison of real-time attenuation achieved using adaptive and linear virtual microphones controlling an acoustic resonance in a duct with absorptive ends.

		Weights				
	Separation distance	1	2	3	4	5
Two microphone	0h	-0.09	-	-	-	1.22
	1h	-0.56	-	-	-	1.64
	2h	-1.07	-	-	-	2.09
	3h	-1.42	-	-	-	2.35
	4h	-1.56	-	-	-	2.39
Three microphone	0h	-0.97	-	-0.09	-	1.24
	1h	-1.44	-	0.5	-	1.16
	2h	-1.86	-	0.77	-	1.22
	3h	-2.21	-	0.9	-	1.28
	4h	-2.61	-	1.05	-	1.36
Five microphone	0h	-1.15	-0.5	0.48	1.06	0.67
	1h	-1.6	-0.7	1.03	1.15	0.67
	2h	-1.76	-1.12	1.67	1.31	0.55
	3h	-2.0	-1.49	2.06	1.53	0.47
	4h	-2.2	-1.83	2.5	1.62	0.55

Table 6.19: Adaptive weights for damped one-dimensional waveguide

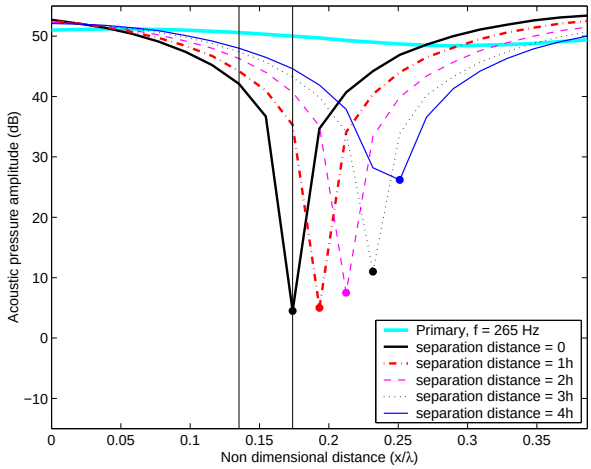

(a) Two microphone

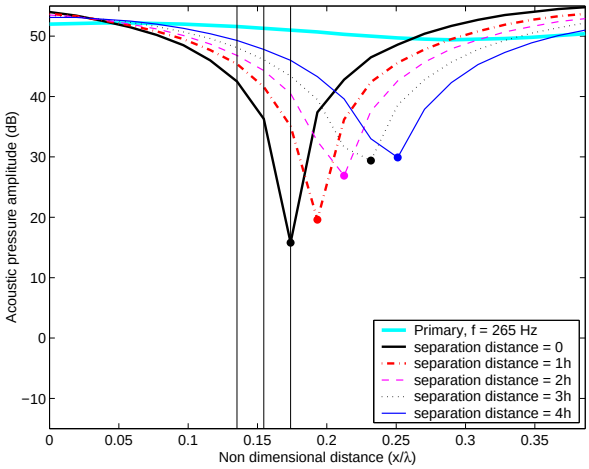

(b) Three microphone

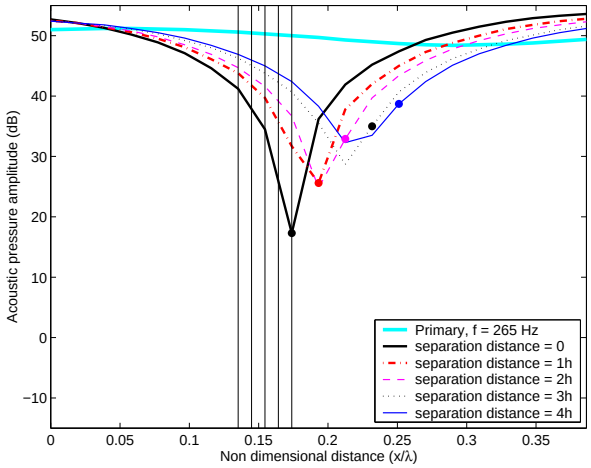

(c) Five microphone

Figure 6.17: Results of real-time control of an acoustic anti-resonance in a duct with absorptive ends using adaptive virtual microphones.

drops by up to 20 dB. The control results achieved using the three-element adaptive virtual microphone are presented in Figure 6.17(b). This figure indicates that the three-element adaptive virtual sensor is capable of producing a zone of quiet at all virtual locations although the level of control decreases with increasing separation distance. Once again the result produced using the five-element adaptive virtual microphone is quite disappointing compared to the other adaptive virtual microphones (see Figure 6.17(c)). This figure shows poor attenuation levels compared to the other adaptive virtual microphones. Also the zone of quiet is not centred around the virtual location for separation distances larger than h.

Figure 6.18 compares the control results achieved at all separation distances for the linear fixed weight and adaptive virtual microphones. This figure shows that again the two-element adaptive virtual microphone is the best predictor of sound pressure level at the virtual location which corresponds to a high level of attenuation. All of the other virtual microphones achieve fairly similar levels of attenuation. The three-element linear virtual microphone produces slightly higher levels of attenuation than the five-element adaptive virtual microphone, clearly indicating that increasing the number of elements in adaptive virtual microphone arrays decreases prediction performance.

The extent of the 10 dB zone of quiet situated at the virtual location is 0.07λ.

The adaptive weights are shown in Table 6.19. Since the adaption process is carried out using broadband noise, the adaptive microphone weights for the anti-resonance frequency are the same as for the resonance frequency in the duct with absorptive ends.

6.6 Conclusions

The work in this chapter examined the use of an adaptive virtual microphone consisting of two, three or five-element prediction arrays in a one-dimensional waveguide. The analysis of the adaptive virtual microphone was two-fold; numerical and experimental. For the numerical

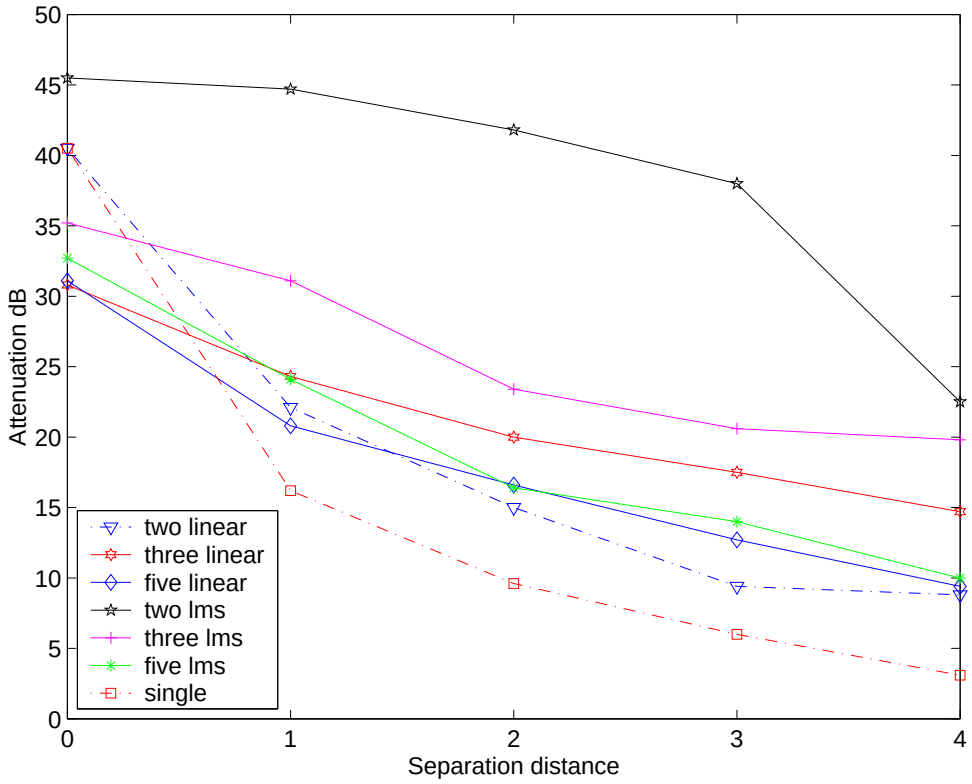

Figure 6.18: A comparison of real-time attenuation achieved using adaptive and linear virtual microphones controlling an acoustic anti-resonance in a duct with absorptive ends.

work, a SIMULINK model was used to assess the capacity of the adaptive virtual microphone to accommodate errors due to phase, sensitivity and position mismatch between sensing elements. It has been shown that the adaptive virtual microphone is able to compensate completely for sensitivity and position errors and partially compensate for phase mismatch errors. The simulated work also investigated the effect of higher-order modes in the acoustic fields on the prediction accuracy of the sound pressure at the virtual location. Three acoustic models were used: the first used the first four axial modes; the second incorporated all axial modes up to cut-on; and the third introduced cross-modes. This work showed that the cross modes have little effect on the prediction accuracy of the fixed weight and adaptive virtual microphones. However, the inclusion of the 23 axial modes up to cut-on increased the normalised mean squared error considerably. Although spatial aliasing is not occurring in this model, the shorter wavelengths in the axial direction clearly diminished the prediction accuracy of the virtual error sensors. The presence of cross modes in the acoustic model resulted in smaller values of normalised mean squared error than in the presence of all modes up to cut on. This result suggests that the number of modes included in the axial direction has the greatest impact on the accuracy on the sound pressure level prediction at the virtual location of the virtual microphones. This is not surprising as the microphone array was one-dimensional and operated in the axial direction.

The experimental work incorporated the use of real-time control in a real duct using the SIMULINK model and a dSpace board. In a real-time control scenario, the adaptive virtual microphones certainly are able to overcome some of the errors that affect the performance of the fixed weight virtual microphones. In almost all the examples presented here, the zone of quiet was centred around the virtual location. Results indicated that using a two-element prediction array produced the highest levels of attenuation.

The real-time performance of the five-element adaptive virtual microphone was contrary to the results of the SIMULINK model. In the SIMULINK model the use of the five-element adaptive virtual microphone resulted in a reduced NRMS error compared to that obtained using

the other adaptive virtual microphones. Therefore it was anticipated that in the real-time control scenario that the five-element adaptive virtual microphone may perform better than the other adaptive virtual microphones. However, this was not the case as the five-element adaptive virtual microphone produced considerably lower levels of attenuation than the two and three-element adaptive virtual microphones. This indicates that the adaptive LMS algorithm is unable to compensate for the errors associated with the five elements in the prediction array in a practical situation.

It has been shown using both simulated and experimental results that the use of the adaptive virtual microphone can greatly improve the performance of the forward-difference virtual microphones.

Chapter 7

Comparison with the Transfer Function Virtual Microphone Formulation

7.1 Introduction

The first virtual microphone formulation was developed by Elliott and David (1992) and investigated extensively by Garcia-Bonito et al. (1996) and Garcia-Bonito et al. (1997b). This method is significantly different than the forward-difference virtual microphones investigated in this thesis. The method employed by Elliott and David (1992) used a single permanently-located microphone and a temporarily-placed microphone at the intended virtual microphone location. A number of transfer functions were measured between the secondary source and the permanently and temporarily placed microphones and these, in addition to the signal from the permanent microphone, were used to create the virtual microphone. The virtual microphone developed by Elliott and David (1992) will be called the transfer function virtual microphone in this chapter to differentiate it from the virtual microphones that are the subject of this thesis.

In this chapter the performance of the three-element linear virtual microphone and the three-element adaptive virtual microphone will be compared with the transfer function method using

theoretically derived transfer functions. Control has been simulated in both the reactive sound field of the one-dimensional waveguide and the free field. Real-time application of the transfer function virtual microphone method is quite complicated as taps are required and consequently it was not investigated here; rather the investigation here is limited to simulations. The transfer function virtual microphone is not affected by phase and sensitivity mismatch as only a single microphone can be used in this method. Therefore the performance of the virtual microphone and the three-element linear virtual microphone will be compared in both an error free environment, and with errors incorporated into the simulation. For the case with the errors present, the performance of the three-element adaptive LMS virtual microphone will also be assessed.

7.2 The Transfer Function Virtual Microphone

The theory of the transfer function virtual microphone is presented here. The total pressure at a microphone at location, x during active control is given by (Elliott and David, 1992)

$$p(x) = p_p(x) + Zq \tag{7.1}$$

where $p_p(x)$ is the primary or uncontrolled pressure, Z is the transfer impedence between the secondary source and the microphone and q is the secondary source control strength.

The microphone temporarily located at the virtual location, x_v has a similar equation to Equation 7.1 for the total pressure:

$$p_v(x_v) = p_p(x_v) + Z_v q \tag{7.2}$$

where $p_p(x_v)$ is the primary field pressure measured using the microphone located at the virtual location and Z_v is the transfer function measured between the secondary source and the microphone at the virtual location. Garcia-Bonito et al. (1997b) assume that the pressure at x due to the primary sound field and the pressure at the virtual location due to the primary sound field are approximately equal, ie. $p_p(x) \approx p_p(x_v)$ because at low frequencies the spatial rate of

change of the primary field will be low. Therefore using Equations (7.1) and (7.2), the pressure at the virtual location can be estimated as follows:

$$\widehat{p_v}(x_v) = p(x) - (Z - Z_v)\, q \tag{7.3}$$

7.3 The LMS Virtual Microphone

For this performance comparison the adaptive virtual microphone was implemented using the following method in MATLAB. The sound pressure at the virtual location is calculated using the following equation:

$$p_v = \mathbf{W}\mathbf{p}_3 \tag{7.4}$$

where $\mathbf{W}$ is row vector of the three optimal weights, $\mathbf{p}_3$ is the vector of measured pressure at the three microphones of the prediction array. Splitting Equation 7.4 into real and imaginary parts yields:

$$\begin{aligned}\begin{bmatrix} \mathbf{Re}(p_v) & \mathbf{Im}(p_v) \end{bmatrix} = & \begin{bmatrix} W_1 & W_3 & W_5 \end{bmatrix} \mathbf{Re}\left(\begin{bmatrix} p_1 \\ p_3 \\ p_5 \end{bmatrix} \right) \\ & + \begin{bmatrix} W_1 & W_3 & W_5 \end{bmatrix} \mathbf{Im}\left(\begin{bmatrix} p_1 \\ p_3 \\ p_5 \end{bmatrix} \right)\end{aligned} \tag{7.5}$$

Equation 7.5 can be rewritten as:

$$\mathbf{p}_v = \mathbf{W}\mathbf{P}_3 \tag{7.6}$$

where $\mathbf{p}_v = \begin{bmatrix} \mathbf{Re}(p_v) & \mathbf{Im}(p_v) \end{bmatrix}$ and $\mathbf{P}_3 = \begin{bmatrix} \mathbf{Re}\begin{pmatrix} p_1 \\ p_3 \\ p_5 \end{pmatrix}, \mathbf{Im}\begin{pmatrix} p_1 \\ p_3 \\ p_5 \end{pmatrix} \end{bmatrix}$

Splitting Equation 7.6 into real and imaginary parts enables a real solution for the optimal weights to be obtained as would occur in real-time experiments. The optimal weights, $\mathbf{W}$ were calculated by taking the pseudo inverse of $\mathbf{P}_3$.

$$\mathbf{W} = \mathbf{p}_v \mathbf{P}_3^{-1} \tag{7.7}$$

The optimal weights were calculated at a single frequency and not over a broad frequency range as was done in Chapter 7 with the SIMULINK simulation.

7.4 Method

Two sound fields were considered, namely a one-dimensional waveguide and a free field. Using the analytical model of the one-dimensional waveguide detailed in Chapter 3, the performance of the three-element linear virtual microphone is compared with the transfer function virtual microphone. The three-element linear virtual microphone was selected as it has consistently proved to be the most robust of the forward-difference virtual microphones in the presence of experimental error. The same four acoustic conditions from Chapter 3 were used; an acoustic resonance and anti-resonance with both rigid and damped terminations. The arrangement of the modelled system was identical to that described in Chapter 3.

The free field was modelled using the analytical expression, Equation 5.14, described in Chapter 5. The physical system modelled for this analysis is the same as the system modelled in Chapter 5. Two frequencies were used in the free field evaluations namely 200Hz and 400 Hz. As this performance comparison is off-line, quadratic optimisation was used to simulate control for all cases.

The errors incorporated into the simulation were a 2° phase mismatch and a 4% sensitivity error across the three microphones.

7.5 Simulations in the Absence of Measurement Errors

This section compares the performance of the transfer function virtual microphone and the three-element linear virtual microphone in the one-dimensional waveguide and the free field with no introduced errors.

7.5.1 Results for Rigidly Terminated Duct

7.5.1.1 Resonance

Figure 7.1 compares the performance of the three-element linear forward-difference virtual microphone with the transfer function virtual microphone in a one-dimensional waveguide when controlling a resonance frequency of the seventh axial mode. The top curve represents the primary or uncontrolled sound field. The other lines indicate the controlled sound field achieved with the virtual microphones. The circles indicate the virtual location and the diamonds represent the physical locations of the prediction microphones. Figure 7.1(a) depicts the uncontrolled and the controlled sound fields produced using the virtual microphones predicting at a separation distance of h. The transfer function virtual microphone produces a broad zone of attenuation of 10-15 dB. The forward-difference virtual microphone achieves at least the same amount of attenuation but at the virtual location the level of attenuation increases to 40 dB. Figure 7.1(b) illustrates the control results with the separation distance increased from h to $4h$. The performance of the transfer function virtual microphone has markedly reduced as the separation distance has increased, achieving only 5 dB attenuation at $4h$. By contrast, the forward-difference virtual microphone achieves 40 dB attenuation at a separation distance of

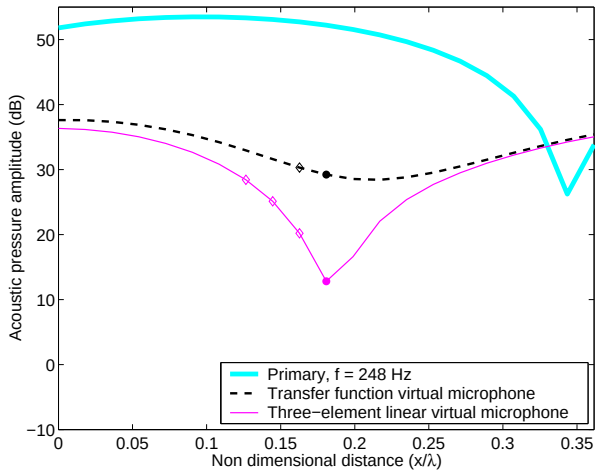

(a) Separation distance- h

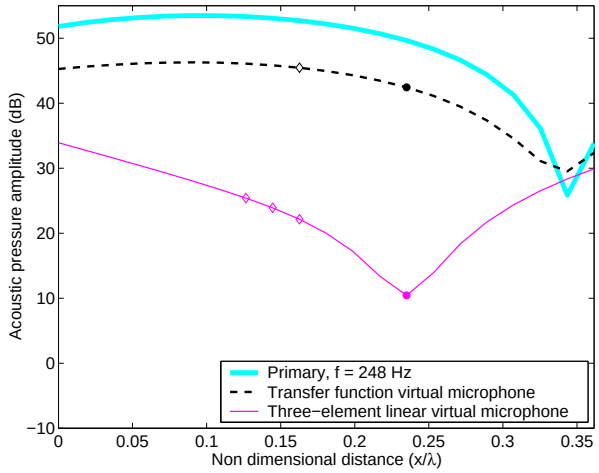

(b) Separation distance - 4h

Figure 7.1: Performance comparison between forward-difference and transfer function virtual microphones in a one-dimensional waveguide for control of an acoustic resonance. The circles indicate the virtual location and the diamonds represent the location of the prediction microphones.

4h. The poor performance of the transfer function virtual microphone could be a result of the invalid assumption that the pressure at the permanent microphone location due to the primary sound field is equal to that at the virtual microphone location. In a reactive sound field, at a separation distance of 100 mm and a frequency of 248 Hz this assumption is unlikely to hold.

7.5.1.2 Anti-resonance

The effectiveness of the two different virtual microphone formulations were also assessed in a rigid duct at an acoustic anti-resonance frequency of 267 Hz. This acoustic environment differs from the resonant sound field in that many modes contribute to the resultant sound field, whereas in a resonant field a single mode dominates the response. Figure 7.2(a) shows the results for the two virtual microphones for a separation distance of h. The transfer function virtual microphone produces 15 dB of attenuation at the virtual location while the forward-difference virtual microphone achieves 28 dB at the same location. The results for a separation distance of 4h are displayed in Figure 7.2(b). At a separation distance of 4h, the use of the transfer function virtual microphone results in an increase of the primary sound field at the virtual location. Again, the poor performance of the transfer function virtual microphone can be attributed to the incorrect assumption that $p_p \approx p_{p_v}$. The use of the forward-difference virtual microphone results in attenuation of around 2 dB at the virtual location.

7.5.2 Results for a Duct with Absorptive Ends

7.5.2.1 Resonance

Figures 7.3(a) and (b) show the results obtained when controlling an acoustic resonance in a duct with absorptive ends at separation distances of h and 4h respectively. In Figure 7.3(a), the transfer function virtual microphone produces the maximum attenuation of 22 dB at the virtual location. The use of the forward-difference virtual microphone results in 35 dB of

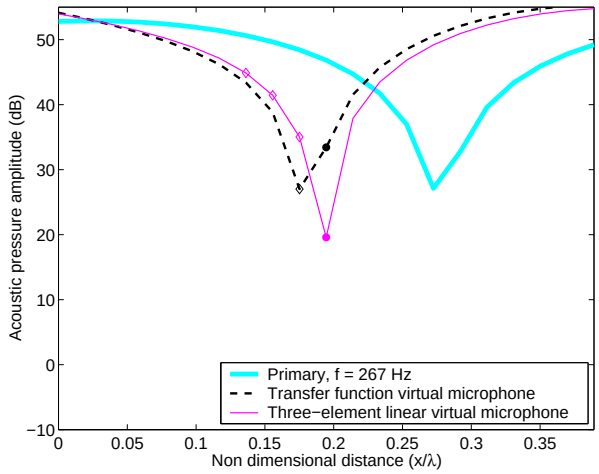

(a) Separation distance - h

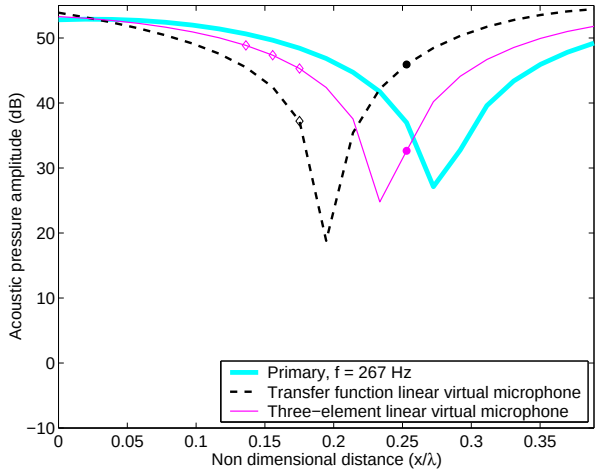

(b) Separation distance - 4h

Figure 7.2: Performance comparison between forward-difference and transfer function virtual microphones in a one-dimensional waveguide for the control of an acoustic anti-resonance. The circles indicate the location of the virtual microphone and the diamonds indicate the location of the prediction microphones.

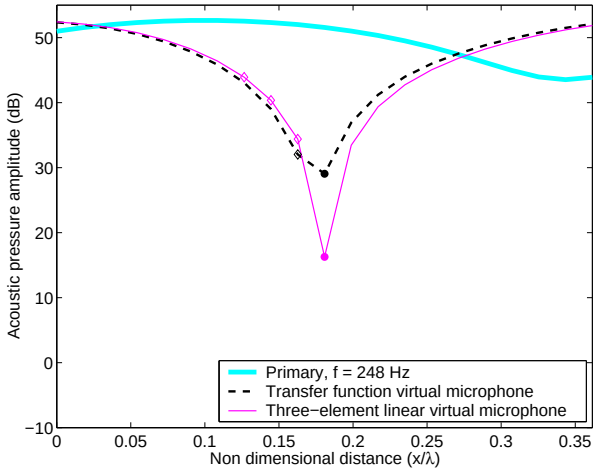

(a) Separation distance - h

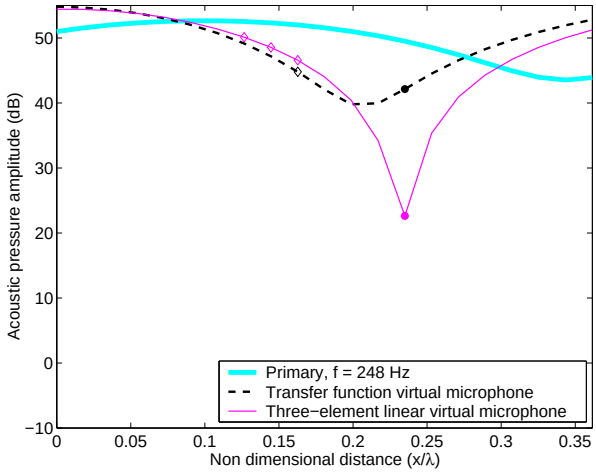

(b) Separation distance - 4h

Figure 7.3: Performance comparison between forward-difference and transfer function virtual microphones in a one-dimensional waveguide with absorptive ends controlling an acoustic resonance. The circles indicate the location of the virtual microphone and the diamonds represent the location of the prediction microphones.

attenuation at the virtual location. Once again the performance of the transfer function virtual microphone reduces notably with increasing separation distance. With the virtual microphone located $4h$ away from the permanent remote microphone, the use of the transfer function virtual microphone results in only 8 dB of attenuation (see Figure 7.3(b)). At the same separation distance the forward-difference virtual microphone results in 28 dB attenuation.

7.5.3 Anti-resonance

The results obtained when controlling an acoustic anti-resonance using transfer function and forward-difference virtual microphones in a duct with absorptive ends are presented in Figure 7.4. Figure 7.4(a) presents the control profiles for the two virtual microphone formulations attempting to produce a zone of quiet at a separation distance of h. The transfer function virtual microphone achieves 15 dB of attenuation at the virtual location, while the forward-difference virtual microphone produces of 33 dB attenuation. The results obtained with the virtual location at a separation distance of $4h$ are presented in Figure 7.4(b). The use of the transfer function virtual microphone results in a small increase in the sound pressure level at the virtual location. The forward-difference virtual microphone results in 15 dB of attenuation at a separation distance of $4h$.

7.5.4 Results for a Free Field

The performance of the transfer function virtual microphone was compared to that of the three-element linear virtual microphone in a free field. It was thought that the transfer function virtual microphone would perform better in this acoustic environment because in the far field the spatial rate of change in the pressure field is low and therefore the assumption of $p_p \approx p_{p_v}$ is more valid.

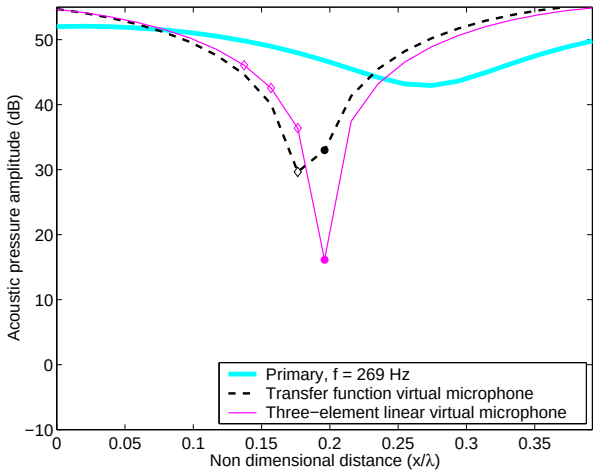

(a) Separation distance - h

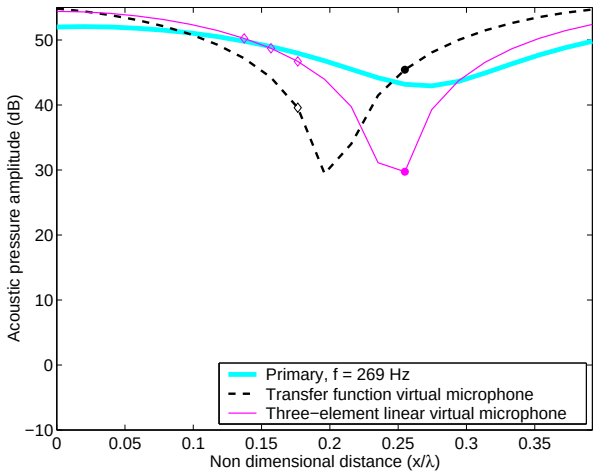

(b) Separation distance - 4h

Figure 7.4: Performance comparison between forward-difference and transfer function virtual microphones in a one-dimensional waveguide with absorptive ends for control of an acoustic anti-resonance. The circles indicate the location of the virtual microphone and the diamonds indicate the location of the prediction microphones.

7.5.4.1 200 Hz

Figure 7.5 presents the results obtained when controlling a 200 Hz tone in a free field using the transfer function and the forward-difference virtual microphones. At a separation distance of h, the transfer function virtual microphone achieves 28 dB attenuation and the forward-difference virtual microphone achieves 40 dB attenuation (see Figure 7.5(a)). The effective attenuation achieved with the transfer function virtual microphone in a free field is a result of low rate of spatial variation in the primary field, especially when compared to that of a reactive field. Figure 7.5(b) shows the results with the separation distance between the permanent microphone and the virtual microphone increased from h to $4h$. The forward-difference virtual microphone outperforms the transfer function virtual microphone by 17 dB attenuation at $4h$.

7.5.4.2 400 Hz

Figure 7.6 illustrates the results obtained when controlling a 400 Hz tone in the free field with transfer function and forward-difference virtual microphones. Figure 7.6(a) shows the control results with the virtual microphone located h away from the prediction microphones. The transfer function virtual microphone produces 25 dB attenuation at the virtual location while the forward-difference virtual microphone produces an extra 15 dB attenuation at the virtual location. The separation distance was then increased to $4h$ and the results of virtual control at this location are presented in Figure 7.6(b). These results indicate that increasing the separation distance from 25 mm to 100 mm results in a decrease in the amount of attenuation achieved for both types of virtual microphone. The transfer function virtual microphone produces 3 dB attenuation at the virtual microphone location and the forward-difference virtual microphone achieves 9 dB attenuation at the same position.

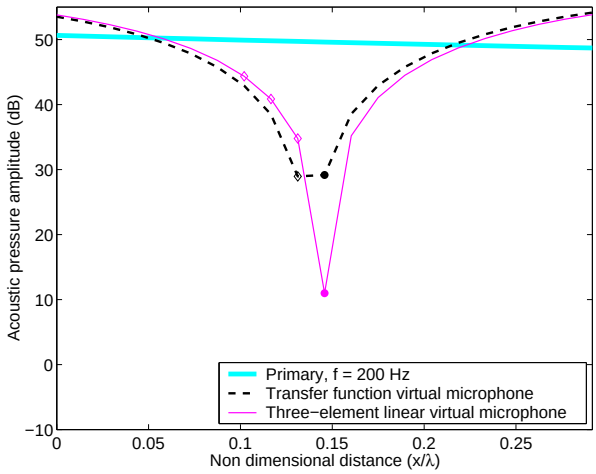

(a) Separation distance - h

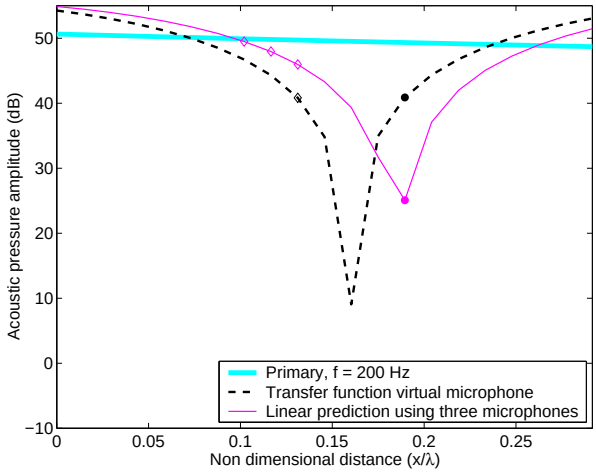

(b) Separation distance - 4h

Figure 7.5: Performance comparison between forward-difference and transfer function virtual microphones in a free field at 200 Hz. The circles indicate the location of the virtual microphone and the diamonds represent the location of the prediction microphones.

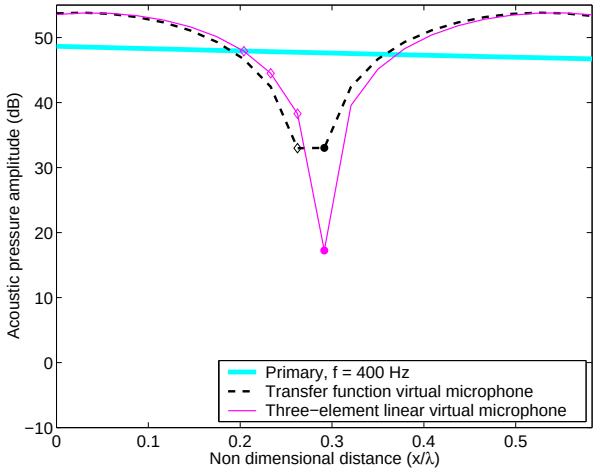

(a) Separation distance - h

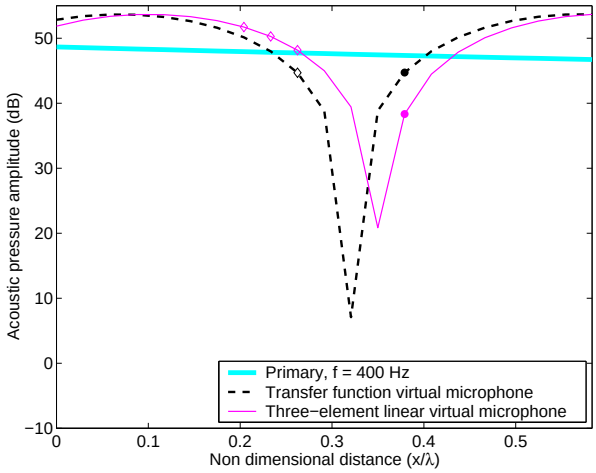

(b) Separation distance - 4h

Figure 7.6: Performance comparison between forward-difference and transfer function virtual microphones in a free field at 400 Hz. The circles indicate the location of the virtual microphone and the diamonds represent the location of the prediction microphones.

7.5.5 Discussion

The transfer function virtual microphone is based on the assumption that the primary pressure at the permanent microphone and the virtual location are approximately equal. This assumption becomes increasingly inaccurate as the frequency of the excitation is increased or as the separation distance between the permanent and virtual microphones is increased. Table 7.1 presents a comparison of attenuation achieved at various frequencies using the transfer function virtual microphone and the three-element linear virtual microphone in the free field. Results presented in Chapter 5 showed that the quadratic virtual microphone produces higher levels of attenuation than the linear virtual microphone in error free simulations. Since the results presented in Table 7.1 show that the linear virtual microphone out-performs the transfer function virtual microphone, it can be assumed that the quadratic virtual microphone would produce higher levels of attenuation and the comparison is unnecessary. The results presented in Table 7.1 illustrate the deficiencies of the transfer function virtual microphone at higher frequencies and with large separation distances. At 600 Hz and at a separation distance of $4h$, the transfer function virtual microphone produces 1 dB gain. This is not unexpected as the assumption $p_p \approx p_{p_v}$ is not very accurate at separation distances that are a significant fraction of the wavelength. However, the performance of the forward-difference virtual microphone also degrades with increasing frequency and separation distance but not as markedly as the transfer function virtual microphone.

	Transfer Function		Forward-difference	
	h	$4h$	h	$4h$
100 Hz	26 dB	20 dB	40 dB	36 dB
200 Hz	21 dB	15 dB	40 dB	25 dB
400 Hz	15 dB	3 dB	30 dB	9 dB
600 Hz	10 dB	-1 dB	20 dB	2 dB

Table 7.1: Attenuation in a free field using the transfer function and forward-difference virtual microphones at different frequencies.

Garcia-Bonito et al. (1997b) presented the results of their transfer function virtual microphone control simulation in two-dimensional plots for various frequencies ranging from 100 Hz to 1000 Hz. The physical set-up for the control source and the sensing microphone and the location of the virtual microphone is quite different from the set-up presented here. However, despite the differences, comparisons can be drawn between the performance of the transfer function virtual microphone results presented here and those presented by Garcia-Bonito et al. (1997b). In Garcia-Bonito et al.'s (1997b) work the separation distance between the sensing microphone and the virtual microphone location is approximately 0.07 m which is approximately half way between h and $4h$ for the experiments presented here. The results presented by Garcia-Bonito et al. (1997b) indicate that at around 100 Hz, an attenuation of at least 20 dB is achieved at the virtual location. From the results presented in Table 7.1 which show an attenuation at 100 Hz of 26 dB and 20 dB at separation distance of h and $4h$ respectively. This suggests that the results presented here and previous published results are in agreement. This frequency was presented as an example of the agreement between the two results, however the agreement does exist at other frequencies. Kestell (2000) also presented a performance comparison between the forward-difference virtual microphones and the transfer function virtual microphones. Control was implemented using post-processed experimental data measured within a mock aircraft cabin and the distance between the virtual location and the permanent remote microphone was 0.05m. The results presented showed that the transfer function virtual microphone achieved 38 dB attenuation at the virtual location compared with 7 dB and 13 dB achieved using the quadratic and linear virtual microphones respectively at 254 Hz. Garcia-Bonito et al. (1997b) presented results at 250 Hz which showed an attenuation of just 10 dB at the virtual location. Although the experimental set-ups of Garcia-Bonito et al. (1997b) and Kestell (2000) were quite different, one would expect the level of attenuation achieved to be similar for both cases. The reason for the discrepancy is not known.

7.6 Comparison with Errors Present

In this section the performance of the transfer function virtual microphone, the three-element linear virtual microphone and the three-element adaptive virtual microphone will be considered with phase and sensitivity errors incorporated into the simulation. The presence of these errors will influence the performance of the three-element linear virtual microphone while the transfer function virtual microphone is unaffected by these introduced errors because a single microphone can be used for the prediction. The adaptive virtual microphone should be able to at least partly compensate for the introduced errors.

7.6.1 Results for Rigidly Terminated Duct

7.6.1.1 Resonance

Figure 7.7 presents the results obtained using the transfer function, three-element linear and the adaptive virtual microphones when controlling an acoustic resonance in the presence of phase and sensitivity errors. Figure 7.7(a) shows the control profiles achieved when controlling at a separation distance of h. The three-element linear virtual microphone is shown to be slightly affected by the errors reducing the attenuation from 40 dB (see Figure 7.1(a)) to 36 dB at the virtual location. Even though the three-element linear virtual microphone is affected by the introduced errors, it still out-performs the transfer function virtual microphone which is unaffected by the errors. The adaptive virtual microphone achieves 40 dB of attenuation at the virtual location. Figure 7.7(b) shows the results obtained when the separation distance is increased from h to $4h$. At the larger separation distance the performance of the three-element linear virtual microphone is more influenced by the errors, with the level of attenuation reducing to 20 dB from 40 dB (compare with Figure 7.1(b)), which is still significantly greater than is achieved using the transfer function virtual microphone. The adaptive virtual microphone achieves 25 dB of attenuation at the virtual location. Using the method described in Section

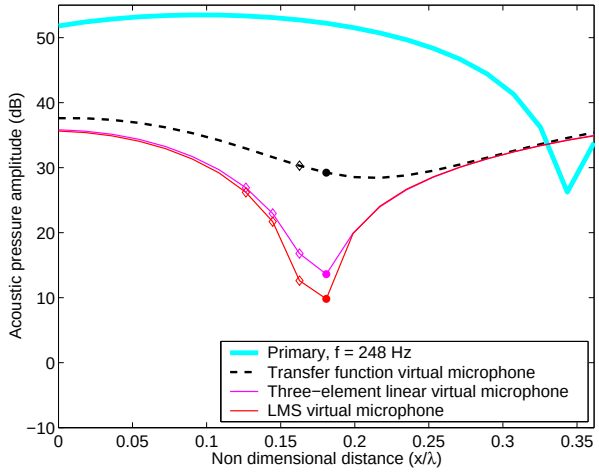

(a) Separation distance - h

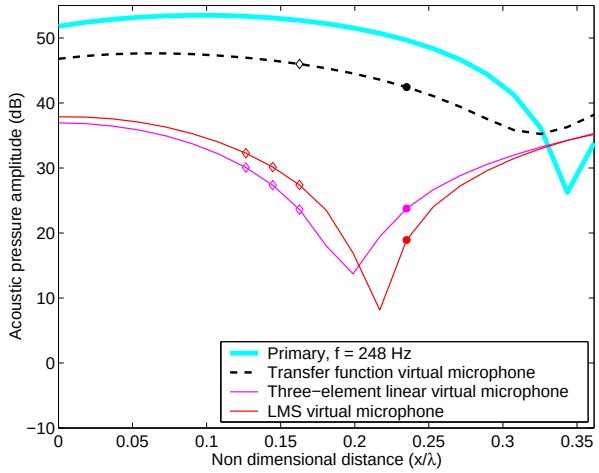

(b) Separation distance - 4h

Figure 7.7: Performance comparison between adaptive, forward-difference and transfer function virtual microphones in a one-dimensional waveguide for control of an acoustic resonance in the presence of errors. The circles indicate the virtual location and the diamonds represent the location of the prediction microphones.

7.3 to calculate the optimal weights at a single frequency, the prediction of the primary pressure at the virtual location will be exact but the estimation of the transfer function between the secondary source and the virtual microphone will not. At the larger separation distances the estimation of the secondary transfer function will degrade, resulting in lower levels of attenuation. The results presented here again highlight the poor performance of the transfer function virtual microphone in the reactive environment where the spatial rate of change of the acoustic pressure amplitude is high. This is because the assumption upon which this formulation is based is no longer valid.

7.6.1.2 Anti-resonance

Figures 7.8(a) and (b) show the results obtained when controlling an acoustic anti-resonance in a one-dimensional waveguide at separation distances of h and $4h$ respectively. In Figure 7.8(a), the three-element linear virtual microphone produces just 17 dB of attenuation at the virtual location and the transfer function virtual microphone achieves 15 dB attenuation. The adaptive virtual microphone produces 24 dB of attenuation at the location of the virtual microphone. Figure 7.8(b) illustrates the poor performance of all three virtual microphone formulations at a separation distance of $4h$, as the implementation of the virtual microphones results in an increase in the sound pressure level at the virtual location. In the presence of the introduced errors, the performance of the three-element linear virtual microphone reduces to that of the transfer function virtual microphone and results in an increase in the primary field of approximately 10 dB. The use of the adaptive virtual microphone results in an increase of the primary field of 2 dB at a separation distance of $4h$.

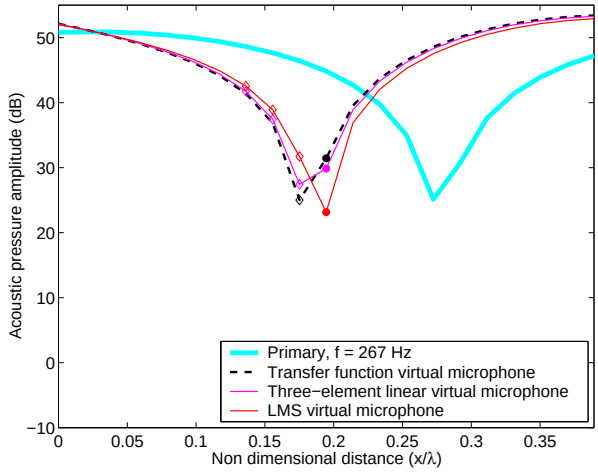

(a) Separation distance - h

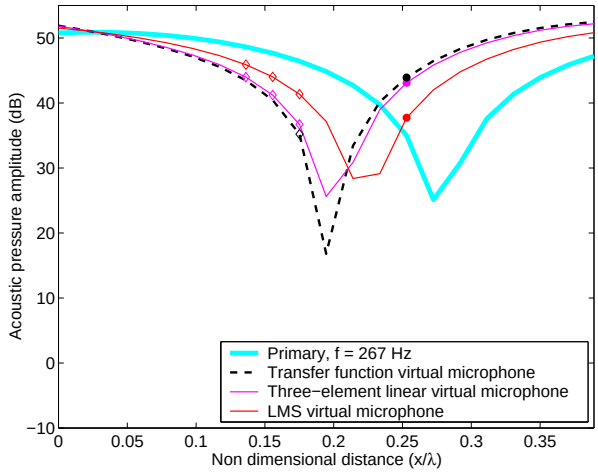

(b) Sepapration distance - 4h

Figure 7.8: Performance comparison between adaptive, forward-difference and transfer function virtual microphones in a one-dimensional waveguide for control of an acoustic anti-resonance in the presence of errors. The circles indicate the virtual location and the diamonds represent the location of the prediction microphones.

7.6.2 Results for Duct with Absorptive Ends

7.6.2.1 Resonance

The performances of the three different virtual microphone formulations were assessed in a one dimensional waveguide with absorptive ends at an acoustic resonance. Figure 7.9(a) presents the results at a separation distance of h. In the presence of phase and sensitivity errors the performance of the three-element linear virtual microphone is markedly reduced, producing a similar level of attenuation as is achieved using the transfer function virtual microphone. Figure 7.9(a) shows that the adaptive virtual microphone produces 30 dB of attenuation at a separation distance of $1h$. Figure 7.9(b) presents the results for the increased separation distance of $4h$. Once again, the presence of the errors has reduced the level of attenuation achieved using the three-element linear virtual microphone to be equivalent to that achieved using the transfer function virtual microphone. With the distance between the virtual microphone and the permanent remote microphone set to $4h$, the use of the transfer function virtual microphone results in 8 dB of attenuation and the use of the three-element linear virtual microphones results in 9 dB of attenuation. The adaptive virtual microphone produces 18 dB of attenuation at a separation of $4h$.

7.6.2.2 Anti-resonance

Figure 7.10 presents a performance comparison between the three-element linear virtual microphone, transfer function virtual microphone and the adaptive virtual microphone when controlling an anti-resonance in a one-dimensional waveguide with absorptive ends. Figure 7.10(a) shows the control result achieved at a separation distance of h. As occurred in the previous examples, the presence of the errors reduced the level of control achieved with the three-element linear virtual microphone to be similar to that achieved with the transfer function virtual microphone. The transfer function virtual microphone achieves 15 dB of attenuation at the virtual

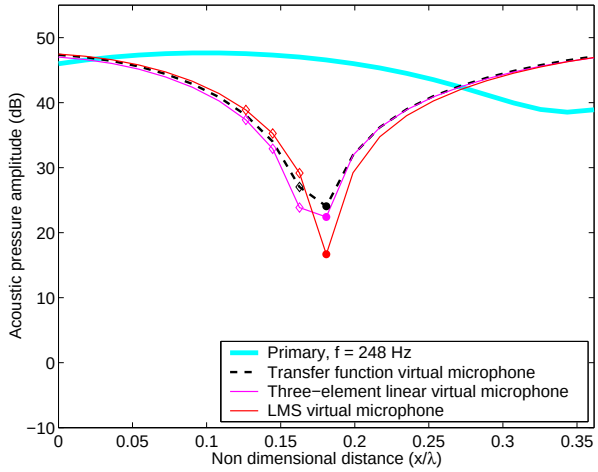

(a) Separation distance - h

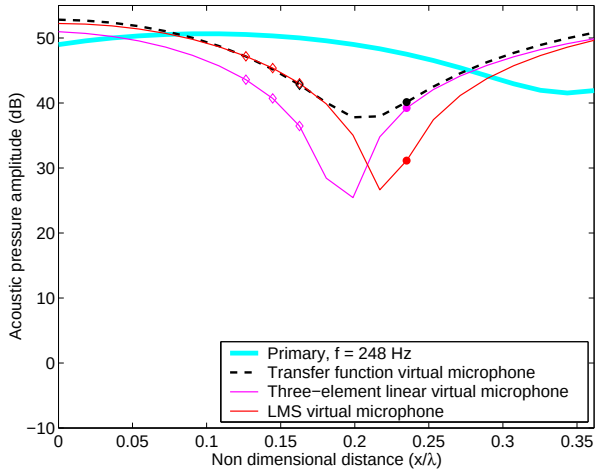

(b) Separation distance - 4h

Figure 7.9: Performance comparison between adaptive, forward-difference and transfer function virtual microphones in a one-dimensional waveguide with absorptive ends for control of an acoustic resonance in the presence of errors. The circles indicate the virtual location and the diamonds represent the location of the prediction microphones.

location while the three-element linear virtual microphone achieves 16 dB of attenuation. The adaptive virtual microphone produces 20 dB of attenuation at the virtual location which is h from the outermost microphone of the array. Figure 7.10(b) presents the results obtained when controlling pressure at a separation distance of $4h$. The use of the three-element linear virtual microphone and the transfer function virtual microphone results in an increase of the primary field of 2 dB while the adaptive virtual microphone achieves 12 dB of attenuation at the virtual location.

7.6.3 Results for a Free Field

7.6.3.1 200 Hz

Figure 7.11 presents a performance comparison of the adaptive, forward-difference and the transfer function virtual microphone when controlling a 200 Hz tone in the free field. With the phase and sensitivity errors present, the linear forward-difference virtual microphone achieves a similar level of attenuation as the transfer function virtual microphone at a separation distance of h as depicted in Figure 7.11(a). Separation distance is defined as the distance between the outer-most prediction microphone and the location of the virtual microphone, and h is 25 mm. The adaptive virtual microphone achieves approximately 5 dB additional attenuation compared to the transfer function and forward-difference virtual microphone at a separation distance of h. Figure 7.11(b) shows that for the separation distance of $4h$, the adaptive virtual microphone achieves approximately 20 dB attenuation which is around 12 dB more than the transfer function virtual microphone. In the presence of the introduced errors the three-element linear virtual microphone achieves 2 dB less attenuation than the transfer function virtual microphone.

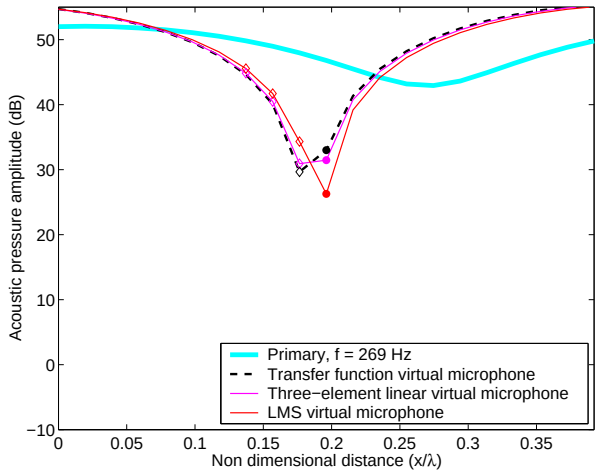

(a) Separation distance - h

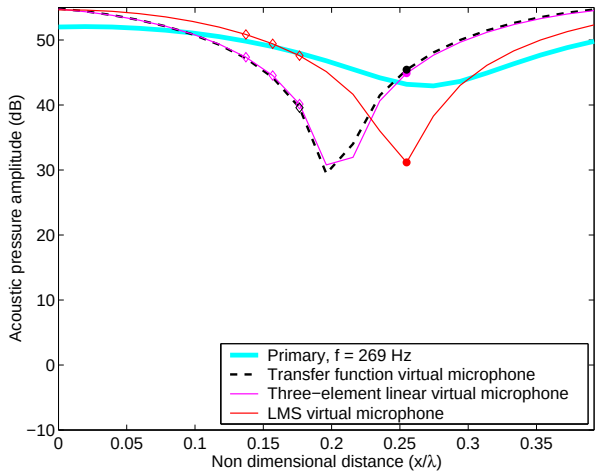

(b) Separation distance - 4h

Figure 7.10: Performance comparison between adaptive, forward-difference and transfer function virtual microphones in a one-dimensional waveguide with absorptive ends for control of an acoustic anti-resonance in the presence of errors. The circles indicate the virtual location and the diamonds represent the location of the prediction microphones.

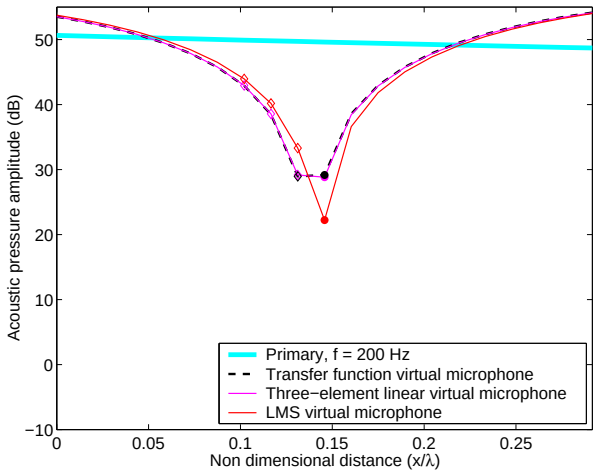

(a) Separation distance - h

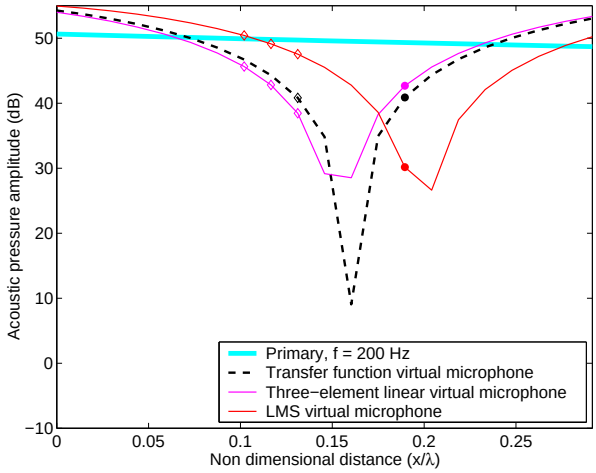

(b) Separation distance - 4h

Figure 7.11: Performance comparison between adaptive, forward-difference and transfer function virtual microphones in a free field at 200 Hz with errors present. The circles indicate the location of the virtual microphone and the diamonds represent the location of the prediction microphones.

7.6.3.2 400 Hz

Figure 7.12 compares the performance of the three-element adaptive virtual microphone, the three-element linear virtual microphone and the transfer function virtual microphone with errors present when controlling a 400 Hz tone in a free field. Figure 7.12(a) depicts the uncontrolled and controlled sound fields produced using the virtual microphones predicting at a separation distance of h with phase and sensitivity errors present. As occurred when controlling a 200 Hz tone, the attenuations achieved using the transfer function and linear virtual microphone are equal. In the presence of errors the attenuation achieved using the three-element linear virtual microphone decreases to 15 dB from 30 dB in an error free environment. The adaptive virtual microphone produces 28 dB attenuation at a separation distance of h. Figure 7.12(b) presents the results obtained when controlling a 400 Hz tone with introduced phase and sensitivity errors. In this case the transfer function virtual microphone marginally outperforms the linear virtual microphone, while the adaptive virtual microphone demonstrates its ability to compensate for the introduced errors with attenuation of 25 dB.

7.6.4 Discussion

In the error free simulations the forward-difference virtual microphone significantly out-performed the transfer function virtual microphone in both a reactive field and a free field. The performance comparison in an error free environment highlighted the deficiency of the transfer function virtual microphone being based on the assumption that $p_p \approx p_{p_v}$. However, one advantage of the transfer function virtual microphone is that it only requires one microphone and therefore is unaffected by phase and sensitivity mismatch between multiple microphones. In this section errors were introduced into the simulation and the performance of the transfer function, three-element linear virtual microphone and the adaptive virtual microphone were compared in a free field and in a reactive field. The presence of errors greatly reduced the level of attenuation achieved with the forward-difference virtual microphone to levels similar

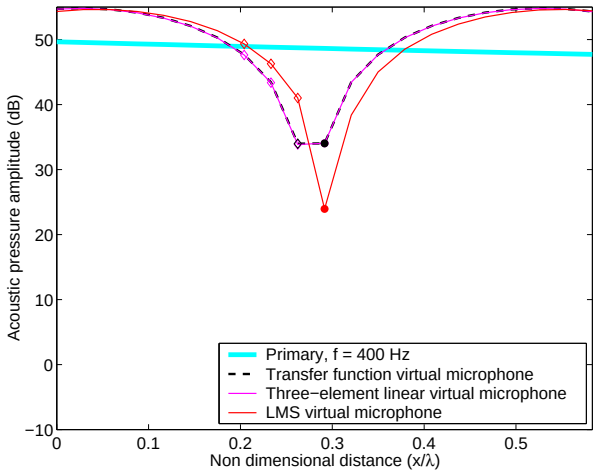

(a) Separation distance - h

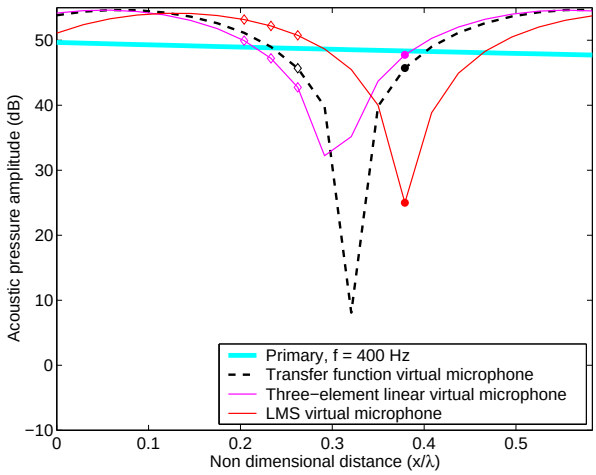

(b) Separation distance - 4h

Figure 7.12: Performance comparison between adaptive, forward-difference and transfer function virtual microphones in a free field at 400 Hz with errors present. The circles indicate the location of the virtual microphone and the diamonds represent the location of the prediction microphones.

to that of the transfer function virtual microphone. The adaptive virtual microphone proved that it was able to partly compensate for the introduced errors and it consistently produced the highest levels of attenuation.

7.7 Conclusion

A performance comparison has been presented between the three-element linear virtual microphone, the transfer function virtual microphone and the adaptive virtual microphone. This comparison was carried out in the reactive environment of a one-dimensional waveguide and in a free field, with and without introduced phase and sensitivity errors. These results were obtained using simulated acoustic response and control.

The results presented for the error free environment indicate that in a reactive sound field, the forward-difference virtual microphone performs significantly better than the transfer function virtual microphone, especially at larger separation distances between the physical microphones and virtual microphone location. This is because the assumption that the primary pressure at the physical microphone location is approximately equal to the primary pressure at the virtual location no longer holds, as the spatial rate of change of pressure in a reactive field can be considerable. The forward-difference virtual microphone predicts the sound pressure at the virtual microphone location by estimating the pressure gradient and this makes the forward-difference method more effective in a reactive environment.

In the free field without introduced errors, the transfer function virtual microphone is more effective than in reactive environments. In the far field at low frequencies, the spatial rate of change is sufficiently low that the assumption upon which the transfer function virtual microphone is based is valid (provided the separation distance is not too large). The comparison between the two methods in the free field still showed the three-element linear virtual microphone to be a much more effective virtual sensor than the transfer function virtual microphone.

With the introduced errors, the level of attenuation achieved with the three-element linear virtual microphone was significantly reduced while the transfer function virtual microphone performance was unaffected in both the free field and reactive field. In the presence of the errors, the three-element linear virtual microphone achieved similar levels of attenuation to those achieved using the transfer function virtual microphone. The adaptive virtual microphone demonstrated an ability to compensate for the introduced errors by producing the highest levels of attenuation in all the examples presented.

Chapter 8

Conclusions and Future Work

8.1 Conclusions

The aim of this thesis was to gain an understanding of the factors which influence the performance of the forward-difference virtual microphones and to use this information to develop novel and robust virtual microphones. The drive behind the development of virtual error sensing techniques comes from the need to provide personal hearing protection for people working within the enclosed sound fields such as aircraft and automobiles. Virtual sensing provides an alternative to the traditional passive headsets and can be an adequate solution to the noise problem without the need to attempt global control of the sound field.

Initial experiments using lower-order linear and quadratic virtual microphones in a real-time control scenario were conducted in a reactive acoustic environment. Results from these experiments indicated that the forward-difference method of predicting the sound pressure level at a location remote to the array of prediction microphones showed promise. However, these results suggested some experimental factors may be affecting the accuracy of the prediction. The real-time control results indicated that the prediction accuracy of both algorithms was compromised by phase and sensitivity mismatches that exist between the transducers in the

prediction array. The use of the linear virtual microphone proved to be the most robust of the two types of virtual microphone. The accuracy of the pressure prediction using the quadratic virtual microphone was adversely affected by the presence of short wavelength extraneous noise. An error analysis was conducted in an attempt to understand why the performance of the prediction algorithms was poor under certain conditions. Results of the error analysis confirmed that the quadratic virtual microphone was more prone to corruption due to calibration and other physical system errors than the linear virtual microphone.

The performance of the lower-order virtual microphones was also assessed using simulated control of analytical models and post-processed experimental transfer functions. Two types of transfer functions were measured; broadband (0 - 400 Hz) and tonal. Results of the simulated control using the broadband transfer functions were extremely poor and showed lower levels of attenuation than was achieved using real-time control, a situation that was completely unexpected. The control results obtained using the tonal transfer function showed results similar to the analytical model results and produced higher levels of attenuation than using real-time control. Further investigation indicated that the post-processed transfer functions obtained using random noise were affected by resolution bias errors.

Following the thorough investigation into the performance of the lower-order virtual microphones, two novel virtual microphone techniques were developed. The first was the higher-order virtual microphone, which still utilised the linear and quadratic prediction algorithms but additional microphone elements were added to the microphone array. This resulted in an over-constrained prediction algorithm which was designed to improve the prediction accuracy of both algorithms by spatially filtering out the short wavelength extraneous noise. The ability of the higher-order virtual microphones to improve prediction accuracy was tested in a one-dimensional waveguide using real-time control. Results from these experiments showed that the higher-order virtual microphones using the linear algorithm greatly improved the prediction accuracy over the lower-order virtual microphones. However, the performance of the higher-order virtual microphones using the over-constrained quadratic prediction algorithm

was disappointing as it resulted in a decrease in the level of attenuation achieved at the virtual location when compared to the results of the lower-order quadratic virtual microphone. The reason for the poor performance of the higher-order quadratic virtual microphone was a result of the increased level of errors (such as phase and sensitivity mismatch) introduced through the use of the extra microphone, thus increasing the likelihood of phase and sensitivity mismatches.

The performances of the lower-order and higher-order virtual microphones were also tested in a free field. These tests were conducted in the anechoic chamber located at The University of Adelaide. Once again, the higher-order virtual microphones using the linear prediction algorithm performed significantly better than higher-order quadratic virtual microphones. There was not a clear improvement in the performance of the linear higher-order virtual microphone compared with the linear lower-order virtual microphone as was observed in the reactive sound field. This is a result of the low rate of spatial change in the primary field in the far field, thus making extra microphones unnecessary to adequately describe the primary sound field.

The second novel virtual microphone technique developed was an adaptive LMS virtual microphone. Real-time experiment results indicated that the accuracy of the forward-difference virtual microphone was influenced by phase and sensitivity mismatch between the elements of the microphone array. To overcome this problem adaptive LMS virtual microphones were investigated. This type of virtual microphone determines the optimal microphone signal weights using the LMS algorithm by placing a microphone at the intended location of the virtual microphone and adapting the weights applied to the signals from the microphone array until the estimated pressure matches the pressure measured at the virtual location. The weights are then fixed and the microphone is removed from the virtual location. This method of determining the microphone weights takes into account the phase, sensitivity and position mismatch that exists in the microphone array whereas the fixed weights of the forward-difference virtual microphones does not.

A SIMULINK model of the adaptive virtual microphone was built to analytically assess its

performance in a reactive sound field. The model allowed the incorporation of phase, sensitivity and position errors to determine how well the adaptive algorithm accommodated for these errors. The results of this study showed that the adaptive algorithm could completely compensate for the sensitivity and position errors and partly compensate for the phase errors. The inability to deal with the phase errors is because the adaptive algorithm only modifies the weights applied to each microphone signal used to predict the remote sound pressure level, and simply modifying the weights cannot compensate for phase errors.

The SIMULINK model also examined the effect that each of the errors has on the fixed weight forward-difference virtual microphones. This work again proved that the quadratic virtual microphone is much more susceptible to gain, phase or position calibration errors than the linear virtual microphone. The adaptive virtual microphone was finally implemented using real-time control in the reactive environment of a one-dimensional waveguide. Results of this investigation were very positive, with a significant increase in the level of attenuation achieved at the virtual location compared to the fixed weight virtual microphones.

Elliott and David (1992) proposed the first virtual microphone which used modified transfer functions to predict the sound pressure at a remote location. The performance of this method was compared to the performance offered by the forward-difference virtual microphone in both the free field and in the reactive environment of the one-dimensional waveguide using analytical models of the sound fields in the absence of errors. The performance of the transfer function virtual microphone was found to be poor in the reactive sound field. This was because this virtual microphone formulation relies on the assumption that the primary pressure at the virtual location and the permanent remote microphone is equal. In a reactive environment this assumption will not hold since there is a high rate of spatial change in the primary sound field. Thus in the reactive environment the linear forward-difference virtual microphone performs significantly better than the transfer function virtual microphone. In the free field, the transfer function virtual microphone performed much better than in the reactive environment, since at low frequencies the spatial rate of change of the primary field is low and thus

the assumption upon which this virtual microphone is based is satisfied. Despite the improved performance in the free field, the transfer function virtual microphone was out-performed by the linear forward-difference virtual microphone. The performance of the transfer function virtual microphone formulation was also compared with that of the forward-difference virtual microphone and the adaptive virtual microphone in the presence of phase and sensitivity errors in both the free field and one-dimensional waveguide. The presence of the introduced errors greatly reduced the level of attenuation achieved using the forward-difference virtual microphone. The performance of the transfer function virtual microphone was unaffected by these introduced errors because it can be implemented with only one microphone. The adaptive virtual microphone consistently produced the highest levels of attenuation in the presence of the errors.

The research presented in this thesis has addressed the issues which arose from previous research on the forward-difference method of virtual sensing and provides a framework to draw on in the development of more practical virtual sensing techniques such as a three-dimensional virtual sensor. It has identified and quantified the errors which affect the accuracy of the prediction of the pressure at the virtual location, which will aid in the development of future novel virtual microphone techniques. The performance of the two novel virtual microphones developed here have been extensively investigated in a real-time control scenario.

8.2 Future Work

8.2.1 Inter-element Spacing

Results presented in this thesis showed that the five element higher-order virtual microphone performed very poorly in real-time control experiments in both the free field and in the reactive environment of the one-dimensional waveguide. This has been attributed to the increased error as a result of phase and sensitivity mismatch. This could also be because the phase

mismatch between the microphones may be greater than the actual phase change across this region. Varying the inter-element spacing of the five element virtual microphone will answer this question.

8.2.2 Testing of Forward-difference Virtual Microphones in the presence of a "*head*"

To date the forward-difference virtual microphones have not been tested in a headrest arrangement using real-time control. Garcia-Bonito et al. (1997b) presented results using the transfer function virtual microphone with a rigid sphere in the diffuse field to represent the head and in a headrest arrangement. This work showed that the presence of the "head" reduces the spatial rate of change of the primary sound field and therefore their transfer function virtual microphone produced a larger zone of attenuation. It would be interesting to observe the performance of the forward-difference virtual microphones in the presence of the "head", especially to determine if the reduction in the spatial gradient will also improve the performance of these virtual sensors.

8.2.3 Three-Dimensional Virtual Microphone

The virtual microphone theory developed in this thesis was focused on one-dimensional virtual sensors and the performance of these sensors was primarily analysed in a one-dimensional sound field. To be a truly effective virtual sensor, a sensor is required which is able to produce remote zones of quiet in a three-dimensional sound field. It is anticipated that the one-dimensional virtual microphones will not perform as well in a three-dimensional sound field and thus the development of a three-dimensional virtual microphone is required. For a linear prediction three-dimensional virtual microphone, the measurement of the pressure gradient is required in each of the three orthogonal directions and possibly cross derivatives, such as $\frac{\partial^2 P}{\partial x \partial y}$, $\frac{\partial^2 P}{\partial x \partial z}$ and $\frac{\partial^2 P}{\partial y \partial z}$ will need to be investigated.

8.2.4 Three- Dimensional Virtual Energy Density Sensors

Kestell (2000) investigated the use of a one-dimensional virtual energy density sensor and found this type of virtual sensor produced a broader zone of quiet than was achieved using virtual microphones. The real-time implementation of a virtual energy density sensor has not yet been investigated. Thus the virtual energy density sensor requires considerably more investigation and development. Ultimately, a three-dimensional virtual energy density sensor could be developed.

8.2.5 Virtual Sensing with a Proximity Sensor

For the virtual sensors to be truly affective in a practical application, the zone of quiet created must be able to move with the movement of the human head. Thus a proximity sensor could be used to track the movement of the head. The use of the proximity sensor with the virtual microphones was first suggested by Kestell (2000). Implementation of the proximity sensor would enable the zone of quiet to follow the movement of the human head, therefore maintaining the zone of quiet at the observer's ear. This could be achieved in conjunction with the adaptive LMS virtual microphone whereby a type of system identification process could be carried out. To produce a practical sized zone of quiet multiple sets of virtual microphones may need to be spaced throughout the region where control is required. The use of multiple sets of virtual microphones producing a zone of quiet at the virtual location should result in a spatially larger zone of attenuation as well as greatly improving the robustness of the virtual sensing system. A number of possible locations of the head within a confined spatial region could be identified and the adaptive algorithm could be used to determine the optimum weights for each location for the zone of quiet. Once the active control system is working with the proximity sensor, the proximity sensor could determine the location of the head with respect to the locations for which the optimal weights are known and appropriate weights could be applied using a look up table.

8.2.6 Higher-order Virtual Microphone Error Analysis

An error analysis similar to that presented in Chapter 4 could be performed for the higher-order virtual microphones. This analysis would give insight into how the extra microphones affect the prediction accuracy.

The equations for the normalised inherent error for the three element linear virtual microphone at all separation distances are:

$$e(p_{0h}) = \frac{h^2k^2}{6} - \frac{7h^4k^4}{72} + \frac{h^3k^3}{6}\tan(kx) \tag{8.1}$$

$$e(p_{1h}) = \frac{5h^2k^2}{3} - \frac{71h^4k^4}{36} + \frac{7h^3k^3}{3}\tan(kx) \tag{8.2}$$

$$e(p_{2h}) = \frac{25h^2k^2}{6} - \frac{727h^4k^4}{72} + \frac{17h^3k^3}{2}\tan(kx) \tag{8.3}$$

$$e(p_{3h}) = \frac{23h^2k^2}{3} - \frac{1151h^4k^4}{36} + \frac{62h^3k^3}{3}\tan(kx) \tag{8.4}$$

$$e(p_{4h}) = \frac{43h^2k^2}{6} - \frac{5623h^4k^4}{72} + \frac{245h^3k^3}{6}\tan(kx) \tag{8.5}$$

Figure 8.1 presents the inherent error for the two and three element linear virtual microphone in a one-dimensional reactive sound field. It is interesting to note that the inherent error for the three element linear virtual microphone is much larger than the two element linear virtual microphone. Also the higher-order virtual microphone has inherent errors at a separation distance of $0h$ as a result of the over-constrained formulation. Experimental results presented in Chapter 5 showed a reduction in the performance of the higher-order virtual microphones at $0h$ compared with the lower-order virtual microphones.

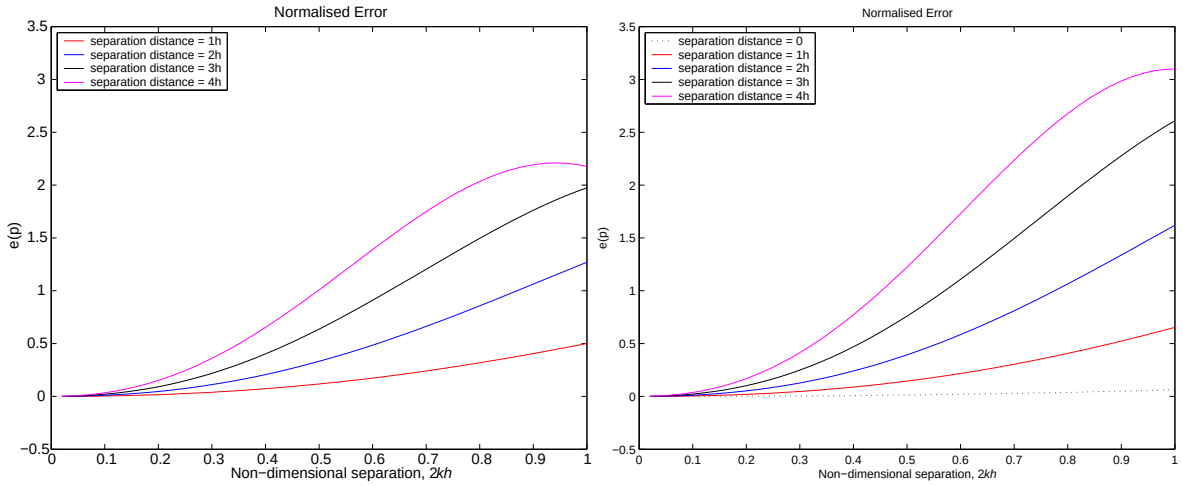

(a) Two Microphone *(b) Three Microphone*

Figure 8.1: Inherent errors of the linear virtual microphones as a function of the non-dimensional separation distance (2kh) for a reactive one-dimensional sound field with $x/L = 1/4$.

Bibliography

C. Bao and J. Pan. Use of adaptive filters in active ear defenders. In *Inter-noise 96*, pages 1175–1178, Liverpool, UK, 1996.

J. S. Bendat and A. G. Piersol. *Engineering applications of correlation and spectral analysis*. John Wiley and Sons Inc., second edition, 1993.

J.S. Bendat and A.G. Piersol. *Random Data: Analysis and Measurement Procedures*. John Wiley and Sons, 1971.

A. Berry, X. Qui, and C. H. Hansen. Near-field pressure, intensity and wavenumber distributions for active control of structural acoustic control of plate radiation. *Journal of the Acoustical Society of America*, 106(6):3394–3406, 1999.

G. V. Borgiotti. The power radiated by a vibrating body in an acoustic fluid and its determination from boundary measurements. *Journal of the Acoustical Society of America*, 88(4): 1884–1893, October 1990.

A.J. Brammer, G.J. Pan, and R.B. Crabtree. Adaptive feedforward active noise reduction headset for low frequency noise. In *Active 97*, pages 365–372, Budapest, Hungary, 1997.

M. Brothanek and O. Jiricek. Formating of zones of quiet around a head simulator. In *Active 2002, ISVR, Southampton, UK*, 15-17 July 2002.

A.J. Bullmore, P.A. Nelson, A.R.D. Curtis, and S.J. Elliott. The active minimisation of harmonic enclosed sound fields, part II: A computer simulation. *Journal of Sound and Vibration*, 117(1):15–33, 1987.

A.J. Bullmore, P.A. Nelson, and S.J. Elliott. Theoretical studies of the active control of propeller-induced cabin noise. *Journal of Sound and Vibration*, 140(2):191–217, 1990.

S. E. Burke and J. E. Jr. Hubbard. Distributed transducer vibration control of thin plates. *Journal of the Acoustical Society of America*, 90(2):937–944, 1991.

B. S. Cazzolato and C. H. Hansen. Structural sensing of sound transmission into a cavity for active structural-acoustic control. In *Proceedings of the Fifth International Congress on Sound and Vibration*, pages 2391–2401, 1997.

B.S. Cazzolato. *Sensing systems for active control of sound transmission into cavities*. Ph.D. Thesis, The University of Adelaide, Adelaide, South Australia, April 1999.

B.S. Cazzolato and C.H. Hansen. Active control of sound transmission using structural error sensing. *Journal of the Acoustical Society of America*, 104(5):2878–2889, 1998.

B.S. Cazzolato and C.H. Hansen. Errors arising from three-dimensional energy density sensing in one-dimensional sound fields. *Journal of Sound and Vibration*, 236(3):375–400, 2000a.

B.S. Cazzolato and C.H. Hansen. Errors in the measurement of acoustic energy density in one-dimensional sound fields. *Journal of Sound and Vibration*, 236(5):801–831, 2000b.

B.S. Cazzolato and C.H. Hansen. Active control of enclosed sound fields using three-axis energy density sensors. *accepted for publication by the International Journal of Acoustics and Vibration*, 2003.

F. Charette, A. Berry, and C. Guigou. Active control of sound radiation from a plate using a polyvinylidene flouride volume displacement sensor. *Journal of the Acoustical Society of America*, 103(3):1493–1503, 1998.

F. Charette, C. Guigou, and A. Berry. Development of volume velocity sensors for plates using PVDF film. In *Proceedings of Active 95*, pages 241–252, 1995.

R. L. Clark and C. R. Fuller. Control of sound radiation with adaptive structures. *Journal of Intelligent Material Systems and Structures*, 2:431–452, July 1991.

R. L. Clark and C. R. Fuller. Active structural acoustic control with adaptive structures including wavenumber considerations. *Journal of Intelligent Materials Systems and Structures*, 3:296–315, April 1992a.

R. L. Clark and C. R. Fuller. Modal sensing of efficient acoustic radiators with polyvinylidene fluoride distributed sensors in active structural acoustic control approaches. *Journal of the Acoustical Society of America*, 91(6):3321–3329, June 1992b.

K. A. Cunefare. The minimum radiation efficiency of baffled finite beams. *Journal of the Acoustical Society of America*, 90(2194-2204), 1991.

K. A. Cunefare and M. N. Currey. On the exterior acoustic radiation modes of structures. *Journal of the Acoustical Society of America*, 96(4):2302–2312, October 1994.

A. David and S.J. Elliott. Numerical studies of actively generated quiet zones. *Applied Acoustics*, 41(1):63–79, 1994.

S.J. Elliott, A.R.D. Curtis, A.J. Bullmore, and P.A. Nelson. The active minimisation of harmonic enclosed sound fields, Part III: Experimental verification. *Journal of Sound and Vibration*, 117(1):35–58, 1987.

S.J. Elliott and A. David. A virtual microphone arrangement for local active sound control. In *1st International Conference on Motion and Vibration Control*, pages 1027–1031, Yokohama, Japan, September 1992.

S.J. Elliott and J. Garcia-Bonito. Active cancellation of pressure and pressure gradient in a diffuse sound field. *Journal of Sound and Vibration*, 186(4):696–704, 1995.

S.J. Elliott and M.E. Johnson. Radiation modes and the active control of sound power. *Journal of the Acoustical Society of America*, 94(4):2194–2204, October 1993.

S.J. Elliott, P. Joseph, A.J. Bullmore, and P.A. Nelson. Active cancellation at a point in a pure tone diffuse sound field. *Journal of Sound and Vibration*, 120(1):183–189, 1988.

S.J. Elliott and P.A. Nelson. The active control of enclosed sound fields. In *Proceedings of Noise-Con 87*, pages 359–364, 1987.

F.J. Fahy. *Sound Intensity*. E and FN Spon, London, 2nd edition, 1995.

C. R. Fuller, C. H. Hansen, and S. D. Snyder. Active control of sound radiation from a vibrating rectangular panel by sound sources and vibrational inputs: An experimental comparsion. *Journal of Sound and Vibration*, 145(2):195–215, 1991.

C. R. Fuller and J. D. Jones. Experiments on reduction of propeller induced interior noise by active control of cylinder vibration. *Journal of Sound and Vibration*, 112(3):389–395, 1987.

C. R. Fuller, C. A. Rogers, and H. H. Robertshaw. Active structural acoustic control with smart structures. In *Proceedings of SPIE Conference on Fiber Optic Smart Structurs and Skins II, VOl. 1170*, pages 338–358, 1989a.

C. R. Fuller, R. J. Silcox, V. L. Metcalf, and D.E. Brown. Experiments on structural control of sound transmitted through an elastic plate. In *Proceedings of the American Control Conference*, pages 2079–2084, 1989b.

J. Garcia-Bonito, S. J. Elliott, and M. Bonilha. Active cancellation of pressure at a point in a pure diffracted diffuse sound field. *Journal of Sound and Vibration*, 201(1):43–65, 1997a.

J. Garcia-Bonito and S.J. Elliott. Local active control of diffracted diffuse sound fields. *Journal of the Acoustical Society of America*, 98(2):1017–1024, 1995a.

J. Garcia-Bonito and S.J. Elliott. Strategies for local active control in diffuse sound fields. In *Proceedings of Active 95*, pages 561–572, 1995b.

J. Garcia-Bonito, S.J. Elliott, and C.C. Boucher. A virtual microphone arrangement in a practical active headrest. In *Proceedings of Inter-noise 96*, pages 1115–1120, 1996.

J. Garcia-Bonito, S.J. Elliott, and C.C. Boucher. Generation of zones of quiet using a virtual microphone arrangement. *Journal of the Acoustical Society of America*, 101(6):3498–3516, 1997b.

J. Ghan, B.S. Cazzolato, and S. Snyder. Expression for the estimation of time-averaged acoustic energy density using the two-microphone method. *Submitted to Journal of the Acoustical Society of America*, 2002.

J. Ghan, B.S. Cazzolato, and S.D. Snyder. Statistical errors in the estimation of time-averaged acoustic energy density using the two-microphone method. *Submitted to Journal of the Acoustical Society of America*, 2003.

C. Guigou, Z. Li, and C. R. Fuller. The relationship between volume velocity and far-field radiated pressure of a planar structure. *Journal of Sound and Vibration*, 197(2):252–254, 1996.

J. Guo, J. Pan, and M. Hodgson. Local or global control - the applicable active noise control strategy in enclosed environments. In *Active 2002*, pages 93–104, 15-17 July 2002.

C.H. Hansen and S.D. Snyder. *Active control of noise and vibration*. E and FN Spon, London, 1997.

S. Johansson, P. Persson, and I. Claesson. Active control of propeller-induced noise in an aircraft mock-up. In *Active 99*, pages 741–752, 1999.

S. Johansson and M. Winberg. A new active headset for helicopter applications. In *5th International Congress on Sound and Vibration*. The University of Adelaide, Adelaide, Australia 1997.

M. E. Johnson and S. J. Elliott. Volume velocity snesors for active control. *Proc. Inst. Acoust.*, 15(3):411–420, 1993.

J. D. Jones and C. R. Fuller. Active control of sound fields in elastic cylinders by multicontrol forces. *AIAA Journal*, 27(7), 1989.

P. Joseph, S. J. Elliott, and P. A. Nelson. Near field zones of quiet. *Journal of the Acoustical Society of America*, 172(5):605–627, 1994.

S.W. Kang and Y.H. Kim. Active intensity control for the reduction of reduction of radiated duct noise. *Journal of Sound and Vibration*, 201(5):595–611, 1997.

C. D. Kestell. *Active control of sound in a light aircraft cabin with virtual sensors*. PhD thesis, The University of Adelaide, Adelaide, Australia, 2000.

C.D. Kestell, B.S. Cazzolato, and C.H. Hansen. Active noise control with virtual sensors in a long narrow duct. *International Journal of Acoustics and Vibration*, 5(2):63–76, 2000.

C.D. Kestell, B.S. Cazzolato, and C.H. Hansen. Active noise control in a free field with virtual sensors. *Journal of the Acoustical Society of America*, 109(1):232–243, 2001a.

C.D. Kestell, B.S. Cazzolato, and C.H. Hansen. Virtual sensors in active noise control. *Journal of the Australian Acoustical Society*, 29(2):57–61, 2001b.

C.D. Kestell and C.H. Hansen. Active noise control with virtual sensors. In *Proceedings of the 8th ICSV, Hong Kong*, 2001.

R. Koehler. *Intensity error sensing in the active control of free field sound radiation*. PhD thesis, Department of Mechanical Engineering, The University of Adelaide, Australia, 2001.

H. Kuttruff. *Room acoustics*. Spon Press, London UK, 2000.

C. K. Lee and F. C. Moon. Modal sensors/actuators. *Transactions of the ASME*, 57:434–440, June 1990.

J.P. Maillard and C.R. Fuller. Comparison of two structural sensing approaches for active structural acoustic control. *Journal of the Acoustical Society of America*, 103(1):396–400, 1998.

M. Miyoshi, J. Shimizu, and N. Koizumi. One arrangements of noise-controlled points for producing larger quiet zones with multi-point active noise control. In *Inter-noise 94*, pages 1299–1304, Yokohama, Japan, August 1994.

M. L. Munjal. *Acoustics of ducts and mufflers*. 1987.

P.J. Nashif and S.D. Sommerfeldt. An active control strategy for minimising the energy density in enclosures. In *Proceedings of Inter Noise 92*, pages 357–361, 1992.

P.A. Nelson, A.R.D. Curtis, S.J. Elliott, and A.J. Bullmore. The active minimization of harmonic enclose sound fields part 1: Theory, part 2: A computer simulation part 3,: Experimental verification. *Journal of Sound and Vibration*, 117(1):1–13, 15–33, 35–58, 1987a.

P.A. Nelson, A.R.D. Curtis, S.J. Elliott, and A.J. Bullmore. The active minimization of harmonic enclosed sound fields, part I: Theory. *Journal of Sound and Vibration*, 117(1): 1–13, 1987b.

P.A. Nelson and S.J. Elliott. *Active Control of Sound*. Academic Press, London, 1992.

H. F. Olson and E. G. May. Electronic sound absorber. *The Journal of the Acoustical Society of America*, 25(6):1130–1136, November 1953.

G.J. Pan, A.J. Brammer, J. Zera, and R. Goubran. Application of adaptive feed-forward active noise control to a circumaural hearing protector. In *Active 95*, pages 1319–1326, Newport Beach, CA, USA, 06-08 July 1995 1995.

Y.C. Park and S.D. Sommerfeldt. Global attenuation of broadband noise fields using energy density control. *Journal of the Acoustical Society of America*, 101(1):350–359, 1997.

J. W. Parkins, S. D. Sommerfeldt, and J. Tichy. Narrowband and broadband acoustic control in an enclosure using the acoustic energy density. *Journal of the Acoustical Society of America*, 108(1):192–203, July 2000a.

J. W. Parkins, J. Tichy, and S. D. Sommerfeldt. A comparison of two active control methods through an investigation of node structures. In *Active 99, Fort Lauderdale, USA*, 1999.

J.W. Parkins. *Active minimization of energy density in a three dimensional enclosure*. PhD thesis, Pennsylvania State University, 1998.

J.W. Parkins, S.D. Sommerfeldt, and J. Tichy. Error analysis of a practical energy density sensor. *Journal of the Acoustical Society of America*, 108(1):211–222, 2000b.

W.H. Press, S.A. Teukolsky, W.T. Vetterling, and B.P. Flannery. *Numerial Recipes in C - The art of scientific computing*. Cambridge University Press, Cambridge, UK, 1992.

X. Qui and C. H. Hansen. An adaptive sound intensity control algorithm for active control of transformer noise. In *Fifth International Congress on Sound and Vibration*, Adelaide, Australia, 1997.

X. Qui, C. H. Hansen, and X. Li. A comparsion of near-field acoustic error sensing strategies for active control of harmonic free field radiation. *Journal of Sound and Vibration*, 215(1): 81–103, 1998.

B. Rafaely. Active noise reducing headset - an overview. In *Inter-noise 2001*, The Hague, The Netherlands, 2001.

B. Rafaely, J. Garcia-Bonito, and S.J. Elliott. Feedback control of sound in headrest. In *Active 97*, pages 445–456, Budapest, Hungary, August 1997.

B. Rafaely, J. Garcia-Bonito, and S.J. Elliott. Broadband performance of an active headrest. *Journal of the Acoustical Society of America*, 106(2):787–793, August 1999.

B. Rafaely and M. Jones. Combined feedback-feedforward active noise reducing headsets - The effect of the acoustics on broadband performance. *Journal of the Acoustical Society of America*, 112(3):981–989, September 2002.

K.M. Reichard, D.C. Swanson, and S.M. Hirsch. Control of acoustic intensity using the frequency domain filtered-x algorithm. In *Active 95*, pages 395–406, Newport Beach, USA, July 1995.

J. Rex and S. J. Elliott. The qwsis - a new snesor for structural radiation control. In 339-343, editor, *1st International Conference of Motion and Vibration Control*, 1992.

C. F. Ross. *Active control of sound.* PhD thesis, Cambridge University, England, 1980.

D.J. Rossetti and M.A. Norris. A comparison of actuation and sensing techniques for aircraft cabin noise control. *Noise Control Engineering Journal*, 44(1):53–58, 1996.

A. Roure and A. Albarrazin. The remote microphone technique for active noise control. In *Active 99*, pages 1233–1244, 1999.

S. D. Snyder and C. H. Hansen. Mechanisms of active control by vibration sources. *Journal of Sound and Vibration*, 147(3):519–525, 1991a.

S.D. Snyder, C. H. Hansen, and G. Volalek. *EZ-ANC II User's Guide*. Causal Systems, 2000.

S.D. Snyder, C.H. Hansen, and N. Tanaka. Shaped sensors for feedforward control of structural radiation. In *The second conference on recent advances in active control*, Blacksburg, VA, 1993. Virginia Tech.

S.D. Snyder and N. Tanaka. Calculating total acoustic power using modal radiation efficienies. *Journal of the Acoustical Society of America*, 97(3):1702–1709, March 1995.

S. D. Sommerfeldt and J. W. Parkins. An evaluation of active noise attenuation in rectangular enclosures. In *Inter-noise 94*, pages 1351–1356, Yokohama, Japan, 1994.

S.D. Sommerfeldt and P.J. Nashif. A comparision of control strategies for minimising the sound field in enclosures. In *Proceedings of Noise-Con 91*, pages 299–306, 1991.

S.D. Sommerfeldt and P.J. Nashif. An adaptive filtered-x algorithm for energy based active control. *Journal of the Acoustical Society of America*, 96(1):300–306, 1994.

S.D. Sommerfeldt, J.W. Parkins, and Y.C. Park. Global active noise control in rectangular enclosures. In *Proceedings of Active 95*, pages 477–488, 1995.

J. Sullivan, J. E. Jr. Hubbard, and S. Burke. Modelling approach for two-dimensional distributed transducers of arbitary spatial distribution. *Journal fo the Acoustical Society of America*, 99(5):2965–2974, 1999.

J. Q. Sun, M. A. Norris, D. J. Rossetti, and J. H. Highfill. Distributed piezoelectric actuators for shell interior noise. *Transactions of the ASME*, 118(3):676–681, October 1996.

D.C. Swanson. Active control of acoustic intensity using a frequency domain filtered-x algorithm. In *Inter-noise 94*, pages 1253–1258, Yokohama, Japan, August 1994.

N. Tanaka, S.D. Snyder, and C. H. Hansen. Distributed parameter modal filtering using smart sensors. *Journal of vibration and acoustics*, 118:630–640, October 1996.

D. R. Thomas, P. A. Nelson, and S. J. Elliott. Active control of the transmission of sound through a thin cylindrical shell, part i: The minimisation of vibrational energy. *Journal of Sound and Vibration*, 167(1):91–111, 1993a.

D. R. Thomas, P. A. Nelson, and Elliott S. J. Active control of the transmission of sound through a thin cylindrical shell, part ii: The minimisation of acoustic potential energy. *Journal of Sound and Vibration*, 167(1):113–128, 1993b.

B. Tseng, W. Rafaely and S.J. Elliott. Performance limits and real-time implementation of a virtual microphone active headrest. In *Active 2002*, pages 1231–1242, 15-17 July 2002.

Appendix A

Error Analysis

A.1 Inherent Errors

A.1.1 One-dimensional Reactive Sound Field

The pressure fluctuation of a one-dimensional harmonic sound field is given by

$$p(x,t) = P_o cos(kx)\Re\left\{e^{j\omega t}\right\} \tag{A.1}$$

where ω is the harmonic frequency of excitation and where k is the wavenumber. Therefore the pressure fluctuation from Equation A.1 can be written as

$$p(x,t) = P_o \cos(kx)\cos(\omega t) \tag{A.2}$$

Differentiating Equation A.1 with respect to x yields the pressure and gradients

$$P = P_o \cos(kx) \tag{A.3}$$

$$P^{(1)} = -kP_o \sin(kx) \tag{A.4}$$

$$P^{(2)} = -k^2 P\cos(kx) = -k^2 P \tag{A.5}$$

$$P^{(3)} = -k^3 P\sin(kx) = -k^2 P^{(1)} \tag{A.6}$$

A.1.1.1 Linear Virtual Microphone

For the case of two microphones separated by $2h$ predicting the pressure at a distance of h, the pressure at h is given by

$$p_e = 1.5p_5 - 0.5p_1 \tag{A.7}$$

where $p_5 = p(x-h)$ and $p_1 = p(x-3h)$. The Taylors series expansion of p_1 and p_5 is given by

$$p_1 = P - 3hP^{(1)} + \frac{(3h)^2}{2}P^{(2)} - \frac{(3h)^3}{6}P^{(3)} + \frac{(3h)^4}{24}P^{(4)} + .. \tag{A.8}$$

$$p_5 = P - hP^{(1)} + \frac{(h)^2}{2}P^{(2)} - \frac{(h)^3}{6}P^{(3)} + \frac{(h)^4}{24}P^{(4)} + .. \tag{A.9}$$

Substituting Equations A.8 and A.9 into Equation A.7 yields

$$p_e = P - 1.5h^2P^{(2)} + 2h^3P^{(3)} - 1.625h^4P^{(4)} \tag{A.10}$$

Therefore using the pressure and pressure gradients the normalised error in the estimate of p is given by

$$e(p) = \frac{p_e - p}{p} \tag{A.11}$$

By substituting Equations (A.3) to (A.6) into Equation (A.11), the normalised error in the estimate of p at a separation distance of h is given by

$$e(p_h) = \frac{3h^2k^2}{2} - \frac{13h^4k^4}{8} + 2h^3k^3\tan(kx) \tag{A.12}$$

The above procedure is repeated for all separation distances.

A.1.1.2 Quadratic Virtual Microphone

For the case of three microphones each separated by h predicting the pressure at a distance of h, the estimated pressure at h is given by

$$p_e = p_1 - 3p_3 + 3p_5 \tag{A.13}$$

where $p_1 = x - 3h$, $p_3 = x - 2h$ and $p_5 = x - h$. The Taylors Series expansion of p_1, p_3 and p_5 is

$$p_1 = P - 3hP^{(1)} + \frac{(3h)^2}{2}P^{(2)} - \frac{(3h)^3}{6}P^{(3)} + \frac{(3h)^4}{24}P^{(4)} + .. \tag{A.14}$$

$$p_3 = P - 2hP^{(1)} + \frac{(2h)^2}{2}P^{(2)} - \frac{(2h)^3}{6}P^{(3)} + \frac{(2h)^4}{24}P^{(4)} + .. \tag{A.15}$$

$$p_5 = P - hP^{(1)} + \frac{(h)^2}{2}P^{(2)} - \frac{(h)^3}{6}P^{(3)} + \frac{(h)^4}{24}P^{(4)} + .. \tag{A.16}$$

Thus

$$p_e = P - h^3P^{(3)} + \frac{3}{2}h^4P^{(4)} \tag{A.17}$$

The normalised error for a quadratic prediction algorithm at a separation distance of h is calculated by substituting Equation (A.17) into Equation (A.11) and thus is given by:

$$e(p_h) = \frac{3h^4k^4}{2} + h^3k^3\tan(kx) \tag{A.18}$$

A.1.2 Plane Progressive Wave

Plane waves can be defined by

$$p(x,t) = \Re\left\{P_o e^{j\omega t - jkx}\right\} \tag{A.19}$$

The pressure and pressure gradients

$$P = P_o e^{jkx} \tag{A.20}$$

$$P^{(1)} = -jkP \tag{A.21}$$

$$P^{(2)} = -k^2P \tag{A.22}$$

$$P^{(3)} = jk^3P = -k^2P^{(1)} \tag{A.23}$$

A.1.2.1 Linear Virtual Microphone

Considering only the separation distance of h, the normalised error in the pressure estimate is calculated using the same method described in Section A.1.1.1 by inserting Equations (A.20) to (A.23) into Equation (A.11). Therefore the Taylors series expansion of the estimated pressure at the virtual location is given by Equation A.10 and therefore the normalised virtual pressure error is

$$e(p_h) = \frac{3h^2k^2}{2} - \frac{13h^4k^4}{8} + 2jh^3k^3 \tag{A.24}$$

A.1.2.2 Quadratic Virtual Microphone

The normalised error in the pressure estimate using a quadratic virtual microphone in plane wave conditions is calculated using the same procedure as outlined in Section A.1.1.2 but using the pressure and pressure gradients (Equations (A.20) to (A.23))that describe a plane wave field. This yields an analytical expression for the normalised error at a separation distance of h using a quadratic virtual microphone of:

$$e(p_h) = -jh^3k^3 + \frac{3h^4k^4}{2} \tag{A.25}$$

A.2 Phase Errors

In the case of simple harmonic fields the pressure responses of the two microphones with a phase mismatch of $2\phi_s$ are given by the products of the true pressures with $e^{\pm j\phi_s}$, that is

$$\hat{p}_1(x,t) = p_1(x,t)e^{j\phi_s} \tag{A.26}$$

$$\hat{p}_5(x,t) = p_5(x,t)e^{-j\phi_s} \tag{A.27}$$

The effect of phase mismatch errors depends upon the relative magnitudes of the phase mismatch and the actual phase difference of the sound pressure at the sensor locations.

A.2.1 One-dimensional Reactive Sound Field

A.2.1.1 Linear Virtual Microphone

As with the other derivations presented above, an example derivative for the linear virtual microphone with phase mismatch at a separation distance of h will be presented.

$$\widehat{p_e} = P_o 1.5\cos(kx-kh)\cos(\omega t-\phi_s) - P_o 0.5\cos(kx-3kh)\cos(\omega t+\phi_s) \tag{A.28}$$

Expanding the time dependent terms gives

$$\begin{aligned}\widehat{p_e} &= P_o 1.5\cos(kx-kh)[\cos(\omega t)\cos(\phi_s)+\sin(\omega t)\sin(\phi_s)] \\ &- P_o 0.5\cos(kx-3kh)[\cos(\omega t)\cos(\phi_s)-\sin(\omega t)\sin(\phi_s)]\end{aligned} \tag{A.29}$$

For small ϕ_s then $\cos(\phi_s) = 1 - \frac{\phi_s^{1/2}}{2} + ... \approx 1$ and $\sin(\phi_s) \approx \phi_s$ therefore the pressure estimate becomes

$$\begin{aligned} \widehat{p_e} &= P_o 1.5\cos(kx-kh)[\cos(\omega t)+\sin(\omega t)\phi_s] \\ &- P_o 0.5\cos(kx-3kh)[\cos(\omega t)-\sin(\omega t)\phi_s] \end{aligned} \tag{A.30}$$

Rearranging

$$\begin{aligned} \widehat{p_e} &= P_o\cos(\omega t)[1.5\cos(kx-kh)-0.5\cos(kx-3kh)] \\ &+ P_o\sin(\omega t)\phi_s[1.5\cos(kx-kh)+0.5\cos(kx-3kh)] \end{aligned} \tag{A.31}$$

The first term in the above expression is the virtual pressure estimate without any phase error present; therefore the pressure estimate can be written as

$$\widehat{p_e} = p_e + \alpha_{p2} \tag{A.32}$$

and normalised error in the estimate of $\widehat{p_e}$ is given by

$$e(\widehat{p}) = \frac{\widehat{p_e} - p}{p} \tag{A.33}$$

where α is the additional error due to phase mismatch and hence the normalised error at a separation distance of h using a linear virtual microphone is

$$e(\widehat{p_h}) = e(p_h) + \phi_s j\sec(kx)(-1.5\cos(kx-kh)-0.5\cos(kx-3kh)) \tag{A.34}$$

A.2.1.2 Quadratic Virtual Microphone

The equation estimating the pressure at a separation distance of $1h$ using a quadratic virtual microphone with total microphone mismatch of $2\phi_s$ is

$$\widehat{p_e} = P_o(\cos(kx-kh))\cos(\omega t+\phi_s)) - 3P_o(\cos(kx-2kh))\cos(\omega t)) + 3P_o(\cos(kx-3kh))\cos(\omega t-\phi_s)) \tag{A.35}$$

Expanding the time dependent terms gives

$$\begin{aligned} \widehat{p_e} &= P_o\cos(kx-kh)[\cos(\omega t)\cos(\phi_s)+\sin(\omega t)\sin(\phi_s)] \\ &+ 3P_o\cos(kx-3kh)[\cos(\omega t)\cos(\phi_s)-\sin(\omega t)\sin(\phi_s)] \\ &- 3P_o\cos(kx-2kh)\cos(\omega t) \end{aligned} \tag{A.36}$$

For small ϕ_s than $\cos(\phi_s) = 1 - \frac{\phi_s^{1/2}}{2} + \ldots \approx 1$ and $\sin(\phi_s) \approx \phi_s$ therefore the pressure estimate becomes

$$\begin{aligned} \widehat{p_e} &= P_o\cos(\omega t)[\cos(kx-kh) - 3\cos(kx-2kh) + 3\cos(kx-3kh)] \\ &+ P_o\sin(\omega t)[\cos(kx-kh) + 3\cos(kx-3kh)] \end{aligned} \tag{A.37}$$

The first term in Equation (A.37) is the virtual pressure estimate without any phase error present; therefore as in the linear virtual microphone case, the pressure estimate can be written as

$$\widehat{p_e} = p_e + \alpha_{p3} \tag{A.38}$$

The normalised error using a quadratic virtual microphone at a separation distance of h with phase mismatch between the transducers is given by:

$$e(\widehat{p_h}) = e(p_h) + j\phi_s\sec(kx)(3\cos(kx-kh) - \cos(kx-3kh)) \tag{A.39}$$

A.2.2 Plane Progressive Wave

A.2.2.1 Linear Virtual Microphone

In a plane progressive wave, phase mismatch between sensors corresponds to a modification of the sensor separation distance such that $k\hat{h} = kh - \phi_s$. The normalised error can be calculated using the procedure described in Section A.1.2 substituting $k\hat{h}$ for kh**.** At a separation distance of h the normalised error for a linear virtual microphone with phase mismatch is

$$e(p_h) = \frac{3}{2}\widehat{h}^2k^2 + 2j\widehat{h}^3k^3 - \frac{13}{8}\widehat{h}^4k^4 \tag{A.40}$$

A.3 Sensitivity Errors

Sensitivity differences between microphone elements may affect the accuracy of the pressure estimation at the virtual location. The pressure sum and difference are altered in both phase and magnitude by sensitivity mismatch (Fahy, 1995). Let the sensitivity difference between the two transducers be $\pm T$ such that the ratio of the sensitivities is given by $(1+T)/(1-T) \approx 1+2T$ for small T

$$\widetilde{p}_1 = p_1(x,t)(1-T) \qquad \widetilde{p}_5 = p_5(x,t)(1+T) \tag{A.41}$$

A.3.1 One-dimensional Reactive Sound Field

A.3.1.1 Linear Virtual Microphone

For a separation distance of h, the estimated pressure at the virtual location with sensitivity mismatch between the elements is

$$\widetilde{p}_e = 1.5\widetilde{p}_5 - 0.5\widetilde{p}_1 = 1.5P_o\cos(kx-kh)(1+T) - 0.5P_o\cos(kx-3kh)(1-T) \tag{A.42}$$

Expanding the sensitivity terms yields

$$\widetilde{p}_e = P_o(1.5\cos(kx-kh) - 0.5\cos(kx-3kh)) + P_oT(1.5\cos(kx-kh) + 0.5\cos(kx-3kh)) \tag{A.43}$$

The first term in Equation (A.43) is the pressure estimate without the sensitivity mismatch and thus this equation can be written as follows

$$\widetilde{p}_e = p_e + \beta_{p2} \tag{A.44}$$

where β_{p2} is the additional error as a result of the sensitivity mismatch.

$$\beta_{p2} = P_oT(1.5\cos(kx-kh) + 0.5\cos(kx-3kh)) \tag{A.45}$$

Using Equation (A.33) the normalised error for the linear virtual microphone with sensitivity mismatch is

$$e(\widetilde{p}_h) = e(p_h) + T\sec(kx)(1.5\cos(kx-kh) + 0.5\cos(kx-3kh)) \tag{A.46}$$

A.3.1.2 Quadratic Virtual Microphone

For the three element quadratic virtual microphone with sensitivity mismatch, the estimated pressure at h is given by

$$\widetilde{p}_e = P_o(\cos(kx-kh))(1+T) - 3P_o(\cos(kx-2kh)) + 3P_o(\cos(kx-3kh))(1-T) \tag{A.47}$$

Expanding sensitivity terms yields

$$\widetilde{p}_e = P_o(\cos(kx-kh) - 3\cos(kx-2kh) + 3\cos(kx-3kh)) + P_oT(\cos(kx-kh) - 3\cos(kx-3kh)) \tag{A.48}$$

The first term in Equation (A.48) is the pressure estimate without the sensitivity mismatch, therefore

$$\widetilde{p}_e = p_e + \beta_{p3} \tag{A.49}$$

where β_{p3} is the additional error as a result of the sensitivity mismatch.

$$\beta_{p3} = P_o T(\cos(kx-kh) - 3\cos(kx-3kh)) \tag{A.50}$$

Using Equation (A.33) the normalised error for the quadratic virtual microphone with sensitivity mismatch is

$$e(\widetilde{p}_h) \quad = \quad e(p_h) + T\sec(kx)(3\cos(kx-kh) - \cos(kx-3kh)) \tag{A.51}$$

A.3.2 Plane Progressive Wave

A.3.2.1 Linear Virtual Microphone

The prediction equation for the linear virtual microphone with a separation distance of *h* with sensitivity mismatch is given by

$$\widetilde{p}_e = 1.5\widetilde{p}_5 - 0.5\widetilde{p}_1 = 1.5p_5(1+T) - 0.5p_1(1-T) \tag{A.52}$$

Expanding sensitivity terms yields

$$\widetilde{p}_e = 1.5p_5 - 0.5p_1 + T(1.5p_5 + 0.5p_1) \tag{A.53}$$

The first term in the above expression is the equation for the pressure estimate without the sensitivity mismatch and therefore

$$\widetilde{p}_e = p_e + \beta_{p2} \tag{A.54}$$

where β_{p2} is the additional error due to the sensitivity mismatch, given by

$$\beta_{p2} = T(1.5p_5 + 0.5p_1) \tag{A.55}$$

The normalised error of the pressure estimate is calculated using the same method outlined in Section A.1.2 using Equation (A.33) which yields

$$e(\widetilde{p}_h) = e(p_h) + T(1 + 3jhk + 3h^2k^2 - \frac{5}{2}jh^3k^3 + \frac{7}{4}h^4k^4) \tag{A.56}$$

A.3.2.2 Quadratic Virtual Microphone

The pressure estimate using a quadratic virtual microphone at a separation distance of *h* with sensitivity mismatch is given by

$$\widetilde{p}_e = 3\widetilde{p}_5 - 3p_3 + \widetilde{p}_1 = 3p_5(1+T) - 3p_3 + p_1(1-T) \tag{A.57}$$

Expanding sensitivity terms yields

$$\widetilde{p}_e = p_1 - 3p_3 + 3p_5 + T(p_1 + 3p_5) \tag{A.58}$$

The first term in the above expression is the equation for the pressure estimate without the sensitivity mismatch and therefore

$$\widetilde{p}_e = p_e + \beta_{p3} \tag{A.59}$$

where β_{p3} is the additional error due to the sensitivity mismatch, given by

$$\beta_{p3} = T(p_1 + 3p_5) \tag{A.60}$$

The normalised error of the pressure estimate is calculated using the same method outlined in Section A.1.2 using Equation (A.33) which yields

$$e(\widetilde{p}_h) = e(p_h) + T\left(1 + 3h^2k^2 + 4jh^3k^3 - \frac{13h^4k^4}{4}\right) \tag{A.61}$$

Appendix B

Publications arising from this thesis

This section lists the publications from international journals and conference proceedings that have directly resulted from the work undertaken for the thesis.

B.1 International Journals

J.M. Munn, B.S. Cazzolato, C.D. Kestell, and C.H. Hansen. Virtual error sensing for active noise control in a one-dimensional waveguide: Performance prediction vs. measurement. *Journal of the Acoustical Society of America.*, 113(1):35-38, 2003.

B.2 Refereed Conference Papers

J.M. Munn, B.S. Cazzolato, C.D. Kestell, and C.H. Hansen. Real-time feedforward active control using virtual sensors in a long narrow duct. In *Proceedings of the Australian Acoustical Society Annual Conference, Canberra*, Australia, 2001

J.M. Munn, B.S. Cazzolato, and C.H. Hansen. Virtual sensing: Open loop versus adaptive LMS. In *Proceedings of the Australian Acoustical Society Annual Conference,* Adelaide, Australia, 2002

J.M. Munn, B.S. Cazzolato, and C.H. Hansen. Virtual sensing using an adaptive LMS algorithm. In *Proceedings of the Wespac VIII* Melbourne, Australia, 2003

B.3 International Conference Papers

J.M. Munn, B.S. Cazzolato, C.D. Kestell, and C.H. Hansen. Real-time feedforward active noise control using virtual sensors. In *Proceedings of the 2001 International Congress and Exhibition on Noise Control Engineering,* The Hague, The Netherlands, 2001

J.M. Munn, B.S. Cazzolato, C.D. Kestell, and C.H. Hansen. Higher-order virtual sensing for remote active noise control. In *Proceedings of Active 2002,* ISVR, Southampton, UK, 2002

Appendix C

Glossary

Vectors and martices and vectors are shown in bold face

Symbol	Description
a	coefficient
$\mathbf{a}_2, \mathbf{a}_{2o}, \mathbf{a}_{3o}$	coefficient
b	coefficient
c	coefficient
c_o	speed of sound in air
e	error signal
$e(p)$	normalised error
f	frequency
h	microphone spacing
$\mathbf{H}_2, \mathbf{H}_{2o}, \mathbf{H}_3$	matrix of microphone locations
j	complex number
J	cost function
k	wavenumber, iteration number
L_x	length of the duct
L_y	width of the duct

L_z	breadth of the duct
m	modal index
n	modal index
o	model index
p	acoustic pressure
p_e	estimated pressure
$\widehat{p}_e$	estimated pressure with phase mismatch
$\widetilde{p}_e$	estimated pressure with sensitivity mismatch
p_p	primary (uncontrolled) pressure
p_v	estimated acoustic pressure at the virtual location
p_r	free field pressure amplitude
$\mathbf{p}_2, \mathbf{p}_3$	vector of acoustic pressure
P_o	pressure magnitude
q	source strength
$\mathbf{q}$	optimal control source strength
r	distance from source
t	time
T	sensitivity mismatch
$\mathbf{w}$	microphone weights
x	spatial location of microphones, co-ordinate direction
x_v	separation distance
$\mathbf{x}$	microphone location, input
y	co-ordinate direction, measured pressure
y_{est}	estimated pressure
z	co-ordinate direction
$\mathbf{Z}$	transfer impedence matrix
α	leakage coefficient
α_{p2}, α_{p3}	addition error due to phase mismatch

β_{p2}, β_{p3}	additional error due to sensitivity mismatch
μ	convergence coefficient
ϕ_s	phase mismatch
$\varepsilon_x, \varepsilon_y, \varepsilon_z$	normalisation factors
ω	angular frequency
ψ	acoustic mode shapes
ρ_o	density of air
λ	wavelength